Low-temperature experimental studies in molecular biophysics: a review

Yu. P. Blagoi, G. G. Sheina, A. Yu. Ivanov, E. D. Radchenko,
M. V. Kosevich, V. S. Shelkovsky, O. A. Boryak, and Yu. V. Rubin

*B. Verkin Institute for Low Temperature Physics and Engineering, National Academy of Sciences of the Ukraine, 310164 Kharkov, Ukraine**)
(Submitted April 7, 1999)
Fiz. Nizk. Temp. **25**, 1003–1020 (October 1999)

The enormous contribution of Academician Boris I. Verkin in laying the foundation of the biophysics research school in Kharkov are recalled in the Jubilee year commemorating his 80th birthday. This review describes the development and realization of his ideas during the last two decades at Molecular Biophysics Department of the Institute for Low Temperature Physics and Engineering (ILTPE) in Kharkov. Main results of the studies of physical and chemical properties of biopolymer fragments and biologically active compounds using methods of low-temperature electron–vibrational spectroscopy, low-temperature secondary-emission mass spectrometry, and low-temperature luminescence spectroscopy are presented. [S1063-777X(99)00110-3]

1. INTRODUCTION

The multi-faceted talent of Academician Boris Ieremievich Verkin was manifested, among other things, in his interest in the application of physical ideas, techniques and methods for studying the physics of biological molecules. His untiring organizational activity over the entire span of his creative lifetime culminated in the foundation of the biophysical research school in Kharkov, which won widespread recognition in the erstwhile USSR as well as abroad. Several biophysics research departments were opened at the Institute for Low Temperature Physics and Engineering (ILTPE) at the end of 1960's. The chair of molecular and applied biophysics at the Radiophysics Faculty of the Kharkov State University was instituted in 1978, and Boris Ieremievich was its head for several years. In 1972, the Institute of Cryobiological and Cryomedical Problems was opened in Kharkov by the Ukrainian Academy of Sciences with the support of B. I. Verkin. Kharkov became the center and meeting point of scientific fraternity comprising specialists in the field of biophysics. The Departments of Biophysics at the Institute of Radiophysics and Electronics and ILTPE of the Ukrainian Academy of Sciences organized seven All-Union conferences on the ''Spectroscopy of Biopolymers,'' five seminar-cum-schools on the biophysics of nucleic acids, and two schools on the application of mass spectrometry in biology and medicine. The Institute of Cryobiological and Cryomedical Problems organized several International Conferences on ''Achievements and Prospects of Growth in Cryobiology and Cryomedicine Research.'' Academician B. I. Verkin was a member of the Organizing Committees of these scientific forums.

Under the guidance of B. I. Verkin, scientists at ILTPE completed several academic projects on fundamental research in the field of biopolymer physics. The results of these investigations were published in several hundred scientific papers,[1] generalized in monographs,[2–4] and used in many important economic programs on the application of cryogenic technologies in agriculture, food industry, medicine, and fabrication of medical and cryosurgical instruments.[5,6]

At the behest and under the guidance of B. I. Verkin, new experimental and theoretical methods developed earlier in the physics of condensed state and low temperatures at ILTPE were applied for studying the physical properties of biomacromolecules and their components. Beginning from 1969, various problems in biophysics were studied in several departments of ILTPE under the supervision of leading specialists in various branches of physics, e.g., physics of the liquid state (head of department Yu. P. Blagoi), physics of biological molecular crystals (head of department B. Ya. Sukharevskii), tunnel spectroscopy (head of department I. K. Yanson), molecular interaction of biomolecules (head of department L. F. Sukhodub), theory of the properties of biological macromolecules (head of department A. M. Kosevich), and theory of superconductivity (head of department I. O. Kulik). These investigations are being carried out even today in the department of molecular biophysics headed by Yu. P. Blagoi.[4] New unorthodox and unique techniques in tunnel spectroscopy, temperature-dependent field mass-spectroscopy, low-temperature quartz resonator, vibrational spectroscopy of molecules isolated in the host matrix of solidified inert gases, and luminescence spectroscopy were developed and successfully used for solving a number of problems. Many new results were obtained from the molecular biophysics research with active participation, persistent interest and support of Boris Ieremievich.

Conformational and phase transitions in polymer DNA's were studied experimentally and theoretically. The interaction of native DNA with synthetic oligonucleotides with heavy metal ions was investigated. The heat capacity of DNA and proteins was studied for the first time in the temperature interval 4.2–400 K, and the dynamics of DNA considered in the glass-type model. A series of pioneering works was aimed at studying the energetics of molecular interaction

of nitrogenous bases simulating intramolecular interaction in DNA and RNA, hydration of bases, evaluation of the contribution from various types of interactions to the stabilization of the DNA molecular structure. The inelastic tunnel spectroscopy method was used to study the energy spectra of nitrous bases. The interaction of DNA and its components with pharmacological, chemical and therapeutical preparations and dyes was studied and the molecular mechanism of action of many anticancerous preparations was determined.

Many inventions associated with the fabrication of cryosurgical instrument and application of cryogrinding and sublimative drying in food industry were patented.[1]

Over the years, the research activity started by B. I. Verkin has continued to develop. Special attention has been paid to the use of experimental low-temperature technology. For example, the method of matrix isolation was considerably modified for investigating thermally unstable molecules, and a new method of low-temperature mass spectroscopy involving bombardment of fast atoms was developed for studying frozen aqueous solutions of biologically active compounds. The present review is aimed at describing the main results obtained with the help of the above-mentioned methods of biophysical research.

2. LOW-TEMPERATURE HIGH-RESOLUTION OPTICAL SPECTROSCOPY OF ISOMERIC AND CONFORMATIONAL TRANSITIONS IN NUCLEOTIDE BASES AND AMINO ACIDS

The application of modern methods of low-temperature experiment, which are not conventional for molecular biology studies, has shed new light on the properties of biological objects. Many important questions concerning the storage and reproduction of genetic information are connected with the isomeric nature of the simplest fragments of biopolymers in various molecular surroundings. Spectroscopic methods are the most effective among the wide range of physical methods used for studying molecular isomerism. In many cases, the low-temperature matrix isolation spectroscopy offers the only possibility of recording isomers of isolated molecules. This technique was employed for the first time in the biophysics department of ILTPE in 1981[7–10] and was developed side by side with other European and American research centers,[11–13] thus laying the foundations of a new trend in the matrix isolation spectroscopy, viz., the low-temperature spectroscopy of isolated bio-organic molecules.

Under conditions of matrix isolation, the method of low-temperature molecular spectroscopy has received wide recognition owing to a number of unique advantages over standard spectroscopic techniques. It is based on freezing of the gaseous phase of the molecules under investigation in a rigid inert medium (matrix), which considerably reduces the width of spectral bands due to weakening of molecular interaction and the absence of rotational broadening. This phenomenon is illustrated quite well in the infrared absorption spectra of uracil obtained in gaseous phase,[14] amorphous film, as well as in Ar matrix (Fig. 1). The high resolution of spectra in the matrix makes it possible to isolate the nearly degenerate spectral bands which completely overlap one another in other states of aggregation. A significant advantage of the

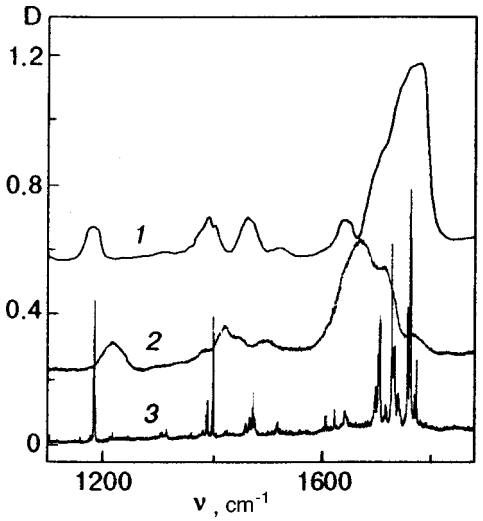

FIG. 1. IR Fourier spectra of uracil in different states of aggregation: *1*–gaseous phase, $T=570$ K[14] (curve *1*), amorphous uracil film $T=12$ K (curve *2*), *3*—Ar matrix for molar ratio $M=1:1000$, $T=12$ K, D is the optical density and ν the wave number (curve *3*).

spectroscopy of matrix isolation in comparison with the gaseous phase spectroscopy is its high sensitivity and lower temperatures of evaporation of the thermally unstable bio-organic materials under investigation. The required amount of the substance is accumulated over a long time in the matrix. At low temperatures, the matrix acts as a trap for various isomers of the evaporating substance. The efficiency of this trap depends on the height of the barriers between energy states of isomers and temperature of the matrix. Hence the temperature must be below 10 K for the investigated low-barrier conformational isomers.

In order to realize the potentialities of the modern technique, two universal setups were developed. One of them is based on the modernized IR spectrophotometer Specord-IR 75 and the UV spectrophotometer Hitachi-M65. The other is based on the evacuated Fourier spectrometer FS-01. Unlike the widely used closed-cycle microrefrigerators which also lower the temperature to 10 K, we cooled multiple position holders of optical substrates by using helium cryostats designed at the experimental construction bureau of ILTPE, which were capable of cooling the substrate to 3 K and providing several matrix samples.

In addition to the traditional Ar, Kr, and Xe matrices, we also used in our experiments Ne matrices requiring temperatures below 5 K. The obtained matrix samples were transparent over a wide spectral range from vacuum ultraviolet (UV) to far infrared (IR) region. An important part of the devices designed by the authors is a low-temperature differential quartz microbalance (QMB) having a sensitivity of 10^{-9} g/Hz, used for measuring the rate of condensation of sample components and thus for obtaining the required concentration of substances in the matrix with a high degree of accuracy. The QMB were directly calibrated at 5 K,[15] which made it possible to carry out experiments on the measurement of absolute intensities of absorption bands in infrared spectra of isolated bases and amino acids.[15,16]

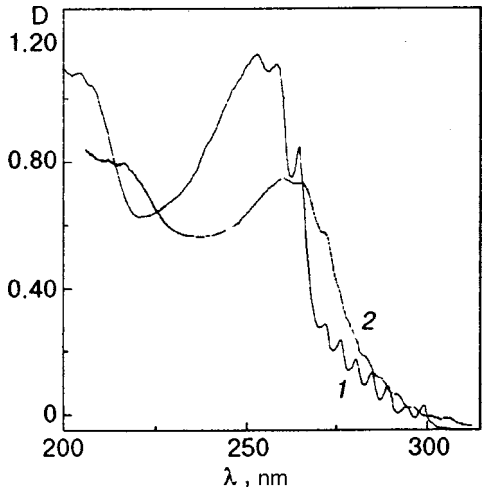

FIG. 2. Electron-vibration spectra of cytosine in Ar matrix at $T=12$ K, curve *1* corresponds to $M=1:500$ and curve *2* to $M=1:50$.

2.1. Ultraviolet absorption spectra and electron transitions of nucleotide bases in Ar matrices

Traditional methods of UV spectroscopy are not useful for solving a number of problems in molecular biophysics. Hence we used the low-temperature technique for directly observing electron transitions responsible for charge transport in complexes of nucleotide bases. The interaction of bases with a strong electron acceptor revealed specific broad absorption bands whose peaks are linearly connected with the ionization potential of nucleotide bases.[17,18] The experimental proof for the formation of purine and pyrimidine bases of complexes with charge transfer can be used for considering the possibility of charge transport in stacks of DNA bases and intercalating biologically active compounds.

The longwave band of the absorption spectrum of a cytosine film at 77 K differs considerably from that of cytosine in solutions. Studies of the electron absorption bands of pyrimidine nucleotide bases under conditions of weak molecular interaction in inert matrices at low temperatures showed that electron absorption spectra of cytosine, 1-methylcytosine, isocytosine, 2-oxy-and 2-aminopyrimidine, uracil, and thymine in argon matrices have broad longwave absorption bands with a well-defined vibrational structure[8] (curve *1* in Fig. 2). The obtained values of the low-frequency vibron bands correspond to the 0–0 electron transition in the compounds under investigation. Theoretical computations of the electron spectra of nucleotide bases available in literature can be compared correctly only with the values for the electron transition obtained in inert matrices. An increase in the concentration of matter in matrices causes a broadening of vibron bands and their smoothing, as well as the disappearance of the vibrational structure (curve *2* in Fig. 2). A distinguishing feature of the electron spectra of pyrimidine bases in argon matrices is a clear manifestation of the $n\pi^*$ absorption bands with a well-developed vibrational structure (curve *1* in Fig. 2, $\nu_{00}\simeq 300$ nm). These bands are connected with the transitions of *n*-electrons of heterocyclic nitrogen on π^* level of the pyrimidine ring as a result of excitation. The formation of hydrogen bonds in homoassociates (curve *2* in Fig. 2) decreases the intensity of the $n\pi^*$ bands, blurs the vibrational structure and displaces the bands towards the shortwave spectral region. However, the identification of isomers of nucleotide bases from the absorption spectra in the UV region is complicated. Hence it was necessary to use the vibrational characteristics of molecules which help in identifying the structure of one-ion molecules and their isomers.

2.2. Studies of rare prototropic tautomers of bases of nucleic acids and model compounds

In 1953 Watson and Crick[19] proposed the molecular mechanism of violation of the precision of copying the genetic information through tautomeric transitions. However, rare tautomers of nucleotide bases were not observed experimentally although the presence of carbonyl and amino groups as well as heterocyclic nitrogen in molecules leads to the possibility of formation of tautomers. High-resolution vibrational spectra were obtained for the canonical bases of nucleic acids and over 20 model compounds.[7,9,10,20–29] It was found that, in the isolated state, some of the nucleotide bases exist in the form of two structures in thermodynamic equilibrium, viz., the traditional ketoamine structure and the amino-enol structure which was discovered experimentally for the first time.[7,10,20] Owing to the high resolution of the matrix isolation spectroscopy and the characteristic nature of the vibrational bands of the proton-donor groups, the tautomerism is determined unequivocally right at the level of the phenomenological group-function analysis with the help of IR spectra of auxiliary compounds. The proton participating in the tautomeric transition is easily identified by replacing it with the methyl group in 1-methylcytosine (Fig. 3).[20] In this case, peaks of OH^- as well as N_1H vibrations ($\nu=3468\ \mathrm{cm}^{-1}$) disappear. The remaining two bands correspond to the vibrations of the NH_2 group, their frequencies coinciding with the frequencies of the corresponding peaks of 2-aminopyrimidine. Such an analysis (Fig. 4) together with the calculations of the vibrational spectra led to the discovery of rare enol tautomers of 9-methylguanine,[22] isocytosine,[26] and hypoxanthine.[23,26] The intensities of the spectral bands were used to determine the keto-enol equilibrium constants for studying the molecules (see Table I). It was shown that guanine and hypoxanthine have the peculiar property of existing in two tautomeric forms. A transition of these molecules to the enol form can apparently cause the formation of ''incorrect'' pairs in DNA and lead to a violation of the genetic code.

2.3. Molecular interactions of nucleotide bases and their model compounds in matrices

The spectroscopy of matrix isolation offers great potentialities for studying the spectral characteristics of homoassociates, and of hydrogen-bound complexes in particular. Broad bands of hydrogen-bound vibrations with a low peak intensity are seen clearly in autocomplexes of cytosine, 1-methylcytosine and uracil.[27] Investigations of spectral characteristics of model molecules in argon matrices over a wide range of concentrations (1:1000–1:60) and tempera-

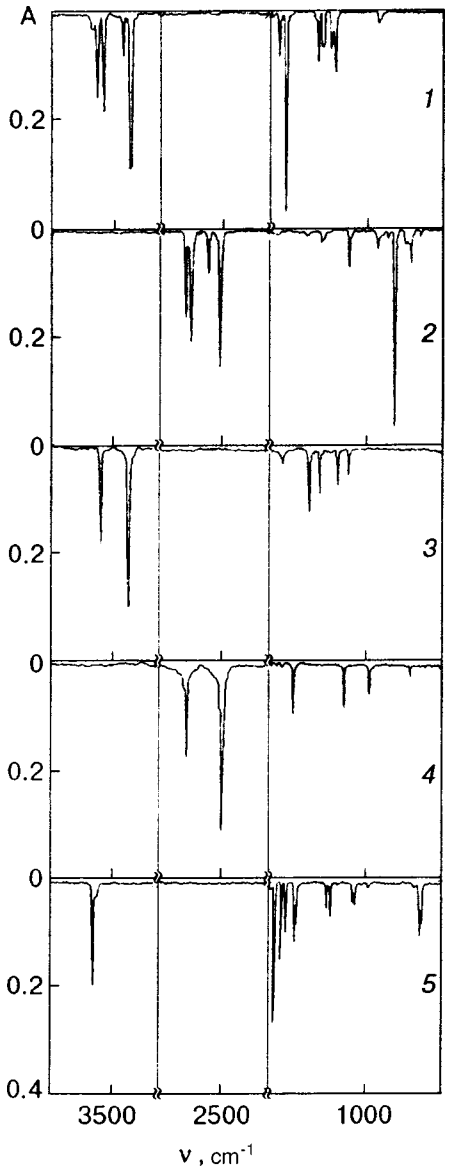

FIG. 3. IR transmission spectra of tautomers of cytosine (curve *1*), deuterocytasine (curve *2*), 1-methyl cytosine (curve *3*), 1-methyl deuterocytosine (curve *4*), and 2-oxypyrimidine (curve *5*) in Ar matrix; *A* is the transmission coefficient.

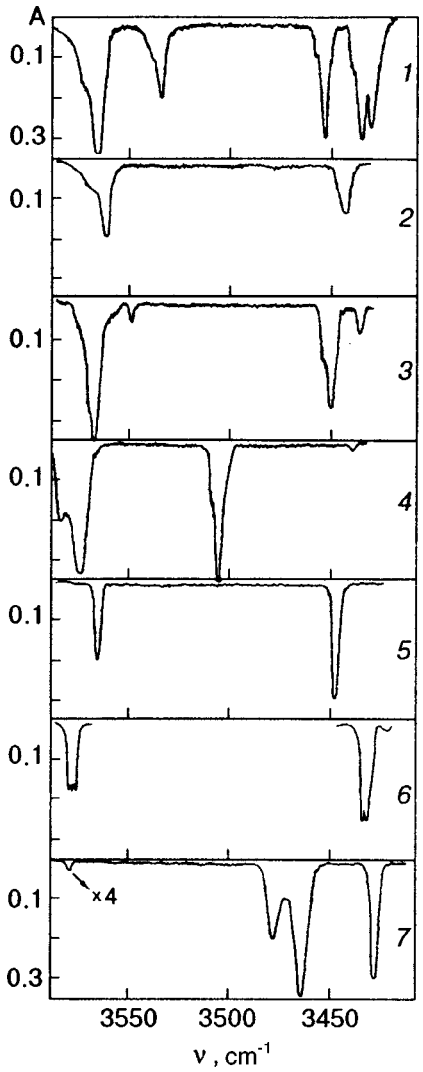

FIG. 4. IR spectra of tautomers of 9-methylguanine (curve *1*), N_2-9-trimethylguanine (curve *2*), isocytosine (curve *3*), N_2-methylisocytosine (curve *4*), 2-aminopyrimidine (curve *5*), 4-oxypyrimidine (curve *6*), and hypoxanthine (curve *7*) in Ar matrix.

tures (12–30 K) led to quantitative data on the composition of multimers in matrices.[30] It was shown that the hydrogen-bound complexes of phenols in Ar matrix, in the concentration range 1:500–1:100, are mainly represented by dimers. Upon annealing of the Ar matrix with impurity molecules of geometric size of benzene or naphthalene type, orientational diffusion of impurity molecules dominates and translational diffusion does not take place in the temperature interval 25–30 K. The quantitative experimental data obtained by MacCarthy *et al.*[31,32] on the association of molecules in matrices made it possible to study the mechanism of coupling of pyrimidine dimers. It was shown that the main contribution to the coupling during the formation of dimers of pyrimidine and 2-oxypyrimidine in Ar-matrix comes from paired Van der Waals interactions, and stacking structures of associates are formed in this case. At the same time, oxy-derivatives of benzene form predominantly hydrogen-bound dimers in matrices with the benzene rings oriented in a single plane. The experimentally observed peculiarity of formation of pyrimidine bases of stacking dimers in matrices correlates with the stacking structure of pyrimidine and purine bases in the DNA molecule.

TABLE I. Thermodynamic parameters of the Keto-Enol equilibrium in nucleotide bases. K_{eq} is the equilibrium constant at evaporation temperature T_{ev}, ΔH is the difference enthalpy, and ΔS the difference entropy.

Compound	T_{ev}·K	K_{eq}	ΔH kJ/mol	ΔS J/mol.deg
Cytosine	473	0.5	-	-
Isocytosine	458	0.16	6.3	−1.5
2-oxypyrimidine	393	0.033	10.5	−1.65
9-methyl guanyl	540	0.74	-	-
Hypoxanthine	553	32.2	−13.0	5.4

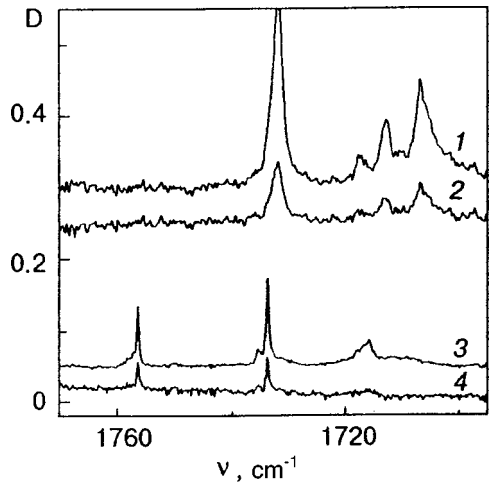

FIG. 5. Effect of evaporation temperature on the population density of isocytosine and 2-oxypyrimidine tautomers. Spectrum *1* is the IR Fourier spectrum of isocytosine in Ar matrix ($T=12$ K, $M=1:1000$) at evaporation temperature $T_{ev}=378$ K, spectrum *2* is the difference spectrum at $T_{ev}=458$ K, spectrum *3* is the spectrum of 2-oxypyrimidine in Ne matrix ($T=5$ K, $M=1:800$) at $T_{ev}=315$ K, and spectrum *4* is the difference spectrum at $T_{ev}=380$ K.

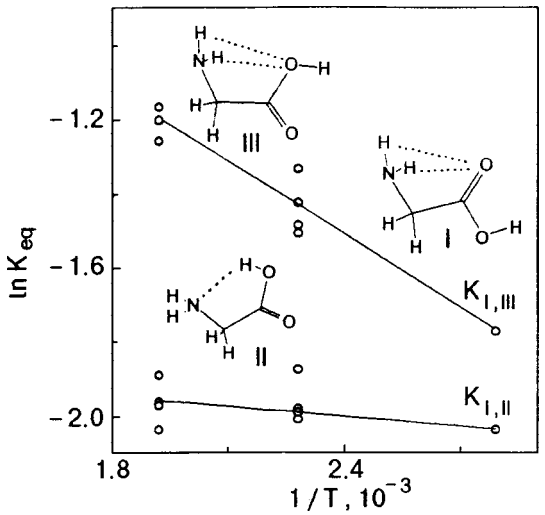

FIG. 6. Temperature dependence of the equilibrium constants of glycine II and III conformers.

2.4. Experimental evaluation of the thermodynamic parameters of prototropic tautomers of bases and glycine conformers from the data of infrared absorption spectra in matrices

Experimental evaluation of equilibrium constants, difference enthalpies, and entropies of isomers in the isolated state, for which only data of quantum-chemical calculations were available earlier, is of considerable practical significance. Such experimental and theoretical studies were extended widely to highly volatile thermally stable compounds, but have not been used so far for bio-organic molecules. To solve this problem, the matrix isolation technique was perfected and measurements were made for thermally unstable pyrimidine and purine bases and amino acids. The temperature dependence of tautomeric equilibrium constant of the gaseous phase, which can be fixed precisely in the low-temperature matrix, can be obtained by varying the evaporation temperature. The temperature variation range was extended ($\Delta T=80-120$ K) by using Knudsen cells of various efficiencies.[16] In order to determine the temperature dependence of the equilibrium constant, all matrix spectra were reduced to the same intensity of the bands of one of the tautomers, and departure from equilibrium was measured from the ratios of intensities of bands of the second tautomer. It can be seen in Fig. 5 that an increase in the evaporation temperature increases the intensity of the C=O valence vibrations, and hence the population density of the less stable keto-forms of 2-oxypyrimidine and isocytosine. The formation of tautomers in the Knudsen cell occurs as a result of rupture of molecular hydrogen bonds accompanied by the transport of a proton between molecules. The proton transport in an isolated molecule and analogous redistribution of the population of tautomers were achieved by exposing the matrix sample to shortwave ultraviolet radiation ($\lambda<240$ nm), which made it possible to determine the ratio of the molar absorption coefficients for bands of OH^-, NH^- valence vibrations and hence the keto-enol equilibrium constants K_{eq} at the evaporation temperature T_{ev} (see Table 1). These data were used to determine the difference enthalpies ΔH and entropies ΔS of tautomers of 2-oxypyrimidine, isocytosine[33] and hypoxanthine (see Table 1).

Amino acids exist in the form of polar zwitterion structure in crystalline state and in solutions, but are transformed into conformationally immobile neutral molecular form in the gaseous phase.[34,35] In this case, the matrix isolation technique made it possible to obtain the vibrational spectra of amino acids of aliphatic series[16,36–42] and to record the low-barrier conformer[29] of glycine III (Fig. 6). The conformers of glycine I and II (Fig. 6) with intramolecular hydrogen bond were first detected experimentally by microwave spectroscopic techniques.[35] However, the low thermal stability of glycine and the low sensitivity of the gaseous phase spectroscopy hamper the investigations of thermodynamic characteristics of conformers. Apart from Knudsen cells of different efficiencies,[16] the hot nozzle technique,[43] which increases the upper threshold of the molecular beam temperature due to the short duration for which molecules remain in the hot band, was also used for varying the temperature of glycine molecular beam. Earlier, this method was used only for highly volatile molecules which were in gaseous phase at room temperature. In order to increase the temperature of the molecular beam of glycine, a heat exchanger was installed between the vaporization cell and the low-temperature mirror substrate. The van't Hoff temperature dependences of the conformational equilibrium constants $K_{I,II}$ and $K_{I,III}$ are shown in Fig. 6. These data led to the following values: $\Delta H_{I,II}=0.8$ and $\Delta H_{I,III}=5.5$ kJ/mole, as well as $\Delta S_{I,II}=-14.7$, $\Delta S_{I,III}=0.12$ J/(mole·K).[16] The considerably high value of $\Delta S_{I,II}$ can be due to a significant contribution of the low-frequency torsional vibrations about the C–C bond to the vibrational entropy of the conformer I. This correlates with the experimental data[16,39,41] which show that the barrier of rotation around this bond is much higher than in conformer II owing to a strong intramolecular hydrogen bond

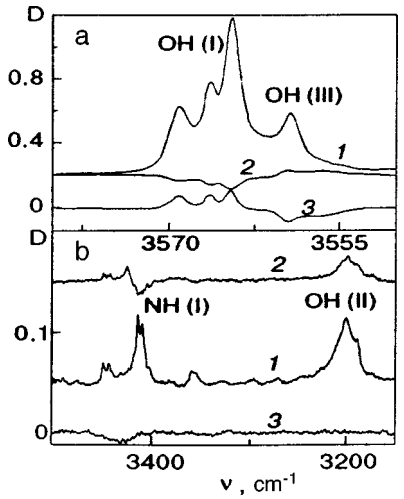

FIG. 7. IR Fourier spectrum of glycine in Ar matrix ($T=12$ K, $M=1:500$) in the region of valence OH-vibrations (a) and valence NH_2-vibrations (b). Curve *1* is the spectrum before UV irradiation of the sample, curve *2* is the difference spectrum after exposure, curve *3* is the difference spectrum after annealing of the exposed sample at 20 K.

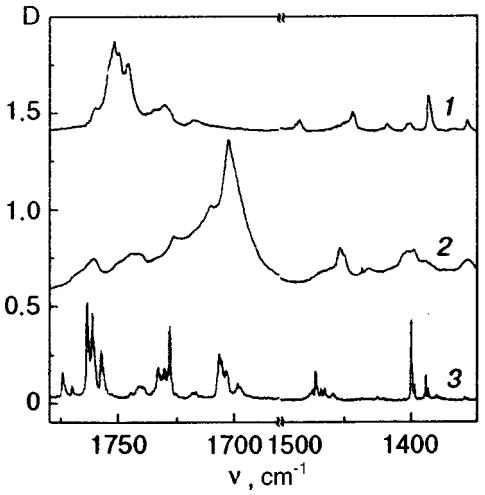

FIG. 8. Broadening of bands in the IR-Fourier spectra of nonplanar molecules in Ar matrix ($T=12$ K, $M=1:500$). Curves *1*, *2* and *3* correspond to uridine, 5,6-dihydrouracil, and uracil, respectively.

N–HO. The considerable difference in the vibrational entropies between conformers of type I and II is also characteristic of other amino acids of the aliphatic series.

2.5. Effect of inert matrixes and UV radiation on vibrational spectra of nucleotide bases and Amino acids

In spite of a relatively weak interaction between the inert matrix and an isolated molecule, the number of bands in the vibrational spectra of isolated polyatomic molecules exceeds the number of vibrational degrees of freedom. In this case, the individual spectral bands are converted into groups of closely spaced peaks (multiplets). In order to single out the isomeric and matrix splitting of bands, additional information is required and can be obtained by displacing the equilibrium of the isomers by evaporation temperature or by UV irradiation of the matrix. The rapid relaxation of the excitation energy and the matrix cell prevent the destruction of the molecule absorbing a UV quantum, while local annealing of the matrix cell facilitates the rotation of individual molecular groups. It can be seen from Fig. 7 that the UV irradiation of glycine isolated in the Ar matrix increases the intensity of the valence vibration bands of low-population conformers II and III, but decreases the intensity of the bands of the basic conformer I.[40]

The splitting of the impurity molecule bands in the matrix is mainly connected with the conformations of the matrix cell. An increase in the number of conformations, which depends on the geometry of an impurity molecule, leads to a broadening of the spectral bands. The large body of data that has been accumulated from the spectra of bio-organic molecules shows that the maximum narrowing of the spectral band (up to $0.2-0.3\,\mathrm{cm}^{-1}$) is attained for plane nucleotide bases of the type uracil,[15] 2-oxypyrimidine,[33] or hypoxanthine.[26] This effect is associated with the arrangement of plane molecules in the matrix lattice band[15] and hence a decrease in the conformational irregularity of the matrix cell of the impurity molecule. For nonplanar molecules (5,6-dihydrouracil, nucleosides, sugar), the set of conformations of matrix cells is so large that the bands are broadened to $3-10\,\mathrm{cm}^{-1}$ (Fig. 8).

2.6. Fermi resonance in matrix spectra of nucleotide bases and Amino acids

The splitting of intramolecular vibrational bands (Fermi resonance), caused by removal of random degeneracy, is observed frequently in vibrational spectra of polyatomic molecules.[4] It is possible to isolate spectral regions in which the probability of observing resonance splitting is the highest. As a rule, the splitting of C–H valence vibrations is also observed for all molecules with methyl and methylene groups, since the first frequency overtone of the deformation vibrations of the C–H bond is close to the symmetric valence vibration of the same bond.[44] In the matrix spectra of amino acids and bases, this effect is observed in the interval $2800-3100\,\mathrm{cm}^{-1}$, but it is more interesting to study its manifestation in the region of C=O valence vibrations, ($1700-1800\,\mathrm{cm}^{-1}$), which is very important for studying the isomerism. In all nucleotide bases studied by us, we observed a splitting of the C=O valence vibration bands caused by Fermi resonance (Figs. 5 and 9). Significant variations of resonance splitting can be attained by going over from Ar or Kr matrix to the Ne matrix. This effect is associated with notable variations of the valence vibration frequencies, which may differ in magnitude and direction from frequency shifts in the overtone or Raman vibrations.[15] It can be seen from Fig. 9 that the fundamental and Raman bands of C_4O thymine are reversed upon a transition from Ar or Kr matrix to the Ne matrix. This makes it possible to use the set of Kr, Ar and Ne matrices for identifying resonance doublets.

2.7. Intramolecular Hydrogen bonds and conformational behavior of Nucleosides

In contrast to nuleotide bases and amino acids, it is much more difficult to important clasees of biomolecules like sugar

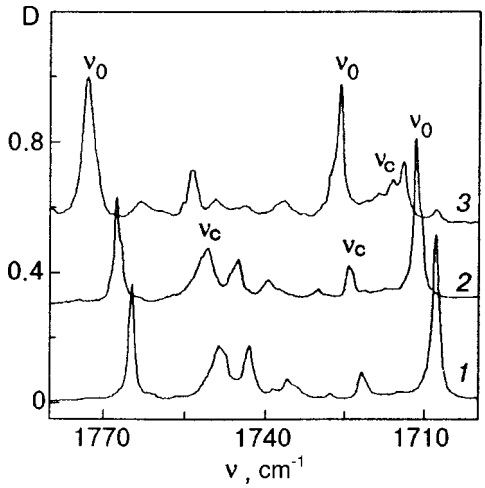

FIG. 9. Frequency shifts and Fermi resonance in the region of valence C=O vibrations of thymine in different matrices. Curves *1*, *2* and *3* correspond to Kr ($T=12$ K, $M=1:1000$), Ar ($T=12$ K, $M=1:1000$) and Ne ($T=5$ K, $M=1:800$), respectively.

and nucleosides transform to gaseous phase without thermal destruction. Hence these classes of molecules were not studied earlier under conditions of weak molecular interactions. In order to study these molecules, we increased the efficiency of the vaporizing system and obtained the infrared absorption spectra of matrix-isolated sugars like glucose, ribose, 2-desoxyribose, and nucleosides like thymidine, uridine,[45] and adenosine. It was shown that, in the isolated state, sugars exist in cyclic form, and equilibrium of equatorial and axial conformations stabilized by intramolecular hydrogen bonds between adjacent OH groups is observed. As a rule, nucleosides thymidine and uridine are in anticonformation in the crystalline state. However, syn/anticonformational equilibrium was observed in the isolated state.[45] The syn-conformations of uridine and thymidine are stabilized by intramolecular hydrogen bond between the hydroxymethyl O_5H group of ribose and the C_2O group of the pyrimidine ring (Fig. 10). Unlike uracil and thymine, adenosine in the

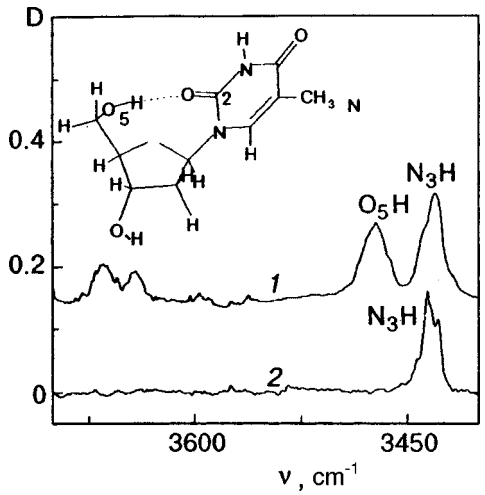

FIG. 10. IR Fourier spectra of nucleoside (thymidine) (curve *1*) and its analog 1-methylthymine (curve *2*) in an Ar matrix ($T=12$ K, $M=1:1000$).

matrix and in crystalline state is in anticonformation.

The results presented here show that the use of low-temperature technique is quite promising in biophysics for quantitative measurements of spectral and thermodynamic characteristics of thermally unstable bioorganic molecules. Among other things, the method of low-temperature matrix isolation shows that

1. isolated purine and pyrimidine nucleotide bases and their derivatives exist in the form of two tautomeric structures which are in thermodynamic equilibrium (keto-amine and amino-enol forms);

2. the main molecular mechanism of tautomeric transitions in nucleotide bases is the synchronous transition of a proton in a system of intermolecular hydrogen bonds in associates;

3. the main conformers of aliphatic amino acids are characterized by a considerable difference in vibrational entropies, caused by the effect of intramolecular hydrogen bonds on the rigidity of the structure of conformers.

3. INVESTIGATION OF FROZEN AQUEOUS SOLUTIONS OF BIOLOGICALLY ACTIVE COMPOUNDS BY LOW-TEMPERATURE SECONDARY-ION MASS SPECTROMETRY

The emergence of soft-ionization mass-spectrometric technique in the beginning of 1970's opened new possibilities for low-volatile thermally unstable biomolecules and for studying their nonvalent interactions. The rapid advancements in experimental mass-spectroscopic technique over the last decades and the peculiar ''conversion'' of methods used earlier in nuclear physics removed practically all restrictions on the molecular weight and state of aggregation of the investigated materials and made possible the transition of macromolecules of biopolymers to the gaseous phase. Such a rapid and successful development of mass-spectrometric techniques was caused by an ever-increasing public interest towards research in the field of health, medicine, pharmacology, and ecology. Mass spectrometry is being used at present with great success in all these fields of scientific research.[46–49]

However, the above-mentioned conversion did not cover the low-temperature secondary-emission techniques which were mainly employed for physical and chemical investigations aimed at obtaining large clusters of highly volatile compounds.[50,51] In 1992, research activity was started at ILTPE to develop the experimental technique and equipment for low-temperature secondary-ion mass-spectrometry (SIMS) and its version involving bombardment by fast atoms (BFA) for studying objects and phenomena that are of interest in cryobiophysics, cryomedicine, cryobiology, and ecology.[51–63] These methods are based on emission of secondary ions from the surface of the condensed sample under the action of a high-energy beam of primary ions (SIMS) or neutral atoms (BFA).[64–67] An analysis of mass and distribution of the sputtered ions provides direct information about the chemical composition of the sample and possible molecular interactions of its components, as well as additional information about its physical and chemical properties. A specialized secondary-emission ion source with a cryogenic

block for thermal stabilization of the sample were constructed for low-temperature investigations.[52] The substrate containing the sample frozen preliminarily or directly in the ion source was mounted in the cavity of the cryoblock. The temperature was recorded by a thermal resistance installed on the substrate. An automatic control by the thermal stabilization system makes it possible to maintain a fixed temperature of the sample, and to cool or heat it under the chosen conditions.

It should be observed that for the few physical and chemical low-temperature investigations carried out earlier on individual substances, there were no adequate models to explain the mechanisms of formation of ionic clusters, structure of mass spectra and its dependence on temperature.[68]

The novelty of the proposed mass-spectrometric technique lies in the approach developed for studying multicomponent aqueous solutions. One of the main achievements facilitating the low-temperature secondary-emission studies is the development of the method for interpreting low-temperature BFA mass spectra.[51,53,55,56,59] An important aspect of this approach is that the heterogeneous structure of the condensed sample formed during freezing of the solutions is taken into consideration, and a correlation is established between phase diagrams for investigated systems and the nature of their low-temperature mass spectra.

An analysis of the data available in literature on the investigations of the structure of frozen aqueous solutions by the method of electron cryomicroscopy[67,69,70] led to the conclusion that the geometrical size of the structural elements of the frozen sample surface (crystallites, grains, eutectic channels), which varies on the average from 10^{-4} to 10^{-6} m, is several orders of magnitude larger than the diameter ($\sim 10^{-8}$ m) of the zone excited by the impact of a single bombarding particle under the conditions of BFA/SIMS.[64,65] An important consequence of such a relation is that each individual particle knocks ions from the surface domain of a certain chemical composition, and the integral spectrum is a superposition of the spectra corresponding to individual components of the system. This observation explained several aspects of formation of ionic clusters.[53–58] In particular, the spectrum will contain only homoassociates in the case of a complete phase separation of individual substances, while the emergence of mixed (hetero) clusters in the spectrum indicates the emergence of a new compound (say, crystal hydrate) in the system, or the presence of homogeneous amorphized regions, or the melting of the eutectic phase.[59,63] The observed regularities were used successfully for interpretation of low-temperature BFA mass spectra.[53–63] Low-temperature mass spectra and their temperature dependence in the interval 77–273 K were obtained for the first time for a large series of cooled and frozen solutions of organic and inorganic compounds in water and organic solvents, including

1. aqueous solutions of salts of alkali and bivalent metals[56,57,63,71] which perform vital biological functions in live organisms and are parts of several cryoprotecting mixtures,

2. aqueous solutions of acids[72] which are of interest in ecological studies and can be used to determine the effect of the pH of the initial solution on the nature of mass spectra,

3. aqueous solutions of cryoprotectors, including alcohols,[53,58,63]

4. solutions of nitrous bases of nucleic acids in waters and cryoprotectors with addition of metal salts,[54,55,71] and

5. solutions of amino acids in alcohols.[73]

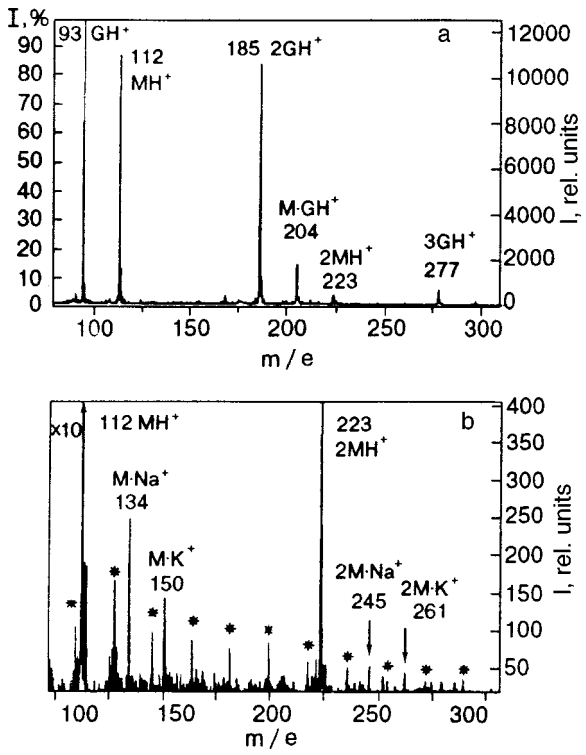

FIG. 11. Low-temperature BFA mass spectra of frozen solutions of cytosine ($C=10^{-3}$ M) containing traces ($C=10^{-5}$ M) of alkali metal ions: in the cryoprotector glycerine, $T=220$ K. M stands for cytosine and G for glycerine (a) and in deionized water, $T=210$ K, corresponds to the cluster series of water $(H_2O)_n \cdot H^+$ (b).

The following main results were obtained by studying the physical and chemical properties of the above systems.

Peculiar differences were observed in the low-temperature BFA mass spectra of solutions of nitrous bases of nucleic acids in water and cryoprotectors, reflecting the properties of these two types of systems upon freezing (Fig. 11).[54,55] In the case of aqueous solutions, cooling leads to phase separation and formation of water crystals, while the dissolved substances are expelled into the space between the crystallites. Two effects derogatory to the functioning of biomolecules are observed in this case: on the one hand, organic molecules lose their hydrated shell, while on the other hand contacts of molecules in channels between crystallites leads to a stronger coupling of organic molecules with metal ions. These effects are reflected in the nature of the mass spectra. In addition to the series of water clusters $(H_2O)_n \cdot H^+$ clusters sputtered from ice crystals and the protonized molecular ion MH^+ of the biomolecule (in the present case, the nitrous base of cytosine), the spectrum [Fig. 11(b)] also contains ions of the monomer and dimer complexes of the base with alkali metal ions MNa^+, MK^+, $2MNa^+$, $2MK^+$, but no hydrated clusters of bases are present in this case. Quantitative estimates reveal that if the molar concentration of alkali

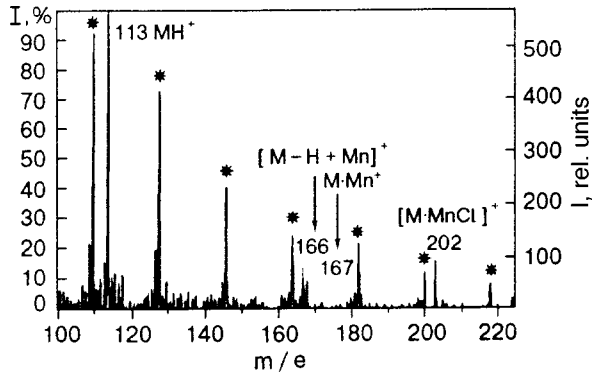

FIG. 12. Low-temperature BFA mass spectra of frozen aqueous-salt solution of the nitrous base of uracil in $MnCl_2$ in equimolar concentrations (10^{-3} M), $T=190$ K, M stands for the base molecule.

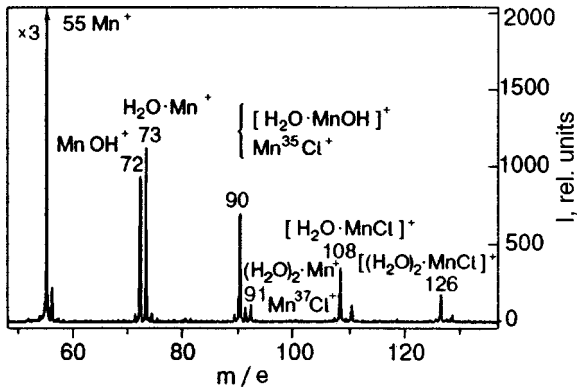

FIG. 13. BFA mass spectra of frozen 0.1M aqueous solution of the salt $MnCl_2$; $T=210$ K.

metal ions in the initial solution is two orders of magnitude lower than that of the organic matter (10^{-5} M as against 10^{-3} M), the intensity of cationized peaks is ~5% of the molecular ion intensity. In other words, practically all the metal ions are associated with the bases. Unlike the aqueous solution, the low-temperature spectrum of solutions of the same substances in the cryoprotector glycerine [Fig. 11(a)] does not contain ions corresponding to alkali metals or their complexes with bases. However, the spectrum does contain solvate clusters of the base and its dimer with glycerine (MGH^+,$2MGH^+$). These features of the spectrum characterize the cryoprotector properties of glycerine which solidifies amorphously upon cooling. The homogeneous distribution of substances, which is characteristic of the solution, is preserved in this case, and complexes of bases with alkali metal ions are practically absent because of an extremely small coupling constant.[3] However, hydrogen bonds of molecules of dissolved substances with the solvent are preserved. Thus, this method seems to be promising for further investigations of damaging factors during freezing of biomolecular solutions and for estimating the efficiency of various cryoprotectors over a wide range of temperatures.

Studies of the coupling of divalent metal ions with bases of nucleic acids revealed a certain similarity in the types of coupling in solutions at room temperature and in the frozen state.[71] By way of an example, Fig. 12 shows the spectrum of aqueous solution of the uracil base with admixtures of the salt $MnCl_2$. As in the case mentioned above [see Fig. 11(b)], the spectrum contains a series of clusters of water, protonized molecular ion of the base and its clusters with bivalent metal ions. However, in addition to the simple association $M\cdot Mn^+$, coupling through expulsion of a proton from the $[M-H+Mn]^+$ base molecule is observed, as well addition of the metal ion cluster with the counterion $[M\cdot MnCl]^+$. These results show that products of interaction of the type $(M-H^++Mn^{2+})$, which were registered earlier in aqueous solutions,[3] are preserved as a result of freezing of the system.

The observed effect of fixing the phase of hydrolysis products during nonequilibrium freezing of aqueous solutions of chlorides of bivalent metals may have negative consequences upon heating of the biomaterial frozen in aqueous salt solutions. Figure 13 shows the low-temperature mass spectrum of the frozen aqueous solution of the salt $MnCl_2$.[71] According to the phase diagram of this system, its freezing must be accompanied under equilibrium conditions by the formation of the hydrated crystal phase whose mass spectrum has the ions MN^+, $(H_2O)_n\cdot Mn^+$, $(H_2O)_n\cdot MnCl^+$ corresponding to it. The emergence of $MnOH^+$ and $[(H_2O)_n\cdot MnOH]^+$ ions in the spectra of this salt as well as other ions was attributed to the precipitation of the phase of hydrated crystal product of hydrolysis, viz., the basic salt, from the solution as a result of rapid freezing employed in cryopreservation. Such an effect was not observed in the case of aqueous solutions of alkali metal chlorides for which hydrolysis is not a characteristic phenomenon.[56,57]

Studies of organic solvents possessing cryoprotector properties, e.g., alcohols and their aqueous solutions, led to a correlation between the phase transitions in the sample and characteristic variations in the mass spectra.[53,58–63] The evaluation of the temperature interval (140–165 K) over which the monatomic ethyl alcohol may exist in liquid state under low pressures (10^{-5}–10^{-7} Pa) in the mass-spectrometer[60,62] makes it possible to carry out mass-spectrometric studies of liquid solutions at low temperatures.[73] Figure 14 shows the mass spectrum of the solution of amino acid proline in ethanol at 150 K. Together with intense protonized hydrogen-bound clusters of ethanol, the spectrum also contains a protonized molecular ion of proline and its clusters with alcohol molecules. Such spectra provide a qualitative estimate of the liquid eutectic composition as the last fragment of solution left in the liquid state before complete solidification of the sample upon cooling.[73]

We studied a number of effects associated with the hydration of organic and inorganic compounds. The secondary-emission mass spectra of crystal hydrates of salts and acids were obtained at low temperatures for the first time and interpreted.[56,63,72] Atomization of gigantic clusters of aqueous solutions of the primary alcohols is recorded, reflecting the presence of stable hydrates in liquid form at low temperatures.[58,61,63] The hydrate clusters obtained from samples of polyoxymethylene oligomers is the first case of mass-spectrometric observation of water with strong bonds (i.e., water which does not freeze into ice crystals but re-

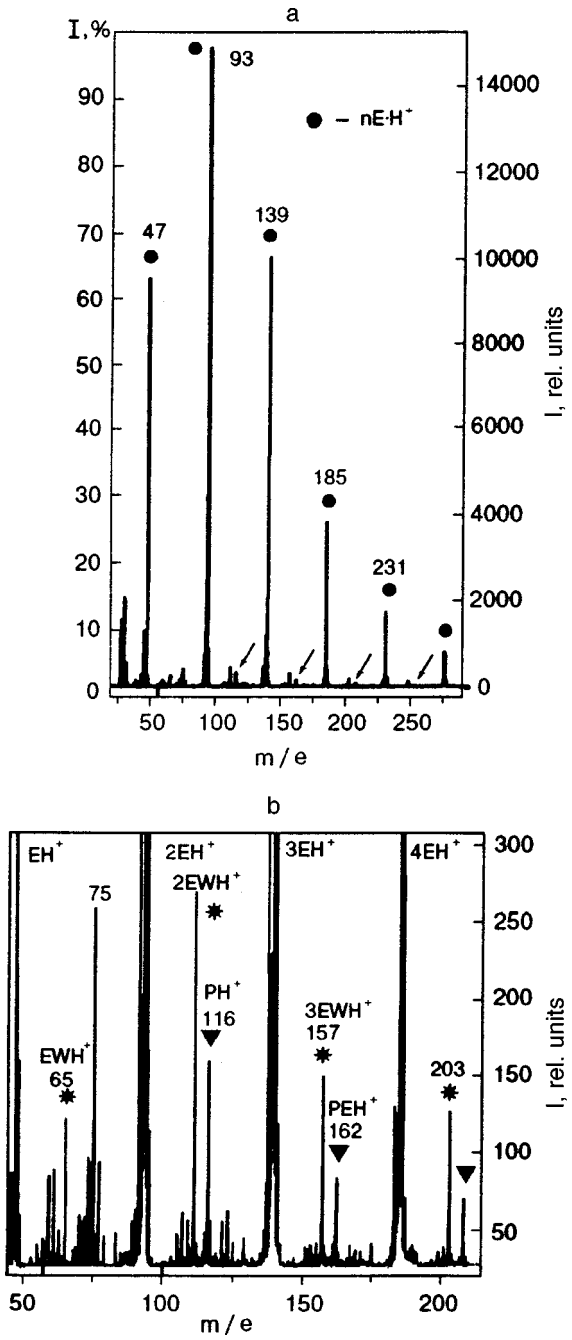

FIG. 14. Low-temperature mass spectrum of a solution of the amino acid of proline in ethanol, obtained from the liquid phase at 150 K complete spectrum (a) and a fragment of the spectrum (b) All ions are in protonized form, *P*, *E* and *W* indicate proline, ethanol and water molecules appearing in cluster ions.

mains bound to the organic molecules upon freezing) in the solid phase.[58,63]

Note that the secondary ion mass-spectrometry can also be used in ecological studies and in simulation of processes in the upper atmospheric layers involving ice crystals with organic and inorganic compounds of natural and anthropogenic origin adsorbed on their surface.[72]

The method of low-temperature mass spectrometry has proved its effectiveness in studies of the chemical composition, phase transitions and the effect of cooling on molecular interaction parameters in frozen aqueous solutions of biologically active compounds. The most interesting results include

1. evaluation of the enhancement of coupling between metal ions and components of biopolymers as a result of an increase in concentration during cooling and freezing of aqueous solutions in comparison with analogous solutions in cryoprotectors;

2. establishing a correlation between the presence of certain types of clusters hydrates in mass spectra and the presence of stable hydrates and water with strong bonds in cooled samples; and

3. detection of the precipitated phase corresponding to the hydrolysis products, formed as a result of rapid freezing of bivalent metal ions.

Thus, the wide range of objects discussed above demonstrates the potentialities of the low-temperature mass-spectrometric technique in solving many problems of molecular cryophysics associated with the processes occurring in cooled and frozen systems on molecular level.

4. INVESTIGATION OF NUCLEIC ACIDS, THEIR COMPONENTS AND ANALOGS WITH THE HELP OF LOW-TEMPERATURE LUMINESCENCE SPECTROSCOPY

A distinguishing feature of the luminescence of nucleic acids and their components is its low quantum yield (10^{-4}–10^{-6}) at room temperature, especially the quantum yield of phosphorescence (10^{-7},10^{-8}).[74] Hence low-temperature techniques are widely employed for studying luminescence of nucleic acids and their components.

In order to study the parameters of luminescence of nucleic acids and their components at low temperatures, we created a universal device which makes it possible to study spectra of luminescence and its excitation, as well as the polarization and phosphorescence attenuation times in the temperature range 4.2–273 K.[75] The device is equipped with a PC which controls the experiment automatically, including heating of the sample at rates varying from 0.5 to 50 °C/min. In order to study biopolymer solusions, we constructed cells with heating, intended for investigation of aqueous solutions at low temperatures. For polarization studies, we designed a vacuumless optical cryostat, capable of working in continuous flow as well as steady-state regime.[76]

This device was used to study ionic and tautomeric (isomeric) equilibrium states of minor RNA bases 4-thiouracil (4SU) and antitumor preparation 6-thioguanine (6SG), quasiparticle excitations in DNA, RNA and polyG, as well as structural and phase transitions in alcohols, aqueous solutions of cryoprotectors and DNA in the temperature interval 4.2–273 K. Luminescence studies were supplemented by UV-absorption spectroscopy and circular dichroism (CD) studies, as well as by theoretical calculations on supercomputers supplied by Silicon Graphics.

Different isomers of 6SG in polar solvent were detected and spectrally isolated in low-temperature luminescence spectra with a well-resolved vibrational structure. Detailed investigations of luminescence spectra of the ionic forms 4SU and 6SG led to the construction of a scheme for the oxygen-base and tautomeric equilibrium of these compounds

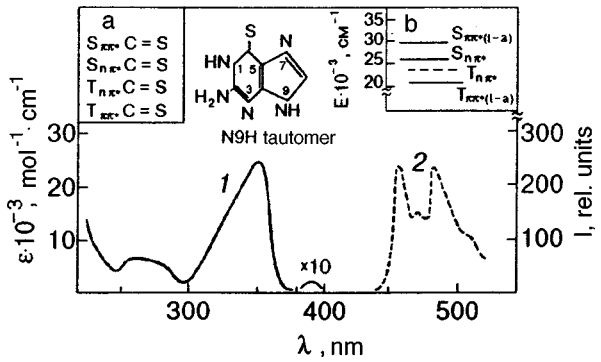

FIG. 15. UV-absorption (curve *1*) and phosphorescence (curve *2*) spectra of the N9H tautomer of 6-thioguanine (left ordinate axis corresponds to molecular extinction coefficient ε and the right ordinate axis to luminescence intensity I_e), as well as excitation localization in lower electron-excited state (inset *a*), and the diagram of electron-excited states of the N9H tautomer of 6-thioguanine (inset *b*).

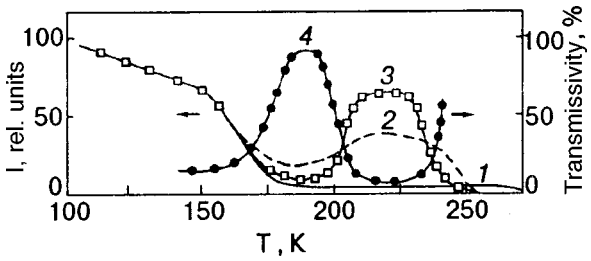

FIG. 16. Temperature dependence of the luminescence of the 6SGR probe in aqueous solutions of propanediol for different concentration of propanediol (%): 15% (curve *1*), 40% (curve *2*), 55% (curve *3*), and transparency of samples with propanediol concentration 55% (curve *4*).

in polar solvents.[77–80] Study of luminescence parameters (ratio of intensities of fluorescence and phosphorescence, polarization, and phosphorescence attenuation times) together with UV and CD spectroscopy made it possible to construct a diagram of electron-excited states 4SU and 6SG (Fig. 15).[81–83] It was shown that electron transitions induced by intramolecular charge transport exist in the investigated molecules. The existence of $n\pi^*$-type low-energy electron transitions in bases of nucleic acids was reliably established for the first time.[81,82,84]

Investigations of low-temperature luminiscence spectra of DNA, RNA, polyG and model systems with different concentrations of 6SG, 4SU and Tb^{3+} ions made it possible to study processes of energy migration in these polymers and, in particular, to determine the singlet transport radii, triplet transport rate, etc.[85–89] For example, studies of the luminescence spectra of aqueous solutions of DNA at 77 K with the built-in technique of biosynthesis by 6-thioguanine and without it revealed considerable differences in these spectra. Luminescence spectra of DNA with 6SG are characterized by high-intensity emission in the interval $\lambda = 450–550$ nm, which is characteristic of 6SG phosphorescence. At the same time, low concentration of 6SG in DNA (relative concentration of 6SG in DNA was 1:600 and 1:3000) and a very weak absorption of 6SG in the vicinity of the region 280 nm at which luminescence was excited in DNA do not make it possible to explain the observed difference in the spectra by simply including 6SG in DNA. It was shown that the 6SG absorption spectrum overlaps considerably the DNA luminescence spectrum. This is a prerequisite for effective transport of excitation on 6SG in DNA according to inductive-resonance mechanism. Calculation of the singlet excitation transport radius according to Förster's formula gives the value $R_0 = 28$ Å.[85]

An analysis of the luminescence spectra of model systems with different concentrations of 4SU imitating t-RNA led to the conclusion about migration of energy in t-RNA according to inductive-and exchange-resonance mechanisms, and allowed an interpretation of the spectrum of t-RNA which contains 4-thiouracil.[86,87] Our investigations of photophysical processes in the 4-thiouracil molecule ensures a wide application of 4-thiouracil as a luminescence mark as well as a target for the formation of photochemical bond in the complex with the participation of 4-thiouracil for studies of riboses and various protein-nucleic complexes.[90,91]

It is well known that double-helix DNA molecules are quasi-one-dimensional structures. In order to find the peculiarities of energy migration in low-dimensional systems, we studied the low-temperature luminescence spectra and kinetics of phosphorescence attenuation of polyguanilic acid with Tb^{+3} ions playing the role of electron excitation traps.[88,89] It was shown that attenuation of the trap phosphorescence is described by a nonexponential dependence as a result of migration of triplet excitation in the quasi-one-dimensional system, and that the triplet excitation jump occurs (at a rate $\sim 2 \cdot 10^5\ s^{-1}$).

Low-temperature studies of biopolymers led to the creation and development of the phosphorescence probe technique.[82,85,88] Detailed studies of the spectroscopic properties of 6SG made it possible to use it as a phosphorescent probe for studying structural and phase transitions in alcohols (glycerine, propanediol, ethanol) which are used as cryoprotectors in cryobiology. 6SG was also used for studying structural transitions in aqueous and alcohol solutions as well as DNA solutions.

Studies of aqueous solutions with different concentrations of propanediol revealed (Fig. 16) the existence of structural and phase transitions in these solutions in temperature interval 150–273 K, viz., devitrification of the amorphous phase of the solutions, secondary crystallization, and melting of the crystalline phase. These investigations are in good agreement with the calorimetric studies of these systems and with nonequilibrium diagrams of the liquid–solid state.[92]

Our investigations confirmed the existence of molecular mobility in solid glasses of alcohols in the temperature range 4.2–120 K. Structural variations in aqueous solutions of propanediol in the interval 60–90 K were also detected. An analysis of the temperature dependences of the 6-thioguanine luminescence together with the calorimetric data lead to the assumption concerning the formation of the liquid-crystal phase in aqueous solutions of propanediol at temperatures below 170 K.[82]

Studies of aqueous solutions of DNA with the built-in technique of biosynthesis with 6-thioguanine in the temperature range 4.2–273 K (Fig. 17) showed the presence of struc-

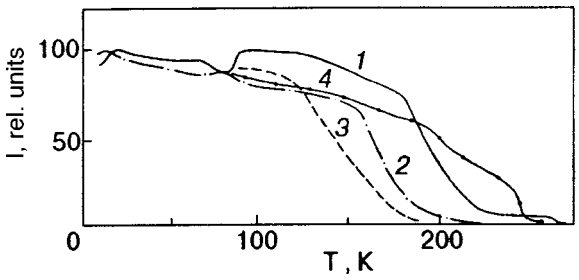

FIG. 17. Temperature dependence of the 6SGR emission introduced into DNA, under different conditions: aqueous solution (curve *1*), 15% propanediol solution (curve *2*), 15% dimethyl sulfoxide solution (curve *3*), and temperature dependence of the 6SGR emission in a hydrated DNA film (the probe was not introduced in the DNA).

tural variations in the DNA solutions in the interval 75–90K. It was also found that devitrification of the hydrated shell of DNA occurs in the interval 180–200 K.[82,85]

The investigations carried out by us reveal enormous potentialities of the luminescent (phosphorescent) probe technique for studying structural transitions in biophysical systems.

Low-temperature luminescence studies of nucleic acids and their components lead to the following results:

1. oxygen-base and tautomeric equilibrium diagrams are constructed for sulfurous components of nucleic acids, as well as the diagrams for their electron-excited states;

2. the migration of energy in nucleic acids is revealed; in particular, the migration radii and excitation transition rates are determined and the migration mechanisms established in t-RNA;

3. the low-temperature luminescent probe technique is used to determine the temperature intervals corresponding to structural variations in aqueous solutions of DNA and DNA solutions with cryoprotectors in the temperature interval 4.2–273 K.

CONCLUSION

The data presented in this review show that the use of low-temperature technique in biophysical research may lead to the solution of problems of different levels. In actual practice, it helps in broadening the concepts about the structure and properties of biologically active molecules over a wide temperature interval, thus allowing a more precise evaluation of the integral thermodynamic characteristics of objects used as the empirical data for further computations. On the other hand, the fine structure of IR, UV, luminescence and mass spectra revealed at low temperatures makes it possible to single out effects associated with the interaction of biomolecules with the surroundings, and caused by self-association or inherent in the isolated state. Separation of such components is quite important for solving global biophysical problems aimed at finding the forces of evolution of live organisms, mechanisms of recognition at macromolecular level, and at finding possible reasons of their malfunctioning.

The complex experimental approach providing information about the structure, dynamics and energetics of molecular interaction, obtained by mutually complementary spectral techniques, provides rich information about associated scientific disciplines like cryobiology, medicine, pharmacology and ecology. At present, pioneering results are mainly obtained at the boundary of scientific disciplines by using nontrivial methods for solving conventional problems. Large research centers including ILTPE and, in particular, the department of molecular biophysics founded by Academician B. I. Verkin, are among the propitious combinations of the experimental base, methodological designs and developed theoretical approach, ensuring an integration of interdisciplinary data and foundation of independent research schools which have won worldwide recognition.

The results presented in the present review are a good illustration of the potentialities of such investigations.

*)E-mail: blagoi@ilt.kharkov.ua

[1] *Contribution of ILTPE in Medicine*, Annotated Reference Book Listing Publications by Scientists at ILTPE in 1965–1989 [in Russian], ILTPE, Kharkov (1989).
[2] B. I. Verkin, I. K. Yanson, L. F. Sukhodub, and A. B. Teplitskii, *Interaction of Biomolecules. New Experimental Techniques and Methods* [in Russian], Naukova Dumka, Kiev (1985).
[3] Yu. P. Blagoi, V. L. Galkin, G. O. Gladchenko *et al.*, *Metal Complexes of Nucleic Acids in Solutions* [in Russian], Naukova Dumka, Kiev (1991).
[4] B. I. Verkin, Yu. P. Blagoi, A. M. Kosevich, and L. F. Sukhodub, in *Physics of the Condensed State* [in Russian], Naukova Dumka, Kiev (1985).
[5] B. I. Verkin, V. A. Nikitin, B. N. Murinets-Markevich, and K. V. Grigor'eva, *Cryosurgery in Stomatology* [in Russian], Naukova Dumka, Kiev (1984).
[6] B. I. Verkin, B. N. Murinets-Markevich, A. R. Krasnikov *et al.*, in *Cryogenic Systems: Development and Research* [in Russian], Naukova Dumka, Kiev (1984).
[7] E. D. Radchenko, A. M. Plokhotnichenko, G. G. Sheina, and Yu. P. Blagoi, Studia Biophys. **87**, 251 (1982).
[8] G. G. Sheina, E. D. Radchenko, A. M. Plokhotnichenko, and Yu. P. Blagoi, Biofizika **27**, 983 (1982).
[9] E. D. Radchenko, A. M. Plokhotnichenko, G. G. Sheina, and Yu. P. Blagoi, Biofizika **28**, 559 (1983).
[10] E. D. Radchenko, A. M. Plokhotnichenko, G. G. Sheina, and Yu. P. Blagoi, Biofizika **28**, 923 (1983).
[11] M. Szczesniak, M. J. Nowak, H. Roskowska *et al.*, J. Am. Chem. Soc. **105**, 5969 (1983).
[12] A. J. Barnes, M. A. Stuckey, and L. Le Gall, Spectrochim. Acta A **40A**, 419 (1984).
[13] M. Graindourze, J. Smets, Th. Zeegers-Huyskens, and G. Maes, J. Mol. Struct. **222**, 345 (1990).
[14] P. Colarusso, K. Zhang, B. Guo, and P. F. Bernath, Chin. Phys. Lasers **269**, 39 (1997).
[15] A. Yu. Ivanov, A. M. Plokhotnichenko, E. D. Radchenko *et al.*, J. Mol. Struct. **372**, 91 (1995).
[16] A. Yu. Ivanov, G. G. Sheina, and Yu. P. Blagoi, Spectrochimic Acta, **55**, 219 (1999).
[17] G. G. Sheina, E. D. Radchenko, Yu. P. Blagoi, and B. I. Verkin, Dokl. Akad. Nauk SSSR **240**, 463 (1978).
[18] G. G. Sheina, E. D. Radchenko, S. A. Egupov *et al.*, Int. J. Quantum Chem. **16**, 387 (1979).
[19] J. D. Watson and F. H. C. Crick, Nature (London) **171**, 964 (1953).
[20] E. D. Radchenko, N. A. Smorygo, and Yu. P. Blagoi, J. Mol. Struct. **116**, 387 (1984).
[21] E. D. Radchenko, A. M. Plokhotnichenko, G. G. Sheina, and Yu. P. Blagoi, Biofizika **29**, 553 (1984).
[22] G. G. Sheina, E. D. Radchenko, and Yu. P. Blagoi, Dokl. Akad. Nauk SSSR **282**, 1497 (1985).
[23] G. G. Sheina, E. D. Radchenko, S. G. Stepanian *et al.*, Biofizika **31**, 555 (1986).

[24] E. D. Radchenko, A. M. Plokhotnichenko, A. Yu. Ivanov *et al.*, Biofizika **31**, 373 (1986).
[25] S. G. Stepanian, G. G. Sheina, E. D. Radchenko, and Yu. P. Blagoi, J. Mol. Struct. **124**, 333 (1985).
[26] G. G. Sheina, S. G. Stepanian, E. D. Radchenko, and Yu. P. Blagoi, J. Mol. Struct. **158**, 275 (1987).
[27] G. G. Sheina, E. D. Radchenko, A. M. Plokhotnichenko, and Yu. P. Blagoi, Biofizika **33**, 741 (1988).
[28] S. G. Stepanian, G. G. Sheina, E. D. Radchenko, and Yu. P. Blagoi, Zh. Fiz. Khim. **63**, 3008 (1989).
[29] Yu. P. Blagoi, E. D. Radchenko, S. G. Stepanian, and G. G. Sheina, J. Mol. Struct. **219**, 311 (1990).
[30] A. M. Plokhotnichenko, A. Yu. Ivanov, E. D. Radchenko *et al.*, Fiz. Nizk. Temp. **19**, 1029 (1993) [Low Temp. Phys. **19**, 9 (1993)].
[31] W. MacCarthy, A. M. Plokhotnichenko, E. D. Radchenko *et al.*, J. Phys. Chem. A **101A**, 7208 (1997).
[32] W. MacCarthy, J. Smets, L. Adamowicz *et al.*, Mol. Phys. **91**, 513 (1997).
[33] G. G. Sheina, A. Yu. Ivanov, S. A. Krasnokutsky, and Yu. P. Blagoi, in *Abstracts of Proceedings of Int. Conf. on Hydrogen Bond*, Kiev (May 10–15, 1998).
[34] Y. Grenie, J. C. Lassegues and C. G. Lagrange, J. Chem. Phys. **53**, 2980 (1970).
[35] R. D. Suenram and F. J. Lovas, J. Am. Chem. Soc. **102**, 7180 (1980).
[36] G. G. Sheina, E. D. Radchenko, A. Yu. Ivanov, and S. G. Stepanian, Zh. Fiz. Khim. **62**, 985 (1988).
[37] I. D. Reva, S. G. Stepanian, and E. D. Radchenko, Khim. Fiz. **12**, 966 (1993).
[38] I. D. Reva, S. G. Stepanian, A. M. Plokhotnichenko *et al.*, J. Mol. Struct. **318**, 1 (1994).
[39] I. D. Reva, A. M. Plokhotnichenko, S. G. Stepanian *et al.*, Chin. Phys. Lasers **232**, 141 (1995).
[40] A. Yu. Ivanov, A. M. Plokhotnichenko, V. Izvekov *et al.*, J. Mol. Struct. **408**, 459 (1997).
[41] S. G. Stepanian, I. D. Reva, E. D. Radchenko *et al.*, J. Phys. Chem. A **102A**, 1041 (1998).
[42] S. G. Stepanian, I. D. Reva, E. D. Radchenko, and L. Adamowicz, J. Phys. Chem. A **102A**, 4623 (1998).
[43] P. Klaeboe, Vib. Spectrosc. **9**, 3 (1995).
[44] M. P. Lisitsa and A. M. Yaremko, *Fermi Resonance* [in Russian], Naukova Dumka, Kiev (1984).
[45] S. A. Krasnokutski, A. Yu. Ivanov, V. Izvekov *et al.*, J. Mol. Struct. **482–483**, 249 (1998).
[46] G. Ziuzdak, *Mass Spectrometry for Biotechnology*, Academic Press, San Diego (1996).
[47] S. J. Gaskell (Ed.), *Mass Spectrometry in Biomedical Research*, J. Wiley and Sons, Chichester (1986).
[48] D. M. Desidero (Ed.), *Mass Spectrometry. Clinical and Biological Applications*, vol. 2, Plenum, New York (1994).
[49] T. Matsuo, *Biological Mass Spectrometry. Present and Future*, Wiley, Chichester and New York (1994).
[50] J. Michl, Int. J. Mass Spectrom. Ion Processes **53**, 255 (1983).
[51] M. V. Kosevich, Eur. Mass Spectrom. **4**, 251 (1998).
[52] O. A. Boryak, M. V. Kosevich, and V. S. Shelkovsky, Prib. Tekh. Éksp. **No. 6**, 176 (1993).
[53] O. A. Boryak, M. V. Kosevich, V. S. Shelkovsky, Yu. P. Blagoy, Rapid Commun. Mass Spectrom. **9**, 978 (1995).
[54] O. A. Boryak, M. V. Kosevich, V. S. Shelkovsky, and Yu. P. Blagoi, Biofizika **41**, 1207 (1996).
[55] O. A. Boryak, M. V. Kosevich, V. S. Shelkovsky, and Yu. P. Blagoy, Rapid Commun. Mass Spectrom. **10**, 197 (1996).
[56] O. A. Boryak, I. O. Stepanov, M. V. Kosevich *et al.*, Eur. Mass Spectrom. **2**, 329 (1996).
[57] M. V. Kosevich, O. A. Boryak, I. O. Stepanov, and V. S. Shelkovsky, Eur. Mass Spectrom. **3**, 11 (1997).
[58] M. V. Kosevich, O. A. Boryak, V. S. Shelkovsky, and P. J. Derrick, Eur. Mass Spectrom. **4**, 31 (1998).
[59] M. V. Kosevich, Eur. Mass Spectrom. **3**, 320 (1997).
[60] O. A. Boryak, M. V. Kosevich, and V. S. Shelkovsky, Int. J. Mass Spectrom. Ion Processes **163**, 177 (1997).
[61] M. V. Kosevich, G. Czira, O. A. Boryak *et al.*, Rapid Commun. Mass Spectrom. **11**, 1411 (1997).
[62] M. V. Kosevich, G. Czira, O. A. Boryak *et al.*, J. Mass Spectrom. **33**, 843 (1998).
[63] M. V. Kosevich, Kharkov Univ. Newsletter (in Ukrainian), No. 422; Biophysics Newsletter (in Ukrainian) **2**, 5 (1998).
[64] A. Benninghoven, F. G. Rudenauer and H. W. Werner, *Secondary Ion Mass Spectrometry. Basic Concepts, Instrumental Aspects, Applications and Trends*, J. Wiley and Sons, New York (1987).
[65] V. Cherepin, *Secondary Ion Mass Spectrometry of Solid Surfaces*, Science Press, Utrecht (1987).
[66] V. A. Pokrovsky and V. V. Mosin, Teor. Éksp. Khim. **23**, 62 (1987).
[67] T. N. Yurchenko, V. F. Kozlova, B. A. Skornyakov *et al.*, *Effect of Cryoprotectors on Biological Systems* [in Russian], Naukova Dumka, Kiev (1989).
[68] L. D. Detter, O. W. Hand, R. G. Cooks and R. A. Walton, Mass Spectrom. Rev. **7**, 465 (1988).
[69] F. Franks, *Water and Aqueous Solutions at Temperatures Below* 0 °C [Russian translation]. Naukova Dumka, Kiev (1985).
[70] A. M. Belous, E. A. Gordienko, and L. F. Rozanov, *Freezing and Cryoprotection* [in Russian], Vyssha Shkola, Moscow (1987).
[71] O. A. Boryak, M. V. Kosevich, V. S. Shelkovsky *et al.*, in *Abstracts of Papers to the II Congress of Ukr. Biophys. Assoc.* (in Ukrainian) (1978).
[72] M. V. Kosevich, O. A. Boryak and V. S. Shelkovsky, in *Abstracts of the 14th International Mass Spectrometry Conference*, Tampere, Finland 25–29 Aug. 1997.
[73] O. A. Boryak, I. K. Galetich, M. V. Kosevich *et al.*, *Abstracts of the 14th International Mass Spectrometry Conference*, Tampere, Finland 25–29 Aug. 1997.
[74] N. M. Emanuel (Ed.), *Physical and Chemical Properties of Nucleic Acids* [Russian translation], Mir, Moscow (1976).
[75] Yu. V. Rubin, in *Luminescence Analysis in Medical and Biological Research* [in Russian], RMI, Riga (1983).
[76] Yu. V. Rubin and Yu. P. Blagoi, *Optical Cryostat*, Author's certificate No. 134 3212 dated July 8, 1987.
[77] M. Stewart, J. Leszczynski, Yu. V. Rubin, and Yu. P. Blagoi, J. Phys. Chem. **101**, 4753 (1997).
[78] Yu. V. Rubin, and J. Leszczynski, Nucleosides and Nucleotides **18**, 78 (1999).
[79] Yu. V. Rubin, Yu. V. Morozov, D. Venkateswarlu, and J. Leszczynski, J. Phys. Chem. **102**, 2194 (1998).
[80] Yu. V. Rubin and F. A. Savin, in *Luminescence Analysis in Medical and Biological Research* [in Russian], RMI, Riga (1990).
[81] Yu. V. Rubin, F. A. Savin, and Yu. P. Blagoi, Stud. Biophys. **123**, 205 (1988).
[82] Yu. V. Rubin, V. A. Bokovoy, and Yu. P. Blagoi, J. Fluoresc. **5**, 263 (1995).
[83] Yu. V. Rubin and J. Leszczynski, in *Jablonski Centennial Conference on Luminescence and Photophysics; Abstract book*, Torun, Poland (1998).
[84] Yu. V. Rubin, Yu. P. Blagoi, and E. A. Leibina, Studia Biophysica **85**, 89 (1981).
[85] Yu. V. Rubin, V. A. Bokovoy, Yu. P. Blagoi, and R. G. Lee, Int. J. Quant. Chem., Quant. Biol Symp. **21**, 187 (1994).
[86] Yu. V. Rubin, Yu. P. Blagoi, and E. A. Leibina, Studia Biophysica **71**, 133 (1978).
[87] Yu. V. Rubin and S. A. Egupov, Biofizika **32**, 373 (1987).
[88] Yu. P. Blagoi, I. A. Levitsky, and Yu. V. Rubin, J. Mol. Struct. **294**, 123 (1993).
[89] Yu. P. Blagoi, I. A. Levitsky, Yu. V. Rubin, and V. A. Slavin, Chin. Phys. Lasers **203**, 263 (1993).
[90] A. Favre, in *Bioorganic Photochemistry: Biophotochemistry and the Nucleic Acids*, Vol 1 (Edited by H. Morrison) Wiley and Sons, London, New York (1990).
[91] K. M. Meisenheimer and T. H. Koch, Crit. Rev. Biochem. **32**, 101 (1997).
[92] A. V. Zinchenko, V. V. Mank, V. A. Moiseev *et al.*, Dokl. Akad. Nauk SSSR **269**, 144 (1983) [Sov. Phys. Dokl. **28**, 841 (1983)].

Translated by R. S. Wadhwa

QUANTUM LIQUIDS AND QUANTUM CRYSTALS

Optical generation of the first and second sounds in superfluid ^{3}He–^{4}He solutions

T. Kh. Salikhov

*Department of Physics, Dushanbe State Teacher's Training Institutes, 121 Rudaki Str., 734003 Dushanbe, Tadjikistan**)

(Submitted September 15, 1998; revised March 16, 1999)
Fiz. Nizk. Temp. **25**, 1021–1026 (October 1999)

An optical method of generation of the first and second sounds in superfluid ^{3}He–^{4}He solutions is proposed. The method is based on illumination by amplitude-modulated laser beam with wavelength corresponding to a region of absorption. Numerical calculations of pressure and temperature as a function of time are carried out. It was found that the presence of ^{3}He isotopes in the solution provides strong coupling between these parameters. As a result, the waves of the first sound involve oscillations of the temperature, while the waves of the second sound involve oscillations of the pressure. © *1999 American Institute of Physics.* [S1063-777X(99)00210-8]

1. INTRODUCTION

As in He-II, the waves of the first and the second sounds can propagate in superfluid ^{3}He–^{4}He solutions.[1] Rudavsky and Serbin[2] have considered generation of acoustical waves involving oscillations of pressure and temperature in the solutions. They extended the method, which was developed by Lifshitz[3] for superfluid helium, to the superfluid ^{3}He–^{4}He solutions. It was shown that a surface with periodically varying temperature generates waves of both the first and second sounds in the solutions, and that intensities of the waves are of the same order of magnitude. Such an important difference between the solutions and He-II is due to strong coupling between the density of the medium and the concentration of ^{3}He isotopes. This coupling gives rise to a strong relation between the oscillating parts of the pressure $P'(t,\mathbf{r})$ and the temperature $T'(t,\mathbf{r})$. As a result, the waves of the second sound lead to oscillations of the pressure, while the waves of the first sound give rise to oscillations of the temperature. This effect has been observed and studied in detail experimentally.[4,5] Because of its simplicity, this method is now widely used.

In this paper we propose an optical method allowing one to generate waves of the first and second sounds in superfluid ^{3}He–^{4}He solutions. The advantage of the proposed method is that it is contactless. It is worth mentioning that there are many theoretical and experimental studies of optical generation of acoustic waves in classical liquids and solids (see the review article[7]). In the case of He-II such a method of generation of the second sound was studied theoretically.[8] It was shown that waves of the second sound can be generated by laser radiation. In this paper our aim is to extend the results obtained in Ref. 8 to superfluid ^{3}He–^{4}He solutions.

Let us assume that the system under consideration has regions of absorption in various ranges of the spectrum (for example, the ^{4}He isotope has an absorption line in the ultraviolet region ~600 Å with the absorption coefficient about 1 cm^{-1} (Refs. 9 and 10) and is described by the absorption coefficient α. Then, generation of waves of the first and second sounds by amplitude-modulated laser radiation (for example, an excimer laser) is possible. The illuminated medium due to periodically changing temperature and thermal expansion emits waves of the first and second sounds. Due to the strong coupling between $P'(t,\mathbf{r})$ and $T'(t,\mathbf{r})$, the oscillations of one of these parameters give rise to the oscillations of the other parameter.

2. EQUATIONS FOR WAVES OF THE FIRST AND SECOND SOUNDS

We assume a solution of ^{3}He–^{4}He to be confined in a cylindrical container with volume V and radius R. A monochromatic laser beam with the amplitude and Gaussian shape of the spatial distribution, changing in time is assumed to move along the axis of the cylinder. Absorption in the system provides dissipation of the radiation energy and generation of acoustic waves according to the thermal mechanism described in Ref. 7. We assume that the oscillation amplitudes of the hydrodynamic parameters are much lower than their average magnitudes. This allows us to apply a system of linear hydrodynamic equations. This system consists of the mass conservation law, the equation describing the movement of the liquid, the equation for entropy taking into account the heat source, the equation for concentration taking into account the solvent only to the normal mode, and the equation for the superfluid component.[1] Further, we ignore the dissipation terms in the hydrodynamic equations and use the system of equations[1]

$$\frac{\partial \rho}{\partial t} + \rho_s \nabla \cdot \mathbf{v}_s + \rho_n \nabla \cdot \mathbf{v}_n = 0, \tag{1}$$

$$\rho_s \frac{\partial \mathbf{v}_s}{\partial t} + \rho_n \frac{\partial \mathbf{v}_n}{\partial t} + \nabla P' = 0, \tag{2}$$

$$\rho_0 \frac{\partial \sigma'}{\partial t} + \sigma_0 \rho_s \nabla \cdot (\mathbf{v}_n - \mathbf{v}_s) = \frac{1}{T_0} f(t,\mathbf{r}), \tag{3}$$

$$\sigma_0 \frac{\partial c'}{\partial t} - c_0 \frac{\partial \sigma'}{\partial t} = -\frac{c_0}{\rho_0 T_0} f(t,\mathbf{r}), \tag{4}$$

$$\frac{\partial \mathbf{v}_s}{\partial t} + \nabla \left(\mu - \frac{Zc}{\rho} \right) = 0, \tag{5}$$

where $\rho = \rho_s + \rho_n$, σ_0 and c_0 are the average values of the mass, the entropy per unit mass, and the concentration, ρ', σ', and c' are their amplitudes, ρ_s and ρ_n are the densities and $\mathbf{v}_s$ and $\mathbf{v}_n$ are the velocities of the superfluid and the normal components, respectively, and

$$Z = \rho(\mu_3 - \mu_4), \quad \mu = c\mu_3 + (1-c)\mu_4, \tag{6}$$

where $\mu_{3,4}$ is the chemical potential of ^{3}He and ^{4}He, and $f(t,\mathbf{r})$ is the heat source due to the absorbed light.

We then ignore the terms on the right side of (4), i.e., we consider the case of small concentration. Excluding from (1)–(5) $\mathbf{v}_s$, $\mathbf{v}_n$, and c' and using the thermodynamic expression[1] which connects μ' and σ' with the perturbations of pressure P' and temperature T', we obtain

$$\frac{\partial^2 p'}{\partial t^2} - C_1^2 \left(1 + \frac{\rho_s}{\rho_n}\beta^2 + \frac{\beta \alpha_T C_2^2}{\overline{\sigma}} \right) \Delta P' + \frac{\rho_0 \beta C_p C_1^2 C_2^2}{T_0 \overline{\sigma}} \Delta T' = -\frac{\beta C_1^2}{T_0 \sigma_0} \frac{\partial f}{\partial t}, \tag{7}$$

$$\frac{\partial^2 T'}{\partial t^2} - C_2^2 \left(1 - \frac{\beta \alpha_T C_2^2}{\overline{\sigma}} \right) \Delta T' - \frac{T_0}{\rho_0 C_P} \left[(C_1^2 - C_2^2)\alpha_T + \frac{\rho_s}{\rho_n} \alpha_T \beta^2 C_1^2 - \frac{\rho_s}{\rho_n} \beta \overline{\sigma} + \frac{\beta \alpha_T^2 C_1^2 C_2^2}{\overline{\sigma}} \right] \Delta P' = \frac{1}{\rho_0 \sigma_0 C_P} (\overline{\sigma} - \beta \alpha_T C_1^2) \frac{\partial f}{\partial t}, \tag{8}$$

$$\overline{\sigma} = \sigma_0 - c_0 \frac{\partial \sigma}{\partial c}, \quad \beta = \frac{\overline{\sigma}}{\rho_0} \left(\frac{\partial \rho}{\partial T} \right)_{Pc} \left(\frac{\partial T}{\partial \sigma} \right)_{Pc} + \frac{c_0}{\rho_0} \left(\frac{\partial \rho}{\partial c} \right)_{PT}. \tag{9}$$

Heat sources of sound are taken into account on the right-hand sides of Eqs. (7) and (8). The system of wave equations (7) and (8) describes the dependence of temperature and pressure of superfluid ^{3}He–^{4}He solution on time and spatial coordinates when an electromagnetic wave with varying amplitude and wavelength corresponding to the absorption range propagates in the sample. For example, the terms with the factors $\Delta T'$ in Eq. (7) and $\Delta P'$ in Eq. (8) due to large value of $|\beta| \approx 0.1 - 0.4$ provide the strong relation between the amplitudes of temperature and pressure as the first and second sound waves propagate.

3. SOLUTION OF THE SYSTEM OF ACOUSTICAL EQUATIONS FOR THE FIRST AND SECOND SOUNDS. ANALYSIS AND NUMERICAL RESULTS

The heat sources in Eqs. (7) and (8) provide a transfer of electromagnetic wave energy to acoustical energy. The transfer goes according to the heat mechanism, i.e., due to the heat expansion, the strong dependence of the density on the concentration ($|(c_0/\rho_0)(\partial\rho/\partial c)| \gg \alpha_T$), and the periodic changing of the temperature at the surface of the illuminated volume.

Further, for simplicity we ignore the variation of the intensity in the medium caused by absorption. We assume that the laser beam propagates along the axis of the cylindrical container. This allows us to set

$$f(t,\mathbf{r}) = \alpha I_0 \varphi(t) \varphi_1(r), \tag{10}$$

where $\varphi(t)$ is a function describing the oscillating part of the intensity, $\varphi_1(\mathbf{r}) = (2/\pi w^2)\exp[-2r^2/w^2]$ describes its radial distribution, and I_0 and w are the power and radius of the stretching of the light beam, respectively. We also assume that w is much smaller than the radius of the cylindrical container.

Taking the Hankel transfer of Eqs. (7) and (8) with respect to r

$$\overline{A}'(t,s) = \int_0^\infty \overline{A}'(t,r) J_0(rs) r\, dr, \tag{11}$$

where J_0 is the Bessel function, and $\overline{A}'(t,s) = \overline{T}'(t,s)$ or $\overline{P}'(t,s)$, we obtain

$$\frac{\partial^2 \overline{P}'}{\partial t^2} + C_1^2 s^2 \left(1 + \frac{\rho_s}{\rho_n}\beta^2 + \frac{\alpha_T \beta C_2^2}{\overline{\sigma}} \right) \overline{P}' - \frac{\rho_0 \beta C_P C_2^2 C_1^2 s^2}{T_0 \overline{\sigma}} \overline{T}' = -\frac{\alpha I_0 \beta C_1^2 \varphi_1}{T_0 \sigma_0} \frac{\partial \varphi}{\partial t}, \tag{12}$$

$$\frac{\partial^2 \overline{T}'}{\partial t^2} + C_2^2 s^2 \left(1 - \frac{\alpha_T \beta C_1^2}{\overline{\sigma}} \right) \overline{T}' + \frac{T_0 s^2}{\rho_0 C_P} \left[\alpha_T (C_1^2 - C_2^2) + \frac{\rho_s}{\rho_n} \alpha_T \beta^2 C_1^2 - \frac{\rho_s}{\rho_n} \beta \overline{\sigma} + \frac{\beta \alpha_T^2 C_1^2 C_2^2}{\overline{\sigma}} \right] \overline{P}' = \frac{\alpha I_0 \varphi_1(s)}{\rho_0 \sigma_0 C_P} (\overline{\sigma} - \beta \alpha_T C_1^2) \frac{\partial \varphi}{\partial t}. \tag{13}$$

It is assumed that $T'(r) \to 0$ and $\partial T'(r)/\partial r \to 0$ as $r \to \infty$. We also use the notation

$$\varphi_1(s) = \int_0^\infty \varphi_1(r) J_0(rs) r\, dr = \frac{1}{2\pi} \exp(-w^2 s^2/8). \tag{14}$$

We will consider two cases: instantaneous switching and harmonic law.

Instant switching

In the case of instantaneous switching $\varphi(t)$ is equal to the Heaviside unit step function $\theta(t)$ and its time derivative is equal to the Dirac function $\delta(t)$. Using the Laplace transform of Eqs. (12) and (13)

$$\hat{A}(p,s)=\int_0^\infty dt\exp(-pt)\overline{A}'(t,s) \tag{15}$$

with the initial conditions $T'(0,s)=P'(0,s)=0$, we obtain

$$A_{11}\hat{P}(p,s)+A_{12}\hat{T}(p,s)=-\frac{\alpha I_0\beta C_1^2\varphi_1(s)}{T_0\sigma_0},$$

$$A_{21}\hat{P}(p,s)+A_{22}\hat{T}(p,s)=\frac{\alpha I_0\varphi_1(s)}{\rho_0\sigma_0 C_P}(\overline{\sigma}-\beta\alpha_T C_1^2), \tag{16}$$

where the coefficients A_{ij} are defined as

$$A_{11}=p^2+s^2C_1^2\left(1+\frac{\rho_s}{\rho_n}\beta^2+\frac{\alpha_T\beta C_2^2}{\overline{\sigma}}\right),$$

$$A_{12}=-\frac{\rho_0\beta C_P}{T_0\overline{\sigma}}C_1^2C_2^2s^2,$$

$$A_{21}=\frac{T_0s^2}{\rho_0C_P}\left[\alpha_T(C_1^2-C_2^2)+\frac{\rho_s}{\rho_n}\alpha_T\beta^2C_1^2-\frac{\rho_s}{\rho_n}\beta\overline{\sigma}+\frac{\beta\alpha_T^2C_1^2C_2^2}{\overline{\sigma}}\right],$$

$$A_{22}=p^2+s^2C_2^2\left(1-\frac{\alpha_T\beta C_1^2}{\overline{\sigma}}\right).$$

The system of linear equations (16) has a solution if $A_{11}A_{22}-A_{12}A_{21}=0$. This condition can be rewritten as

$$p^4+p^2s^2\left(C_1^2+C_2^2+\frac{\rho_s}{\rho_n}\beta^2C_1^2\right)+s^4C_1^2C_2^2=0. \tag{17}$$

The roots of Eq. (17) can be found as $p_{1,2}^2=-s^2U_{1,2}^2$

$$U_1^2=C_1^2\left(1+\frac{C_1^2}{C_1^2-C_2^2}\frac{\rho_s}{\rho_n}\beta^2\right), \tag{18}$$

$$U_2^2=C_2^2\left(1+\frac{C_1^2}{C_1^2-C_2^2}\frac{\rho_s}{\rho_n}\beta^2\right)^{-1}, \tag{19}$$

where $U_{1,2}$ are the velocities of the first and second sounds, respectively. It should be mentioned that we have simplified expressions for $p_{1,2}^2$ using the small parameter $(\rho_s/\rho_n)\beta^2\ll 1$. A solution of Eq. (16) is given by

$$\hat{P}(p,s)=-\frac{\alpha I_0\beta C_1^2}{T_0\sigma_0}\frac{\varphi_1(s)p^2}{(p^2-p_1^2)(p^2-p_2^2)}, \tag{20}$$

$$\hat{T}(p,s)=\frac{\alpha I_0\varphi_1(s)}{\rho_0\sigma_0C_P}\frac{p^2(\overline{\sigma}-\alpha_T\beta C_1^2)+\overline{\sigma}s^2C_1^2}{(p^2-p_1^2)(p^2-p_2^2)}. \tag{21}$$

To find $P'(t,r)$ and $T'(t,r)$ one should use the inverse Laplace and Hankel transforms of Eqs. (20) and (21). The inverse Laplace transform gives rise to

$$\overline{P}'(t,s)=-\frac{\alpha I_0\beta C_1^2\varphi_1(s)}{T_0\sigma_0}\frac{1}{2\pi i}\int_{\sigma-i\infty}^{\sigma+i\infty}\frac{dpp^2\exp(pt)}{(p^2-p_1^2)(p^2-p_2^2)}$$

$$=-\frac{\alpha I_0\beta C_1^2U_1}{T_0\sigma_0(U_1^2-U_2^2)}\left[\sin(sU_1t)-\frac{U_2}{U_1}\sin(sU_2t)\right]\frac{\varphi_1(s)}{s}, \tag{22}$$

$$\overline{T}'(t,s)=\frac{\alpha I_0\overline{\sigma}}{\rho_0\sigma_0C_PU_2}\left[(1+G_2)\sin(sU_2t)-G_1\frac{U_2}{U_1}\sin(sU_1t)\right]\frac{\varphi_1(s)}{s}, \tag{23}$$

where

$$G_1=\frac{C_1^2(\alpha_T\beta U_1^2-\overline{\sigma\gamma})}{\overline{\sigma}(U_1^2-U_2^2)},\quad G_2=\frac{C_1^2(\alpha_T\beta U_2^2-\overline{\sigma\gamma})}{\overline{\sigma}(U_1^2-U_2^2)},$$

$$\overline{\gamma}=\frac{C_1^2}{C_1^2-C_2^2}\frac{\rho_s}{\rho_n}\beta^2=\frac{U_1^2-C_1^2}{C_1^2}=\frac{C_2^2-U_2^2}{U_2^2}>0. \tag{24}$$

Using the Hankel transfer of Eqs. (22) and (23), we can write

$$P'(t,r)=-\frac{\alpha I_0\beta C_1^2U_1}{T_0\sigma_0(U_1^2-U_2^2)}\int_0^\infty ds\,J_0(sr)\varphi_1(s)\times\left[\sin(sU_1t)-\frac{U_2}{U_1}\sin(sU_2t)\right], \tag{25}$$

$$T'(t,r)=\frac{\alpha I_0\overline{\sigma}}{\rho_0C_P\sigma_0U_2}\int_0^\infty ds\,J_0(sr)\varphi_1(s)\times\left[(1+G_2)\sin(sU_2t)-G_1\frac{U_2}{U_1}\sin(sU_1t)\right]. \tag{26}$$

If we set in Eq. (24) $U_1^2\approx C_1^2$, we obtain

$$\overline{\gamma}=0,\quad G_2=\frac{\alpha_T\beta U_1^2U_2^2}{\overline{\sigma}(U_1^2-U_2^2)}=G,\quad G_1=G\frac{U_1^2}{U_2^2}, \tag{27}$$

and Eq. (26) can be written as

$$T'(t,r)=\frac{\alpha I_0\overline{\sigma}}{\rho_0C_P\sigma_0U_2}\int_0^\infty dsJ_0(sr)\varphi_1(s)\times\left[(1+G)\sin(sU_2t)-G\frac{U_1}{U_2}\sin(sU_1t)\right]. \tag{28}$$

The first term in Eq. (25) corresponds to impulse of the first sound, and the second term corresponds to the variation in temperature of the first sound wave. It always has an opposite phase. Since $\beta=(c_0/\rho_0)(\partial\rho/\partial c)<0$, the amplitude of the first sound, $P_{\max}=-\alpha I_0\beta U_1^3/T_0\sigma_0(U_1^2-U_2^2)$, is always positive. The first term in the expression for $T'(t,r)$ is a heat impulse of the second sound, while the second term corresponds to the variation of pressure when temperature waves pass in the considered solution. It is worth mentioning that according to Eq. (26) or Eq. (28), a sign of the phase of $P'_{(2)}$ depends of the sign of G_1 and can either be opposite to the

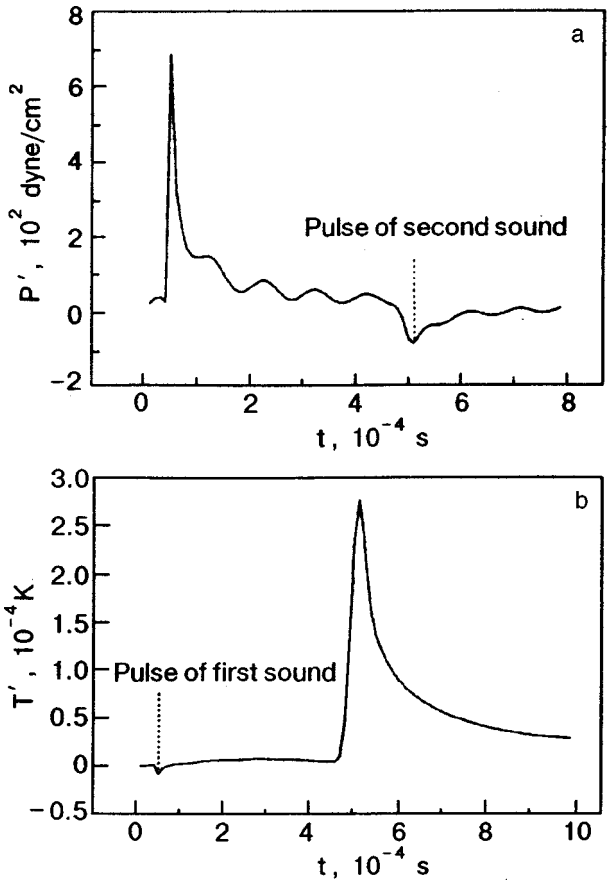

FIG. 1. Pressure (a) and temperature (b) against time for a superfluid ^{3}He–^{4}He solution. The calculation was carried out for instantaneous switching and $r=1$ cm.

sign of the phase of the impulse or coincide with it. In the range of temperature and concentration where $\alpha_T<0$ the phases of $P'_{(2)}(t,r)$ and $T'_{(2)}(t,r)$ are opposite to each other, but for $\alpha_T>0$, which provides $\alpha_T\beta U_1^2<\overline{\sigma\gamma}$ or $G_1<0$, the phases coincide.

Figures 1a and 1b show the amplitudes of the pressure and temperature against time. The calculation was carried out on the basis of Eqs. (25) and (28) for $r=1$ cm, $w=0.05$ cm, $\alpha=1\ \mathrm{cm}^{-1}$, $I_0=1$ W, $T_0=1.5$ K, $\alpha_T=-12\cdot10^{-3}\ \mathrm{K}^{-1}$, $\beta=-0.3$ (Ref. 11), $U_1=220$ m/s, $U_2=20$ m/s, $\overline{\sigma}=620$ J/(kg·K) (Ref. 6), $\sigma_0=2.3\times10^3$ J/(kg·K), $\rho_0=0.12\ \mathrm{g/cm}^3$, and $C_P=3\times10^3\ \mathrm{J/kg}^3$. It is easy to see in the figures that there are signatures of impulses of the first and second sounds at $t_{(1)}\approx r/U_1$ and $t_{(2)}\approx r/U_2$. The amplitudes of the impulses are large enough to be recorded by using modern methods.

Harmonic law

Let us now consider the case where the intensity of the laser beam changes in time with acoustical frequency ω. It is instructive to carry out calculations using the complex functions

$$\varphi(t)=\exp(-i\omega t),\quad \frac{\partial\varphi}{\partial t}=-i\omega\varphi(t), \tag{29}$$

but keep in mind that we should finally take only the real parts. We assume that all the other variables vary according to the same law:

$$\overline{P'}(t,s)=\overline{P'}(\omega,s)\exp(-i\omega t),$$
$$\overline{T'}(t,s)=\overline{T'}(\omega,s)\exp(-i\omega t). \tag{30}$$

Using

$$\frac{d^2\overline{P'}}{dt^2}=-\omega^2\overline{P'}(t,s),\quad \frac{d^2\overline{T'}}{dt^2}=-\omega^2\overline{T'}(t,s) \tag{31}$$

in Eqs. (12) and (13), we obtain

$$\left[\omega^2-C_1^2s^2\left(1+\frac{\rho_s}{\rho_n}\beta^2+\frac{\alpha_T\beta C_2^2}{\overline{\sigma}}\right)\right]\overline{P'}(\omega,s)$$
$$+\frac{\rho_0\beta C_P C_1^2C_2^2s^2}{T_0\overline{\sigma}}\overline{T}(\omega,s)=\frac{\alpha I_0\beta C_1^2 i\omega\varphi_1(s)}{T_0\sigma_0}, \tag{32}$$

$$\frac{T_0s^2}{\rho_0C_P}\left[\alpha_T(C_1^2-C_2^2)-\frac{\rho_s}{\rho_n}\beta\overline{\sigma}+\frac{\rho_s}{\rho_n}\alpha_T\beta^2C_1^2\right.$$
$$\left.+\frac{\beta\alpha_T^2C_1^2C_2^2}{\overline{\sigma}}\right]\overline{P'}(\omega,s)-\left[\omega^2-s^2C_2^2\left(1-\frac{\alpha_T\beta C_1^2}{\overline{\sigma}}\right)\right]$$
$$\times\overline{T'}(\omega,s)=-\frac{i\omega(\overline{\sigma}-\beta\alpha_TC_1^2)\alpha I_0\varphi_1(s)}{\rho_0C_P\sigma_0}.$$

The solution of Eq. (32) is similar to that of Eq. (16). It is given by

$$\overline{P'}(\omega,s)$$
$$=-\frac{i\alpha\omega I_0\beta C_1^2\varphi_1(s)\omega^2}{T_0\sigma_0[\omega^4-\omega^2s^2(C_1^2+C_2^2+\rho_s/\rho_n\beta^2C_1^2)+C_1^2C_2^2s^4]}, \tag{33}$$

$$\overline{T'}(\omega,s)$$
$$=\frac{i\omega\alpha I_0\varphi_1(s)[\omega^2(\overline{\sigma}-\alpha_T\beta C_1^2)-C_1^2\overline{\sigma}s^2]}{\rho_0\sigma_0C_P[\omega^4-\omega^2s^2(C_1^2+C_2^2+\rho_s/\rho_n\beta^2C_1^2)+C_1^2C_2^2s^4]}. \tag{34}$$

The frequency ω must satisfy the equation

$$\omega^4-\omega^2s^2\left(C_1^2+C_2^2+\frac{\rho_s}{\rho_n}\beta^2C_1^2\right)+C_1^2C_2^2s^4=0. \tag{35}$$

Its roots can be written as

$$\omega_1^2=U_1^2s^2,\quad \omega_2^2=U_2^2s^2. \tag{36}$$

Simple calculation allows one to express Eqs. (33) and (34) in the form

$$\overline{P'}(\omega,s)=\frac{i\omega\alpha I_0\beta U_1^2\varphi_1(s)}{T_0\sigma_0(U_1^2-U_2^2)}\left(\frac{1}{s^2-k_1^2}-\frac{1}{s^2-k_2^2}\right), \tag{37}$$

$$\overline{T'}(\omega,s)=-\frac{i\omega\alpha I_0\varphi_1(s)\overline{\sigma}}{\rho_0C_P\sigma_0U_2^2}\left(\frac{1+G_2}{s^2-k_2^2}-\frac{G_1U_2^2}{U_1^2}\frac{1}{s^2-k^2}\right). \tag{38}$$

The inverse Hankel transfer of Eqs. (37) and (38) yields

$$P'(t,r)=-\frac{\alpha\omega I_0\beta U_1^2}{4T_0\sigma_0(U_1^2-U_2^2)}\left[H_0^{(1)}(k_1r)\exp\left(-\frac{k_1^2w^2}{8}\right)-H_0^{(1)}(k_2r)\exp\left(-\frac{k_2^2w^2}{8}\right)\right]\exp(-i\omega t). \quad (39)$$

$$T'(t,r)=\frac{\omega\omega I_0\overline{\sigma}}{4\rho_0\sigma_0C_PU_2^2}\left[(1+G_2)H_0^{(1)}(k_2r)\times\exp\left(-\frac{k_2^2w^2}{8}\right)-\frac{GU_2^2}{U_1^2}H_0^{(1)}(k_1r)\times\exp\left(-\frac{k_1^2w^2}{8}\right)\right]\exp(-i\omega t), \quad (40)$$

where $H_0^{(1)}$ is the Hankel function. It is evident from Eqs. (39) and (40) that the system generates a cylindrical wave. In the far zone, where $r\gg U_{1,2}/\omega$, the needed expressions take the form

$$P'(t,r)=-\frac{\alpha\omega I_0\beta U_1^2\exp(-i(\omega t+\pi/4))}{2T_0\sigma_0(U_1^2-U_2^2)\sqrt{2\pi r}}\times\left[k_1^{-1/2}\exp\left(irk_1-\frac{k_1^2w^2}{8}\right)-k_2^{-1/2}\times\exp\left(irk_2-\frac{k_2^2w^2}{8}\right)\right], \quad (41)$$

$$T'(t,r)=\frac{\alpha\omega I_0\overline{\sigma}\exp(-i(\omega t+\pi/4))}{2\rho_0C_P\sigma_0U_2^2\sqrt{2\pi r}}\times\left[\frac{1+G_2}{\sqrt{k_2}}\exp\left(irk_2-\frac{k_2^2w^2}{8}\right)-\frac{G_1U_2^2}{U_1^2\sqrt{k_1}}\exp\left(irk_1-\frac{k_1^2w^2}{8}\right)\right]. \quad (42)$$

The expressions obtained by us show that the amplitudes of excited oscillations are proportional to $\sqrt{\omega}$. There are maxima at the frequencies $\omega_{\max_{1,2}}=\sqrt{2}U_{1,2}/w$ in the dependence of the amplitudes of impulses on frequency. For $w=0.05$ cm they are $\omega_1\approx10^6\ \mathrm{s}^{-1}$ and $\omega_2\approx10^5\ \mathrm{s}^{-1}$ for the first and second sound, respectively. Note that signals of heat impulses were reported[12] to be firmly recorded, and that their amplitude is of the order of 10^{-6} K. This allows one to reduce I_0 by a factor of 10–100, while w can be reduced to a tolerable possibility (with allowance for the diffraction effects). The maximal amplitudes of the recorded signal of the second sound can be increased to $10^7-10^8\ \mathrm{s}^{-1}$.

4. CONCLUSIONS

We have considered the possibility of an optical generation of the first and second sounds in the superfluid ^{3}He–^{4}He solutions. It has been shown that a synchronous generation of waves of the first and second sound is quite realistic if a solution is illuminated by amplitude-modulated laser radiation with the wavelength corresponding to the range of absorption of the system. It has been shown that this method covers the range of frequencies of the second sound, which is hardly achievable by means of other methods.

I wish to thank Prof. V. P. Romanov for detailed discussions and Dr. A. A. Karabutov for useful advice.

*)E-mail: sebak@td.silk.org

[1] I. M. Khalatnikov, Introduction to the Theory of Superfluids, Benjamin, New York (1965).
[2] E. Ya. Rudavsky and I. A. Serbin, Sov. Phys. JETP **51**, 1930 (1966).
[3] E. M. Lifshitz, J. Phys. USSR **8**, 110 (1944).
[4] L. S. Dikina, E. Ya. Rudavsky, and I. A. Serbin, Sov. Phys. JETP **58**, 843 (1970).
[5] B. N. Yesel'son, M. I. Kaganov, E. Ya. Rudavsky, and I. A. Serbin, Sov. Phys. Usp. **112**, 591 (1974).
[6] D. A. Rockwell, R. F. Benjamin, and T. J. Greytak, J. Low Temp. Phys. **18**, 389 (1975).
[7] L. M. Lyarashev, *Laser Thermooptical Excitations of Sound*, Nauka, Moscow (1969).
[8] V. P. Romanov and T. Kh. Salikhov, Phys. Lett. A **161**, 161 (1991).
[9] C. M. Surko, R. E. Packerd, G. J. Dick, and F. Reif, Phys. Rev. Lett. **24**, 657 (1970).
[10] M. Stockton, J. W. Keto, and W. A. Fitzsimmons, Phys. Rev. A **5**, 372 (1972).
[11] B. N. Yesel'son, V. G. Ivantzov, V. A. Koval, E. Ya. Rudavsky, and I. A. Serbin, *Properties of Liquid and Solid Helium. Solutions* ^{3}He–^{4}He, Kiev (1962).
[12] N. E. Dyumin, N. N. Grigor'ev, and C. V. Svatko, Fiz. Nizk. Temp. **15**, 253 (1989) [Sov. J. Low Temp. Phys. **15**, 142 (1989)].

This article was published in English in the original Russian journal. It was edited by S. J. Amoretty.

SUPERCONDUCTIVITY, HIGH-TEMPERATURE SUPERCONDUCTIVITY

Vortex lattice melting in layered HTSC in the field of defects

M. E. Gracheva, V. A. Kashurnikov, O. A. Nikitenko, and I. A. Rudnev

*Moscow State Institute of Engineering and Physics (Technical University), 115409 Moscow, Russia**

(Submitted June 26, 1998; revised March 29, 1999)
Fiz. Nizk. Temp. **25**, 1027–1031 (October 1999)

The effect of defect potential on the melting temperature of the vortex lattice in a layered HTSC is investigated. It is found that an increase in the value of the defect potential leads to a shifting of the phase transition point to the critical temperature, thus increasing considerably the range of the intermediate phase ''rotating lattice''. © *1999 American Institute of Physics.* [S1063-777X(99)00310-2]

1. INTRODUCTION

Processes occurring in the vortex phase of high-temperature superconductors (HTSC) have been the subject of intensive research in recent years. Both theoretical and experimental studies are being carried out, and the complexity of the problems necessitates the use of numerical simulation (see our review in Ref. 1), It has been established reliably that the Abrikosov[2] lattice is not the only state in which the vortex system can exist in an HTSC. An increase in temperature results in melting of the vortex lattice and leads to a vortex lattice–vortex liquid phase transition. The existence of such a phase transition was proved convincingly, among others, by Schneider *et al.*[3] who used numerical simulation to analyze short-range correlations in the vortex lattice and calculated the melting temperature (melting point) of the vortex lattice. The melting point can be determined from the Lindemann criterion, i.e., from a comparison of the mean-square deviation of vortices and the lattice parameter.[4,5] Ruy *et al.*[4] also employed a convenient phase-transition criterion, selecting the singularity on the temperature dependence $C(T)$ of the heat capacity of the vortex system for determining the phase transition point.

Defect field studies[6,7] are especially interesting since a change in the phase transformation pattern occurs in this case. Thus, we discussed in our recent publication[7] the melting of vortex lattice in the presence of a pinning center. It was shown that melting occurs in three stages. In the beginning, the trigonal lattice begins to disintegrate at low temperatures away from the pinning centers. Lattice islets are formed in the complete absence of a rigorous long-range order. The ''islets'' begin to rotate around fixed pinning centers, forming a ''rotating lattice'' phase. At the final stage, the lattice melts completely (vortex liquid phase).[6] The point of transition from the ''rotating lattice'' to the vortex liquid is expected to depend strongly on the magnitude of the defect potential. The present communication aims mainly at deriving this dependence, i.e., at determining the boundary of the ''rotating lattice''–vortex liquid phase transition as a function of the defect potential.

2. DESCRIPTION OF THE MODEL

The Monte Carlo (MC) method is used in most cases to study the behavior of the Abrikosov vortex lattice in HTSC.

In contrast to the molecular dynamics method which also describes the dynamic characteristics, the Monte Carlo method provides information about the configurational characteristics of the system. By choosing an appropriate ensemble, say, canonical, we can use the Monte Carlo technique to calculate the observed physical quantities for fixed values of the number of particles, volume and temperature.

The main advantage of the Monte Carlo technique is that it does not require any approximation, and takes interactions into account exactly. The system is described by the most convenient model Hamiltonian for the problem.[1] In this work, we use the standard Monte Carlo technique together with the Metropolis algorithm for a canonical ensemble.[8,9]

Let us consider a two-dimensional system of Abrikosov vortices which can be treated as classical particles with long-range interaction arranged over a rectangular mesh. The discreteness of the three-dimensional mesh is chosen in such a way that its period is much smaller than the trigonal lattice period. This model takes into account the contribution to the energy coming from the interaction of vortices with one another and with defects. Calculations are made for the shortest distance between vortices, taking periodicity into account. In view of all that has been stated above, we can present the model Hamiltonian in the form

$$H=\frac{1}{2}\sum_{i\neq j}^{N} H(r_i,r_j)n_i n_j+\sum_{i=1}^{N} U_p(r_i)n_i, \tag{1}$$

where

$$H(r_i,r_j)=[\Phi_0^2 d/2\pi\lambda^2(T)\mu_0]K_0\left(\frac{|r_i-r_j|}{\lambda(T)}\right)$$

$$=U_0(T)K_0\left(\frac{|r_i-r_j|}{\lambda(T)}\right). \tag{2}$$

Here, $U_p(r_i)$ is the energy of interaction of a vortex with a defect at site i, n_i the occupancy of vortices (0 or 1) at the ith site of the three-dimensional mesh, $\Phi_0 = hc/2e$ the magnetic flux quantum, K_0 the zeroth order Bessel function of the imaginary argument, d the superconducting layer thickness, $\mu_0 = 4\pi \cdot 10^{-7}$ H-m^{-1}, and $\lambda(T) = \lambda(0)/[1-(T/T_c)^{3.3}]^{1/2}$ is the magnetic field penetration depth.

3. COMPUTATIONAL TECHNIQUE

Parameters close to the characteristics for the layered HTSC $Bi_2Sr_2CaCu_2O_x$ were used for specific computations: $d = 2.7$ Å; $\lambda(T=0) = 1800$ Å; $T_c = 84$ K. The three-dimensional vortices in $Bi_2Sr_2CaCu_2O_x$ disintegrate into plane two-dimensional ''vortex pancakes'' connected with one another through weak bonds. Hence in this case we can speak of quasi-two- dimensionality of the vortex structure and consider a two-dimensional model. The external field B is chosen equal to 0.01 T, corresponding to the real scale of field induction for which the melting of the vortex lattice in bismuth-based HTSC's is observed.

Calculations were made on a two-dimensional spatial mesh of size 200×200 with periodic boundary conditions. The main results were obtained for the numbers $N_v = 150$ of vortices and $N_d = 5$ of defects (two-dimensional concentration of defects $\sim 10^{10}$ cm^{-2}). The defects were distributed randomly over the mesh. The actual concentration of vortices corresponding to the given field B was reproduced by varying the value of each division on the spatial cell in such a way that the period a_v of the trigonal vortex network satisfies the relation $a_v = (2\Phi_0/B\sqrt{3})^{1/2}$. In other words, a variation of the external magnetic field changes only the vortex concentration, as reflected in the model: a variation of the magnetic field changes the area of the region under consideration for a fixed value of the simulation parameter, i.e., the number of vortices. Thus the vortex concentration changes with the field.

Defects were simulated as point-like wells with the same potential, and the energy of interaction of a vortex with a pinning center assumes the form[10,11]

$$U_p(r,T) = -[U_0(T)/8]\delta_{r,ri}. \tag{3}$$

In actual practice, the concentration of vortex filaments is much higher than the defect concentration in the magnetic fields under consideration. Moreover, our calculations were based on the defect concentrations close to the experimental values.[12]

The results of numerical computations were used for reproducing the heat capacity (as a function of temperature) which can be presented in the following form in terms of the internal energy fluctuation ($k_B = 1$):

$$C(T) = |\langle E^2\rangle - \langle E\rangle^2|/T^2. \tag{4}$$

By way of an example. Fig. 1 shows the $C(T)$ dependence and the melting point T_m for two values of the defect potential, viz. $U_p = 1$ and 100 meV. Calculations were made for defect potentials between 1 and 100 meV for the number of vortices $N_v = 150$.

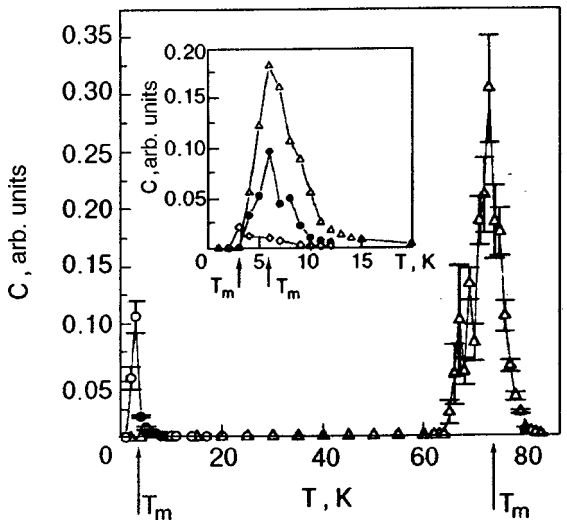

FIG. 1. Temperature dependence of heat capacity in defect field $U_p = 1$ meV (○), $U_p = 100$ meV (△). The inset shows the effect of vortex concentration N_v on the melting point, $N_v = 50$ (◇), 100 (●); 150 (△), for $U_p = 70$ meV.

In order to confirm that the number of vortices is macroscopically large for the problem under consideration, we calculated the heat capacity for the same value of the defect potential, but for different numbers of vortices (e.g., $N_v = 50,100,150$). The results are shown in the inset to Fig. 1. It can be seen that even for $N_v = 100$ and 150, the values of T_m coincide within the error limits, while an increase in the number of vortices from 50 to 100 displaces the heat capacity peak towards higher temperatures and increases its height. The temperature peak does not shift any more for $N_v = 150$. This leads to the conclusion that the number of vortex points $N_v = 150$ is macroscopically large for our problem. We also carried out test computations of heat capacity for different numbers of MC-steps.

The standard Monte Carlo procedure can be described as follows (see also Refs. 8 and 9). Initially, the vortices are distributed at random over the phase space mesh simulating the HTSC plane. Obviously, the initial arbitrary distribution of vortices does not correspond to the minimum energy; hence the system is made to evolve and the most favorable configurations from energy point of view are selected in accordance with the Metropolis algorithm realizing Gibbs' distribution. A typical value of the number of Monte Carlo steps was 60000. The number of steps leading to a complete thermalization of the system (when the system assumes stable configurations with the minimum energy) is 30000, and the system under consideration attained equilibrium after such a number of Monte Carlo steps. The minimum variation of the instantaneous configuration of the system involves an elementary displacement of a single vortex. By a Monte Carlo step we mean a single displacement of all vortices in the system, i.e., each vortex is displaced on the average once in each Monte Carlo step. Estimates show that such a number of MC steps is sufficient for calculating heat capacity with the minimum statistical error.

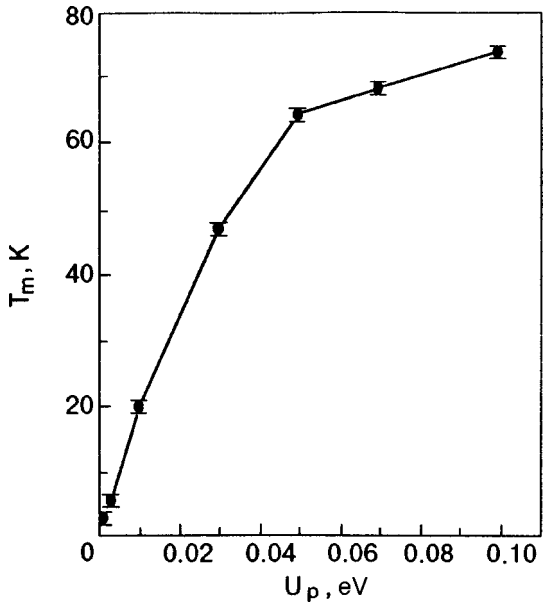

FIG. 2. Dependence of the melting point on the defect potential.

4. CALCULATIONS AND DISCUSSION OF RESULTS

All three stages of melting of vortex lattice mentioned above were considered in calculations.[7] The heat capacity of the system was calculated for different values of the defect potential as a function of temperature. The singularities on the temperature dependence $C(T)$ could be used for determining exactly the transition temperature at which the vortex lattice split into islets trapped at the defects is transformed into the vortex liquid phase. This is the temperature T_m (or T_{m2} in the terminology used in Ref. 7).

Having determined the value of T_m, we obtained the dependence of the transition temperature on the defect potential (Fig. 2). It can be seen that an increase in the defect potential leads to a monotonic increase in the melting temperature. The obtained results can be interpreted in a simple physical picture of the processes occurring in the vortex lattice of an HTSC in the presence of defects. Let us consider a vortex lattice for a certain value of the defect potential. Three types of interactions compete in this lattice, namely, mutual interaction of vortices which determines the lattice rigidity, thermal fluctuations, and the interaction of vortices with defects. At low temperatures, the lattice preserves its rigidity. A vortex trapped in the potential well of a defect has a high probability of being localized at this well. As the temperature is increased, the lattice begins to lose its rigidity away from the defect at first. A vortex trapped at a defect holds an islet of the coherent region of the vortex lattice around it (''rotating lattice'' phase[7]). Away from the vortex, the lattice begins to crumble. A further increase in temperature increases thermal fluctuations, and the size of the ''confined'' region decreases. This increases the probability that the vortex (together with the coherent region confined by it) leaves the potential well. Finally, at still higher temperatures, the islets are destroyed, the vortices break loose from the defects, and the vortex system melts completely. For large values of the defect potentials, the defect will trap a vortex around it, and this explains the increase in the value of T_m with increasing depth of the potential well of defects in the complex ''rotating lattice'' phase.[7] We believe that a slower increase in the value of T_m near the critical region (Fig. 2) is simply due to the temperature dependence of the depth of the defect potential well inherent in formula (3). Moreover, calculations show that the renormalization of the potential well depth taking temperature into consideration ''linearizes'' the $T_m(U_p)$ dependence.

Finally, it should be noted that the experiments have repeatedly revealed the existence of a certain intermediate phase in the model considered by us with a non-trigonal lattice and a vortex liquid dynamics. For example, Perkins *et al.*[13] obtained a scaling dependence of the normalized velocity of screened currents relaxation in $TmBa_2Cu_3O_{6.9}$ crystals: $S/T=f_s(H/H_{\max})$, where $S=d\log M_{\rm irr}/d\log v$; $v=dH/dt$, $M_{\rm irr}$ being the hysteresis width and v the magnetic field sweep rate. The dependence of S/T on $H/H_{\max}$ clearly shows three regions with different magnetic flux dynamics. According to Fuchs *et al.*,[14] the first region is qualitatively in accord with the elastic theory of collective creep for small vortex bundles. The second region was attributed by the authors to the emergence of plastic deformation in the vortex lattice, and the third region corresponds to the formation of the vortex liquid.

The existence of the intermediate phase on the phase diagram of bismuth-based HTSC was proved experimentally in a recent publication[14] according to which the solid phase below the melting curve is apparently divided into two phases. In the first (I) phase, the vortices are stationary, while in the second (II) phase they begin to move, and a transition to the vortex liquid occurs upon a further increase in temperature. The authors define the first phase as a ''weakly disordered Bragg's glass,'' while the second phase is treated as a ''strongly disordered Josephson glass.'' The effect of point pinning on the system of vortices and the formation of a reverse curve on the phase diagram was shown qualitatively by Nelson[15] who proved that the point pinning in the two- dimensional case affects the vortex liquid in a certain region below the melting curve. In our case, this region corresponds to the ''rotating lattice'' phase (orientational melting), i.e., to phase II.

Recent publications on the experimental observation of the heat capacity of a vortex system also display clearly peaks on the temperature dependences of the heat capacity of $YBa_2Cu_3O_{7-\delta}$ single crystals, corresponding to a transition to the vortex liquid.[16,17] The origin of the transition remains unclear. However, since the emergence of the heat capacity peak in the experiments is accompanied by a jump in the magnetization of the system, it can be only assumed that this is a first-order thermodynamic transition.[16,17]

5. CONCLUSION

Studies of the vortex system melting in HTSC in the presence of defects reveal that the defect potential affects strongly the temperature of transition between the ''rotating lattice'' and the vortex liquid phases. An increase in the depth of the defect potential well increases the temperature

of this transition and extends the temperature range in which the intermediate ''rotating phase'' is realized. An increase in the temperature region corresponding to the existence of this intermediate phase in the experiments may lead to a considerable broadening of the IVC.[18,19]

This research was supported financially by a grant from the state program on Science and Technology ''Physics of the Condensed State,'' program ''Superconductivity'' project Nos. 99011 and 96026.

*E-mail: kash@cityline.ru

[1] M. E. Gracheva, M. V. Katargin, V. A. Kashurnikov, and I. A. Rudnev, Fiz. Nizk. Temp. **23**, 1151 (1997) [Low Temp. Phys. **23**, 863 (1997)].
[2] A. A. Abrikosov, Zh. Éksp. Teor. Fiz. **32**, 1442 (1957) [Sov. Phys. JETP **6**, 1174 (1957)].
[3] J. W. Schneider, S. Schafroth, and P. F. Meier, Phys. Rev. B **52**, R13149 (1995).
[4] S. Ruy, S. Doniach, G. Deutscher, and A. Kapitulnik, Phys. Rev. Lett. **68**, 710 (1992).
[5] K. Yates, D. J. Newman, and P. A. J. de Groot, Physica C **241**, 111 (1995).
[6] K. Yates, D. J. Newman, and P. A. J. de Groot, Phys. Rev. B **52**, R13, 149 (1995).
[7] M. E. Gracheva, V. A. Kashurnikov, and I. A. Rudnev, Pis'ma Zh. Éksp. Teor. Fiz. **66**, 269 (1997) [JETP Lett. **66**, 291 (1997)].
[8] D. V. Heerman, *Computer Simulation Methods in Theoretical Physics*, Springer-Verlag, NY (1986).
[9] K. Binder and D. V. Heerman, *Monte-Carlo Simulation Methods in Statistical Physics* (Russian translation), Nauka, Moscow (1995).
[10] K. Moon, R. T. Scalettar, and G. T. Zimanyi, Phys. Rev. Lett. **77**, 2778 (1996).
[11] S. Ryu, M. Hellerqvist, S. Doniach *et al.*, Phys. Rev. Lett. **77**, 5114 (1996).
[12] G. Blatter, M. V. Feigel'man, V. B. Geshkenbein *et al.*, Rev. Mod. Phys. **66**, 1125 (1994).
[13] G. K. Perkins, L. F. Cohen, A. A. Zhukov, and A. D. Caplin, Phys. Rev. B **55**, 8110 (1997).
[14] D. T. Fuchs, E. Zeldov, T. Tamegai *et al.*, Phys. Rev. Lett. **80**, 4971 (1998).
[15] D. R. Nelson, Physica C **263**, 12 (1996).
[16] A. Schilling, R. A. Fisher, N. E. Phillips *et al.*, Phys. Rev. Lett. **78**, 4833 (1997)].
[17] M. Roulin, A. Junod, A. Erb, and E. Walker, Phys. Rev. Lett. **80**, 1722 (1998).
[18] A. N. Lykov, C. Attanasio, L. Maritato, and S. L. Prischepa, Supercond. Sci. Technol. **10**, 119 (1997).
[19] V. F. Elesin, I. A. Esin, I. A. Rudnev *et al.*, Sverkhprovodimost: Fiz., Khim., Tekh. **6**, 807 (1993).

Translated by R. S. Wadhwa

Effect of anomalously small dose of fast neutron radiation on the surface impedance of a Pb single crystal near H_{c3}

L. I. Jorjishvili

*Institute of Physics, Georgian Academy of Sciences, 380077 Tbilisi, Georgia**)
(Submitted November 24, 1998)
Fiz. Nizk. Temp. **25**, 1032–1034 (October 1999)

It is shown experimentally that the exposure of a Pb single crystal to an anomalously small dose of fast neutrons ($\sim 4\times 10^6$ neutrons/cm^2) leads to suppression of cyclotron resonance and surface superconductivity. This effect is explained by geometrical factors. © *1999 American Institute of Physics.* [S1063-777X(99)00410-7]

This research is a continuation of our previous publications[1–6] in which the results of analysis of the effect of small doses of fast neutrons on the cyclotron resonance (CR),[1] microwave (MW) impedance[2] of monocrystalline lead, and the effect of radiation on CR in a preliminarily deformed single crystal[5] were considered.

Measurements were made on spectrometers with frequency modulation[7,8] in the autodyne mode and with a frequency-modulated klystron. Stripline resonators operated at frequency $f=9.6$ GHz. The temperature of measurements $T=1.4$–1.25 K was attained by pumping helium vapor. Single crystals of diameter 17.8 mm and thickness varying from 0.8 to 1.8 mm (for different samples) were prepared by the method described by Khaikin *et al.*[9] The quality of the grown single crystals was estimated by the parameter $\omega\tau$ whose values varied from 15 to 95 for different samples at $T=1.4$ K. The sample served as the bottom of the stripline resonator. The side facing the interior of the resonator is referred to as the front and the opposite side is called the back.

The samples at $T=300$ K were exposed to radiation emitted by a Pu–Be source[10] with integral intensity 4.7×10^6 neutrons/cm$^2\cdot$s in a solid angle 4π. The neutron flux was measured by a radiation dosimeter KRAN-1 equipped with neutron-sensitive detectors for fast, intermediate, and thermal neutrons. Anomalously small doses of neutrons were obtained by using a filter made of boron and paraffin. Measurements led to the following values of neutron fluxes in the region of location of the sample exposed to radiation: 380 neutrons/cm$^2\cdot$s for fast neutrons, 125 neutrons/cm$^2\cdot$s for intermediate phonons, and 65 neutrons/cm$^2\cdot$s for thermal neutrons (error of measurements was 30%).

Figure 1 shows the dependence of the microwave surface impedance of Pb-13 single crystal ($\omega\tau=95$) on the applied magnetic field for unexposed sample (a) and after its exposure for two hours (b). It can be seen from the figure that irradiation leads to suppression of not only CR, but also the surface superconductivity. The electron beam ''heats'' the sample surface during electron-microscopic photography to such an extent that it leads to an explosion of a gas bubble in the surface layer (as in the case of Pb-15 single crystal). For this reason, sample Pb-13 (being the best sample) was not subjected to any effect (radiation by the electron beam in the electron microscope, deformation, or annealing in vacuum) except irradiation by neutrons.

Further irradiation of the crystal led to unexpected results. It did not cause a noticeable ''damage'' of the sample, but even improved its quality: the transmission band of the microwave resonator was narrowed, and the CR was observed.[2] This is obviously due to homogenization of the single crystal surface by a neutron flow, when not only the order, but also the disorder can be violated. Neutron beam also stimulated surface diffusion,[11] and the surface is not only recovered with time, but also becomes smoother: the parameter $\omega\tau$ of the Pb-13 sample became equal to 130 after three years following irradiation.

It is well known that CR and surface superconductivity are phenomena occurring in the skin layer: $\delta_{an}=2.8\times 10^{-5}$ cm at the frequency $f=9.6$ GHz for CR[12] and over the coherence length $\xi_{Pb}=8.3\times 10^{-6}$ cm for surface superconductivity.[13] Consequently, we can associate the suppression of CR and degradation of surface superconductivity with the damage of the surface relief of the single crystal as a result of its bombardment by neutrons.

Let us consider in greater detail the processes occurring in a Pb single crystal bombarded by neutrons. Samples were exposed to radiation from the back, Neutrons knocked out Pb atoms from the sample surface and were capable of ejecting cascades of atoms to the front. These processes lead either to scattering of Pb atoms in space and formation of indentations on the sample surface, or to the formation of humps of ejected atoms in the form of ant-hills (in the case of the emergence of cascades at the surface). This can be seen clearly on the electron-microscopic photograph of the surface of irradiated Pb-15 sample (Fig. 2). The estimation of surface defect size from the photograph proved that the defects have a size of the order of skin depth ($\geqslant 10^{-5}$ cm) in the plane; in this case, the scattering of microwave current at frequency $f=9.6$ GHz is most effective.

According to De Gennes,[13] the nuclei of surface superconductivity are formed when the magnetic field is parallel to the sample surface carrying microwave currents. But since wells and humps (''ant-hills'') whose size is comparable

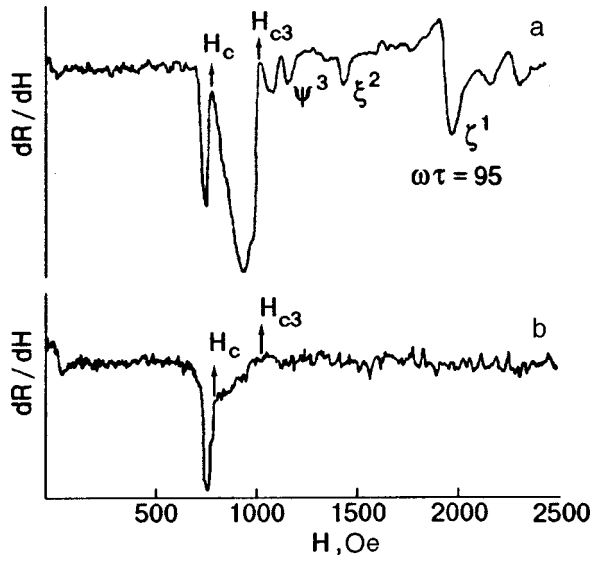

FIG. 1. Suppression of CR at $T=1.4$ K and $\nu=9.375\times10^9\ s^{-1}$: Pb-13 sample not subjected to bombardment (a) and after its exposure to a fast neutron dose of 4.1×10^6 neutrons/cm$^2\cdot$s (for 2 h in a flux of 570 neutrons/cm$^2\cdot$s) (b).

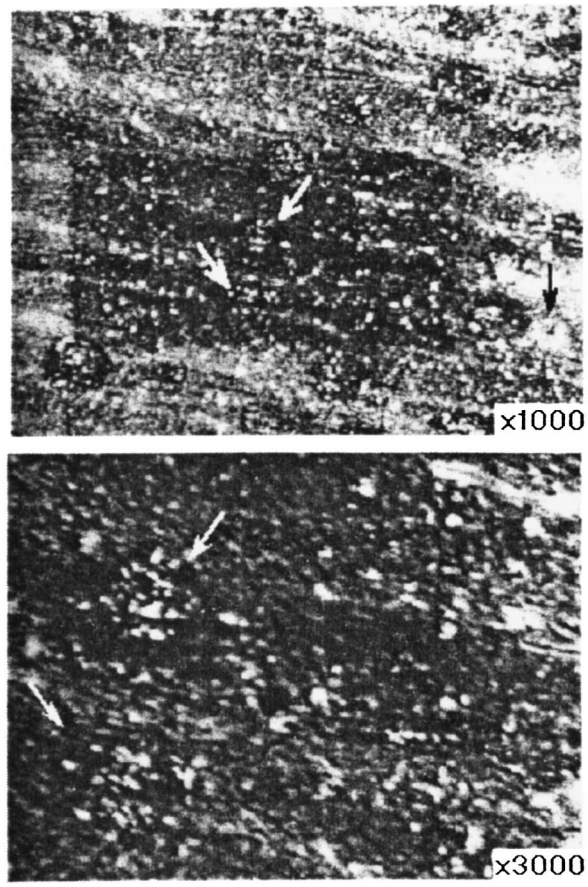

FIG. 2. Electron-microscopic photograph of the front of the Pb-15 sample irradiated from the back, obtained with JSM-50 microscope with the beam voltage 35 kV. The Pb-15 sample was bombarded for 2 h by a flux of 570 neutrons/cm$^2\cdot$s (a radiation dose of $4.1\cdot10^6$ neutrons/cm^2). Typical ''ant-hills'' with craters are indicated by arrows. Magnification ×1000 and ×3000, photographic enlargement ×2.94.

with the skin depth (coherence length) are formed on the sample surface as a result of irradiation, the magnetic field is no longer strictly parallel to the surface. In order to verify this assumption, a test experiment was made,[6] in which we proved that the superconducting transition near H_{c3} becomes less sharp and has a smaller width even when the magnetic field is tilted to the sample surface at an angle 2.5°. We could estimate the average size of hills in the plane using the photograph of the front face of the Pb-15 sample shown in Fig. 2. It was found to be 5–30 μm (with a microscope magnification ×1000 and a photographic enlargement ×2.94). The height of the hills could not be evaluated since the electron microscope has no vertical resolution. However, the height of a hill can be estimated on the basis of the results of special test experiments[6] and the present results. The generator of the cone of the hill clearly forms an angle larger than 2.5° with the magnetic field (since CR or transition is not observed at H_{c3} are observed). If the average diameter of the cone base is $\sim10^{-4}$ cm, the slanting angle between the cone generator and the base, which is equal to 2.5°, corresponds to the average height of the cone $\sim2.2\times10^{-6}$ cm. The height must be larger in the case of complete suppression of the surface superconductivity peak.

The average density of large hills on the photograph of the surface of irradiated Pb-15 sample is $\sim1.4\times10^6$ cm^{-2}. Apart from large hills, there are many small hills (white spots) whose average density is $\sim8.6\times10^6$ cm^{-2}. They can also make a contribution to the violation of conditions for the formation of surface superconductivity nuclei in a magnetic field. For small hills, the ratio of the cone height to the diameter must be larger, i.e., the angle formed by the cone generator with the magnetic field is larger than for an ''ant-hill.'' (Exact values of these parameters could be obtained with the help of an atomic-force microscope.)

Let us estimate the area of the surface of a Pb single crystal left out due to the formation of wells and hills during irradiation of the sample. The number of such surface defects is $n\sim10^6$ cm^{-2} and the average size of a defect is $2r\sim10^{-3}$ cm. Consequently, the sought area is $S=n\pi r^2\approx1$ cm^2. The area of the front face of the sample is $S_0=\pi d^2/4\simeq2.54$ cm^2, i.e., approximately 0.4 of the sample surface is excluded. In actual practice, the excluded fraction of the surface can be slightly smaller since linear microwave currents actually flow in a certain region under the resonant strip having a size $13\times0.6\times0.1$ cm.

According to our investigations, we can conclude that the bombardment of the back of a Pb single crystal by ultrasmall flux of fast neutrons (570 neutrons/cm$^2\cdot$s) for two hours leads to a damage of the front face which suppresses not only CR, but also the surface superconductivity. This is due to purely geometrical factors: the conditions under which CR is observed are violated[12] as well as the conditions for the formation of surface superconductivity nuclei since the sample surface becomes corrugated, i.e., its considerable fraction is not parallel to the applied magnetic field.

*)E-mail: jorj@physics.iberiapac.ge

[1] L. I. Jorjishvili, Fiz. Nizk. Temp. **4**, 454 (1977) [Sov. J. Low Temp. Phys. **4**, 218 (1977)].
[2] L. I. Jorjishvili, Fiz. Tverd. Tela (Leningrad) **22**, 2018 (1980) [Sov. Phys. Solid State **22**, 1176 (1980)].
[3] L. I. Jorjishvili, Soobshch. Akad. Nauk. GSSR **98**, 77 (1980).
[4] L. I. Jorjishvili, Fiz. Tverd. Tela (Leningrad) **24**, 333 (1982) [Sov. Phys. Solid State **24**, 191 (1982)].
[5] L. I. Jorjishvili, Soobshch. Akad. Nauk. GSSR **106**, 285 (1982).
[6] L. I. Jorjishvili, Fiz. Nizk. Temp. **12**, 533 (1986) [Sov. J. Low Temp. Phys. **12**, 301 (1986)].
[7] M. S. Khaikin, Prib. Tekh. Éksp. No. 3, 104 (1961).
[8] L. I. Jorjishvili and T. L. Kalabegishvili, Prib. Tekh. Éksp. No. 1, 135 (1972).
[9] M. S. Khaikin, S. M. Cheremisin, and V. S. Edelman, Prib. Tekh. Éksp. No. 4, 225 (1970).
[10] L. Stewart, Phys. Rev. **98**, 740 (1955).
[11] U. Daunert, D.Sc thesis, Munich (1964).
[12] A. A. Abrikosov, *Fundamentals of the Theory of Metals*, No. Holland, Amsterdam, 1988.
[13] P. De Gennes, *Superconductivity of Metals and Alloys*, Benjamin, New York (1966).

Translated by R. S. Wadhwa

LOW-TEMPERATURE MAGNETISM

The state of mercury vacancies in semimagnetic semiconductor $Hg_{1-x-y}Cd_xMn_yTe$

V. D. Prozorovskii and I. Yu. Reshidova

*A. Galkin Physicotechnical Institute, National Academy of Sciences of the Ukraine, 340114 Donetsk, Ukraine**

(Submitted February 19, 1999)
Fiz. Nizk. Temp. **25**, 1035–1039 (October 1999)

It is established directly, on the basis of investigations of the Shubnikov–de Haas effect at microwave frequencies and nonresonance cyclotron absorption in solid solution of semimagnetic semiconductor $Hg_{1-x-y}Cd_xMn_yTe$, that resonant acceptor states associated with mercury vacancies of two types are present in its conduction band. The dependence of the ground state energy of these acceptors on the energy gap is in agreement with the theoretical concepts concerning the long-range Coulomb potential of mercury vacancies. © *1999 American Institute of Physics.* [S1063-777X(99)00510-1]

It has been established that a semiconducting crystal HgTe and the solid solution $Hg_{1-x}Cd_xTe$ on its basis contain intrinsic point defects of three types: mercury vacancies, tellurium vacancies, and interstitial mercury atoms determined by the extent of deviation from the stoichiometry. Defects of the first type are acceptors, while defects of the second and third type are donors.[1] Obviously, defects of this type must also be present in the quaternary system $Hg_{1-x-y}Cd_xMn_yTe$. The determination of the influence of intrinsic point defects on electrical parameters and on the course of nonequilibrium processes in it is especially important for application of the solid solution $Hg_{1-x-y}Cd_xMn_yTe$ as a material for preparing active elements of electronic devices and for an analysis of physical phenomena occurring in it. Since the n- or p-type conductivity in zero-gap and narrow-band semiconducting materials such as $Hg_{1-x}Cd_xTe$ and $Hg_{1-x-y}Cd_xMn_yTe$ is determined by the excess of chalcogen or metal vacancies, the type of conductivity can be changed by appropriate thermal treatment of the crystal without additional doping with an impurity, which is equivalent to the change in the ratio of acceptor and donor concentrations. The strong dependence of electrical properties of a zero-gap semiconductor on the type and number of vacancies presumes a more intense study of the properties of their donor and acceptor states. An analysis of galvanomagnetic and magnetooptical phenomena in $Hg_{1-x}Cd_xTe$ mainly in the range of compositions in which the given semiconductor is a semimetal, i.e., for the energy gap $E_g \leqslant 0$ proved that these phenomena can be explained by the presence of resonant states of the acceptor type in the conduction band of $Hg_{1-x}Cd_xTe$. The theories developed for determining the ground-state energy of the acceptor are based on two models: the strongly-localized (delta-shaped) potential of the vacancy and the long-range Coulomb potential taking into account the exchange interaction between electrons. It follows from the first model that the acceptor ground-state energy E_A depends strongly on E_g, while in the second model the dependence of the position of acceptor states on E_g is comparatively weak.[2] Difficulties appear when these theories are compared with the available experimental results on observation of resonant acceptor levels obtained from an analysis of transport phenomena or magnetooptical phenomena in zero-gap and narrow-band semiconductors. The difficulty in experimental solution of the problem on determining E_A lies in identification of absorption spectra in a magnetic field and in the inclusion of the exchange interaction. On the other hand, in an analysis of transport phenomena we must take into account two or three types of free charge carriers simultaneously.[1] Depending on the temperature T and magnetic field H, the contribution of each type of charge carriers to kinetic coefficients varies, which allows us to determine their concentration and mobility. The value of E_A can be determined on the basis of the electroneutrality equation and from experimental temperature dependences of concentrations $n(T)$ and $p(T)$ of conduction electrons and holes.[1]

However, the concentrations of donors and acceptors cannot be always determined to a sufficient degree of accuracy, which leads to considerable errors in determining E_A. Thus, a certain discrepancy between the available data does not allow us to draw a final conclusion concerning the origin of acceptor impurities in narrow-band semiconductors. A new method developed recently makes it possible to establish directly the presence of acceptor levels in the conduction band and to determine their ground-state energy.[3] It was also interesting to apply the method[3] for analyzing the dependence of E_A on E_g in semimagnetic semiconductor $Hg_{1-x-y}Cd_xMn_yTe$ and for determining the theoretical model (first or second) that correspond to experimental data.

ANALYSIS OF QUANTUM OSCILLATIONS AT MICROWAVE FREQUENCIES

According to Tsidilkovskii *et al.*,[4] the fixation of the Fermi level E_F at an energy level of the donor or acceptor

TABLE I. Physical parameters of $Hg_{1-x-y}Cd_xMn_yTe$ samples.

Sample	x	y	E_{F1}, eV	m_c/m_0	n_1,10^{16} cm^{-3}	E_q, eV	E_{F2}, eV	m_c/m_0	n_2,10^{16} cm^{-3}
1	0.012	0.007	0.0024	0.0200	0.150	−0.250	-	-	-
2	0.050	0.020	0.0023	0.0100	0.053	−0.127	-	-	-
3	0.057	0.023	0.0023	0.0073	0.031	−0.096	0.0110	0.0086	0.420
4	0.045	0.030	0.0070	0.0040	0.094	−0.056	0.0200	0.0070	0.800
5	0.130	0.005	0.0100	0.0035	0.094	−0.026	-	-	-
6	0.060	0.035	-	-	-	−0.020	0.0042	0.0031	0.021
7	0.056	0.044	-	-	-	0.010	0.0041	0.0036	0.026
8	0.110	0.030	-	-	-	0.020	0.0040	0.0034	0.023
9	0.100	0.038	-	0.0036	0.050	0.037	-	-	-

origin located in the conduction band can lead to oscillations of conduction electron concentration in a quantizing magnetic field upon the intersection of E_F by Landau levels. In this case, the relation between n and E_F is described by the following expression:[4]

$$n=\frac{N_c\hbar\omega_c}{2k_BT}\sum_{L,\sigma}F_{-1/2}\left(\frac{E_F-E_L\sigma}{k_BT}\right). \quad (1)$$

Here $F_{-1/2}$ is the Fermi integral, $E_{L\sigma}$ the energy of the Landau level with the quantum number of a harmonic oscillator $L=0,1,2,\ldots$ and with the spin index $\sigma=\pm1$. $E_{L\sigma}=\hbar\omega_c(L+1/2+\sigma\nu/2)$, $\nu=gm_c/2m_0$, g is the Landé factor of the electron, m_c the effective cyclotron mass of the electron, ω_c the cyclotron frequency, $N_c=2(m_ck_BT/2\pi\hbar^2)^{3/2}$ the density of states and k_B the Boltzmann constant.

According to formula (1), the Fermi energy E_F for degenerate n-type semiconductors for $n(H)=\text{const}$ is an oscillating function of the magnetic field H. On the contrary, if $E_F(H)=R_A=\text{const}$, oscillations of the concentration $n(H)$ periodic in the reciprocal magnetic field $1/H$ take place. This in turn causes oscillations of the absorption coefficient A, and hence of its derivative dA/dH with respect to the magnetic field for a certain configuration of the magnetic field **H** and the microwave electric field **E**. The observed oscillations of A or dA/dH must also be periodic in $1/H$.

For this reason, in order to determine the ground state energy of a resonant acceptor in $Hg_{1-x-y}Cd_xMn_yTe$, we analyze the derivative dA/dH of absorption coefficient with respect to magnetic field in the temperature range 1.6–8 K on a radiospectrometer operating at frequencies 26.1 and 36 GHz. The construction of the radiospectrometer allowed us to make measurements for ordinary and extraordinary waves[1)] in two configurations: the Faraday configuration with circular polarization of the microwave field and the Voigt configuration with linear polarization.

In the Voigt configuration, dA/dH for both waves turned out to be an oscillating function of magnetic field, whose typical shape for sample No. 1 (see Table I) is shown in Fig. 1. Oscillations of the absorption coefficient A are periodic in $1/H$ (Fig. 2), the position of the extrema of dA/dH in a magnetic field being independent of the sample thickness and working frequency. In the Faraday configuration, no oscillations of dA/dH were observed, but nonresonance cyclotron absorption (NCA) in the form of a solitary extremum is observed for an extraordinary wave in weak fields.[5]

Thus, according to Ref. 3 and our experimental results, we attribute the observed oscillations to the quantum-mechanical Shubnikov–de Haas (SdH) effect. On the basis

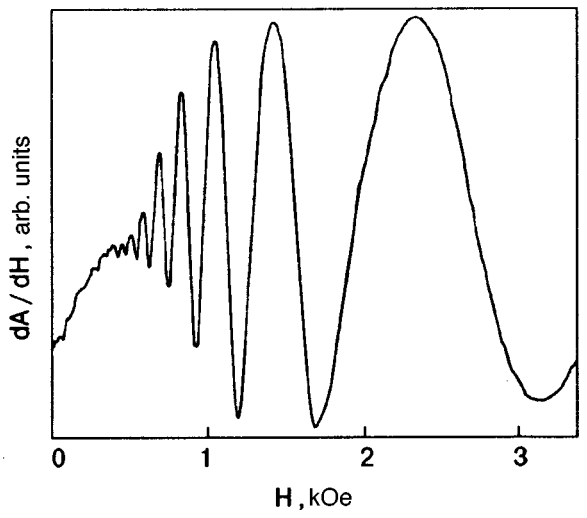

FIG. 1. Oscillation curve describing dA/dH at temperature 2 K for sample No. 1.

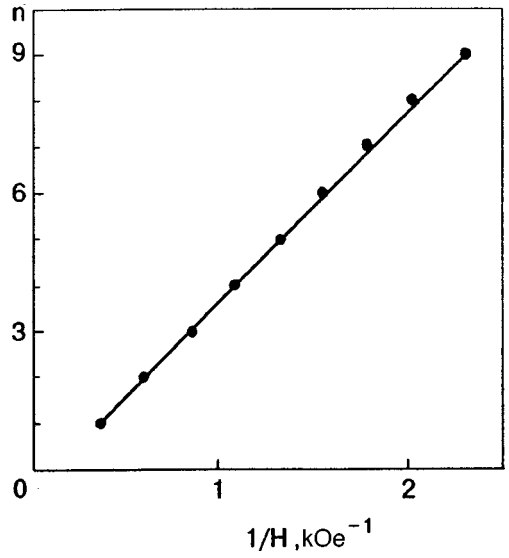

FIG. 2. Dependence of the number of oscillation of absorption coefficient on reciprocal magnetic field for sample No. 1.

of the obtained experimental data, we can determine te position of E_F relative to the bottom of the conduction band, and hence the ground-state energy E_A of the acceptor level in the conduction band for $E_g \leqslant 0$ or the energy corresponding to the position of the acceptor level in the conduction band for $E_g > 0$.

Shubnikov–de Haas oscillations at microwave frequencies were studied on a series of $Hg_{1-x-y}Cd_xMn_yTe$ single crystals (see Table I) grown by the Bridgeman technique with subsequent annealing in Hg vapor. The samples were subjected to different regimes of thermal treatment in order to obtain samples with different values of n and to vary the concentrations of singly and doubly charged mercury vacancies. It should be noted that each of the numbers 3 and 4 in Table I actually corresponds to two samples cut from the same plate of a certain composition, but subjected to different thermal treatments. For example, the energy of the Fermi level for samples annealed at a lower temperature is E_{F1}, while its value for samples annealed at a higher temperature is E_{F2}. The composition and homogeneity of the samples were determined with the help of x-ray microscopic analyzer and the method of electron spin resonance (ESR) since the low concentration of Mn in the samples under investigation could not be determined unambiguously with the help of a microanalyzer. The molar fraction of CdTe (x) was determined directly with the help of the microanalyzer, while the molar fraction of MnTe (y) was calculated from the ratio of integral intensities of ESR absorption lines at Mn ions respectively for investigated and reference samples with the known concentration of Mn atoms, determined with the help of the microanalyzer.

We calculated the values of E_g presented in Table I on the basis of determined values of x and y and the results obtained in Refs. 6 and 7. Since $E_F(H) = \text{const}$, we can use, according to Akerov,[8] the following expression for determining E_F:

$$E_F = \frac{(3\pi^2 n)^{2/3}\hbar^2}{2m_c}, \tag{2}$$

$$\Delta(1/H) = 3.2 \times 10^6 n^{-2/3} [\text{Oe}^{-1}]. \tag{3}$$

It follows from (2) and (3) that, using the period $\Delta(1/H)$ of the SdH oscillations and the effective cyclotron mass of conduction electrons, we can determine the value of E_F relative to the bottom of the conduction band. The period Δ of oscillations in the given case is determined from the oscillations of dA/dH, while the value of m_c is determined from the nonresonant cyclotron absorption spectrum at two working frequencies.

DISCUSSION AND CONCLUSIONS

Using the experimental and calculated data, we obtained the parameters of the samples under investigation given in Table I. It should be noted that the values of E_{F1} and E_{F2} for $E_g < 0$ are equal respectively to the energies E_{A1} and E_{A2} of acceptor states. Comparing the parameters obtained for $E_g < 0$ with the results obtained in Refs. 1,2,9, we note that the form of the $E_A(E_g)$ dependence is similar to that described in these publications. This means that E_{A1} and E_{A2} are the ground-state energies of resonant acceptor levels in the conduction band and are associated with stoichiometric defects of two types: singly and doubly charged mercury vacancies respectively, whose concentration is determined by the thermal treatment of the crystal.[1,2] Moreover, it follows from Table I that a noticeable change in the acceptor ground-state energy occurs near $E_g = 0$. According to Gelmont *et al.*,[9] this means that the acceptor level is associated with vacancies with a long-range Coulomb potential and $E_A \propto (m_p/m_c)^{3/2}$, where m_p is the effective mass of a heavy hole. For example, $E_A = 0.006$ eV for HgTe in the theory of local potential of a vacancy, while the calculated value of $E_A = 0.0023$ eV when nonlocality is taken into account.[9] The latter value is in accord with the parameter E_{A1} obtained by us in the experiments.

It should be noted that in $Hg_{1-x-y}Cd_xMn_yTe$ samples under investigation for $-0.026\,\text{eV} < E_g < 0.037\,\text{eV}$, we could observe the fixation of the Fermi level only at a level lying approximately 0.004 eV above the bottom of the conduction band, although the concentration of conduction electrons varied from $1.8 \cdot 10^{14}$ to $\sim 10^{16}\,\text{cm}^{-3}$. We attribute this to the fact that inversion of the Γ_6 and Γ_8 bands in $Hg_{1-x-y}Cd_xMn_yTe$ occurs, according to Ref. 10, not at $E_g = 0$, but at a certain minimum value. In the given experiment, this value is confined to the energy range $-0.026\,\text{eV} < E_{g\min} < 0.02\,\text{eV}$, which does not contradict the results of Ref. 10. Consequently, in the case of band inversion, the value of E_g becomes higher than the ground-state energy of the acceptor, the level ''enters'' the forbidden band, and as a result lies below the Fermi level. On the basis of the above arguments we can conclude that the acceptor level E_{A1} lies in the forbidden band for $-0.026\,\text{eV} < E_g < 0.02\,\text{eV}$, and the fixation of the Fermi energy level observed at 0.004 eV above the bottom of the conduction band for the above values of E_g is attributed by us with the acceptor level E_{A2} which in turn enters the forbidden band for $E_g \geqslant 0.037$ eV. This follows from the fact that no fixation of the Fermi level was observed for these values of E_g and the conduction electron concentrations $1.8 \times 10^{14} - 10^{16}\,\text{cm}^{-3}$.

Thus, the following conclusions can be drawn on the basis of experimental data on SdH oscillations at microwave frequencies, nonresonance cyclotron absorption in $Hg_{1-x-y}Cd_xMn_yTe$, and the literature data on intrinsic point defects in mercury chalcogenides: (1) the presence of resonance acceptor states E_{A1} and E_{A2} in the conduction band of $Hg_{1-x-y}Cd_xMn_yTe$ is caused by singly and doubly charged mercury vacancies, respectively; (2) the ground-state energy of acceptors measured by direct methods as a function of the forbidden gap E_g is in accord with the theoretical concepts, taking into account the long-range Coulomb potential of vacancies.

*E-mail: prohorov@pr.fti.ac.donetsk.ua

[1)]Extraordinary and ordinary waves: (1) in Faraday's configuration ($\mathbf{k} \| \mathbf{H}$), these are the waves in which the direction of polarization respectively coincides and does not coincide with the direction of cyclotron rotation of free charge carriers of the same polarity; (2) in Voigt configuration ($\mathbf{k} \perp \mathbf{H}$), these are the waves for which $\mathbf{E} \perp \mathbf{H}$ and $\mathbf{E} \| \mathbf{H}$, respectively, where $\mathbf{k}$ is the wave vector and $\mathbf{E}$ the electric vector of the microwave field.

[1] N. P. Gavaleshko, P. N. Gorlei, and V. A. Shenderovskii, *Narrow-band Semiconductors: Obtaining and Physical Properties* [in Russian], Naukova Dumka, Kiev (1984).
[2] A. V. Lyubchenko, E. A. Sal'kov, and F. F. Sizov, *Physical Foundations of Semiconductor IR Photoelectronics* [in Russian], Naukova Dumka, Kiev (1984).
[3] V. D. Prozorovskii, I. Yu. Reshidova, S. Yu. Paranchich, and L. L. Paranchich, Fiz. Tverd. Tela (Leningrad) **32**, 3290 (1990) [Sov. Phys. Solid State **32**, 1904 (1990)].
[4] I. M. Tsidilkovskii, G. I. Kharus, and N. G. Shelushinina, *Impurity States and Transport Phenomena in Zero-gap Semiconductor* [in Russian], Ural Research Center, Academy of Sciences of the USSR, Sverdlovsk (1987).
[5] J. D. Wiley, P. S. Peercy, and R. N. Dexter, Phys. Rev. **181**, 1173 (1969).
[6] R. Kim, Y. Mita, S. Takeyama, and S. Narita, Lect. Notes Phys. **152**, 316 (1982).
[7] S. Takeyama, and S. Narita, J. Phys. Soc. Jpn. **55**, 274 (1986).
[8] B. M. Askerov, *Kinetic Effects in Semiconductors* [in Russian], Nauka, Leningrad (1970).
[9] B. L. Gelmont, V. I. Ivanov–Omskii, and I. M. Tsidilkovskii, Usp. Fiz. Nauk **120**, 337 (1976) [Sov. Phys. Usp. **19**, 879 (1976)].
[10] V. D. Prozorovskii, I. Yu. Reshidova, S. Yu. Paranchich, and L. L. Paranchich, Fiz. Tverd. Tela (St. Petersburg) **34**, 700 (1992) [Sov. Phys. Solid State **34**, 374 (1992)].

Translated by R. S. Wadhwa

ELECTRONIC PROPERTIES OF METALS AND ALLOYS

Nonlinear resonant tunneling through doubly degenerate local state and strong electron-phonon interaction

V. N. Ermakov

Bogolyubov Institute for Theoretical Physics, National Academy of Sciences of Ukraine, 14-b Metrologichnd and Str., 252143 Kiev, Ukraine)*

(Submitted December 18, 1998; revised March 22, 1999)
Fiz. Nizk. Temp. **25**, 1040–1046 (October 1999)

In an approach of low transparency of the barrier the tunneling of electrons through doubly degenerate local state has been considered with allowance for the Coulomb and electron-phonon interactions. It is shown that in the case of weak electron-phonon and strong electron-electron interactions the dependence of tunneling current on the applied voltage has a step-like character at low temperature. The threshold value of the current was measured for small applied bias. The bistable state of the tunneling current is possible in the region of large bias. In the case of strong electron-phonon and weak electron-electron interactions, the threshold of tunneling current can be bistable. This result is a direct consequence of the electron pairing in local states. [S1063-777X(99)00610-6]

INTRODUCTION

It is well know that electron transport through quantum low-dimensional structures in the ballistic regime is very sensitive to certain resonance conditions.[1–4] This circumstance can be used for effective driving of the tunneling process. One of the most frequently used objects to study this phenomenon is double-barrier resonant tunneling structure (DBRTS), which consists of two potential barriers surrounding a potential well (the quantum well). Peculiarity of such a system is the charge accumulation in interbarrier space. Therefore, many-particle effects can play an important role. For instance, the dynamic charge accumulation within a quantum well leads to an electrostatic feedback mechanism that shifts the resonance energy. Under some conditions, this can result in the appearance of nonlinear effects such as intrinsic bistability,[5,6] self-oscillations,[7,8] Hamiltonian chaos,[9] dissipative chaos,[10] and other effects. These phenomena assume the presence of electronic states in the quantum well. In the case of a local state this is not valid. However, as it has been shown in Refs. 11 and 12, a doubly degenerate local state is sufficient for nonlinearity of resonant tunneling and the appearance of intrinsic bistability. There is, however, another problem. The strong electron-phonon interaction is possible for the local state[13,14] that can essentially change the tunneling nonlinearity. In particular, it can lead to effective electron-electron attraction and appearance of the electron pairing.

In the present paper we consider this problem for the case of double-degenerated electronic state where an accumulation up to four electrons in the local state is possible. Taking into account interaction between electrons and electron-phonon interaction can lead to a number of properties characteristic of nonlinear tunneling, including the appearance of step-like current-voltage curves and the bistability of threshold tunneling. Detailed consideration is restricted to one-dimensional case of resonant tunneling. The study of fluctuations shows that they can be virtually suppressed[15] in such a structure. The latter is typical of double level systems.

1. HAMILTONIAN OF THE SYSTEM

We consider a model of tunneling with a double-degenerate local state in the barrier. The energy profile of this structure is shown in Fig. 1. Electrons are assumed to interact with one another through the Coulomb potential and phonon field in the local state. The Hamiltonian describing the electrons in this system can be written as follows:

$$H = H_0 + H_W + H_T . \tag{1}$$

The first term of the Hamiltonian

$$H_0 = \sum_{k\sigma} \varepsilon_L(k) a^+_{k\sigma} a_{k\sigma} + \sum_{p\sigma} \varepsilon_R(p) a^+_{p\sigma} a_{p\sigma} \tag{2}$$

describes electrons in the left electrode (emitter) and in the right electrode (collector) (regions 1 and 3 in Fig. 1). Here $a^+_{k\sigma}(a_{k\sigma})$ and $a^+_{p\sigma}(a_{p\sigma})$ are the creation (annihilation) operators, respectively; $\varepsilon_L(k) = \varepsilon_L + \hbar^2 k^2/2m_L$ is the energy of electrons in the emitter, $\hbar k$ and m_L are their quasi-momentum and effective mass, respectively, and σ is the electron spin. In the collector (with an external potential V applied across the barrier), $\varepsilon_R(k) = \hbar^2 k^2/2m_R + \varepsilon_R - V$, where m_R is the effective mass.

In Eq. (1) the Hamiltonian H_W describes electrons and their interactions in a local state (region 2 in Fig. 1). We consider the case where the local state is doubly degenerate. Then H_W can be written as follows:

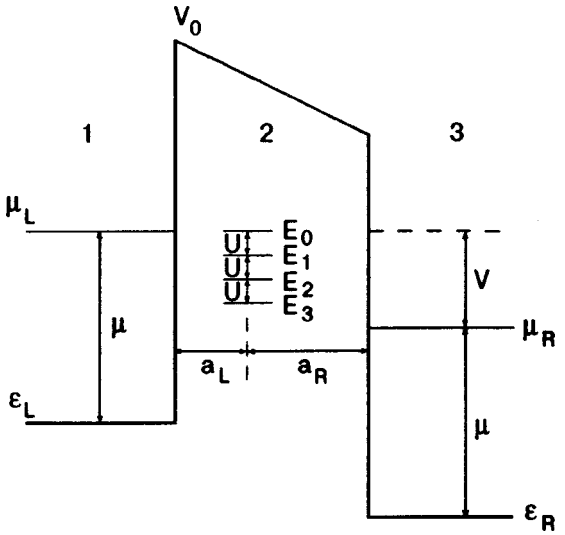

FIG. 1. Energy profile under applied voltage V of a barrier structure with localized energy levels.

$$H_W=\sum_{\alpha} E_0 a_\alpha^+ a_\alpha+\sum_i \hbar\omega_i b_i^+ b_i+\sum_{\alpha i} \varphi_{\alpha i} a_a^+ a_\alpha (b_i+b_i^+)$$
$$+\frac{1}{2}\sum_{\alpha_1\neq\alpha_2} V_{\alpha_1\alpha_2} a_{\alpha_1}^+ a_{\alpha_2}^+ a_{\alpha_2} a_{\alpha_1}. \tag{3}$$

Here $a_\alpha^+(a_\alpha)$ are the creation (annihilation) operators for electrons in the local state, $\alpha=(l,\sigma)$, σ is the spin number, and l is the quantum state number which takes values 1 or 2. The energy of the local state, taking into account the applied bias, is written as follows: $\overline{E_0}=\varepsilon_0-\gamma V$, where ε_0 is the energy of the local state, and γ is a coefficient; $\gamma=a_L/a$, $a=a_L+a_R$, a_L and a_R are the distances of the local state from the left and right borders of the barrier, respectively, and $V_{\alpha_1\alpha_2}$ is a matrix element describing the electron interaction in the local state. For simplicity, we approximate it by the positive constant $V_{\alpha_1\alpha_2}=U_c$, which corresponds to repulsion, $b_i^+(b_i)$ are the creation (annihilation) operators for phonons of the ith mode ($\hbar\omega_i$ is their energy), and $\varphi_{i\alpha}$ is the matrix element of the electron-phonon interaction for local states. The explicit form of such interaction is not important for our goals. It can be an interaction with the acoustic, optical or local vibration modes (see Ref. 14, for example).

The Hamiltonian H_T in Eq. (1) describes the tunneling transition of electrons through the barrier and has the conventional form:[16]

$$H_T=\sum_{k\alpha} T_{k\alpha} a_{k\sigma}^+ a_\alpha+\sum_{\alpha p} T_{p\alpha} a_{p\sigma}^+ a_\alpha+\sum_{kp} T_{kp} a_k^+ a_p+\text{c.c.}, \tag{4}$$

where $T_{k\alpha}$ and $T_{p\alpha}$ are the matrix elements of the tunneling transition to the local states from the left and right electrodes, respectively, and T_{kp} is the matrix element for direct tunneling transition from the emitter to the collector. In general, the matrix elements depend on the applied bias.

2. DENSITY OF STATES

Before considering the density of states it is convenient to transform the Hamiltonian H_W using the unitary transformation

$$S=\exp\left\{-\sum_{i\alpha}\frac{\varphi_{\alpha i}^*}{\hbar\omega_i} a_\alpha^+ a_\alpha (b_i-b_i^+)\right\}. \tag{5}$$

We can thus write H_W in the form

$$\tilde{H}_W=\sum_\alpha E_0 a_\alpha^+ a_\alpha+\sum_i \hbar\omega_i b_i^+ b_i$$
$$+\frac{1}{2}\sum_{\alpha_1\neq\alpha_2} U a_{\alpha_1}^+ a_{\alpha_2}^+ a_{\alpha_2} a_{\alpha_1}, \tag{6}$$

where

$$U=U_c-\sum_i\frac{|\varphi_i|^2}{\hbar\omega_i},\quad E_0=\varepsilon_0-\gamma V-\sum_i\frac{|\varphi_i|^2}{\hbar\omega_i}.$$

For the Hamiltonian H_T we obtain

$$\tilde{H}_T=\sum_{k\alpha} T_{k\alpha} S_b a_{k\sigma}^+ a_\alpha+\sum_{\alpha p} T_{p\alpha} S_b a_{p\sigma}^+ a_\alpha$$
$$+\sum_{kp} T_{kp} a_k^+ a_p+\text{c.c.}, \tag{7}$$

where

$$S_b=\exp\left\{-\sum_i\frac{\varphi_{\alpha i}^*}{\hbar\omega_i}(b_i-b_i^+)\right\}.$$

Next we restrict the analysis to the case of electron tunneling without radiation and absorption of phonons. After averaging Hamiltonians (6) and (7) over the phonon states we obtain

$$H_w=\sum_\alpha E_0 a_\alpha^+ a_\alpha+\frac{1}{2}\sum_{\alpha_1\neq\alpha_2} U a_{\alpha_1}^+ \alpha_{\alpha_2}^+ a_{\alpha_2} a_{\alpha_1}, \tag{8}$$

$$H_t=\sum_{k\alpha}\tilde{T}_{k\alpha} a_{k\sigma}^+ a_\alpha+\sum_{\alpha p}\tilde{T}_{p\alpha} a_{p\sigma}^+ a_\alpha+\sum_{kp} T_{kp} a_k^+ a_p+\text{c.c.}, \tag{9}$$

where

$$\tilde{T}_{p\alpha}=T_{p\alpha}\exp\left\{-\sum_i\left|\frac{\varphi_{\alpha i}}{\hbar\omega_i}\right|^2\left(n_i+\frac{1}{2}\right)\right\}, \tag{10}$$

$$n_i\left[\exp\left(\frac{\hbar\omega_i}{k_B T}\right)-1\right]^{-1}. \tag{11}$$

The density of states $\rho(E)$ of local levels can be determined with the help of Fourier transform of the retarded Green's function $G(\alpha,\alpha,E)$

$$\rho(E)=-\frac{1}{\pi}\sum_\alpha \operatorname{Im} G(\alpha,\alpha,E), \tag{12}$$

where

$$G(\alpha,\alpha,t)=-i\theta(t)\langle[a_\alpha^+(t),a_\alpha(0)]_+\rangle, \tag{13}$$

and $\theta(t)$ is a Heaviside unit step function.

Using the Hamiltonian H_w, the Green's function can be calculated explicitly. For example, for the state α we obtain

$$G(\alpha,\alpha,E)=\frac{1}{E'-E_0}\left\{1+\sum_{m=1}^{3}\sum_{\alpha_1,\ldots,\alpha_m\neq\alpha_{\alpha_1}\neq\alpha_2\neq\ldots\alpha_m}\times\prod_{m_1=1}^{m}n_{\alpha_{m_1}}\frac{U}{E'-E_0-m_1U}\right\}, \tag{14}$$

where $E'=E+i\eta$ in the limit $\eta\to+0$. Here $n_\alpha=\langle a_\alpha^+ a_\alpha\rangle$ are average values of the occupation numbers of the αth state. The Green's function has poles at $E_m=E_0+mU$, where $m=0,1,2,3$. The electron-phonon interaction and the electron-electron interaction therefore lead to a splitting of the local degenerated states. New states are separated by the value U. In this case, however, U may also take negative values. Using Eq. (7), we can calculate the density of states ρ for the local states in the barrier. These states depend on the occupation numbers of states n_α, which are functions of the applied voltage. This is the reason behind the nonlinearity of the tunneling current.

3. OCCUPATION NUMBERS

When the constant external voltage is applied to the system, a nonequilibrium steady-state distribution of electrons sets in. It is assumed that the electron distribution functions in the electrodes are at equilibrium because of their large spatial extent, but their chemical potentials change. The latter are connected through the relation $\mu_L-\mu_R=V$ (where μ_L and μ_R are the chemical potentials of the emitter and the collector, respectively). The electron distribution function $g(E)$ in the local state is essentially nonequilibrium. It can be determined from the condition of equality of the tunneling current through the emitter and the collector[16,17]

$$g(E)=\frac{1}{\Gamma(E)}[\Gamma_L(E)f_L(E)+\Gamma_R(E)f_R(E)], \tag{15}$$

where

$$\Gamma(E)=\Gamma_L(E)+\Gamma_R(E),$$

$$\Gamma_L(E)=\sum_k |T_{k\alpha}|^2\delta[E-\varepsilon_L(k)], \tag{16}$$

$$\Gamma_R(E)=\sum_p |T_{p\alpha}|^2\delta[E-\varepsilon_R(p)],$$

$f_L(E)$ and $f_R(E)$ are electron distribution functions in the emitter and the collector, respectively. The occupancy of local states in the barrier can be determined with the help of the expression[18]

$$n_\alpha=-\frac{1}{\pi}\int dE\, g(E)\,\mathrm{Im}\,G(\alpha,\alpha,E). \tag{17}$$

As follows from (7), the expression for n_α does not depend on the index α. Therefore, the mean values of the occupation numbers are also independent of the number of the quantum state, and we can assume that $n_\alpha=n$. Thus, we finally obtain

$$n=F(n), \tag{18}$$

where

$$F(n)=\sum_{m=0}^{3}C_3^m g_m(1-n)^{3-m}n^m,\quad C_3^m=\frac{3!}{m!(3-m)!}.$$

The functions $g_m=g(E_m)$ determine the occupancy of new states. Thus, Eq. (18) is a cubic equation for the occupation numbers n. In general, this equation can have three solutions in the interval $0\leqslant n\leqslant 1$. According to Eq. (11), for $g_m=g$ we obtain $n=g$. The equation admits three solutions when $g_0=g_1=0$, i.e., if the two states are vacant. These solutions have the form

$$n_1=0,$$

$$n_{2,3}=-\frac{3}{2}\frac{g_2}{g_3-3g_2}\pm\left(\frac{9g_2^2+4(g_3-3g_2)}{4(g_3-3g_2)^2}\right)^{1/2}. \tag{19}$$

According to the condition $0<n<1$, expression (19) leads to

$$0<\frac{3g_2}{3g_2-g_3}<2,$$

$$9g_2^2-4(3g_2-g_3)>0. \tag{20}$$

These inequalities (15) are compatible when

$$g_2\geqslant\frac{2}{3}(1+\sqrt{1-g_3}),\quad g_3>3/4. \tag{21}$$

Thus, Eq. (18) has three solutions when the values of g_1 and g_3 are close to unity. The two solutions n_1 and n_3 are stable, while the third one n_2 is unstable. The stable states correspond to the cases in which the local state does not contain electrons or contains four electrons occupying two upper levels. The latter is possible since the system is essentially out of equilibrium.

Matrix elements for tunneling in the one-dimensional case are given in the Appendix by Eqs. (A1) and (A2). The functions $\Gamma_L(E)$ and $\Gamma_R(E)$ can be approximated by the value

$$\Gamma_{L,R}=\alpha_{L,R}\sqrt{E-\varepsilon_{L,R}(0)}. \tag{22}$$

Here α_L and α_R are the proportionality factors for the emitter and the collector, respectively:

$$\alpha_L=\frac{m_L V_L^2 B(0,a_L;E)}{4\pi m E_s\sqrt{V_0-\varepsilon_0}(V_0-\varepsilon_L)},$$

$$\alpha_R=\frac{m_R V_R^2 B(a_L,a;E)}{4\pi m E_s\sqrt{V_0-\varepsilon_0}(V_L-\varepsilon_R)},$$

and

$$E_s=\frac{\hbar^2}{2ma^2}.$$

Substituting (22) into (15) and taking into account that

$$f_{L,R}=\left[\exp\left(\frac{E-\mu_{L,R}}{k_BT}\right)+1\right]^{-1}, \tag{23}$$

where k_B is Boltzman constant, and T is temperature, we obtain the expression for the electron distribution function

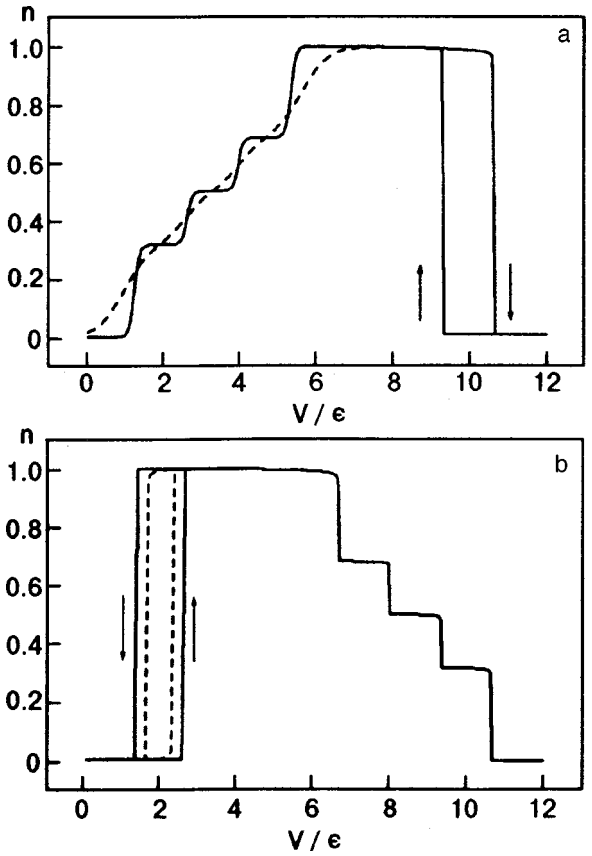

FIG. 2. Dependence of the population density n of the local state on the applied voltage V for $U/\varepsilon=0.2$ (a) and -0.2 (b). Solid line is for $k_BT=0.01$; dashed line is for $k_BT=0.05$.

g_m. For more detailed investigation of the properties of Eq. (18) we will consider the same particular cases.

a. The case of U>0

A plot of the dependence of the occupancy n on the applied voltage obtained by solving Eq. (18) at low temperatures ($k_BT/\varepsilon=0.01$ and 0.05) and the parameters $m_L/m_R=1$, $\gamma=0.5$, $\varepsilon_0/\varepsilon=1.6$, and $U/\varepsilon=0.2$ are represented in Fig. 2a. Here ε is a normalizing constant of the order of magnitude μ. It follows that with increase in the applied voltage, the occupancy of the local state increases stepwize due to consecutive occupation of split states. Above the critical value V_2, the occupation drops abruptly to zero due to the departure of the local states from resonance. If the voltage is lowered below V_2, a jump in the occupation number is observed at a lower value of the voltage V_1. Thus, the voltage range from V_1 to V_2 contains a bistability region, which is connected with the removal of electrons from the lower levels and with their attachment to the upper split states.

b. The case of U<0

In this case the dependence of the occupancy n on the applied voltage is more complicated. This dependence is shown in Fig. 2b at $U=-0.2$. It follows that, with increase in the applied voltage, the occupancy of the local state abruptly jumps to one above the critical value V_2. If the voltage is lowered below V_2, the occupation drops abruptly to zero at a lower value of the voltage V_1. Thus, there is a voltage range from V_1 to V_2 that contains a bistable region. The voltage interval (V_2-V_1) decreases with an increase in temperature. Such character of bistability is a consequence of the negative value of U.

4. TUNNELING CURRENT

In the case of a constant applied voltage the tunneling current through the double-barrier structure can be calculated in various ways (see, for example, Refs. 17 and 19). The following simple expression was obtained for this quantity:

$$J_{cd}=\frac{e}{\hbar}\int dE\,\frac{\Gamma_L(E)\Gamma_R(E)}{\Gamma(E)}[f_L(E)-f_R(E)]\rho(E)+\frac{e}{\hbar}\int dE\,P(E)[f_L(E)-f_R(E)], \tag{24}$$

where e is the electron charge. The second term in Eq. (24) is caused by the direct tunneling of electrons from the emitter to the collector. The transparency coefficient $P(E)$ is defined as follows:

$$P(E)=\sum_{kp}|T_{kp}|^2\delta[E-\varepsilon_L(k)]\delta[E-\varepsilon_R(p)],$$

where T_{kp} is given by Eq. (A3) in the Appendix. For a low barrier transparency, $\Gamma\ll U$, the density of states ρ can be calculated using formulas (12) and (14), which give

$$\rho(E)=\sum_{m=0}^{3}C_3^m(1-n)^{3-m}n^m\delta(E-E_m). \tag{25}$$

Equation (24) then becomes

$$J_{cd}=\frac{e}{\hbar}\sum_{m=0}^{3}\frac{\Gamma_R(E_m)\Gamma_L(E_m)}{\Gamma(E_m)}\{f_L(E_m)-f_R(E_m)\}\times(1-n)^{3-m}n^mC_3^m+\frac{e}{\hbar}\int dE\,P(E)[f_L(E)-f_R(E)]. \tag{26}$$

The results of numerical calculations of $J_{cd}(V)$ for the same parameters as those used for constructing the curves in Fig. 2 for different values of temperature are shown in Fig. 3. A bistability of the tunneling current is due to the filling of electrons in the upper energy levels of the splitting state. The toothed shape of the current in Fig. 3b is due to the departure of the local states from resonance.

CONCLUSIONS

Thus, the electron-electron and electron-phonon interactions in the local degenerate state result in the conductance oscillations of the tunneling system. The later is connected with the splitting of electron states by the Coulomb or electron-phonon interactions. The value of splitting defines a period of the conductance oscillations. The step-like shape of the current-voltage curve and its threshold character have some analogy with an effect of single-electron tunneling[19] when $U>0$. The bistability takes place in the interval of

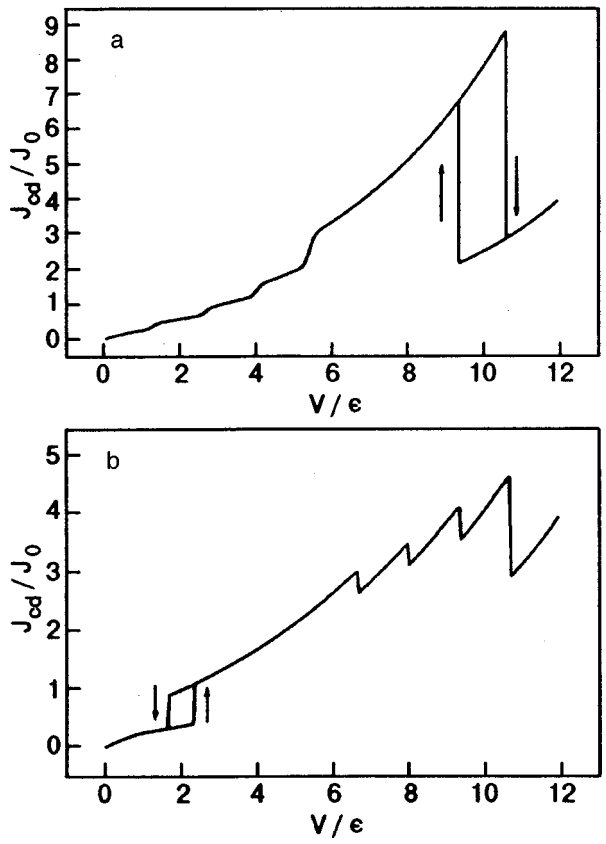

FIG. 3. Dependence of the tunneling current J_{cd}/J_0, where $J_0=e\mu\cdot 10^{-4}/\hbar$ on the applied voltage V for $U/\varepsilon=0.2$ (a) and -0.2 (b).

negative differential conductance. The sign of U determines the shape of the current-voltage characteristics. In the case of a strong electron-phonon interaction ($U<0$) the bistability takes place in the interval of positive differential conductance. Such peculiarity is due to the pairing of two electrons with opposite spins in local states.

An important feature of the present model is its stability with respect to the fluctuations. A simple consideration of the fluctuations of the occupation numbers of the local states results in

$$\langle \delta n^2\rangle=\langle(\hat{n}-n)^2\rangle=n(1-n). \tag{27}$$

In the region of bistability, n takes values in the vicinity of unity or zero. At these values $\sqrt{\langle\delta n^2\rangle}\ll n$. However, in the region of the current steps the fluctuations are comparable with the charge value. This conclusion was confirmed experimentally.[20] With increase in the temperature, the steps quickly smooth out due to the smoothing of the Fermi distribution functions. The region of their existence is limited by temperature $k_BT\ll U$. The temperature dependence of the bistability is due to the change in the functions g_m, which are not so sensitive to temperature. The bistability disappears when $\max g(E)\leqslant 3/4$, which can be achieved at sufficiently high temperatures comparable to μ. In the range of these temperatures one can ignore the spin dependence and the situation becomes similar to the one considered in Ref. 5. When $U<0$, increasing the temperature leads to suppression of the bistability.

APPENDIX

When a constant voltage is applied to the system, the wave function of an electron in the barrier can be found in the WKB approximation

$$\Psi_k(x)=\frac{1}{\sqrt{L}}B(0,x;e_L(k)),$$

$$\Psi_p(x)=\frac{1}{\sqrt{R}}B(x,a;\varepsilon_R(p)),$$

$$\Psi_\alpha(x)=\frac{1}{\sqrt{r}}\begin{cases}B(x,a_L;\varepsilon_\alpha) & \text{if } x<a_L\\ B(a_L,x;\varepsilon_\alpha) & \text{if } x>a_L,\end{cases}$$

where

$$B(x_1,x_2;E)=\exp\left\{-\int_{x_1}^{x_2}\frac{dx}{\hbar}\sqrt{2m(V(x)-E)}\right\},$$

L and R are the collector and emitter regions, respectively, and r is the radius of the local state. It is assumed that $r\ll a_L, a_R$. Under the condition that $E=\varepsilon_L(k)=\varepsilon_R(p)=\varepsilon_\alpha$ is the energy of the tunneling electron, the matrix elements $T_{\alpha k}$, $T_{\alpha p}$, and T_{kp} are

$$T_{k\alpha}=\int_0^{a_L}\Psi_k^*(x)V(x)\Psi_\alpha(x)dx=\overline{V}_LB(0,a_L;E)\frac{a_L}{\sqrt{a_rL}}, \tag{A1}$$

$$T_{p\alpha}=\int_{a_L}^{a}\Psi_p^*(x)V(x)\Psi_\alpha(x)dx=\overline{V}_RB(a_L,a;E)\frac{a_R}{\sqrt{a_rL}}, \tag{A2}$$

$$T_{kp}=\int_0^{a}\Psi_k^*(x)V(x)\Psi_p(x)dx=\overline{V}B(0,a;E)\frac{a}{\sqrt{RL}}, \tag{A3}$$

where $\overline{V}_L$, $\overline{V}_R$, and $\overline{V}$ are the average values of $V(x)$

$$\overline{V}=\frac{1}{a}\int_0^a V(x)dx,$$

$$\overline{V}_L=\frac{1}{a_L}\int_0^{a_L}V(x)dx,$$

$$\overline{V}_R=\frac{1}{a_R}\int_{a_L}^{a}V(x)dx.$$

When $V(x)$ is a linear function of x and the applied voltage V

$$V(x)=V_0-V\frac{x}{a_R+a_L},$$

$B(x_1,x_2;E)$ can be written in the form

$$B(x_1,x_2;E)=\begin{cases}\exp\{Z(x_1)-Z(x_2)\} & \text{if } x_2<x_0\\ \exp\{Z(x_1)\} & \text{if } x_2>x_0\end{cases},$$

where

$$x_0=\frac{x_2-x_1}{V}\left\{V(x_1)+\frac{x_1V}{x_2-x_1}-E\right\},$$

$$Z(x) = -\frac{2(x_0 - x)^{2/3}}{3}\left[\frac{2Vm}{\hbar(x_2 - x_1)}\right]^{1/2}.$$

*)E-mail: vlerm@nonlin.gluk.ape.org

[1] B. Ricco and M. Ya. Azbel, Phys. Rev. B **29**, 1970 (1984).
[2] Low-dimensional Conductors and Superconductors, Vol. 155 of NAT0 Advanced Studies Institute, Series B: Physics, D. Jerome and L. G. Caron (Eds.), Plenum, New York (1987).
[3] Physics of Quantum Electron Devices, F. Capesso (Ed.), Spring-Verlag, New-York (1990).
[4] A. S. Davydov, Molecular Electronics and Molecular Electronic Devices, Vol. 2, K. Sienicki (Ed.), CRC Press, Boca, Raton (1993).
[5] A. S. Davydov and V. N. Ermakov, Physica C **28**, 168 (1987).
[6] V. J. Goldman, D. C. Tsui, and J. E. Cunningham, Phys. Rev. Lett. **56**, 1256 (1987).
[7] V. N. Ermakov and E. A. Ponezha, Phys. Status Solidi B **145**, 545 (1988).
[8] C. Presilla, G. Jona-Lasinio, and F. Cappasso, Phys. Rev. B **43**, 5200 (1991).
[9] G. Jona-Lasinio, C. Presilla, and F. Cappasso, Phys. Rev. Lett. **B68**, 2269 (1992).
[10] B. Galdrikian and B. Birnir, Phys. Rev. Lett. **76**, 3308 (1996).
[11] V. N. Ermakov and E. A. Ponezha, Low Temp. Phys. **23**, 314 (1997).
[12] V. N. Ermakov and E. A. Ponezha, J. Phys.: Condens. Matter **10**, 2993 (1998).
[13] W. A. Harrison, Solid State Theory, McGraw-Hill Book Company, New York (1970).
[14] A. F. Lubchenko, *Quantum Transitions in Impurity Centers of Solid States*, Naukova Dumka, Kiev (1978).
[15] J. H. Davis, P. Hydgaard, S. Hershfield, and J. W. Wilkins, Phys. Rev. B **46**, 9620 (1992).
[16] E. Runge and H. Ehrenreich, Phys. Rev. B **45**, 9145 (1992).
[17] L. Y. Chen and C. S. Ting, Phys. Rev. B **43**, 2097 (1991).
[18] A. S. Davydov, *Quantum Mechanics*, Pergamon Press (1968).
[19] D. V. Averin, A. N. Korotkov, and K. K. Likharev, Phys. Rev. B **44**, 6199 (1991).
[20] Bo Su, V. J. Goldman, and J. E. Cunningham, Phys. Rev. B **46**, 6744 (1992).

This article was published in English in the original Russian journal. It was edited by S. J. Amoretty.

High-frequency ohmic losses in beryllium and its alloy with aluminum

N. N. Prentslau

*B. Verkin Institute for Low Temperature Physics and Engineering, National Academy of Sciences of the Ukraine, 310164 Kharkov, Ukraine**

(Submitted March 11, 1999)
Fiz. Nizk. Temp. **25**, 1047–1051 (October 1999)

The surface resistance of Be of different purity and its alloy with Al·(50%Be–50%Al) is investigated in the temperature range 4.2–300 K in the frequency region $0-10^{10}$ Hz. It is shown that in the temperature interval (in the vicinity of 77 K) where beryllium is a dc hyperconductor, the surface resistance of pure beryllium and the alloy has the lowest value as compared to other metals including aluminum. The temperature dependence of the surface resistance of Be and its alloy is successfully described by classical formulas of electrodynamics.
 [S1063-777X(99)00710-0]

INTRODUCTION

In view of an anomalously high Debye temperature Θ of beryllium [Θ(Be)$\simeq$1160 K], its dc resistivity ρ in the vicinity of 77 K is lower than the value of ρ for metals with a high electrical conductivity (such as Ag, Cu, and Al) by a factor of 5–8. At the same time ρ(Be)$>\rho$(Ag, Al, Cu) at room and helium temperatures.[1–3] Since the surface resistance R_s of metals is a function of ρ in the region of classical ($R_{s(\mathrm{cl})}$) as well as anomalous ($R_{s(\mathrm{an})}$) skin effect,[4–6] it is natural to assume that, like resistivity, R_s(Be) is lower than R_s(Ag, Al, Cu) in a certain temperature range $T_1 > 77\,\mathrm{K} > T_2$. However, the information on high-frequency properties of beryllium itself and its alloy (e.g., with Al) is not available,[7] while the functional dependence between $\rho(T)$ and $R_s(T)$ is not valid for all compounds.[4–6] For some compounds, it is not observed in view of peculiarities on the temperature–frequency dependence of their surface resistance.[8–10] For this reason, the hyperconductivity of Be and its alloy at high frequencies remains unclear.

In this communication, we report on the results of experimental investigation of the resistance of Be with 99.98% purity in the frequency range $0-10^{10}$ Hz and of Be with 99.97% and 99.96% purity as well as the 50%Be–50%Al alloy at frequency 10^9Hz in the temperature range 4.2–300 K. The measured values of resistance are compared with the values of ρ and R_s of aluminum of grade *A*9995. It is known[5,6] that the surface resistance $R_{s(\mathrm{an})}$(Al) of pure aluminum in the anomalous skin effect can be lower than $R_{s(\mathrm{an})}$(Cu, Ag), which dictated the choice of Al as a reference metal.

SAMPLES AND MEASURING TECHNIQUE

We investigated Al and Be samples prepared in the form of rods of diameter 1.5–3.5 mm and samples of Al–Be alloy (*AB*) in the form of a foil of thickness 0.1 mm. DC measurements were made by the bridge technique and ac measurements by the resonator method. Measurements were carried out in a cryostat in helium vapor, and the temperature was varied from 4.2 to 300 K. Before measurements, the samples were annealed for four hours in 5×10^{-7} mmHg vacuum at 900 K for beryllium and 700 K for aluminum. After annealing, the surface of the samples under investigation was subjected to chemical polishing. The samples of Al–Be alloy were not subjected to annealing and polishing.

EXPERIMENTAL RESULTS

The measured values of dc resistivity of the materials under investigation are presented in Table I.

Figure 1 shows the temperature dependence of resistivity ρ(Al) of aluminum (curve *1*) as well as ρ(Be) for Be samples of purity 99.98%, 99.97%, and 99.96% (curves *2*, *3* and *4* respectively). Curves *5–12* describe the temperature dependence of surface resistance of Be of purity 99.98% (curves with even numbers) and aluminum (curves with odd numbers) for frequencies 10^7 Hz (curves *5,6*), 10^8 Hz (curves *7,8*), 10^9 Hz (curves *9,10*), and 10^{10} Hz (curves *11,12*), respectively. It can be seen that ohmic losses R_s(Be)$<R_s$(Al) in the temperature range $T_1-T_2(T_1>T_2)$ as in the case of dc measurements. IT was found that for the same Be sample, $T_1=$const at all measuring frequencies, while the value of T_2 decreases with increasing frequency. For this reason, the temperature range T_1-T_2 expands with increasing frequencies (see Fig. 1), while the ratio R_s(Al)/R_s(Be) increases for $T<T_2$ and decreases for $T_2<T<T_1$.

The impurity concentration in beryllium affects its resistivity as well as surface resistance. The following regularities were established in this case.

TABLE I. Resistivities of materials under investigation.

Sample material	ρ(300)	ρ(4.2)	ρ(300)/ρ(4.2)
	$\Omega\cdot m$		
Be99.98	$4\cdot10^{-8}$	$2\cdot10^{-10}$	200
Be99.97	$4.5\cdot10^{-8}$	$2.9\cdot10^{-10}$	155
Be99.96	$4.6\cdot10^{-8}$	$4\cdot10^{-10}$	115
A9995	$2.75\cdot10^{-8}$	$5\cdot10^{-11}$	550
AB50	$3.75\cdot10^{-8}$	$1.1\cdot10^{-9}$	35

Remark: ρ(Al)/ρ(Be99.98)=6 at $T=77$ K.

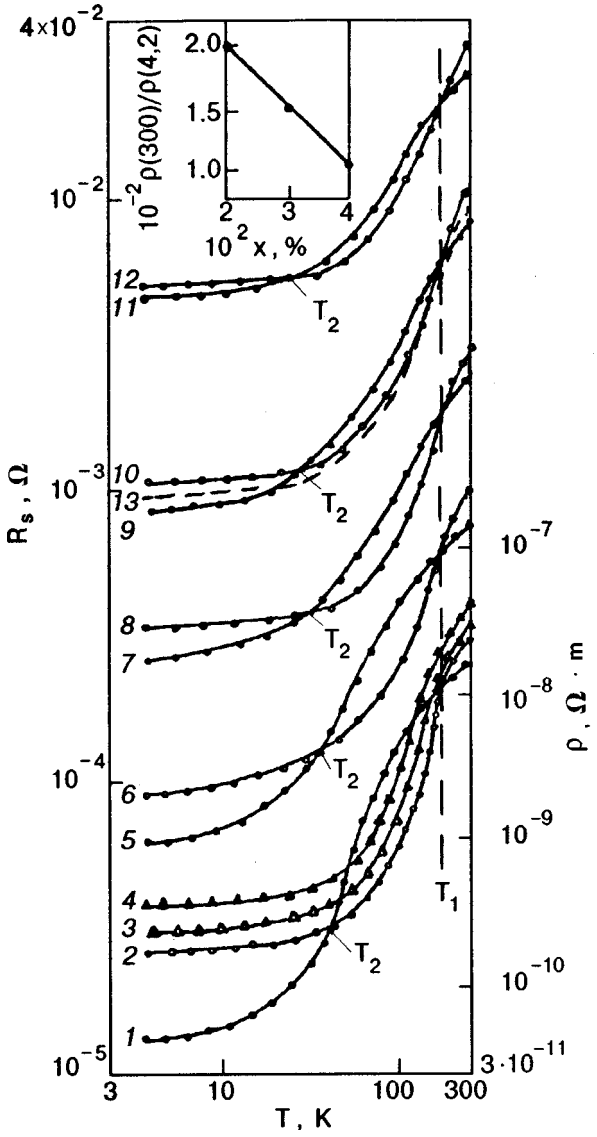

FIG. 1. Temperature dependences of resistivity of aluminum *A*9995 (curve *1*) and beryllium of purity 99.98 (curve *2*), 99.97 (curve *3*), and 99.96% (curve *4*) (on logarithmic scale), and of the surface resistance of Al and Be of purity 99.98% at frequencies 10^7 Hz (curves *5* (Al) and *6* (Be)), 10^8 Hz (curves *7* (Al) and *8* (Be)), 10^9 Hz (curves *9* (Al) and *10* (Be)), and 10^{10} Hz (curves *11* (Al) and *12* (Be)); curve *13* describes the $R_s(T)$ dependence calculated for Be at frequency 10^9 Hz. The inset shows the concentration dependence of the ratio $\rho(300)/\rho(4.2)$ for beryllium.

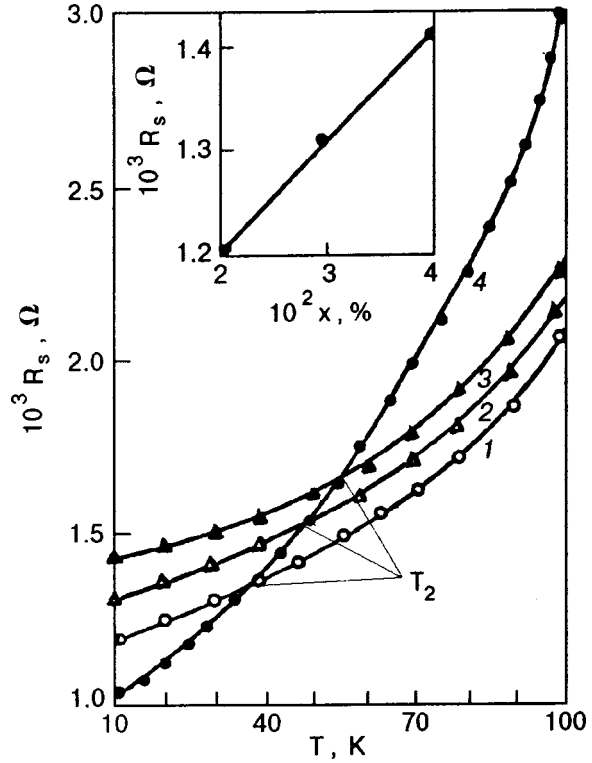

FIG. 2. Temperature dependence of the surface resistance of Be of purity 99.98 (curve *1*), 99.97 (curve *2*), and 99.96% (curve *3*) and of aluminum (curve *4*) at frequency 10^9 Hz. The inset shows the concentration dependence of R_s for Be at frequency 10^9 Hz and $T=10$ K.

As the impurity concentration increases, the resistivity of Be increases in the entire temperature range (see Fig. 1). The inset to Fig. 1 shows the dependence of $\rho(300)/\rho(4.2)$ on the impurity concentration x (in percent) for the Be samples under investigation. It was found that the ratio $\rho(x_1)/\rho(x_2)$ for Be samples with $x_1>x_2$ at $T=300$ K is smaller than at $T=4.2$ K. As the value of x increases, the temperature T_1 becomes lower, while the value of T_2 increases (see Fig. 1). Thus, an increase in the impurity concentration narrows the temperature range T_1-T_2. This also applies to the surface resistance. In this case, the value of T_1 is constant for the sample with a given impurity concentration in the entire frequency range (this is not indicated in the figures), while $T_2 \propto x$. Figure 2 shows the temperature dependence of the surface resistance of Be of purity 99.98% (curve *1*), 99.97% (curve *2*), and 99.96% (curve *3*) measured at frequency 10^9 Hz. The temperature dependence of R_s for Al (curve *4*), measured at the same frequency, is shown for comparison. The inset to Fig. 2 shows the surface resistance of Be at frequency 10^9 Hz and $T=10$ K as a function of impurity concentration in it.

Figure 3(a) (curve *1*) shows the temperature dependence of resistivity of the Al–Be alloy, while curve *2* describes the $\rho(T)$ dependence for Al. Figure 3(b) shows the temperature dependence of the ratio of R_s of the alloy and R_s of aluminum at frequency 10^9 Hz in the temperature range 50–250 K.

DISCUSSION OF RESULTS

The values of $\rho(T)$ for Be and Al in the temperature range 300–4.2 K are close to the values of $\rho(T)$ for these metals reported by other authors (see, for example, Refs. 1–3, 11), and the ratio $\rho(\text{Al})/\rho(\text{Be})=6$ obtained at 77 K is also close to values given, for example, in Refs. 1 and 2. Consequently, the surface resistance of beryllium was studied on samples with typical dc parameters for this metal.

According to Papirov and Tikhinskii,[3] $\rho(\text{Be})$ can be presented in accordance with the Matthiessen rule as the sum of the residual resistivity ρ_0 and the temperature-dependent resistivity ρ_e, and the temperature-dependent resistivity component ρ_e for Be can be described by the Grüneisen–Bloch equation[12] to a fairly high degree of accuracy.

The fact that $\{\rho(x_1)/\rho(x_2)\}(300)<\{\rho(x_1)/\rho(x_2)\}\times(4,2)$, for $x_1>x_2$, which is typical of beryllium[3] as well as

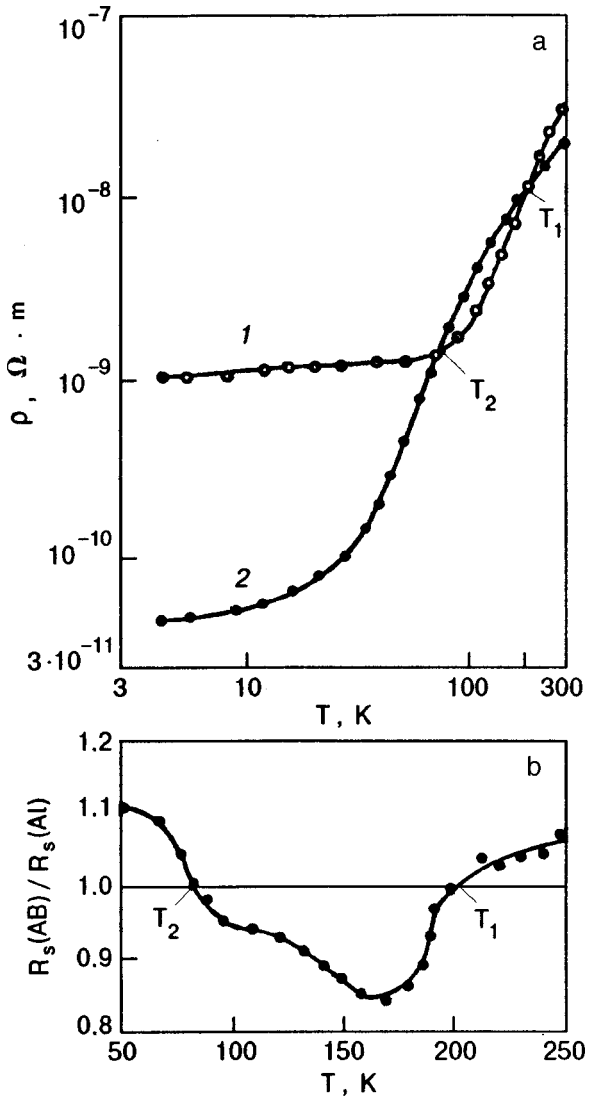

FIG. 3. Temperature dependences of resistivity of aluminum–beryllium alloy (curve *1*) and of aluminum on logarithmic scale (curve *2*) (a) and of the ratio of R_s of the alloy to R_s of Al at frequency 10^9 Hz (b).

for other metal, can be explained by the Matthiessen rule. At high temperatures, the component ρ_e associated with the electron–phonon scattering dominates over the residual resistivity component ρ_0. For this reason, $\rho(x_1)$ and $\rho(x_2)$ depend only slightly on the impurity concentration, and hence differ insignificantly. According to the Grüneisen–Bloch equation, the temperature dependent component ρ_e at low temperatures is smaller than the residual resistivity ρ_0 which increases with impurity concentration almost linearly (see inset to Fig. 1). For this reason, ρ(Be) at low temperatures is mainly determined just by residual resistivity, i.e., resistivity depending on the impurity concentration.

At temperatures below 300 K, beryllium obeys the relation $T/\Theta(\mathrm{Be})<0.5$, i.e., a strong dependence $\rho(\mathrm{Be})(T)$ is observed in this temperature region. As the temperature decreases, it approaches the dependence $\rho(\mathrm{Be})\propto T^5$. On the other hand the ratio $T/\Theta(\mathrm{Al})>0.5$ for Al near 300 K, and hence $\rho(\mathrm{Al})\sim T$ $[\Theta(\mathrm{Al})=420\,\mathrm{K}]$. Thus, $\partial\rho(\mathrm{Be})/\partial T > \partial\rho(\mathrm{Al})/\partial T$ near 300 K. Since ρ(Al) and ρ(Be) differ insignificantly at $T=300$ K, ρ(Be) becomes equal to ρ(Al) even at $T_1\simeq 200$ K, and $\rho(\mathrm{Be})<\rho(\mathrm{Al})$ for $T<T_1$.

At temperatures below 100 K, the value of $\partial\rho(\mathrm{Be})/\partial T$ decreases gradually, and as the temperature decreases, the resistivity of beryllium goes over to the region of residual resistivity (i.e., $\partial\rho(\mathrm{Be})/\partial T=0$). However, the relation $T/\Theta(\mathrm{Al})<0.5$ is observed for Al in this temperature range, i.e., the dependence $\rho(\mathrm{Al})\propto T^5$ can now be observed for Al, and hence $\partial\rho(\mathrm{Al})/\partial T > \partial\rho(\mathrm{Be})/\partial T$. For this reason, ρ(Be) becomes equal to ρ(Al) at a certain temperature T_2, and for $T<T_2$, $\rho(\mathrm{Be})>\rho(\mathrm{Al})$ again (see Fig. 1). Thus, the relation $\rho(\mathrm{Be})/\rho(\mathrm{Al})<1$ is observed in the temperature range T_1-T_2.

The temperature dependence of the surface resistance of Be can be described by the familiar formulas in electrodynamics in the region of classical as well as anomalous skin effect. Curve *13* in Fig. 1 shows the temperature dependence of R_s(Be) for purity 99.98% at frequency 10^9 Hz calculated by formulas Sondheimer and Chambers.[4–6]

An analysis of the temperature dependence $R_s(T)$ for aluminum and beryllium calculated by the formulas proposed in Ref. 5 leads to the conclusion that the classical skin effect in both metals at $T\geqslant 170$ K is observed at all measuring frequencies, while at $T\geqslant 70$ K it is observed at frequencies up to 10^7 Hz. It follows hence that, first, $T_1=\mathrm{const}$ for the same sample at all measuring frequencies including direct current, since this temperature is in the temperature range of the classical skin effect. With increasing *x*, the resistivity of Be at high temperatures increases (although more slowly than at low temperatures). Consequently, the equality of ρ(Be) and ρ(Al) is observed at a lower temperature, i.e., the value of T_1 decreases with increasing *x*.

According to Chambers,[5] the surface resistance $R_{s(\mathrm{an})}$ of a metal in the region of anomalous skin effect can be presented in the form $R_{s(\mathrm{an})}=R_0+R_s(\rho)$. Here $R_0\propto(Af^2)^{1/3}$ is the extremely small value of $R_{s(\mathrm{an})}$ independent of ρ, *A* is the ratio of the Fermi velocity to the charge carrier concentration, and $R_s(\rho)\simeq A^2 f^{(0,3;0,4)}\rho^{(0,82;1,1)}$. (The exponents 0.4 and 0.82 correspond to specular reflection of electrons at the metal surface and 0.3 and 1.1 to diffuse scattering.)

It should be noted that the value of *A* for Be is smaller than for other metals, and hence $R_0(\mathrm{Be})/R_0(\mathrm{Al})<1$. However, in view of a very large value of the ratios $\rho(\mathrm{Be})/\rho(\mathrm{Al})$ and hence $R_s(\rho)(\mathrm{Be})/R_s(\rho)(\mathrm{Al})$ at $T<T_2$, the condition $R_{s(\mathrm{an})}(\mathrm{Be})>R_{s(\mathrm{an})}(\mathrm{Al})$.

These facts lead to the following conclusions.

Since $\partial R_0/\partial f > \partial R_s/\partial f$ for any metal under the conditions of anomalous skin effect and $T=\mathrm{const}$, its R_0 increases with frequency more rapidly than $R_s(\rho)$. Consequently, the ratio $R_0/R_s(\rho)$ will increase with frequency, i.e., $R_{s(\mathrm{an})}$ tends to R_0 more rapidly. And since $R_0(\mathrm{Be})<R_0(\mathrm{Al})$, the ratio $R_{s(\mathrm{an})}(\mathrm{Al})/R_{s(\mathrm{an})}(\mathrm{Be})$ increases with frequency for $T<T_2$, while the value of T_2 decreases in accordance with Fig. 1. It should be noted that according to calculations based on Chambers equations,[5] the relation $R_s(\mathrm{Be})<R_s(\mathrm{Al})$ must be observed for samples of ultrapure or monocrystalline beryllium with the ratio $\rho(300)/\rho(4.2)\simeq 3\cdot10^3$ for any temperature below T_1 irrespective of the residual resistivity of Al at frequencies $\sim 10^{10}$ Hz.[3] In this case, the concept of temperature T_2 becomes meaningless.

The skin depth decreases upon an increase in frequency. However, the temperature dependence of the mean free path remains unchanged. Consequently, the temperature corresponding to the onset of anomalous skin effect (i.e., the temperature at which the skin depth and the mean free path become equal) increases (to 70 K for Al and to 100 K for Be at frequencies $\sim 10^{10}$ Hz). This means that the anomalous skin effect is observed at high frequencies and at temperatures for which $\rho(\mathrm{Al})/\rho(\mathrm{Be})$ has the maximum value and suppresses the effect of ρ on the surface resistance of Al and Be. For this reason, the ratio $R_{s(\mathrm{an})}(\mathrm{Be})/R_{s(\mathrm{an})}(\mathrm{Al})$ increases and tends to unity for $T_2 < T < T_1$.

As in Ref. 3, the samples under investigation display a nearly linear dependence of resistivity of Be on the impurity concentration in it (see inset to Fig. 1). According to Chambers,[5] the experimentally obtained dependence $R_s(x)$ in the region of anomalous skin effect is also close to linear (see inset to Fig. 2).

Beryllium–aluminum alloy, just like beryllium of various purity, is characterized by a temperature interval $(T_1 - T_2)$ in which the value of ρ for the alloy is smaller than the value of ρ for aluminum [Fig. 3(a)].

The residual resistivity of the alloy is much higher than $\rho(\mathrm{Al})$. It follows from Ref. 3, however, that the temperature at which residual resistivity dominates ρ for Be with impurities dominates is higher than the analogous temperature for beryllium of higher purity. This apparently explains the existence of the temperature interval $T_1 - T_2$ for the alloy, the value of T_2 for the alloy being higher than for pure beryllium.

At high frequencies, the temperature range in which the value of R_s for the alloy is smaller than R_s for aluminum also exists [Fig. 3(b)]. However, the temperature dependence $R_s(T)$ within the interval $(T_1 - T_2)$ is not monotonic as in pure beryllium. This is probably due to multiphase composition of the alloy which contains, according to Ref. 7, the brittle Be phase and Al–Be eutectic.

CONCLUSIONS

It has been established experimentally that just as in the case of direct current, the surface resistance R_s of Be of different purity and its alloy with Al is smaller than R_s of any other metal within a certain temperature interval $T_1 - T_2$. The surface resistance of Be can be smaller than the surface resistance of Al by a factor of 1.5–2.5, and the temperature and frequency dependence of R_s for Be and its alloy is successfully described by classical electrodynamic formulas.

The author is pleased to dedicate this work to the blessed memory of Academician B.I. Verkin who is remembered with gratitude by all his colleagues.

The author thanks Prof. V.M. Dmitriev for his interest in this research and fruitful discussions.

*E-mail: dmitriev@ilt.kharkov.ua

[1] G. E. Pletenetskii, G. S. Koshkarev, I. I. Papirov, and G. F. Tikhinskii, Izv. Akad. Nauk. SSSR, Met. **No. 3**, 907 (1979).
[2] G. G. Svalov and D. I. Belyi, *Superconductors and Cryoresistive Wires* [in Russian], Energiya, Moscow (1976).
[3] I. I. Papirov and G. F. Tikhinskii, *Physical Metallurgy of Beryllium* [in Russian], Atomizdat, Moscow (1968).
[4] G. E. H. Reiter and E. H. Sondheimer, Proc. Roy. Soc. **A195**, 336 (1948).
[5] R. G. Chambers, Proc. Roy. Soc. **A215**, 481 (1952).
[6] F. F. Mende, I. N. Bondarenko, and A. V. Trubitsyn, *Superconducting and Cooled Resonant Systems* [in Russian], Naukova Dumka, Kiev (1976).
[7] *Encyclopedic Dictionary. Solid State Physics* [in Russian] (ed. by V. G. Bar'yakhtar), vol. 1 (1998).
[8] P. Lunkenheimer, A. Loidl, C. Tome-Rosa, and H. Adrian, Physica C **C201**, 13 (1992).
[9] V. M. Dmitriev, M. N. Ofitserov, N. N. Prentslau, *et al.*, Fiz. Nizk. Temp. **21**, 906 (1995) [Low Temp. Phys. **21**, 698 (1995)].
[10] A. Behrooz and A. Zettl, Solid State Commun. **70**, 1059 (1989).
[11] G. E. Pletenetskii and G. F. Tikhinskii, Vopr. At. Nauki Tekh., Ser.: Yad. Konstanty **6(6)**, 70 (1978).
[12] M. A. Mitchel, J. Appl. Phys. **46**, 4742 (1975).

Translated by R. S. Wadhwa

Natural electron oscillations in Te granules deposited on rough surfaces

I. N. Shklyarevsky, Yu. Yu. Bondarenko, and N. A. Makarovsky

*Kharkov State University, 310077 Kharkov, Ukraine**)

(Submitted May 28, 1999)
Fiz. Nizk. Temp. **25**, 1052–1055 (October 1999)

Granular tellurium films deposited on rough surfaces of NaCl and KCl single crystals heated to 150 °C consist of two layers in each of which a resonance band is excited simultaneously. A band with frequency ω_0 of natural electron oscillations is excited in isolated granules of the upper layer. The plasma frequency of bulk tellurium is calculated from the measured values of ω_0 and the known permittivities of NaCl and KCl. © *1999 American Institute of Physics.* [S1063-777X(99)00810-5]

This paper is dedicated to the memory of Acad. B. I. Verkin (National Academy of Sciences of the Ukraine) evinced keen interest in this field of research.

1. INTRODUCTION

Plasma resonance in granular Te films was observed by us for the first time in Ref. 1. Continuous Te films are characterized by an intense interband absorption band in the low-frequency spectral region with the peak near $\omega \approx 3.2 \times 10^{15}\,\mathrm{s}^{-1}$ [Refs. 1–3]. After annealing at 150 °C, the continuous tellurium film decomposes in small granules, and a resonant absorption band whose optical properties are identical to those of the plasma resonance band in granular films of noble metals as well as metals of the third group emerges in the near UV spectral range.

The resonance frequency of plasma oscillations in granular films of these metals is given by[4,5]

$$\omega_s^2 = \frac{\omega_p^2}{\varepsilon_m + 2\varepsilon_0} - \frac{\omega_p^2}{3\overline{\varepsilon}}\left(\frac{a_0}{a}\right)^3 S = \omega_0^2 - \omega'^2, \tag{1}$$

where ω_p is the plasma frequency defined as

$$\omega_p = \frac{4\pi N e^2}{m}, \tag{2}$$

N, e, and m are the number density, charge, and mass of electrons, ω_0 is the frequency of natural electron oscillations in a granule, ε_m the permittivity associated with interband transitions in the metal, ε_m the permittivity of the medium surrounding the granule, $\overline{\varepsilon} = q\varepsilon_m + (1-q)\varepsilon_0$ is the permittivity of the granular film, and q the filling factor, i.e., specific volume of granules in the film. The second term in (1) was derived for a model in which spherical granules of the same radius a_0 are at the sites of a quadratic lattice with constant a.[4] The factor s appearing as a result of summation of the fields of dipoles (granules) is equal to 2–3. The ratio a_0/a can be expressed in terms of the filling factor q:

$$\frac{a_0}{a} = \left(\frac{3q}{2\pi}\right)^{1/2}. \tag{3}$$

The field E_d appearing as a result of dipole–dipole interaction noticeably affects the plasma resonance frequency ω_s which emerges in the aggregate of dipole granules of a given metal with permittivity ε_m, ε_0 being the permittivity of the medium surrounding the granules. In addition to the dependence on permittivities ε_m and ε_0, the plasma resonance frequency exhibits a considerable dependence on the filling factor q. Eliminating the dipole–dipole interaction between granules, i.e., going over to an aggregate of isolated granules, we can determine the frequency ω_0 of natural electron oscillations in a granule. For granular films of noble metals and metals of the third group deposited on quartz substrates, only one plasma resonance band of frequency ω_s is always excited. However, for Au[6] and In[7] granular films deposited on specially prepared rough surfaces of NaCl and KCl single crystals, two plasma resonance bands could be obtained: the low-frequency band with frequency ω_s and the high-frequency band with frequency ω_0. For a tilted incidence of light on a granular film, the latter band does not split into the s- and p-components,[8] which is possible only in the absence of dipole–dipole interaction between granules.

2. EXPERIMENTAL RESULTS

We describe here the results of investigation of simultaneous excitation of two plasma resonance bands in granular Te films deposited on rough surfaces of NaCl and KCl single crystals, the measurements of natural frequency ω_0 of electron oscillations in a Te granule, and the calculation of the plasma frequency ω_p of bulk tellurium.

The method of preparing rough surfaces of NaCl and KCl single crystals is described in Refs. 6 and 7. Granular Te films of various thickness were deposited on rough surfaces of these single crystals heated in high vacuum to 150 °C and then held in this vacuum for 30–40 min. After measuring the spectral dependence of transmission T on a SF-26 spectrometer, thick layers of NaCl and KCl were deposited on the obtained films in high vacuum at room temperature. The films were held in vacuum for one hour, and then the spectral dependences of transmission T were measured again, and the spectral dependences of optical density $D(\omega) = -\log T(\omega)$ were plotted. For each film prepared in this way, two spectral dependences of D were obtained: for the initial Te film

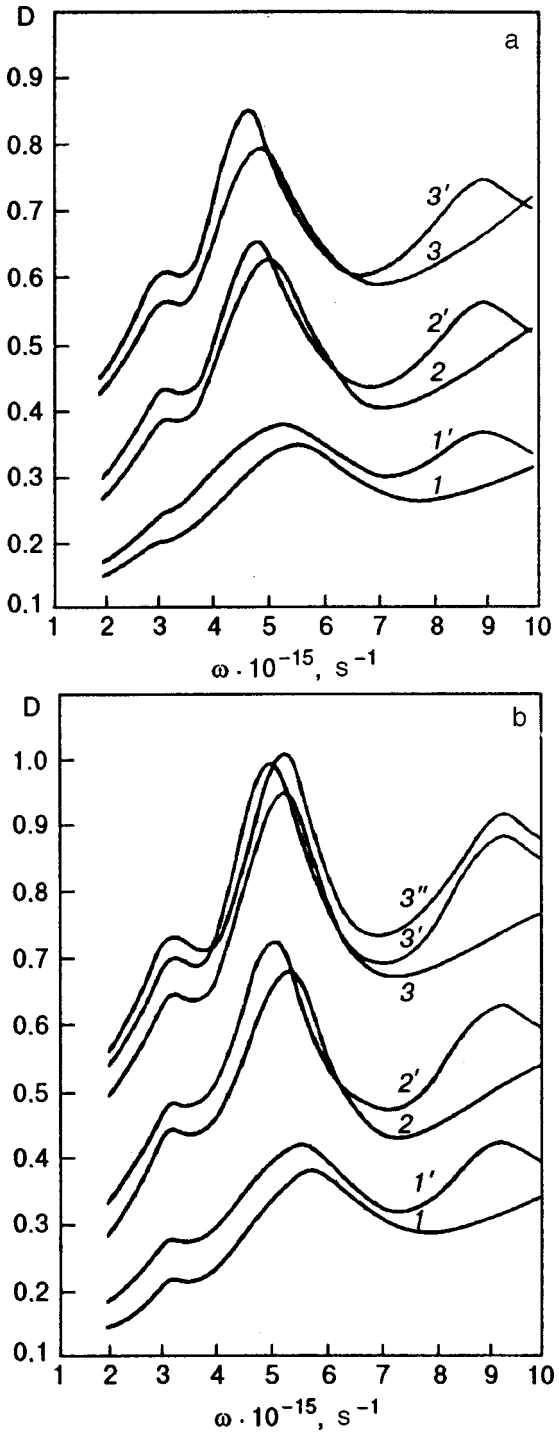

FIG. 1. Spectral dependence of optical density D of granular Te films deposited on NaCl (a) and KCl (b).

deposited on the rough surface of a NaCl (KCl) single crystal and for the same granular film whose granules were surrounded by an insulator.

Figure 1 shows the spectral dependences of optical density D of granular Te films with various effective thicknesses, deposited on rough surfaces of NaCl [Fig. 1(a)] and KCl single crystals [Fig. 1(b)]. Curves *1–3* correspond to initial granular films, while curves $1'-3'$ correspond to the same granular films which were deposited in high vacuum on NaCl and KCl. Curve $3''$ describes the $D(\omega)$ dependence recorded for the p-component for oblique incidence of light on the granular film at an angle $\varphi=45°$. The peaks of high-frequency resonant bands for normal and oblique incidence on the granular film coincide. In contrast to Refs. 6 and 7, the dependences $D(\omega)$ for initial granular Te films deposited on rough surfaces of NaCl and KCl single crystals display only one band of frequency ω_s. As the effective thickness of granular Te films increases, the intensity of resonance bands increases sharply, and their frequency ω_s decreases. The latter is associated with an increase in frequency ω', i.e., with an increase in the field created by dipole granules. The second (high-frequency) plasma resonance band appeared after the deposition of the corresponding insulator on the initial granular Te films. The fact that the peaks of these bands are independent of the effective thickness of granular Te films, i.e., of the size of the granules (curves $1'-3'$) and of the angle of incidence of light on the film [curve $3''$ in Fig. 1(b)] indicate the absence of dipole–dipole interaction between corresponding granules.

Simultaneous emergence of the low-frequency plasma resonance band determined by the dipole–dipole interaction between the granules and the high-frequency resonance band excited in isolated granules is possible only when the granular film consists of two layers. Most of granules penetrating the roughness form the lower layer whose granules are surrounded by the corresponding insulator. A small fraction of granules is deposited on the peaks of the roughness, forming the upper layer of granules that do not interact with one another. Electron vibrations with frequency ω_0 are excited just in these granules.

The Te granules deposited at the tips of the roughnesses in the initial granular films are surrounded by the medium with a small value of permittivity ε_0. After the deposition of the insulator, the permittivity of the medium surrounding granules increases abruptly, and high-frequency resonance bands lying at frequencies inaccessible for the SF-26 spectrometer are shifted to the UV spectral region (curves $1'-3'$).

After the deposition of the insulator on granular Te films, the spectral dependences of D for low-frequency plasma resonance bands differ from $D(\omega)$ of the initial granular films insignificantly since in this case the permittivity ε_0 of the medium surrounding the granules penetrating deeply in the roughness increases insignificantly. The increase in the effective thickness of granular Te films leads to an increase of optical density of plasma resonance bands. Other conditions being equal, the resonance bands of granular Te films in which granules are surrounded by NaCl [see Fig. 1(a)] are displaced due to high values of the permittivity ε_0 of the surrounding medium to the low-frequency spectral region relative to the bands of Te films in which granules are surrounded by KCl [see Fig. 1(b)].

It follows from Fig. 1 that the interband absorption band of Te is superimposed on the low-frequency edge of the low-frequency plasma resonance band. At the frequency $\omega\approx 3.2\times 10^{15}\,\mathrm{s}^{-1}$ (which is naturally independent of the permittivity ε_0), the absorption peak of this band is seen clearly. The asymmetry of plasma resonance bands was also observed in Ref. 1 for granular Te films deposited on quartz substrates.

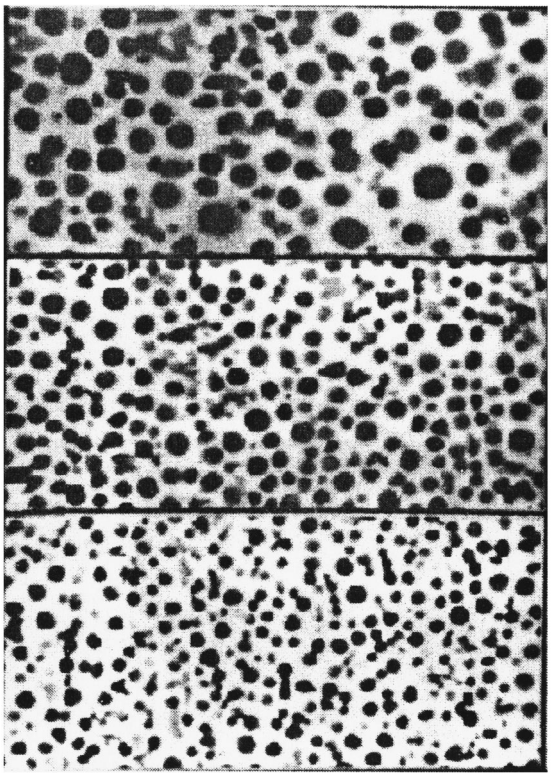

FIG. 2. Electron-microscopic photographs of granular Te films deposited on KCl (magnification 100000).

Figure 2 shows electron-microscopic photographs of granular Te films deposited on the rough surfaces of KCl crystal [the spectral dependences of D for these films are shown in Fig. 1(b)]. The larger the granule size, the higher the intensity of the plasma resonance bands. In contrast of granules investigated in Ref. 1, Te granules have a regular spherical shape, some of them forming well-defined chains as a result of decoration of steps of single crystals formed during annealing.[7] It is impossible to single out the granules in which high-frequency bands are excited. Electron-microscopic photographs of granular Te films deposited on rough surfaces of NaCl single crystals are similar to those shown in Fig. 2.

3. PLASMA FREQUENCY OF TELLURIUM

In the absence of dipole–dipole interaction between Te granules, the frequency of natural electron oscillations in a granule in the spectral regions of Te which do not display interband absorption is given by

$$\omega_0 = \frac{\omega_p}{\sqrt{1+2\varepsilon_0}}. \tag{4}$$

For Te granules surrounded by NaCl, the frequency of natural electron oscillations is $\omega_0 = 9\times10^{15}\,\mathrm{s}^{-1}$, while $\omega_0 = 9.2\times10^{15}\,\mathrm{s}^{-1}$ for Te granules surrounded by KCl. For these frequencies, the permittivity is $\varepsilon_0 = 3.2$ for NaCl and $\varepsilon = 2.88$ for KCl.[9,10] Interband absorption is not observed in tellurium granules in the frequency range of natural electron oscillations, and hence we can calculate its plasma frequency using formula (4). The plasma frequency for isolated Te granules surrounded by NaCl is $\omega_p = 24.5\times10^{15}\,\mathrm{s}^{-1}$, while the value of plasma frequency for the KCl surrounding is $\omega_p = 23.9\times10^{15}\,\mathrm{s}^{-1}$. These values coincide to within the error of measurements and are in good agreement with the plasma frequency $\omega_p = 25.5\times10^{15}\,\mathrm{s}^{-1}$ obtained by measuring electron energy losses in thin Te films[11] as well as with the plasma frequency $\omega_p = 23.4\times10^{15}\,\mathrm{s}^{-1}$ calculated for six free valence electrons per atom.[2]

4. CONCLUSION

In addition to the interband absorption band in granular Te films, a plasma resonance band is also excited. The optical properties of the latter band are similar to those for plasma resonance bands of noble metals and metals of the third group. The elimination of the dipole–dipole interaction between granules leads to the excitation of a resonance band with the frequency ω_0 of electron natural oscillations in a Te granule. The plasma frequency of Te is calculated from the measured value of ω_0 and the known permittivity of the medium surrounding the granule. The obtained results indicate that metallic properties dominate in the granular state of tellurium.

*)E-mail: yurij.y.bondarenko@univer.kharkov.ua

[1] R. B. Al-Abdella, V. P. Kostyuk, and I. N. Shklyarevskii, Opt. Spektrosk. **48**, 1143 (1980).
[2] J. N. Hodgson, J. Phys. Chem. Solids **23**, 1737 (1962).
[3] J. Stuke and H. Keller, Phys. Status Solidi **7**, 189 (1964).
[4] I. N. Shklyarevskii, P. L. Pakhomov, and T. I. Korneeva, Opt. Spektrosk. **34**, 729 (1973).
[5] L. A. Ageev, V. K. Miloslavskii, and I. N. Shklyarevskii, Ukr. Fiz. Zh. (Russ. Ed.) **21**, 1681 (1976).
[6] N. A. Makarovskii and I. N. Shklyarevskii, Opt. Spectrosc. **81**, 248 (1996).
[7] Yu. Yu. Bondarenko, N. A. Makarovskii, and I. N. Shklyarevskii, Zh. Prikl. Spektrosk. **65**, 799 (1998).
[8] I. N. Shklyarevskii and G. S. Blyashenko, Opt. Spektrosk. **44**, 545 (1978).
[9] *Handbook of Physical Quantities* [in Russian], ONTI, Leningrad (1937).
[10] *Tables of Physical Quantities* [in Russian], Atomizdat, Moscow (1976).
[11] J. J. Robins, Proc. Phys. Soc. London **79**, 119 (1962).

Translated by R. S. Wadhwa

LOW-DIMENSIONAL AND DISORDERED SYSTEMS

Reorientation phase transition in temperature in a two-dimensional ferromagnet taking magnetoelasticity into account

Yu. N. Mitsay, Yu. A. Fridman, and D. V. Spirin

*M. V. Frunze State University, 333036 Simferopol, Ukraine**)

(Submitted October 20, 1998; revised February 16, 1999)
Fiz. Nizk. Temp. **25**, 1056–1059 (October 1999)

Elementary excitation spectra are investigated in a thin ferromagnetic film. The temperatures of stability of phase transitions ''easy axis''–angular phase and ''easy plane''–angular phase are obtained. It is shown that the reasons behind the formation of the angular phase is the presence of magnetoelastic interaction. The Curie temperature of the system under investigation is determined. © *1999 American Institute of Physics.* [S1063-777X(99)00910-X]

1. Two-dimensional ferromagnetic systems have become objects of intense investigations in recent years due to some peculiar properties of these materials. For example, it was found[1,2] that the magnetization of thin films of Fe/Cu(100) and Fe/Ag(100) is perpendicular to the plane of the film at low temperatures and is parallel to the film surface at high temperatures. Such systems display reorientation phase transitions (RPT) not only in temperature, but also in the concentration of an impurity responsible for the emergence of perpendicular one-ion anisotropy (OA), while parallel OA is associated with exchange anisotropy.[3]

We analyze possible RPT for a simple model, i.e., we approximate the temperature dependence of OA by a function ensuring the dominance of OA of the ''easy axis'' type at low temperatures and OA of the ''easy plane'' type at high temperatures: $\zeta(T)=\beta(1-T/T_0)$. Consequently, an easy-axis (EA) phase with the magnetization parallel to the z-axis is formed in the system at $T<T_0$, while an easy-plane (EP) phase with magnetization lying in the basal xy plane is realized at $T>T_0$. The temperature T_0 corresponds to PT in the absence of magnetoelastic (ME) interaction. The Hamiltonian of such a system can be presented in the form

$$
\begin{aligned}
H=&-\frac{1}{2}\sum_{n,n'} I(n-n')S_nS_{n'}-\zeta(T)\sum_n (S_n^z)^2\\
&+\lambda\sum_n [(S_n^x)^2u_{xx}+(S_n^y)^2u_{yy}+(S_n^xS_n^y+S_n^yS_n^x)u_{xy}]\\
&+\int dV\frac{E}{2(1-\sigma^2)}[u_{xx}^2+u_{yy}^2+2\sigma u_{xx}u_{yy}\\
&+2(1-\sigma)u_{xy}^2],
\end{aligned}
\tag{1}
$$

where $I(n-n')$ is the Heisenberg exchange constant, S_n^i the spin operator at the lattice site n, λ the ME coupling constant, u_{ij} are the deformation tensor components, E is the Young modulus, and σ the Poisson coefficient.

It was proved in Refs. 4 and 5 that the long-range magnetic order (LMO) in the EP phase is stabilized by the ME interaction. It is well known[6] that LMO is not observed for $2D$-isotropic and easy-plane ferromagnets. This is due to the fact that the frequency of elementary excitations $\omega\propto k$, and the integral determining the average fluctuation of magnetic moment along the equilibrium direction acquires an additional factor $\propto 1/\omega(k)$ associated with the $u-v$ transformation. This leads to divergence of fluctuation integral at the lower limit and to the absence of LMO.

Maleev[7] showed that the inclusion of magnetic dipole interaction in $2D$ ferromagnets leads to a root dispersion relation $\omega\propto\sqrt{k}$ for magnons for small k. This indicates the convergence of fluctuation integral and stabilization of LMO at temperatures below T_c.

The inclusion of ME interaction stabilizes LMO in $2D$ ferromagnets not due to the root modification of the dispersion relation, but due to the emergence of ME gap in the magnon spectrum.

2. We analyze elementary excitation spectra of the system in the EA phase. The quasiparticle spectra will be obtained by using the method of Hubbard operators.[8,9]

The energy levels of a magnetic ion determined from the solution of the Schrödinger equation with a one-node Hamiltonian for $S=1$ have the form

$$
\begin{aligned}
&E_1=\zeta+\frac{\lambda}{2}(u_{xx}^{(0)}+u_{yy}^{(0)})-\chi;\\
&E_0=\lambda(u_{xx}^{(0)}+u_{yy}^{(0)});\\
&E_{-1}=\zeta+\frac{\lambda}{2}(u_{xx}^{(0)}+u_{yy}^{(0)})+\chi;\\
&\chi^2=I_z^2+\frac{\lambda^2}{4}(u_{xx}^{(0)}-u_{yy}^{(0)})^2;\\
&I_z=I_0\langle S^z\rangle;\\
&u_{xx}^{(0)}=u_{yy}^{(0)}=-\frac{\lambda(1-\sigma)}{2E};
\end{aligned}
\tag{2}
$$

$$u_{xy}^{(0)}=0.$$

Solving the dispersion equation (see Refs. 8 and 9), we can easily find the spectra of quasiparticles. It was found that the interaction of the magnetic and elastic subsystems in the EA phase leads to the emergence of spontaneous deformations in the sample, i.e., the appearance in the spectrum of the magnon branch $\omega(k)=\alpha k^2+\zeta(T)+b_0$ of the additional term b_0, viz., the ME gap. Thus, the gap in the magnon spectrum has the form $\omega(0)=b_0+\zeta(T)$, where $b_0=-[\lambda^2(1-\sigma)]/2E$, $\alpha=I_0R^2$ and R is the range of interaction. The magnon spectrum becomes unstable at the temperature

$$T_1=T_0\left(1-\frac{\lambda^2(1-\sigma)}{2E\beta}\right), \tag{3}$$

determined from the condition that the gap in the magnon spectrum is equal to zero.

3. Let us consider the behavior of the system at a temperature $T\geqslant T_1$. We assume that the magnetization vector deviates from a direction parallel to the z-axis through a small angle φ ($\varphi\ll 1$).

The energy levels of a magnetic ion can be determined easily from the corrections to expressions (2) in φ. For the lowest energy level to which we confine our analysis, we obtain (to within φ^6)

$$E_1=E_1^{(0)}+\varphi^2\frac{\lambda u_{yy}+\zeta}{2}-\varphi^4\frac{\lambda u_{yy}+\zeta}{6}+\varphi^6\eta\frac{\lambda u_{yy}+\zeta}{2}, \tag{4}$$

where $E_1^{(0)}$ is the energy level for $\varphi=0,\eta=0.0(4)$.

The dependence of spontaneous deformations on φ can be determined similarly and has the form

$$u_{xx}^{(0)}=-\frac{\lambda}{2E}\left\{1-\sigma-\sigma\left(\varphi^2-\frac{\varphi^4}{3}+\eta\varphi^6\right)\right\},$$

$$u_{yy}^{(0)}=-\frac{\lambda}{2E}\left\{1-\sigma+\varphi^2-\frac{\varphi^4}{3}+\eta\varphi^6\right\}. \tag{5}$$

Using relations (4) and (5), we obtain the free energy of the system under investigation (to within φ^6):

$$F(\varphi)=\varphi^2\left\{\frac{\zeta}{2}-\frac{\lambda^2(1-\sigma)}{4E}\right\}+\frac{\varphi^4}{3}\left\{-\frac{\zeta}{2}-\frac{\lambda^2(1+2\sigma)}{8E}\right\}+\varphi^6\left\{\frac{\lambda^2}{12E}+\frac{\zeta\eta}{2}-\frac{\lambda^2(1-\sigma)\eta}{2E}\right\}. \tag{6}$$

This relation shows that at $T=T_1$, the coefficient of φ^2 is equal to zero, At $T\geqslant T_1$, the coefficients of φ^2 and φ^4 are negative, while the coefficient of φ^6 is positive. Such a behavior of the free energy density indicates that T_1 is the temperature of absolute instability of the EA phase, and the system experiences a first-order RPT from the EA to the angular phase.[10] The equilibrium value of φ is determined from the condition of the free energy density minimum and is given by

$$\varphi^2=\frac{1}{9}\frac{\zeta+\lambda^2(1+2\sigma)/4E}{\lambda^2/6E+\zeta\eta-\lambda^2(1-\sigma)\eta/E}\times\left\{1+\left[1+54\left|\zeta-\frac{\lambda^2(1-\sigma)}{2E}\right|\times\left(\frac{\lambda^2}{6E}+\zeta\eta-\frac{\lambda^2(1-\sigma)}{E}\eta\right)\times\left(\zeta+\frac{\lambda^2(1+2\sigma)}{4E}\right)^{-2}\right]^{1/2}\right\}. \tag{7}$$

4. Let us now analyze the RPT from the EP to the angular phase. Two-dimensional easy-plane ferromagnets were studied in detail in Ref. 5, taking into account the ME interaction. In the case under investigation, the magnetic and elastic subsystems interact actively in the vicinity of the RPT (in contrast to the EA phase). The quasiphonon spectrum has the form

$$\omega^2(k)=\omega_\tau^2(k)\frac{\gamma E_{10}^2-\gamma a_0|E_{10}|-a_0I(k)+a_0I^2(k)/|E_{10}|}{\gamma E_{10}^2}, \tag{8}$$

and the quasimagnon spectrum acquires a ME gap. In relation (8), we have introduced the following notation:

$$|E_{10}|=\frac{\zeta}{2}+I_0+\frac{3\lambda^2}{4E};\quad \gamma=1-\frac{2I(k)}{|E_{10}|}+\frac{I^2(k)}{E_{10}^2};$$

$\omega_\tau(k)=c_\tau k$ is the dispersion relation for free τ-polarized phonons, c_τ is the velocity of sound, and $a_0=\lambda^2(1+\sigma)/(2E)$.

The quasiphonon spectrum (8) becomes unstable at the temperature T_2 determined from the condition

$$\gamma E_{10}^2-\gamma a_0|E_{10}|-I_0a_0+\frac{I_0^2a_0}{|E_{10}|}=0.$$

This temperature is called the temperature of absolute instability of the EP phase and is given by

$$T_2=T_0\left(1-\frac{\lambda^2(1-2\sigma)}{2E\beta}\right). \tag{9}$$

5. Thus, the inclusion of the ME interaction leads to the emergence of angular phase in the thin film. The PT from EA to angular phase and from EP to angular phase are first-order transitions. The temperature interval in which the angular phase is formed is determined by formulas (3) and (9) and is given by

$$\Delta T=T_2-T_1=T_0\frac{\lambda^2\sigma}{2E\beta}. \tag{10}$$

It follows from this expression that this temperature interval is determined primarily by elastic and ME constants. In the absence of ME interaction, $\Delta T=0$, and the PT EA–EP phase occurs jumpwise at $T=T_0$.

Figure 1 shows schematically the temperature dependence of the magnetization of the system under investigation. Pappas *et al.*[11] studied experimentally the behavior of magnetization of thin films of Fe/Cu(100) and described the temperature dependence of the magnetization. The results

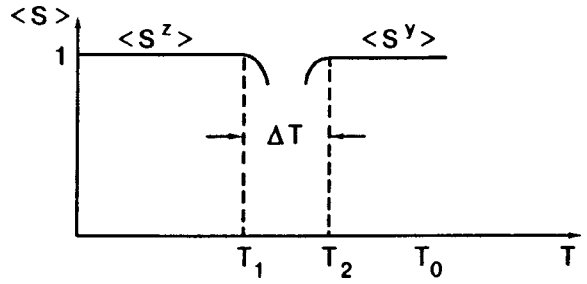

FIG. 1. Temperature dependence of the order parameter of a biaxial two-dimensional ferromagnet.

obtained in Ref. 11 are in qualitative agreement with our results (see Fig. 1), although there is some quantitative difference. This is primarily due to the fact that the spin of Fe ions is $S=3/2$, while in the proposed model it is $S=1$. Introduction of exact value of spin for Fe slightly complicates the mathematical apparatus of the model, in particular, we obtain a four-level problem instead of the three-level problem as in the case under investigation. However, the structure of dispersion energy levels remains unchanged (see Ref. 12). The value of ΔT determined experimentally in Ref. 11 amounts to 20–30 K depending on the film thickness. The estimation of this value on the basis of formula (10) gives 1–10 K for typical values of the parameters E, λ, and β for the bulk Fe.[13]

It was noted above that the inclusion of the ME interaction leads to stabilization of the long- range magnetic order in the EP phase of a two-dimensional ferromagnet.[5] The Curie temperature in this case becomes nonzero and for the system under investigation is given by

$$T_C=\frac{4\pi\alpha}{\ln[4\pi\alpha/\sqrt{\tilde{b}_0(\tilde{b}_0+\zeta(T))}]},\quad \tilde{b}_0=\frac{3\lambda^2}{4E}. \tag{11}$$

It can be seen from this relation that the ME interaction is decisive, and $T_C\to 0$ for $\tilde{b}_0=0$.

*)E-mail: man@expl.cris.crimea.ua

[1] A. Kashuba and V. L. Pokrovsky, Phys. Rev. Lett. **70**, 3155 (1993).
[2] D. Pescia, M. Stampanoni, G. L. Bona *et al.*, Phys. Rev. Lett. **58**, 2126 (1987).
[3] M. A. Ivanov, V. M. Loktev, and Yu. G. Pogorelov, Preprint Inst, Theor. Phys.-84-114R, Kiev (1984).
[4] B. A. Ivanov and E. V. Tartakovskaya, Pis'ma Zh. Éksp. Teor. Fiz. **63**, 792 (1996) [JETP Lett. **63**, 835 (1996)].
[5] Yu. N. Mitsay, Yu. A. Fridman, D. V. Spirin, and K. N. Alekseev, Uchenye Zapiski SGU **7(46)**, 139 (1998).
[6] N. D. Mermin and H. Wagner, Phys. Rev. Lett. **17**, 1133 (1966).
[7] S. V. Maleev, Zh. Éksp. Teor. Fiz. **70**, 2374 (1976) [Sov. Phys. JETP **43**, 1240 (1976)].
[8] Yu. N. Mitsay and Yu. A. Fridman, Teor. Mat. Fiz. **89**, 207 (1989).
[9] R. O. Zaitsev, Zh. Éksp. Teor. Fiz. **68**, 207 (1975) [Sov. Phys. JETP **41**, 100 (1975)].
[10] Yu. A. Izyumov and V. N. Syromyatnikov, *Phase Transitions and Symmetry of Crystals* [in Russian], Nauka, Moscow (1984).
[11] D. P. Pappas, K.-P. Kämper, and H. Hopster, Phys. Rev. Lett. **64**, 3179 (1990).
[12] S. G. Ovchinnikov and T. A. Valkova, Solid State Commun. **54**, 509 (1985).
[13] E. A. Turov, A. A. Lugovoi, V. D. Buchel'nikov *et al.*, *Preprint No. 4, Inst. Metal Phys.*, Sverdlovsk (1986).

Translated by R. S. Wadhwa

Temperature dependence of resistance of $Pr_{0.65}Ca_{0.35}MnO_3$ films prepared by pulsed laser deposition

V. G. Prokhorov, G. G. Kaminsky, and V. S. Flis

*Institute for Metal Physics, National Academy of Sciences of the Ukraine, 252142 Kiev, Ukraine**)

Young Pak Lee

*Sunmoon University, 100 Galsan-Ri, Tangjeong-Myeon Asan, Chongnam, Korea***)

(Submitted November 23, 1998; revised May 5, 1999)
Fiz. Nizk. Temp. **25**, 1060–1066 (October 1999)

Temperature dependence of resistance of $Pr_{0.65}Ca_{0.35}MnO_3$ thin films prepared by pulsed laser deposition method are studied in the temperature range 4.2–300 K. It is shown that an abrupt change in the temperature dependence of resistance is observed in the region of antiferromagnetic ordering temperature T_N. The experimental data are analyzed in the framework of modern theoretical concepts concerning the transport mechanism and perovskite-like manganites. © *1999 American Institute of Physics.* [S1063-777X(99)01010-5]

The compound $Pr_{0.65}Ca_{0.35}MnO_3$ belongs to the class of perovskite-like manganites of the type $R_{1-x}M_xMnO_3$, where R is a trivalent rare-earth element (La, Nd, or Pr) and M a bivalent atom (Ca, Ba, or Sr) substituted for it, exhibiting colossal magnetoresistance (CMR).[1,2] The interest in this class of compounds is due to wide prospects of their practical application as magnetic heads in electronic recorders and sensitive elements for measuring magnetic fields. The CMR phenomenon is essentially a phase transition experienced by doped manganites from the high-temperature paramagnetic state with a large dielectric resistance to the ferromagnetic (or ''tilted'' antiferromagnetic) phase in the concentration range $0.16<x<0.4$. The resistance in this case can drop by several orders of magnitude in a narrow temperature interval in the vicinity of the phase-transition point. The applied magnetic field elevates the Curie temperature and leads to a giant negative magnetoresistance.[3,4]

In most publications, the transition from a paramagnetic insulator to a ferromagnetic metal is described on the basis of the double exchange mechanism and is explained by the formation of an extra ''hole'' in positions of Mn ions, i.e., $Mn^{3+}\rightarrow Mn^{4+}$.[5,6] The ground state of the basic compound $PrMnO_3$ (without doping with bivalent atoms) can be regarded as the state of a paramagnetic band insulator in which an increase in the concentration of extra charge carriers must lead to disappearance of the Mott-Hubbard gap in the electron spectrum and to a metal–insulator transition at certain temperatures.[7] In this case, the behavior of electrical resistance in the high-temperature range can be described by the well-known Mott formula in the VRH (variable-range hopping) model.[8]

However, other opinions concerning possible mechanism of transport in these materials have been expressed recently.

Strong deformations of MnO_6 octahedrons emerging as a result of introduction of a bivalent atom in a unit cell suggest that the charge transport at high temperature is due to the motion of polarons in a small-radius lattice.[9] The main arguments in favor of this hypothesis are the giant isotope effect observed for oxygen atoms[10] and indicating a strong electron–phonon interaction as well as experiments on neutron scattering in which strong local lattice distortions of the Jahn—Teller type were detected.[11]

Another point of view is based on the assumption that in analogy with high-T_c superconductors (cuprates), manganites can acquire regions ''enriched'' and ''depleted'' in charge carriers as a result of phase-separation effect. Gor'kov and Sokol,[12] for example, proved that such phases can appear in the form of a ''foggy'' state with a drop size determined by the Coulomb interaction energy. It is natural to assume that the temperature dependence of resistance of such systems is determined by the thermally activated mechanism of conductivity rather than by peculiarities of the band structure appearing in the Mott model.

An analysis of transport properties of high-quality samples such as films with a high degree of perfection of crystalline structure make it possible to determine the main conductivity mechanism in manganites to a certain degree of accuracy.

In this communication, we report on the results of measurements of the temperature dependence of resistance of $Pr_{0.65}Ca_{0.35}MnO_3$ thin films prepared by pulsed laser deposition method. A detailed analysis of experimental $R(T)$ curves proved that the transport properties of the object under investigation can be described quite accurately on the basis of thermally activated conductivity mechanism. The observed change in the resistance at temperatures below T_N leads to the conclusion that the compound $Pr_{0.65}Ca_{0.35}MnO_3$ is a paramagnetic insulator with inclusions of the drop phase enriched with free charge carriers and can be described in the framework of the model proposed by Gor'kov.[4]

1. EXPERIMENTAL TECHNIQUE

The films were prepared by the method of pulsed laser deposition (ablation). The main advantages of this method

include the possibility of deposition of materials with different conductivities (including insulators), less stringent requirements on the vacuum conditions of deposition, the possibility of obtaining films with the stoichiometric composition corresponding to the composition of the target, and relative simplicity of the technological process. In our experiments, we used Nd–YAG lasers with wavelength 1064 nm, pulse duration 7.8–10.5 ns, and pulse energy 0.3 J. Films were deposited at a pulse-repetition frequency $\simeq$20 Hz. The power density of a laser beam focused on the target varied from 9.5×10^8 to 2×10^9 W/cm^2. In order to decrease the probability of deposition of coarse fractions (drops) of the target on the substrate, the deposition scheme in crossed beams from two lasers was used.[13] The targets were hot-pressed cylindrical samples of diameter 15 mm, prepared from $Pr_{0.65}Ca_{0.35}MnO_3$ powder of the stoichiometric composition. At first, a powder consisting of individual components Pr_6O_{11}, CaO, and Mn_2O_3 was mixed in proportions corresponding to the stoichiometric composition of the compound and annealed in air at 1000 °C for three days with intermediate crushing. The targets were then prepared by hot pressing and annealed in air for four days at 1200 °C. The substrates were made of $LaAlO_3$ single crystals with the working plane (100). The temperature of the substrate during deposition was $\sim$750 °C. The oxygen pressure in the chamber was $\approx$200 mTorr during film growth and $\approx$600 Torr during deposition. Under these conditions, $Pr_{0.65}Ca_{0.35}MnO_3$ films of thickness $d=10-200$ nm were prepared. According to x-ray diffraction analysis, all the samples had the c-axis grain orientation perpendicular to the substrate plane with a deorientation angle $<1°$. The crystal lattice parameters ($a=0.542$ nm, $b=0.545$ nm, and $c=0.767$ nm) were in complete accord with the available data on neutron diffraction for the given compound.[14] The absence of additional peaks on diffraction patterns except the lines belonging to the substrate suggests that the obtained samples contain practically only one phase. Resistivity measurements were carried out by the conventional dc four-probe method on high-resistance instruments. The current from 5.0 nA to 10 μA was controlled and could be commuted in two directions. Measurements were made in the temperature range 4.2–300 K. The prepared samples had a very high resistivity at room temperature ($\rho_{300}=0.405\,\Omega\cdot$cm ($d=10$ nm) and $\rho_{300}=0.375\,\Omega\cdot$cm ($d=200$ nm) which varied insignificantly with the film thickness in the high-temperature range.

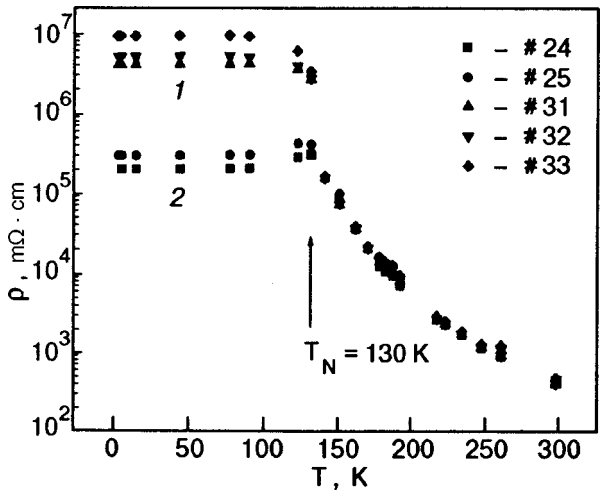

FIG. 1. Temperature dependences of resistivity for five $Pr_{0.65}Ca_{0.35}MnO_3$ films prepared under identical conditions but having different thicknesses d, nm: 10 (curve *1*), 200 (curve *2*); T_N is the point of magnetic phase transition for the given compound.

2. DISCUSSION OF EXPERIMENTAL RESULTS

Figure 1 shows the temperature dependence of the resistivity for $Pr_{0.65}Ca_{0.35}MnO_3$ films of different thickness. It can be seen that above the Néel temperature, which corresponds to $T_N\approx130$ K for the given compound,[14] the $\rho(T)$ curves for the films are virtually identical and are of a clearly manifested exponential nature. However, the temperature coefficient of resistance tends to zero at low temperatures ($T\leqslant T_N$), and the values residual resistivity for thick and thin films differ considerably.

Until recently, it was generally accepted that the compound $Pr_{1-x}Ca_xMnO_3$ remains a paramagnetic insulator for any Ca concentration down to very low temperatures since it exhibits charge ordering at Mn ions, preceding magnetic transformation.[15] Figure 1 shows, however, that film samples exhibit an abrupt change in the $\rho(T)$ dependence just near the antiferromagnetic ordering temperature. Although a complete transition to the metal phase is not observed, predecessors of such a transformation appear quite clearly. At any rate, an insignificant drop in the resistivity was observed for thick films in the temperature range below T_N.

On the other hand, the measurements of temperature dependence of resistance of the films in magnetic fields up to 0.2 T did not reveal any noticeable change in the value of $R(T)$ at $T>T_N$ or at $T<T_N$. it was proved by De Teresa *et al.*[16] that a magnetic field higher than 6.0 T must be applied in order to observe the CMR phenomenon in this compound.

In recent years, the physical nature of transport of charge carriers in perovskite-like manganites in the temperature range preceding the emergence of magnetic ordering and metal-type conductivity has been studied intensely. As a rule, the exponential behavior of resistance is explained either on the basis of the Mott–Hubbard insulator model[8] or with the help of the well-known approximation of thermally activated conductivity without carrying out a detailed analysis of fitting parameters.[17]

Figure 2 shows the theoretical dependences $\rho(T)$ derived with the help of the Mott expression for hopping conductivity of charge carriers over localized states with a variable hopping range (dashed curve) and by using the thermoactivation model (solid curve). In the Mott model, the expression for resistivity can be written in the form

$$\rho(T)=\rho_\infty\exp[(T_0/T)^{1/4}], \tag{1}$$

where ρ_∞ is the resistivity at infinitely high temperatures or the saturation resistivity, and the value of T_0 determines the localization energy for charge carriers.

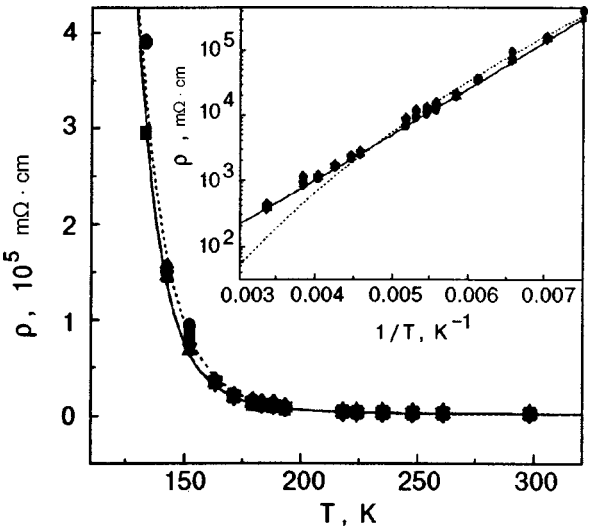

FIG. 2. Temperature dependences of resistivity for $Pr_{0.65}Ca_{0.35}MnO_3$ films at $T>T_N$. The solid curve is the approximation base on the model of thermally activated conductivity and the dashed curve is the approximation based on Mott's (VRH) model.

In the thermally activated conductivity (TAC) approximation, the expression for $\rho(T)$ can be written in the form of the well-known Arrhenius formula:

$$\rho(T)=\rho_0 T\exp(T_0/T), \tag{2}$$

where ρ_0 is a fitting parameter whose physical meaning will be considered below and T_0 is the activation energy of charge carriers.

Both expressions contain two fitting parameters which must be varied during an analysis of experimental curves. The best agreement between experimental and theoretical curves is observed for the following values of the parameters $\rho_\infty\approx 10^{-13}\,\mathrm{m\Omega\cdot cm}$, $T_0=4.4\cdot 10^8\,\mathrm{K}$ for expression (1) and $\rho_0=0.003\,\mathrm{m\Omega\cdot cm\cdot K^{-1}}$, $T_0=1800\,\mathrm{K}$ for expression (2). The mean statistical error in fitting the parameters ρ_∞ and T_0 for the Mott model amounts to 100 and 25% respectively for all experimental curves, while the corresponding errors for the thermally activated conductivity approximation are 1.0 and 13.5%. Moreover, dashed line in the inset to Fig. 2 corresponds to the theoretical dependence obtained in the Mott model with optimal fitting parameters, which differs noticeably from the experimental curve. Thus, we can conclude that only the model of thermally activated conductivity can describe the temperature dependence of the resistance of $Pr_{0.65}Ca_{0.35}MnO_3$ films in the high-temperature region to a high degree of accuracy.

On the other hand, a more detailed analysis of possible physical nature of the fitting parameters is required for correct establishment of the transport mechanism for charge carriers in these objects.

If we assume that the value of ρ_∞ determines the boundary of the minimum metal-type conductivity of the given compound, the electron mean free path can be estimated on the basis of the Ioffe–Regel criterion $k_F l\geqslant 1$ assuming that the electron wave vector is $k_F=(3\pi^2 N/V)^{1/3}$, where N is the number of electrons and V the sample volume. Choosing the valence of Mn^{4+} equal to 0.405,[14] we obtain $k_F\approx 3.75\times 10^7\,\mathrm{cm^{-1}}$. The minimum electron mean free path estimated in this way is $l\approx 0.27\,\mathrm{nm}$, which is approximately half the period of the crystal lattice in the ab plane. The obtained result is not unexpected and just reflects the fact that the transport of charge carriers in these compounds involves the $2p$-band of oxygen atoms. Knowing the width of the e_g band which is equal to $E_{BF}\approx 0.3\,\mathrm{eV}$ according to some estimates,[18] we can estimate the expected value of the minimum resistance:

$$\rho_\infty^T=\frac{\sqrt{m(2E_{BF})}}{ne^2 l}, \tag{3}$$

where m is the electron mass and n the charge carrier concentration which can be determined if we know the valence of Mn ions and the unit cell volume calculated from the x-ray data. In the given case, $n\approx 1.87\times 10^{21}\,\mathrm{cm^{-3}}$, and the calculated value of $\rho_\infty^T=2.2\,\mathrm{m\Omega\cdot cm}$. It can be seen that the obtained value differs from the experimental value by thirteen orders of magnitude, thus proving the inapplicability of the Mott model for describing the transport properties of $Pr_{0.65}Ca_{0.35}MnO_3$ films. A similar situation takes place in an analysis of the second fitting parameter. The value of T_0 in Mott's model depends on the electron localization length l_0 and the density $N(E_F)$ of electron states at the Fermi level: $k_B T_0=18/l_0^3 N(E_F)$.[18] Choosing the width of the e_g band equal approximately to 0.3 eV and the number density of charge carriers $n\approx 1.87\times 10^{21}\,\mathrm{cm^{-3}}$, we obtain the electron localization length $l_0\simeq 2.3\times 10^{-2}\,\mathrm{nm}$, which is deprived of any physical meaning.

The thermally activated behavior of the resistance of $Pr_{0.65}Ca_{0.35}MnO_3$ films can be analyzed on the basis of two concepts concerning the diffuse nature of motion of charge carriers, which are responsible for transport properties of these compounds.

One of them is connected with the formation and movement of lattice polarons of small radius (*Holstein* polarons) whose size is comparable with the parameter of the crystal unit cell. In this case, any small distortion of the lattice leads to polaron localization and thermally activated conductivity mechanism at high temperatures. In the adiabatic approximation, the temperature dependence of resistivity can be written in the form[19,20]

$$\rho(T)=\frac{k_B T}{ne^2\omega_{op}a^2}\exp\left(\frac{E_g/2+W_H}{k_B T}\right), \tag{4}$$

where a is the hopping length of a polaron, n the polaron number density, W_H the energy of polaron formation, E_g the energy difference in the lattice deformation states with and without a polaron, and ω_{op} the optical frequency of phonons. If we choose the optical frequency of phonons equal to $\omega_{op}\approx 10^{14}\,\mathrm{s^{-1}}$,[9] and identify the number density of polarons with the concentration of hole carriers, the first fitting parameter in formula (2) can be used to estimate the hopping length of a polaron, which turns out to be approximately equal to 0.31 nm, i.e., virtually coincides with the crystal

lattice period. If, however, we identify T_0 in formula (2) with the energy of polaron formation (as a rule, $E_g \ll W_H$),[9,21] and estimate the polaron radius following Jaime *et al.*,[9] it turns out to be ~ 0.97 nm, i.e., larger than the hopping length. In this case, we must probably speak not of the hopping mechanism of polaron transport, but on continuous flux creep of local lattice deformations.

Proceeding from the idea proposed by Gor'kov[4] and concerning the possibility of formation of a ''foggy'' or ''drop'' phase of excess charge carriers, we can present the samples under investigation in the form of an insulator matrix with metallic inclusions. It is well known that the conductivity of such a system can be described with the help of the following expressions:

$$\sigma = \frac{ne^2}{k_B T} D_\sigma, \quad D_\sigma = \frac{1}{2} \Gamma a^2, \quad \Gamma = \omega_0 \exp\left(- \frac{T_0}{T} \right), \quad (5)$$

where n is the charge carrier concentration, e the electron charge, D_σ the diffusion coefficient, Γ the hopping frequency for charge carriers, a the mean length of carrier hops, T_0 the activation energy, and ω_0 the attack frequency or hopping probability. Assuming, as in the previous analysis, that e_g-band electrons are mainly responsible for the conductivity of the film, we can determine the number density of charge carriers $n \approx 1.87 \times 10^{21}\ \mathrm{cm}^{-3}$ and the Fermi velocity $v_F \approx 1.02 \times 10^6$ cm/s and present the hopping probability in the form $\omega_0 \approx v_F / a$.

In this case, the expression for the temperature dependence of resistivity can be written in the form

$$\rho(T) = \rho_0 T \exp\left(\frac{T_0}{T} \right), \quad \rho_0 = \frac{2 k_B}{n e^2 a v_F}. \quad (6)$$

If we assume, following Gor'kov,[4] that the Ca^{2+} ion transporting a hole to the Mn^{4+} ion is responsible for the formation of metal ''drops,'' the mean length required for an electron hop can be defined as the product of the ratio of the number of Pr atoms to the number of Ca atoms following from the chemical formula of the compound by the separation between nearest sites averaged over all possible directions of hops, i.e., $a \approx 2.26$ nm. The value of $\rho_0 = 0.0031\ \mathrm{m\Omega \cdot cm}$ calculated in this way corresponds with an astonishing accuracy to the value of fitting parameter that was obtained from an analysis of the experimental curve on the basis of formula (2). If we again use the expression derived by Viret *et al.*[18] for estimating the electron localization length and choose the parameter obtained in the thermoactivated conductivity model (2) as the activation energy, the value of $l_0 \approx 2.65$ nm virtually coincides with the mean electron hopping length. (The fact that the value of l_0 turns out to be slightly larger than the electron hopping length is rather due to approximate nature of the given estimation in the Drude model than due to physical peculiarities of the compound under investigation.)

Thus, we can conclude that the thermal activation model of conductivity based on the assumption concerning phase separation of charge carriers can provide a more correct description of the transport properties of doped manganites in the temperature range preceding the magnetic transition than Mott's model or the polaron model. This approach was confirmed by the results obtained in Refs. 22 and 23, in which the existence of small-radius (1.5–2 nm) ferromagnetic clusters in an insulating paramagnetic matrix was detected with the help of small-angle neutron scattering. Under the action of the external or intrinsic magnetic field (below the magnetic transition temperature), such clusters can be transformed into ferromagnetic domains in which the metal-type conductivity emerges due to the double-exchange mechanism.[24] It should be noted that the size of discovered ferromagnetic clusters are in good agreement with the electron localization length obtained by us from an analysis of the temperature dependence of resistance.

This hypothesis also provides a reasonable explanation for the experimentally observed fact of incomplete transition of films to the metallic phase at temperatures below the magnetic ordering point (see Fig. 1). If we assume that the ferromagnetic order ensures the transport of charge carriers along the Mn^{3+}–O–Mn^{4+} bonds due to double exchange, we can expect the formation of percolation clusters consisting of growing ferromagnetic domains with metal-type conductivity below the transition temperature. At a certain critical concentration of domains, an infinitely large conducting cluster determining the transition of the sample to the metal state can be formed. The value of the percolation threshold in this model depends on the concentration of bivalent substitution ions as well as on the extent of ferromagnetic ordering in the Mn–O planes. Precisely this pattern was observed experimentally. The transition to the metal state in $La_{1-x}Sr_xMnO_3$ compounds occurs at the threshold values of $x > 0.15$, while in bulk $Pr_{2/3}Ca_{1/3}MnO_3$ samples the transition takes place only in magnetic fields above 6 T.[16] If the volume of the ferromagnetic phase is insufficient for the formation of an infinitely large percolation cluster, complete transition to the metallic phase might not occur as in the given case. On the other hand, an increase in the size of ferromagnetic clusters must lead to complete suppression of the thermoactivation conductivity mechanism since one-electron localized states degenerate into a band ensuring the metal-type conductivity within individual domains.

3. CONCLUSION

We obtained experimentally the temperature dependences of the resistivity of $Pr_{0.65}Ca_{0.35}MnO_3$ films of various thickness. In contrast to bulk ceramic samples, a change in the $\rho(T)$ dependence was observed in the vicinity of the magnetic phase transition temperature, which can be attributed to an incomplete transition of samples to the metal phase. The results of experiments were explained using three different models: Mott's model, the polaron model, and the ''foggy'' model of dynamic phase separation of carriers. The best agreement with the obtained results is attained in the framework of the ''foggy'' model presuming the existence of small-size ferromagnetic clusters in a paramagnetic insulating matrix.

*)E-mail: kamin@imp.kiev.ua
**)E-mail: yplee@omega.sunmoon.ac.kr

[1] C. W. Searle and S. T. Wang, Can. J. Phys. **48**, 2023 (1969).
[2] M. McCormack, S. Jin, T. H. Tiefel *et al.*, Appl. Phys. Lett. **64**, 3045 (1994).
[3] D. I. Khomskii and G. A. Sawatzky, Solid State Commun. **102**, 87 (1997).
[4] L. P. Gor'kov, Usp. Fiz. Nauk **168**, 665 (1998) [Phys. Uspekhi. **41**, 589 (1998)].
[5] C. Zener, Phys. Rev. **82**, 403 (1951).
[6] P. W. Anderson and H. Hasegawa, Phys. Rev. **100**, 675 (1955).
[7] J. Zaanen, G. A. Sawatzky, and J. W. Allen, Phys. Rev. Lett. **55**, 418 (1985).
[8] N. F. Mott, *Metal–Insulator Transitions* (2nd. ed.), Taylor and Francis, London (1990).
[9] M. Jaime, M. Salamon, M. Rubinstein *et al.*, Phys. Rev. **54**, 11914 (1996).
[10] Guo-meng Zhao, K. Conder, H. Keller, and K. Muller, Nature (London) **381**, 676 (1996).
[11] Y. Yanada, O. Hino, S. Nohado *et al.*, Phys. Rev. Lett. **77**, 904 (1996).
[12] L. P. Gor'kov and A. V. Sokol, Pis'ma Zh. Éksp. Teor. Fiz. **46**, 333 (1987) [JETP Lett. **46**, 420 (1987)].
[13] V. G. Prokhorov, V. I. Matsui, and V. A. Vas'ko, Sverkhprovodimost' **6**, 505 (1992).
[14] Z. Jirak, S. Krupicka, Z. Simosa *et al.*, J. Magn. Magn. Mater. **53**, 153 (1985).
[15] H. Yoshizawa, H. Kawano, Y. Tomioka, and Y. Tokura, Phys. Rev. B **52**, R13145 (1995).
[16] J. De Teresa, V. Ibarra, C. Matquina *et al.*, Phys. Rev. B **54**, R12689 (1996).
[17] M. Ziese and Ch. Srinitiwarawong, Phys. Rev. B **58**, 11519 (1998).
[18] M. Viret, L. Ranno, and J. Coey, J. Appl. Phys. **81**, 4964 (1997).
[19] D. Emin and T. Holstein, Ann. Phys. **53**, 439 (1969).
[20] I. G. Austin and N. F. Mott., Adv. Phys. **18**, 41 (1969).
[21] E. Iguchi, K. Ueda, and W. Jung, Phys. Rev. B **54**, 17431 (1996).
[22] J. W. Lynn, R. W. Erwin, J. A. Borchers *et al.*, Phys. Rev. Lett. **74**, 4046 (1996).
[23] J. M. De Teresa, M. R. Ibarra, P. A. Algarabel *et al.*, Nature (London) **386**, 256 (1997).
[24] J. B. Goodenough and J.-S. Zhou, Nature (London) **386**, 229 (1997).

Translated by R. S. Wadhwa

Optical surface modes in a system of fine metallic particles

A. Ya. Blank and L. V. Garanina

*Radio Astronomy Institute, National Academy of Sciences of Ukraine, 4 Krasnoznamennaya Str., 310002, Kharkov, Ukraine**)

L. G. Grechko

*Institute of Surface Chemistry, National Academy of Sciences of Ukraine, 31 Nauki Ave., 252022, Kiev, Ukraine***)

(Submitted December 14, 1998; revised April 6, 1999)
Fiz. Nizk. Temp. **25**, 1067–1072 (October 1999)

The interaction of electromagnetic radiation with a low-density disordered system of fine metallic particles located in a dielectric matrix is considered in a quasi-static approach with allowance for dipole-dipole interaction. The electric dipole moment of the system is calculated in a pair approximation. The case of nonidentical particles differing in their sizes or dielectric functions is presented. Allowance for particle nonidentity leads to doubling of the number of their surface modes and to the appearance of band gaps in the spectrum. The spectrum peculiarities are revealed in the fine structure of electromagnetic absorption. © *1999 American Institute of Physics.* [S1063-777X(99)01110-X]

Examination of oscillation spectra of metals is of great importance in connection with the problem of investigation of their absorptive properties. The nonuniform metallic layers, whose thickness is small compared to the skin depth, demonstrate an anomalously large absorptivity. Thin metallic gratings possess a variety of unusual transmissive and reflective features in a wide frequency range.[1] A layer of fine metal particles soluted in a host insulator absorbs nearly totally the radiation incident onto its surface.[2] These properties are attributed to the resonant excitation of the proper oscillation modes in a system and are very sensitive to the interaction between metal particles. Here we consider the last case—a small density system of disordered fine metal particles placed into a dielectric material. The volume fraction of metal particles determined by the filling factor $f=4/3\pi r^3 n$, where r is the particle size and n is the particle density, is assumed to be small, $f \ll 1$ (in fact, $f \sim 0.1-0.2$). Because of this circumstance, we can restrict the discussion to only the pair interaction between metal particles which we consider as electric dipoles. This approach is developed in the theory of interacting hard sphere gas[3] and is commonly used to describe the vibrational spectra of a crystal lattice.[4]

In this paper we study the interaction between nonidentical particles that differ in their sizes or dielectric properties (permittivities). This nonequivalence leads to the appearance of new spectral branches and band gaps. These results are similar to those found in one-dimensional vibrational chain of atoms when some of them are replaced by atoms of other kind.[5,6] It would be interesting to trace this analogy (and distinctions) in the case of infinite chain of metal particles with long-range multipole interaction. However, this will be the subject of another study.

The specific feature of the electromagnetic radiation (EMR) absorption in a system of fine metallic particles is a resonance caused by the existence of a surface mode (SM) in a single particle at the frequency[7]

$$\omega_s = \frac{\omega_p}{\sqrt{\varepsilon_\infty + 2\varepsilon_0}}. \tag{1}$$

Here it is assumed that a metal dielectric function has the form

$$\varepsilon(\omega) = \varepsilon_\infty - \frac{\omega_p^2}{\omega(\omega + i\nu)}, \tag{2}$$

where ε_∞ is the lattice dielectric function; ω_p and ν are the electron plasma frequency and the collisional frequency, respectively; and ε_0 is the dielectric function of the environment.

This mode usually called Fröhlich's mode is related to uniform dipole electron oscillations in a particle.[7] In the electrostatic limit the polarization inside the particle is determined by well-known relation[1]

$$\mathbf{P}(\omega) = \frac{\varepsilon(\omega) - \varepsilon_0}{\varepsilon(\omega) + 2\varepsilon_0} r^3 \mathbf{E}_0,$$

where r is the particle radius, and E_0 is the external alternating electric field which we consider quasistatic. Using the dielectric function of a metal particle in the form (2), we can rewrite it in the form

$$\mathbf{P}(\omega) = \left(\alpha_\infty + \frac{\omega_s^2(1-\alpha_\infty)}{\omega_s^2 - \omega^2 - i\omega\nu} \right) r^3 \mathbf{E}_0, \tag{3}$$

where $\alpha_\infty = (\varepsilon_\infty - \varepsilon_0)/(\varepsilon_\infty + 2\varepsilon_0)$ is the Clausius-Mosotti factor. This expression clearly shows the resonance at the frequency of the surface mode. Thus, the interaction of an alternating field with a metallic particle results in oscillator excitation at the Fröhlich frequency ω_s.

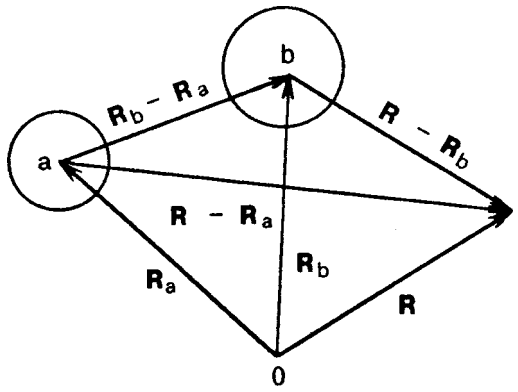

FIG. 1. Geometry of the particle location.

The EMR absorption in a system of metallic particles is sensitive to the magnitude and character of the direct multipole interaction between particles even though their concentration is sufficiently small.[8–11]

This problem was analyzed theoretically by many authors.[12–20] In those studies alternative methods of calculating the effective dielectric parameters of the disperse systems containing different inclusions were developed. At the same time, comparatively not much attention was given to the investigation of the proper surface mode spectra in these systems. Even when considering a very simple system of two or three particles one finds there some peculiar singularities caused by multipole interaction between particles.[9,10,20]

In this paper we investigate the spectrum of surface plasmons of two nonidentical metallic particles with different radii and different dielectric functions. In determining the polarization of the system with allowance for the interaction, we have used the results of the previous paper,[11] where the calculation formalism for the effective dielectric function of disperse systems with metallic inclusions was proposed. In the present analysis we restrict the discussion to a very simple model:

1. The analysis is carried out in the long-wave approximation, i.e., the wavelengths are large compared with the size of the particle and the mean distance between them, $\lambda \gg r, L$.

2. The particle size is assumed to greatly exceed the electron mean free path, $r \gg l$.

3. The allowance for the interaction between particles is carried out in a pair approximation, which we assume to be sufficient because of a small concentration of inclusions.

1. THE *N*-PARTICLES CASE

Let us choose two particles a and b from the ensemble. We can now find the polarization of coupled particles with allowance for multipole interactions with other $N-2$ particles.

We define $\mathbf{R}_a$ as the radius-vector of the center of sphere a, $\mathbf{R}_b$ as the radius-vector of the center of sphere b, and $\mathbf{R}$ is an arbitrary point outside the spheres in the medium (see Fig. 1). In the case of a uniform external field $\mathbf{E}_0$, the potential inside sphere a (which is regular at $\mathbf{R}=\mathbf{R}_a$) has the form[21]

$$\varphi_a^{\text{in}} = -E_0 \sum_{l,m} A_{lm}^{(a)} [|\mathbf{r}-\mathbf{r}_a]^l Y_{lm}(\mathbf{R}-\mathbf{R}_a), \tag{4}$$

where $\mathbf{R}\hat{-}\mathbf{R}_a$ is a unit vector along $\mathbf{R}-\mathbf{R}_a$, and $Y_{lm}(\mathbf{R}\hat{-}\mathbf{R}_a)$ are spherical harmonics. The potentials at the point $\mathbf{R}$ outside sphere a can be represented in the form

$$\begin{aligned}\varphi_a^{\text{out}} = &-E_0 \sum_{l,m} d_{lm} |\mathbf{R}-\mathbf{R}_a|^l Y_{lm}(\mathbf{R}-\mathbf{R}_a) \\ &-E_0 \sum_{l,m} B_{lm}^{(a)} |\mathbf{R}-\mathbf{R}_a|^{-l-1} Y_{lm}(\mathbf{R}-\mathbf{R}_a) \\ &-E_0 \sum_{b\neq a} \sum_{l,m} B_{l,m}^{(b)} |\mathbf{R}-\mathbf{R}_b|^{-l-1} Y_{l,m}(|\mathbf{R}-\mathbf{R}_b|),\end{aligned} \tag{5}$$

where the first term is the potential of the external field, the second term is the potential created by the particle a, and the third term includes the effect of the remaining particles.

The potentials (4) and (5) must satisfy the standard boundary conditions at the surface of sphere a:

$$\varphi_a^{\text{in}}|_{\mathbf{R}=\mathbf{R}_{sa}} = \varphi_a^{\text{out}}|_{\mathbf{R}=\mathbf{R}_{sa}}, \tag{6}$$

$$\varepsilon_a (\nabla \varphi_a^{\text{in}} \mathbf{n}_a)_{\mathbf{R}=\mathbf{R}_{sa}} = \varepsilon_0 (\nabla \varphi_a^{\text{out}} \mathbf{n}_a)_{\mathbf{R}=\mathbf{R}_{sa}}. \tag{7}$$

Accordingly, we must reduce the expressions for the potentials to a single center of the sphere, which can be done with use of the following transformation of tesseral harmonics:[22–24]

$$\begin{aligned}\frac{Y_{l,m}(\mathbf{R}\hat{-}\mathbf{R}_b)}{|\mathbf{R}-\mathbf{R}_b|^{l+1}} = &\sum_{l',m'} Q_{l',m'}^{l,m}(\mathbf{R}_b-\mathbf{R}_a) \\ &\times |\mathbf{R}-\mathbf{R}_a|^{l'} Y_{l',m'}(\mathbf{R}\hat{-}\mathbf{R}_a),\end{aligned} \tag{8}$$

where

$$\begin{aligned}Q_{l',m'}^{l,m}(\mathbf{R}_b-\mathbf{R}_a) = &(-1)^{l+m} \frac{Y_{l+l',m'-m}^*(\mathbf{R}_b\hat{-}\mathbf{R}_a)}{|\mathbf{R}_b-\mathbf{R}_a|^{l'+l+1}} \\ &\times \frac{4\pi(2l+1)(l+l'+m-m')!(l'+l+m'-m)!}{(2l'+1)(2l+2l'+1)(l+m)!(l-m)!(l'-m')!(l'+m')!}.\end{aligned}$$

Here $|\mathbf{R}-\mathbf{R}_a| < |\mathbf{R}_b-\mathbf{R}_a|$.

After putting expressions (4) and (5) in the boundary conditions (6) and (7) and using (8), we obtain a system of equations for the coefficients $B_{l,m}^{(a)}$

$$\frac{B_{l,m}^{(a)}}{\alpha_l^{(a)}} + \sum_{b\neq a} \sum_{l',m'} B_{l',m'}^{(b)} Q_{l,m}^{l',m'}(\mathbf{R}_b-\mathbf{R}_a) = -d_{l,m}. \tag{9}$$

Equation (9), in principle, gives the general solution for finding the polarization of a single particle ($B_{l,m}^{(a)}$) with allowance for the multipole interactions with other particles.

In the case of two particles ($a=i$; $b=j$) we obtain the following expressions from (9):

$$\frac{B_{l,m}^{(i)}}{\alpha_l^{(i)}}+\sum_{l',m'}\left[B_{l',m'}^{(j)}(-1)^{m'+l'}\times\frac{Y_{l+l',m-m'}(\mathbf{R}_j\hat{-}\mathbf{R}_i)}{\mathbf{R}_{ij}^{l+l'+1}}K_{l,m}^{l',m'}\right]=-d_{l,m},$$

$$\frac{B_{l,m}^{(j)}}{\alpha_l^{(j)}}+\sum_{l',m'}\left[B_{l',m'}^{(i)}(-1)^{m'+l'}\times\frac{Y_{l+l',m-m'}(\mathbf{R}_j\hat{-}\mathbf{R}_i)}{\mathbf{R}_{ij}^{l+l'+1}}K_{l,m}^{l',m'}\right]=-d_{l,m}. \quad (10)$$

Here we define

$$K_{l,m}^{l',m'}=\left[\frac{4\pi(2l'+1)(l+l'+m-m')!(l+l'+m'-m)!}{(2l+1)(2l+2l'+1)(l+m)!(l-m)!(l'+m')!(l'-m')!}\right]^{1/2}, \quad (11)$$

and $\alpha_l^{(i)}=l(\varepsilon_i-\varepsilon_0)r_i^{2l+1}/[l\varepsilon_i+(l+1)\varepsilon_0]$, where $R_{ij}=|\mathbf{R}_j-\mathbf{R}_i|$, and r_i is the radius of the particle i.

We will discuss only the case of the dipole-dipole interaction ($l=l'=1$). We choose the axis Z along the vector $(\mathbf{R}_j-\mathbf{R}_i)$. From (5) and (10) we then obtain the dipole moment of the particle i:[11]

$$\mathbf{p}_i(i)\cdot\mathbf{m}=-\mathbf{E}_0\mathbf{m}\sum_{m=-1}^{1}B_{lm}^{(i)}Y_{lm}(\mathbf{R}\hat{-}\mathbf{R}_i)=[X_{10}^{(i)}n_zm_z+X_{11}^{(i)}(n_xm_x+n_ym_y)]E_0, \quad (12)$$

where $\mathbf{m}=(\mathbf{R}-\mathbf{R}_i)/|\mathbf{R}-\mathbf{R}_i|$, $\mathbf{n}=\mathbf{E}_0/E_0$, and

$$X_{10}^{(i)}=\alpha_1^{(j)}\frac{1+2\alpha_1^{(j)}R_{ij}^{-3}}{1-4\alpha_1^{(i)}\alpha_1^{(j)}R_{ij}^{-6}}, \quad (13)$$

$$X_{11}^{(i)}=\alpha_1^{(i)}\frac{1-\alpha_1^{(j)}R_{ij}^{-3}}{1-\alpha_1^{(i)}\alpha_1^{(j)}R_{ij}^{-6}} \quad (14)$$

are the longitudinal and transverse polarizabilities, respectively, and $\alpha_1^{(i)}=(\varepsilon_i-\varepsilon_0)r_i^3/(\varepsilon_i+2\varepsilon_0)$ is the polarizability of an isolated single particle.

2. SURFACE MODES IN A SYSTEM OF TWO PARTICLES

To obtain the spectrum of surface modes we represent the expressions (13) and (14) in a convenient form

$$X_{10}=\frac{A_2(\omega)+2\Delta^3\sigma_1^3}{A_1(\omega)A_2(\omega)-4\Delta^3\sigma_1^6}r_1^3, \quad (15)$$

$$X_{11}=\frac{A_2(\omega)-\Delta^3\sigma_1^3}{A_1(\omega)A_2(\omega)-\Delta^3\sigma_1^6}r_1^3, \quad (16)$$

where $\Delta=r_2/r_1$, $\sigma_1=r_1/R$, and $A_i(\omega)=[\varepsilon_i(\omega)+2\varepsilon_0]/[\varepsilon_i(\omega)-\varepsilon_0]$ $(i=1,2)$.

The spectrum of surface modes is determined by the polarizability singularities, i.e., from the following relations:

$$A_1(\omega)A_2(\omega)-4\Delta^3\sigma_1^6=0 \quad (17)$$

and

$$A_1(\omega)A_2(\omega)-\Delta^3\sigma_1^6=0 \quad (18)$$

for the longitudinal and transverse modes, respectively.

Relations (17) and (18) determine the frequencies of the electron homogeneous oscillations of particles of different sizes and different dielectric functions.

2.1. In the case of the same particles ($r_1=r_2=r$, $\varepsilon_1=\varepsilon_2=\varepsilon$) we have $\Delta=1$, $A_1(\omega)=A_2(\omega)$, the extra poles in expressions (15) and (16) are cancelled, and we obtain the two known surface modes:[10] for the longitudinal mode

$$\omega_\parallel^2=\omega_s^2\frac{1-2(r/R)^3}{1-2(r/R)^3\alpha_\infty}, \quad (19)$$

where ω_s is Fröhlich's surface mode defined by (1), and for the transverse surface mode defined from (18), which is

$$\omega_\perp^2=\omega_s^2\frac{1+(r/R)^3}{1+(r/R)^3\alpha_\infty}. \quad (20)$$

We see, therefore, that allowance for the dipole-dipole interaction between particles in the presence of an external alternating field leads to doubling the proper mode number—to the appearance of longitudinal and transverse modes.

Note that in the case of identical particles with arbitrary orientation of the external field the dipole interaction between particles shifts the longitudinal mode to low-frequency side and the transverse mode to high-frequency side. These nonsymmetrical shifts lead to some absorption peculiarities in the many-particle system [see Eq. (10) in Ref. 11].

Let us now consider the changes in the surface mode spectrum caused by the nonidentity of the particles.

2.2. Let us consider particles of different sizes ($\Delta\neq1$) but with the same dielectric properties ($\varepsilon_1=\varepsilon_2$). In this case from Eqs. (17) and (18) we obtain, in contrast with the case of identical particles, the four surface modes instead of two:

$$\omega_\parallel^2=\omega_s^2\frac{1-2\Delta^{3/2}(r_1/R)^3}{1-2\Delta^{3/2}(r_1/R)^3\alpha_\infty}, \quad (21)$$

$$\tilde{\omega}_\parallel^2=\omega_s^2\frac{1+2\Delta^{3/2}(r_1/R)^3}{1+2\Delta^{3/2}(r_1/R)^3\alpha_\infty}, \quad (22)$$

$$\omega_\perp^2=\omega_s^2\frac{1+\Delta^{3/2}(r_1/R)^3}{1+\Delta^{3/2}(r_1/R)^3\alpha_\infty}, \quad (23)$$

$$\tilde{\omega}_\perp^2=\omega_s^2\frac{1-\Delta^{3/2}(r_1/R)^3}{1-\Delta^{3/2}(r_1/R)^3\alpha_\infty}. \quad (24)$$

We see from these formulas that allowance for the interaction between particles with different sizes leads to splitting of the longitudinal and transverse frequencies, which are shifted (for longitudinal and transverse modes) to the opposite sides. The dependence of the proper frequencies on the particle size ratio is shown in Fig. 2. Note that by setting $\Delta=1$, i.e., passing to the case of identical particles, the extra modes $\tilde{\omega}_\parallel$ and $\tilde{\omega}_\perp$ formally do not disappear. The point is that the oscillator forces corresponding to these modes turn to zero when $\Delta=1$ [see below Eqs. (30) and (31)]. The situation considered here reminds one of the appearance of

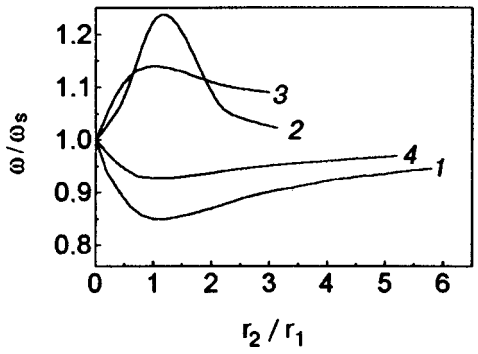

FIG. 2. Dependence of proper frequencies on the particle size ratio: *1*—$\omega_{\parallel}/\omega_s$; *2*—$\tilde{\omega}_{\parallel}/\omega_s$; *3*—$\omega_{\perp}/\omega_s$; *4*—$\tilde{\omega}_{\perp}/\omega_s$.

an optical mode in the one-dimensional infinite chain of two kinds of atoms with different masses in the unit cell.

2.3. Let us examine now another limiting case of particles with the same sizes but with different dielectric properties ($\varepsilon_1 \neq \varepsilon_2$). In this case Eqs. (17) and (18) give the following relations for finding the surface modes:

for the longitudinal mode

$$\frac{\varepsilon_1(\omega)+2\varepsilon_0}{\varepsilon_1(\omega)-\varepsilon_0}\,\frac{\varepsilon_2(\omega)+2\varepsilon_0}{\varepsilon_2(\omega)-\varepsilon_0}=4\left(\frac{r}{R}\right)^6; \tag{25}$$

for the transverse mode

$$\frac{\varepsilon_1(\omega)+2\varepsilon_0}{\varepsilon_1(\omega)-\varepsilon_0}\,\frac{\varepsilon_2(\omega)+2\varepsilon_0}{\varepsilon_2(\omega)-\varepsilon_0}=\left(\frac{r}{R}\right)^6. \tag{26}$$

Using Eq. (2), we can write these relations in the form (here we set $\varepsilon_0=\varepsilon_\infty=1$)

$$(\omega^2-\omega_{s1}^2)(\omega^2-\omega_{s2}^2)\,\frac{1}{\omega_{s1}^2\omega_{s2}^2}=\gamma\left(\frac{r}{R}\right)^6, \tag{27}$$

where

$$\omega_{s1,2}=\frac{\omega_{p1,2}}{\sqrt{3}} \tag{28}$$

are the proper modes of surface oscillations of the separated spheres; $\gamma=4$ or 1 in the case of the longitudinal or transverse mode, respectively.

Introducing a variable $x=\omega^2/\omega_{s1}^2$, we transform (27) to the form

$$(x-1)(\Gamma x-1)=\gamma\left(\frac{r}{R}\right)^6\equiv B,\quad \Gamma=\left(\frac{\omega_{p1}}{\omega_{p2}}\right)^2. \tag{29}$$

The graphical solution of (29) for $\Gamma>1$ is shown in Fig. 3; x_1 and x_2 are the roots of Eq. (29). We see in this figure that the frequency region between $\omega_{p1}^2/3$ and $\omega_{p2}^2/3$ creates the band gap. For the longitudinal mode ($\gamma=4$), when the distance between particles is $R=2r$, we have $x_1=0.22$ and $x_2=1.02$. In this case the analogy with the appearance of band gaps in the one-dimensional vibrational chain is appropriate.

The dependence of the proper frequencies on the distance between particles is shown in Fig. 4.

The general case of nonequivalent spheres ($r_1\neq r_2$, $\varepsilon_1\neq\varepsilon_2$) will be reported elsewhere.

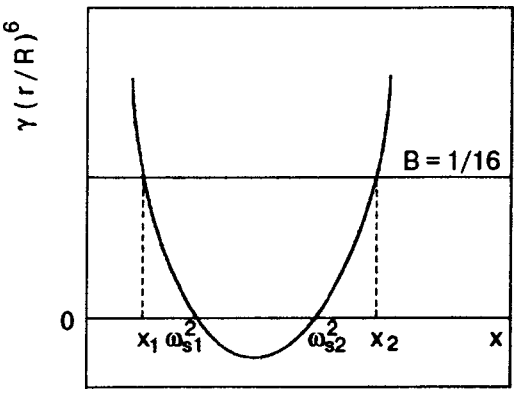

FIG. 3. Graphic solution of Eq. (29) for $\Gamma>1$.

3. DISCUSSION OF THE RESULTS

As is shown in Sec. 2, allowance for the particle nonidentity leads to doubling of the number of proper modes in a system of two spheres. Two supplementary modes, analogous with the optical modes in the one-dimensional lattices, appear together with two known surface modes for equivalent spheres. The longitudinal and transverse parts of the polarization, in accordance with expressions (15) and (16), can be represented in the form

$$X_{10}=\frac{1}{2}\,r_1^3\left[\frac{1+\Delta^{3/2}}{A(\omega)-2\Delta^{3/2}\sigma_1^3}+\frac{1-\Delta^{3/2}}{A(\omega)+2\Delta^{3/2}\sigma_1^3}\right], \tag{30}$$

$$X_{11}=\frac{1}{2}\,r_1^3\left[\frac{1-\Delta^{3/2}}{A(\omega)-\Delta^{3/2}\sigma_1^3}+\frac{1+\Delta^{3/2}}{A(\omega)+\Delta^{3/2}\sigma_1^3}\right], \tag{31}$$

where the poles of the denominators correspond to new modes. The factors $1\pm\Delta^{3/2}$ are oscillator forces which characterize the appropriate oscillations. All the expressions entering into Eq. (30) [Eq. (31), respectively], can be represented in the appropriate form; for example,

$$\frac{1+\Delta^{3/2}}{A(\omega)-2\Delta^{3/2}\sigma_1^3}=\frac{(1+\Delta^{3/2})}{(1-A)(1-\alpha_\infty A)}\times\left(\alpha_\infty(1-A)+\frac{\omega_{\parallel}^2(1-\alpha_\infty)}{\omega_{\parallel}^2-\omega^2-i\omega\nu}\right),$$

where $\omega_{\parallel}$ is given by (21), and $A=2\Delta^{3/2}(r_1/R)^3$.

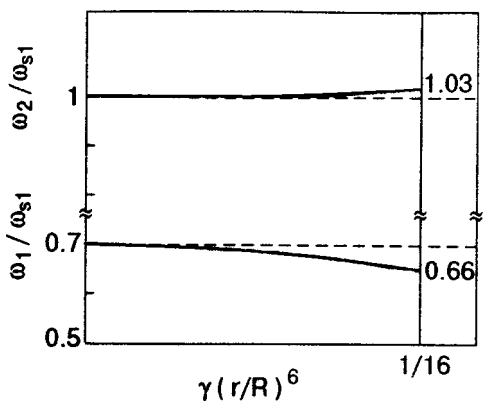

FIG. 4. Frequency spectrum versus the distance between particles.

We see, therefore, that the response of a system of two nonidentical particles is given by the sum of responses corresponding to four independent oscillators; their frequencies are the proper modes of the system (21)–(24).

The same is also true in the case of spheres of equal size but with different dielectric functions.

We appreciate the valuable discussion with E. Syrkin of the analogy of the considered spectra with the vibrational ones.

*E-mail: blank@ira.kharkov.ua
**E-mail: vit@surfchem.freenet.kiev.ua

[1] *Surface Excitations*, V. M. Agranovich and D. L. Mills (Eds.), Amsterdam, North Holland (1985).
[2] A. Ya. Blank and A. Ya. Sharshanov, Fiz. Nizk. Temp. **21**, 336 (1995) [Low Temp. Phys. **21**, 256 (1995)].
[3] R. Balesku, *Equilibrium and Nonequilibrium Statistical Mechanics*, Wiley (1975).
[4] A. M. Kosevich, *Theory of Crystal Lattice*, Vyscha shkola, Kharkov (1988).
[5] F. G. Bass, V. L. Fal'ko, and S. I. Khankina, Ukr. Phys. J. **38**, 901 (1993).
[6] M. A. Marnalul, E. S. Syrkin, and S. B. Feodosjev, Fiz. Nizk. Temp. **24**, 773 (1998) [Low Temp. Phys. **24**, 583 (1998)].
[7] C. F. Bohrea and D. P. Huffman, *Absorption and Scattering of Light by Small Particles*, Wiley and Sons (1983).
[8] U. Kreibig and M. Vollmer, *Optical Properties of Metal Clusters*, *Springer Series in Material Science* 25, Springer (1995).
[9] R. Ruppia, Phys. Rev. B **26**, 3440 (1982).
[10] M. Inoue and K. Ohtaka, J. Phys. Soc. Jpn. **52**, 3853 (1983).
[11] L. G. Grechko, A. Ya. Blank, V. V. Motrich, A. A. Pinchuk, and L. V. Geramina, *Radio Phys. and Radio Astrea*. **2**, 19 (1997).
[12] A. Liebech and B. N. Persson J. Phys. C **16**, 5375 (1983).
[13] R. G. Barrera, G. Mossivals, W. L. Mochan, and E. Anda, Phys. Rev. B **30**, 1989 (1989).
[14] V. A. Davis and L. Schwartz, Phys. Rev. B **31**, 6627 (1986).
[15] B. U. Felderholf, G. W. Ford, and E. G. D. Cohen, J. Stat. Phys. **28**, 649 (1982).
[16] B. U. Felderholf, G. W. Ford, and E. G. D. Cohen, J. Stat. Phys. **28**, 135 (1982).
[17] W. Lamb, D. M. Wood, and N. W. Aschcroft, Phys. Rev. B **21**, 2248 (1980).
[18] L. Fu and L. Resca, Phys. Rev. B **49**, 6625 (1984).
[19] P. Clippe, R. Evrard, and A. A. Lucas, Prog. Inorg. Chem. **14**, 1715 (1976).
[20] J. M. Gerardy and M. Ausloos, Phys. Rev. B **25**, 4204 (1982).
[21] P. M. Morse and H. Feshbach, *Methods of Theoretical Physics*, McGraw-Hill Book Company, Inc. (1953).
[22] M. Danos and L. C. Maximon, J. Math. Phys. **6**, 766 (1965).
[23] O. R. Crusan, Quart. Appl. Math. **20**, 33 (1962).
[24] R. Nozawa, J. Math. Phys. **7**, 1841 (1966).

This article was published in English in the original Russian journal. It was edited by S. J. Amoretty.

Electromagnetic waves in layered conductors and superlattices in a magnetic field

V. M. Gvozdikov and R. Vega-Monroy

*Department of Physics, Kharkov State University, 310077, Kharkov, Ukraine**)

(Submitted January 28, 1999; revised March 12, 1999)
Fiz. Nizk. Temp. **25**, 1073–1081 (October 1999)

The collective electromagnetic wave excitations in layered conductors in an external quantizing magnetic field are studied theoretically. A set of coupled equations for the electric field components and the Green's functions describing collective electromagnetic modes in such a system within the linear-response approach are obtained on the basis of a model of conducting planes embedded into a dielectric matrix. These equations, written in the layer-site representation, provide a basis for studies of the electromagnetic waves in the general case which does not imply either the spatial uniformity across the layers or the homogeneity within the conducting planes. The dispersion relations are obtained for the uniform and homogeneous layered conductors, which give a rich structure of collective electromagnetic modes in layered conductors in an external magnetic field. The dispersion and damping of helicons in layered conductors in the regimes of conventional and quantum Hall effects have been studied, both analytically and numerically. Two new modes propagating perpendicular to the magnetic field with frequencies of the order of the plasma frequency have been found. © *1999 American Institute of Physics.* [S1063-777X(99)01210-4]

1. INTRODUCTION

It is known that weakly damped electromagnetic waves of different types can propagate in metals in a strong magnetic field at low temperatures.[1,2] Among them are the spiral waves, or helicons, whose frequency ω is proportional to the intensity of the magnetic field H (Ref. 3), the magnetoplasma waves,[4,5] the Alfvén waves, the cyclotron waves,[6] surface waves,[7] magnetoimpurity waves,[8,9] and other waves.

A progress gained in fabrication of various artificial superlattices as well as recent extensive research of different types of layered metallic, organic, and other (semi) conductors and superconductors, including high-T_c cuprates, enhances activity in studies of collective electromagnetic oscillations in these systems.

A quasi-two-dimensional (2D) nature of the electron spectrum in superlattices exerts a substantial impact on the shape of a 2D conductivity tensor which, together with Maxwell's equations, determines the spectrum and the damping of the electromagnetic waves in superlattices.

The practical interest in such systems is determined by the possibility of varying the spectral properties of the electromagnetic waves in superlattices by modifying their structural parameters and varying the strength of the external magnetic field.

Extensive literature on the plasma and electromagnetic modes in different types of superlattices is available.[10–21] At the same time, the electromagnetic waves in layered conductors in an external magnetic field have been studied less extensively.[22–26] The 2D dynamics of electrons in a quantizing magnetic field produces some nontrivial phenomena and concepts such as the quantum Hall effect (QHE) (Ref. 27) and anyons (Ref. 28), for example. The QHE was observed experimentally in a superlattice[29] and layered organic conductors.[30,31] The electromagnetic waves (helicons) in layered conductors under the conditions of the QHE have been considered in a number of theoretical studies.[22,24–26] within the model of periodic array of 2D electron gas embedded in a homogeneous dielectric substrate. In this model electrons have no dispersion across the layers so that the quasiclassical approach of the standard electron theory of metals based on the concept of the Fermi surface[2,32] and its version adapted for the semiconducting superlattices[10] should be modified. The dispersion relation for the electromagnetic waves propagating along the field (i.e., across the layers) in such quasi-2D superlattices is governed by the interlayer electromagnetic correlations described by the Maxwell's equations.

The relationship between the electromagnetic field and the current within the layers is determined by the 2D conductivity tensor $\sigma_{\alpha\beta}(H)$, which is the key quantity for the electromagnetic wave dispersion. The dispersion of helicons is determined by the Hall components $\sigma_{xy}=-\sigma_{yx}$, which are quantized in quasi-2D conductors under the conditions of the quantum Hall effect and by the longitudinal component σ_{xx}, which is nonzero at frequency $\omega\neq 0$ due to polarization and displacement currents[26,33] in QHE. The role of the electron dispersion across the layers in high-frequency phenomena and propagation of electromagnetic waves have been considered in Ref. 34. Some specific features of helicons in layered conductors related to the quasi-2D electron energy spectrum were discussed in Ref. 35.

The purpose of this paper (which is the first publication of a series of studies on the wave propagation in layered conductors and superconductors) is twofold. First, we derive a basic system of equations describing electromagnetic field propagation in layered conductors and superlattices in the most general form, in particular, for nonuniform spatial distribution of the dielectric substance between the layers, non-

periodic layer sequence and inhomogeneities within the conducting layers. These equations provide a basis for subsequent studies of the problem in question which will be published elsewhere.

Another aim of this paper is to study further some problems, which have so far not been resolved completely, on the basis of our model in the limiting case of a uniform and homogeneous layered conductors. In particular, we consider the dispersion and damping of the helicon waves in layered conductors under conditions of conventional and quantum Hall effect and study their coupling to the intralayer plasmons.

2. THE MODEL AND BASIC EQUATIONS

Consider an infinite stack of conducting planes separated by dielectric layers of thickness a, which is large enough so that one can ignore hopping between adjacent layers. This model is known to be a good approximation for some natural layered crystals, such as Tl or Bi-based high-T_c superconducting copper oxides, for example, and evidently it may be perfectly well realized in an artificially fabricated semiconductor or metallic superlattices.

In this section we consider the wave equations within the frame of the above model. To this end, we direct the z axis perpendicular to the layers and assume that a constant external magnetic field H is also directed along this axis. We assume that the permeability of the substance between the layers equals to unity, $\mu=1$, and also assume its dielectric constant, $\varepsilon=\varepsilon(z)$, to be a function of z.

Under these assumptions, the Maxwell's equations, written in terms of the electric field $\mathbf{E}$,

$$(\mathrm{div}\mathbf{E})-\Delta\mathbf{E}=-\frac{\varepsilon}{c^2}\frac{\partial^2\mathbf{E}}{\partial t^2}+\frac{4\pi}{c^2}\frac{\partial}{\partial t}\mathbf{J}, \tag{1}$$

after the substitution

$$E_l=E_l(\mathbf{q},z,\omega)\exp[i(q\boldsymbol{\rho}-\omega t)], \quad (l=x,y,z), \tag{2}$$

take the form

$$-\mathbf{q}(\mathbf{q}\mathbf{E}_\perp)+iq\left(\frac{\partial}{\partial z}E_z\right)+\left(q_\omega^2-\frac{\partial^2}{\partial z^2}\right)\mathbf{E}_\perp=-\frac{4\pi i\omega}{c^2}\mathbf{J}_\perp, \tag{3}$$

$$E_z=-\frac{1}{q_\omega^2}\frac{\partial}{\partial z}(i\mathbf{q}\mathbf{E}_\perp), \tag{4}$$

$$q_\omega^2(z)=q^2-\frac{\omega^2}{c^2}\varepsilon(z). \tag{5}$$

Here ρ, q, and ω are the in-plane coordinate, the wave-vector and the frequency of the collective mode, and $\mathbf{E}_\perp$ and $\mathbf{J}_\perp$ are the in-plane field and the current, respectively.

Choosing $\mathbf{q}$ to be parallel to the y axis, we obtain the system of equations

$$\left(\frac{\partial^2}{\partial z^2}-q_\omega^2\right)E_x=\frac{4\pi i\omega}{c^2}J_x, \tag{6}$$

$$\left(\frac{\partial^2}{\partial z^2}-q_\omega^2\right)E_y+U(q,\omega,z)\frac{\partial}{\partial z}E_y=-\frac{4\pi iq_\omega^2}{\omega e(z)}J_y, \tag{7}$$

$$E_z=-\frac{iq}{q_\omega^2}\frac{\partial}{\partial z}E_y, \tag{8}$$

$$U(q,\omega,z)=\left(\frac{q}{q_\omega(z)}\right)^2\varepsilon^{-1}(z)\frac{\partial\varepsilon(z)}{\partial z}. \tag{9}$$

Thus, we see that all three components of the electric field are determined by the two equations (6) and (7), which can be rewritten as follows:

$$E_x(n)=\frac{4\pi i\omega}{c^2}\sum_{n'}G^x_{q_\omega}(n,n')[\sigma_{xx}E_x(n')+\sigma_{xy}E_y(n')], \tag{10}$$

$$E_y(n)=-\frac{4\pi iq_\omega^2}{\omega}\sum_{n'}G^y_{q_\omega}(n,n')[\sigma_{yy}E_y(n')+\sigma_{yx}E_x(n')]\varepsilon^{-1}(an).$$

We took into account here that the current can flow only within the layers and therefore its z axis distribution contains a system of δ-functions

$$J_\alpha=\sum_{\beta,n}\sigma_{\alpha\beta}(\mathbf{q},\omega,H)\delta(z-an)E_\beta(\mathbf{q},\omega,z). \tag{11}$$

The subscripts α and β can take two values x and y. The Green's functions in (10) $G^\alpha_{q_\omega}(n,n')\equiv G^\alpha_{q_\omega}(an,an')$ satisfy the equations

$$\left(\frac{\partial^2}{\partial z^2}-q_\omega^2(z)\right)G^x_{q_\omega}(z,z')=\delta(z-z'), \tag{12}$$

$$\left(\frac{\partial^2}{\partial z^2}+U(\mathbf{q},\omega,z)\frac{\partial}{\partial z}-q_\omega^2(z)\right)G^y_{q_\omega}(z,z')=\delta(z-z'). \tag{13}$$

The in-plane conductivity tensor $\sigma_{\alpha\beta}$ has off-diagonal Hall components because of the external magnetic field H, which we assume to be applied perpendicular to the layers.

The principal difference of our approach from the one developed in the previous papers[22,23] is that we do not imply a spatial uniformity of the $\varepsilon(z)$ across the layers. We also do not imply periodicity of the layer sequence in Eq. (10) since $\varepsilon(z)$ between the layers in fact may have an arbitrary constant value. [In the case of aperiodic layer sequence the quantities a and n in Eq. (11) should be replaced by a_n—the discrete coordinates of the conducting planes.]

In this paper we consider the bulk modes in the case of a regular and uniform layered conductor under conditions of the conventional and quantum Hall regimes, leaving the nonuniform case for separate publication.

In the case of an infinite regular and uniform, $\varepsilon(z)=\mathrm{const}$, layered crystal the U-term in Eq. (13) vanishes and the Green's functions $G^x_{q_\omega}(z,z')$ and $G^y_{q_\omega}(z,z')$ become identical since they both satisfy Eq. (12), in which $q_\omega(z)$ is independent of z. The Green's function of Eq. (12) can then be easily found

$$G_{q_\omega}(z,z')=-\frac{1}{2q_\omega}\exp(-q_\omega|z-z'|). \tag{14}$$

Making the Fourier transform

$$E_\beta(n)=\frac{a}{2\pi}\int_{-\pi/a}^{\pi/a}dk\,\exp(ikan)E_\beta(k) \tag{15}$$

and completing summation over the layer index in Eqs. (10), we can rewrite them in the matrix form

$$\sum_\beta\left[\delta_{\alpha\beta}-\frac{2\pi i\omega}{c^2q_\omega}\,\sigma_{\alpha\beta}(q,\omega,H)V_{\alpha\beta}S(\mathbf{q},k,\omega)\right]\times E_\beta(q,k,\omega)=0. \tag{16}$$

The structural form factor $S(\mathbf{q},k,\omega)$ in Eq. (16) is given by

$$S(\mathbf{q},k,\omega)=\sum_{n=-\infty}^{\infty}\mathbf{e}^{-q_\omega a|n|+ikn}=\frac{\sinh(q_\omega a)}{\cosh(q_\omega a)-\cos(ka)} \tag{17}$$

and the components of the matrix $V_{\alpha\beta}$ are

$$V_{11}=V_{12}=1,\quad V_{21}=V_{22}=-\frac{c^2q_\omega^2}{n_0^2\omega^2}, \tag{18}$$

where $n_0=\sqrt{\varepsilon}$ is the refraction index.

The system of two uniform equations has nonzero solutions if the following condition is satisfield:

$$\det\left[\delta_{\alpha\beta}-\frac{2\pi i\omega}{c^2q_\omega}\,\sigma_{\alpha\beta}(\mathbf{q},\omega,H)V_{\alpha\beta}S(\mathbf{q},k,\omega)\right]=0, \tag{19}$$

which is the dispersion relation for the bulk modes which determine the frequency $\omega=\omega(\mathbf{q},k,H)$ of a wave that can propagate in the volume of a layered conductor. The key quantity in (19) is the 2D conductivity tensor $\sigma_{\alpha\beta}$, which depends on the layer structure and the external magnetic field. Thus, the specific type of the electromagnetic wave is determined by the particular form of the tensor $\sigma_{\alpha\beta}$. We consider some types of bulk waves in the following sections on the basis of the dispersion relation (19).

3. THE HELICON MODES

According to the Eq. (19) the wave dispersion in layered conductors is determined by the in-plane conductivity tensor, which depends on the electronic properties of the layer and the intensity of the external magnetic field.

The in-plane conductivity may be anisotropic without the external magnetic field as is the case, for example, in some layered organic (super) conductors.[30,31]

We consider here a more simple case of a two-dimensional electron gas in a perpendicular magnetic field. The conductivity tensor for this model was calculated elsewhere (see Ref. 36) and has the following components.

$$\sigma_{xx}=\sigma_0\gamma(1+\gamma^2)^{-1},\quad \sigma_{xy}=-\sigma_0+\gamma\sigma_{xx}, \tag{20}$$

$$\sigma_{xx}=\sigma_{yy},\quad \sigma_{xy}=-\sigma_{yx}, \tag{21}$$

where

$$\sigma_0=\frac{Ne^2}{m\Omega},\quad \gamma=\frac{\nu-i\omega}{\Omega}. \tag{22}$$

Here $\Omega=eH/mc$ stands for the cyclotron frequency, $\nu=1/\tau$ is the Landau level damping due to the impurities, and N is the 2D electron density.

Substituting Eqs. (20) and (21) into the dispersion relation (19), we have

$$1+\gamma^2-\frac{i\gamma S(\mathbf{q},k,\omega)}{2\Omega_*}\left(\frac{\omega_*^2\tilde{\omega}}{q_\omega a}-\frac{q_\omega a}{n_0^2\tilde{\omega}}\right)+S^2(\mathbf{q},k,\omega)\times\left(\frac{\omega_*}{\Omega_*}\right)^2\frac{1}{4n_0^2}=0. \tag{23}$$

The dimensionless notation adopted in this relation is

$$\omega_*=\frac{\omega_p a}{c},\quad \Omega_*=\frac{\Omega}{\omega_p},\quad \tilde{\omega}=\frac{\omega}{\omega_p}, \tag{24}$$

and $\omega_p^2=4\pi Ne^2/ma$ is the plasma frequency.

The helicons, as is well known, propagate along the magnetic field direction in the bulk conventional metals[2,3] and in the layered conductors.[22,23] Thus, to study their dispersion and damping we must consider the case $qa=0$. The layer form factor $S(\mathbf{q},k,\omega)$ in this case takes the form

$$S(0,k,\omega)=\frac{i\omega_*\tilde{\omega}n_0}{1-\cos(ka)}. \tag{25}$$

We have taken into account also that $\omega_*\tilde{\omega}n_0\ll 1$ (this statement will be verified below), so that we can approximate $\cosh(\omega_*\tilde{\omega}n_0)\approx 1$ in the denominator of Eq. (17). Using (25), we rewrite the dispersion relation (23) in the form

$$1+(\Gamma-iX)^2-i(\Gamma-iX)X2A-X^2A^2=0, \tag{26}$$

where

$$\Gamma=\frac{\nu}{\Omega},\quad X=\frac{\omega}{\Omega},\quad A=\frac{\omega_*^2}{2(1-\cos ka)}. \tag{27}$$

The equation (26) has an exact solution in the complex form $X=\mathrm{Re}\,X-i\,\mathrm{Im}\,X$, which determines the dispersion of helicons along the magnetic field

$$\mathrm{Re}\,\omega(k)=\frac{\Omega\sin^2(ka/2)}{(\omega_*/2)^2+\sin^2(ka/2)}, \tag{28}$$

and their damping

$$\mathrm{Im}\,\omega(k)=\frac{\nu\sin^2(ka/2)}{(\omega_*/2)^2+\sin^2(ka/2)}. \tag{29}$$

In the long-wavelength limit, $ka\to 0$, the helicon dispersion relation (28) gives the well-known result[22,23]

$$\mathrm{Re}\,\omega(k)\simeq\frac{\Omega}{\omega_p^2}\,k^2c^2. \tag{30}$$

The damping of helicons, as one can see from Eq. (29), is proportional to ν and vanishes in a pure conductor ($\nu=0$). The small quantity $\omega_*\ll 1$ may vary in a wide range, depending on the values of the plasma frequency ω_p and the distance between layers a. The appropriate dispersion $\mathrm{Re}\,\omega(k)$ and the damping $\mathrm{Im}\,\omega(k)$, considered as functions of the wave vector k, are shown in Fig. 1 for different values of ν.

It follows from Eqs. (28) and (29) that the ratio

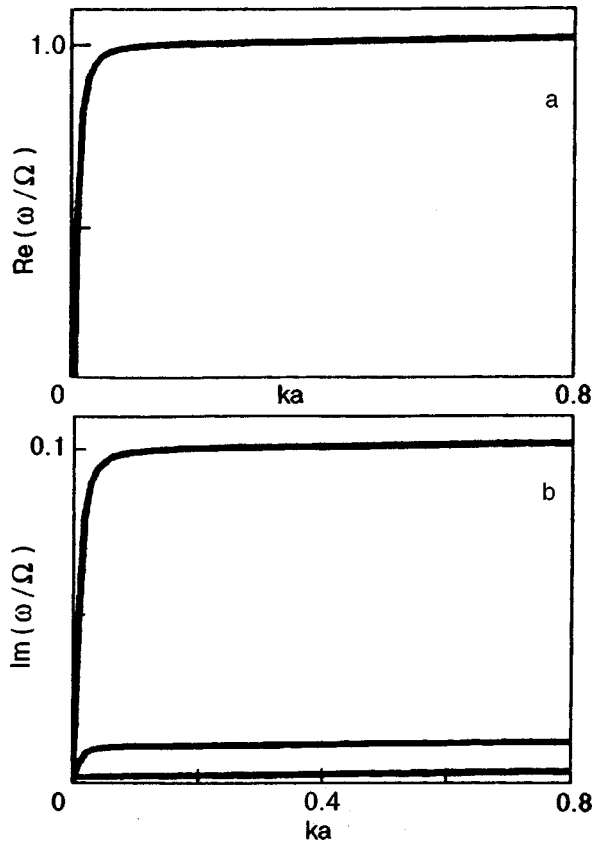

FIG. 1. The dispersion relation (a) and the damping (b) of helicons in a layered conductor under the condition of the Hall effect. The parameter $\omega_*=0.01$ for both pictures. Re ω is independent of the Landau level broadening, whereas Im ω is proportional to v, taken in (b) equal to 0.1, 0.01, and 0.001, respectively, from the top line to the bottom line [see also Eqs. (26) and (29)].

$$\frac{\mathrm{Im}\,\omega(k)}{\mathrm{Re}\,\omega(k)}=\frac{\nu}{\Omega} \tag{31}$$

is independent of the wave vector k, so that for $\nu \ll \Omega$ helicons are damped only slightly at any ka. The above-required smallness of the parameter $\omega_* \tilde{\omega} n_0$ holds since, according to the Eq. (28), $\tilde{\omega} \sim \Omega/\omega_p$ and $\omega_* \tilde{\omega} n_0 \sim \Omega a/c \ll 1$, because in attainable fields for thicknesses $a \simeq 10^{-7}-10^{-5}$ cm, Ω is much lower frequency $c/a \sim 10^{17}-10^{15}\mathrm{s}^{-1}$.

4. THE HELICON WAVES UNDER THE CONDITIONS OF THE QUANTUM HALL EFFECT

The dispersion relation (19) is a general relation which may be applied to various layered conductors with different types of conductivity tensors. The helicon waves of the preceding section are caused by the Hall currents and formally stem from the Hall components of the conventional conductivity tensor $\sigma_{\alpha\beta}$ of the 2D electron gas. On the other hand, $\sigma_{\alpha\beta}$ has a very simple form in a 2D system under the conditions of the quantum Hall effect. In view of this circumstance, it is rather logical to consider the problem of the helicons in layered conductors under the QHE conditions on the basis of our approach, especially since QHE was observed in some layered organic conductors[30,31] and superlattices.[29]

Early theoretical studies of helicons under the conditions of the QHE (Refs. 22, 24, and 25) disregarded the effect of the polarization currents on the $\sigma_{\alpha\beta}(\omega)$ at nonzero frequency,[26,33] which makes the $\mathrm{Im}\,\sigma_{xx}(\omega)\neq 0$. The longitudinal conductivity in this case is

$$\sigma_{xx}(\omega)=i\left(\frac{\omega}{\Omega}\right)\sigma_{xy}, \tag{32}$$

where $\sigma_{xy}=-\sigma_{yx}$ is the quantized, in units of the conductance quantum, e^2/h, static component of the conductivity tensor[27]

$$\sigma_{xy}=\frac{ne^2}{h}, \quad (n=1,2,3...). \tag{33}$$

With respect of Eq. (33), the dispersion relation (19) gives

$$\left[1+\alpha S(\mathbf{q},k,\omega)\left(\frac{\omega}{\Omega}\right)\sigma_{xy}\right]\left[1-\beta S(\mathbf{q},k,\omega)\left(\frac{\omega}{\Omega}\right)\sigma_{xy}\right] + \alpha\beta S^2(\mathbf{q},k,\omega)\sigma_{xy}^2=0, \tag{34}$$

where

$$\alpha=\frac{2\pi\omega}{c^2 q_\omega} \quad \text{and} \quad \beta=\frac{2\pi q_\omega}{\omega n_0}. \tag{35}$$

Setting in Eq. (34) $qa=0$ and using the form factor $S(0,\omega,k)$ in the form (25), we obtain a very simple dispersion relation for helicons under the QHE regime

$$1+2X^2A_n-A_n^2X^2(1-X^2)=0, \tag{36}$$

where $X=\omega/\Omega$, and

$$A_n=\frac{n\alpha_0}{1-\cos(ka)}\frac{\Omega a}{c}, \quad (n=1,2,3,...). \tag{37}$$

Here $\alpha_0=c^2/\hbar c=1/137$ is the fine structure constant.

The solution of Eq. (36) is trivial and yields two modes $\omega_+(ka)$ and $\omega_-(ka)$;

$$\left(\frac{\omega_\pm}{\Omega}\right)^2=\frac{2-A_n\pm\sqrt{A_n(A_n-4)}}{2A_n}\ldots. \tag{38}$$

For small $ka \ll 1$ (when $A_n \to 1$) we have the following relation for the $\omega_-(ka)$ mode, which corresponds to the «minus» sign in Eq. (38),

$$\omega_-(ka)\simeq\frac{2c}{an\alpha_0}\sin^2\frac{ka}{2}. \tag{39}$$

Formally, the magnetic field does not enter Eq. (39) but, in fact, it does since (39) is valid only for fields H which fall within the plateaus in the quantum Hall conductivity.[27]

Another branch of the $\omega(ka)$, which corresponds to the positive sign in the dispersion relation (38), in the long-wavelength limit is given by

$$\omega_+(ka)\simeq\Omega-\frac{2c}{an\alpha_0}\sin^2\frac{ka}{2}. \tag{40}$$

Thus, we have two types of wave in a layered conductor in the QHE regime: one with the acoustic dispersion $[\omega_-(ka)]$ and one with the optic-like dispersion $[\omega_+(ka)]$. The $\omega_+(ka)$ branch has not been considered before. It appears in

the problem in question owing to the term $\sigma_{xx}(\omega)$ (32) in the dispersion relation (34). This term enhances by unity the power of the polynomial in X^2 on the left-hand side of Eq. (36) and, correspondingly, gives an additional root [i.e., the new branch of $\omega_+(ka)$]. Physically, the frequency-dependent longitudinal conductivity (32), as was shown in Refs. 26 and 33, is caused by the polarization currents.

It follows from Eq. (38) that under the condition $A_n(ka)<4$ the right-hand side of Eq. (38) acquires an imaginary part, which implies that $\mathrm{Im}\,\omega(ka)\neq 0$.

An analysis shows that for k less than the threshold value, k^*, the quantum waves in question propagate without damping [$\mathrm{Im}\,\omega(ka)=0$]. The threshold value is

$$k^*(n)=\frac{2}{a}\arcsin\left(\frac{\pi n}{4\alpha_0}\frac{\Omega a}{c}\right)^{1/2}. \tag{41}$$

For $k>k^*$ the $\mathrm{Im}\,\omega_{\pm}(ka)\neq 0$.

The dispersion and the damping of the two modes in layered conductors in the QHE regime are shown in Fig. 2 for the first three values of the integer $n=1,2,3$. We see from Fig. 2 that the decreasing modes $\omega_+(ka)$ do exist only for $k<k^*(n)$ [they terminate exactly at $k=k^*(n)$, as is shown in Fig. 2a] whereas the modes increasing with $ka\,\omega_-(ka)$ are damped when $k>k^*(n)$, because $-\mathrm{Im}\,\omega(ka)\neq 0$. This damping, as one can see in Fig. 2c, increases rapidly with ka, so that the ratio $|\mathrm{Im}\,\omega_-(ka)/\mathrm{Re}\,\omega_-(ka)|\ll 1$ only in a small vicinity of the threshold value k^*.

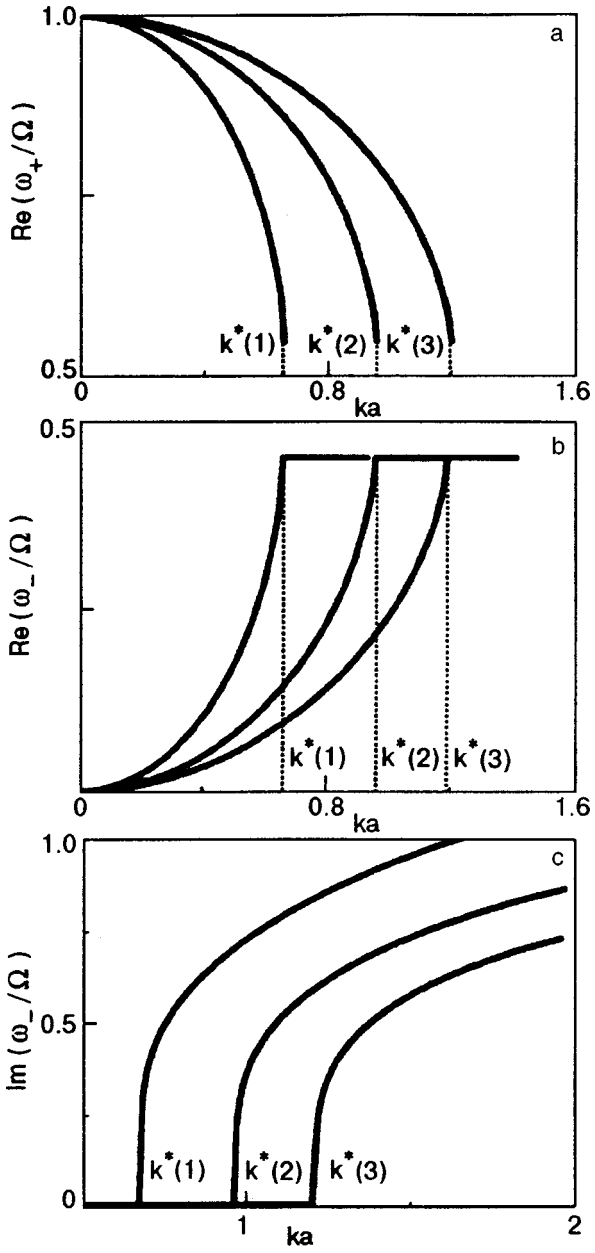

FIG. 2. The dispersion relation and the damping of helicons, given by Eq. (38), under the conditions of the QHE is a layered conductor are shown in (a–c) for integers $n=1,2,3$. The decreasing modes $\omega_+(k)$ in (a) do not exist above the threshold values $k>k^*(n)$ [see Eq. (4) for $k^*(n)$]. The increasing modes $\omega_-(k)$ in (b) are damped when $k>k^*(n)$ since $\mathrm{Im}\,\omega_-(k)\neq 0$ in (c) under this condition.

5. THE BULK MODES WITH DISPERSION ALONG THE LAYERS

The dispersion relation (23) which we have used in Sec. 3 for studies of the helicon waves that propagates along the magnetic field may be also employed for analysis of different types of waves in this model. In this section we will briefly discuss the waves that propagate perpendicular to the magnetic field, i.e., parallel to the layers, and then will consider the case $q\neq 0$, $k\neq 0$, both analytically and numerically.

The analytic solution of Eq. (23) can be obtained, in particular, for the case of waves propagating exactly parallel to the layers, i.e., when $k=0$, provided that $|q_\omega a|\ll 1$, where q_ω is given by Eq. (5). Under these conditions, setting $\nu=0$ and taking into account that the layer form factor (17) in this limit is

$$S(\mathbf{q},0,\omega)\approx\coth\left(\frac{q_\omega a}{2}\right)\approx\frac{2}{q_\omega a}, \tag{42}$$

we have from Eq. (23)

$$y^2-y(1+\beta)+\beta=0, \tag{43}$$

where

$$y=\left(\frac{\omega}{\omega_p}\right)^2 n_0, \quad \beta=\frac{1}{n_0}\left[1+\left(\frac{qa}{\omega_*}\right)^2\right]. \tag{44}$$

The solution of Eq. (43) gives two modes:

$$\omega_1^2=\left(\frac{\omega_p}{n_0}\right)^2\left[1+\left(\frac{qa}{\omega_*}\right)^2\right] \quad \text{and} \quad \omega_2^2=\frac{\omega_p^2}{n_0}. \tag{45}$$

The mode ω_1 belongs to the so-called propagating sector $q_\omega^2<0$ (Ref. 23), which can be checked by the direct substitution of Eq. (45) into the definition for q_ω (6), which yields $q_\omega^2 a^2=-\omega_*^2$. Thus, $|q_\omega a|=|\omega_*|\ll 1$, which has been assumed in the course of the derivation of Eq. (45). We also assume that $|\gamma|=|\omega/\Omega|\gg 1$, which is true for modes ω_1 and ω_2 since $\omega_p\gg\Omega$.

The mode ω_2 after substitution into Eq. (6) yields $q_\omega^2 a^2=(qa)^2-n_0\omega_*^2$, so that the condition $|q_\omega a|\ll 1$ holds for $qa\ll 1$.

On the other hand, it is possible to obtain an analytic solution of Eq. (23) when $qa\gg n_0\omega_*\omega/\omega_p$. In this case

$q_\omega a \approx qa$, so that the form factor of the layer is independent of ω:

$$S(q,k,0) \approx \frac{\sinh(qa)}{\cosh(qa)-\cos(ka)}. \tag{46}$$

Under these conditions the dispersion relation (23) in the limit $\nu=0$ yields

$$\omega^2 = 2qa\left[\frac{\Omega^2}{2qa+S\omega_*^2}+\left(\frac{\omega_p}{2n_0}\right)^2 S\right]. \tag{47}$$

Setting $ka=0$ in Eq. (46), we have for small qa (i.e., for $n_0\omega_*\omega/\omega_p \ll qa \ll 1$) $S(q,0,0)\approx 2/qa$, which, after substitution into the Eq. (47), yields

$$\omega^2 \approx \Omega^2 + \left(\frac{\omega_p}{n_0}\right)^2 \approx \left(\frac{\omega_p}{n_0}\right)^2. \tag{48}$$

We see, therefore, that in this limit the dispersion relation (47) equals the ω_1 mode, given by Eq. (45). Since $\omega_* = \omega_p a/c$ is of the order of $10^{-4}-10^{-2}$ for $\omega_p \simeq 10^{13}-10^{15}$ and $a \simeq 10^{-7}-10^{-5}$, the inequality $qa \gg n_0\omega_*\omega/\omega_p \simeq \omega_*$ holds for ω, given by Eq. (48).

The second term in Eq. (47) is exactly the bulk plasmon dispersion in a layered conductor[12–15]

$$\omega_{pl}(q) = \left(\frac{\omega_p}{n_0}\right)^2 \frac{qa}{2}\,\frac{\sinh(qa)}{\cosh(qa)-\cos(ka)}. \tag{49}$$

The first term in Eq. (47) under the conditions $ka \neq 0$, $qa \ll 1$ may be rewritten in the helicon-like form

$$\Omega^2\left[1+\frac{S\omega_*^2}{2qa}\right]^{-1} \approx \frac{\Omega^2 \sin^2(ka/2)}{\sin^2(ka/2)+(\omega_*/2)^2}. \tag{50}$$

We thus conclude that when the wave vector has both components, parallel (**q**) and perpendicular (k) to the layers, the waves in question are the mixture of helicons and plasmons. For $q=0$ only helicons are excited.

The damping of the mode (47) in the linear approximation on the small parameter $\nu/\Omega \ll 1$ is given by

$$\mathrm{Im}\,\omega(q) = \frac{\nu}{2}(1+\hat{S})^{-1}\left[(2+\hat{S})\left(\frac{\omega}{\omega_p}\right)^2 - \frac{qa}{n_0^2}\right], \tag{51}$$

where

$$\hat{S} = \frac{S(q,k,0)\omega_*^2}{2qa} \tag{52}$$

and $(\omega/\omega_p)^2$ is determined by Eq. (47).

In the case $ka=0$ and for small $qa \ll 1$ the form factor $S(q,0,0)\approx 2/qa$ and the damping is estimated to be

$$\mathrm{Im}\,\omega(q) \approx \frac{\nu}{2}[S(q,0,0)-1]\frac{qa}{n_0^2} \approx \frac{\nu}{n_0^2}. \tag{53}$$

It is easy to find the dependence of helicons on qa in the case of a small qa, $qa \ll 1$. The dispersion relation (23) in this case yields

$$1+(\Gamma-iX)^2-(X+i\Gamma)A\left(2X \sim \frac{\tilde{q}^2}{X}\right) + A^2(\tilde{q}^2-X^2)=0. \tag{54}$$

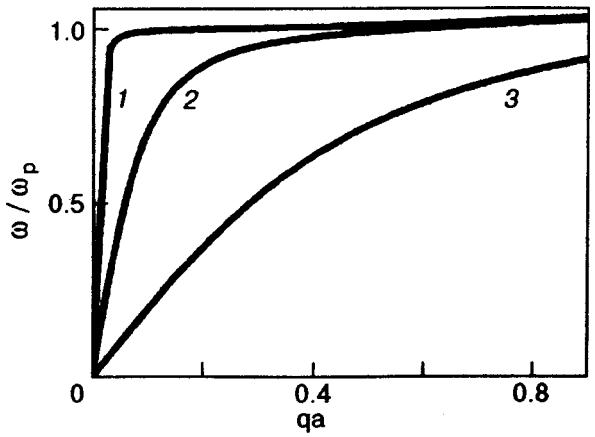

FIG. 3. The dispersion relation $\omega(qa)$ for electromagnetic waves in a layered conductor in an external magnetic field plotted as a function of the in-plane component of the wave vector q, calculated on the basis of Eq. (23) for three different values of the component parallel to the magnetic field: $ka=0.01$ (*1*); 0.1 (*2*); 0.5 (*3*). The other parameters are: $\omega_*=0.01$, $\Omega/\omega_p=0.001$, $\nu=0$, and $n_0=1$.

This equation differs from (26) in the terms containing $\tilde{q}^2$. The latter is defined by the relation

$$\tilde{q} = \frac{qa}{n_0\omega_*\Omega_*}. \tag{55}$$

The $\tilde{q}^2$ terms make the dispersion relation be cubic in powers of X [in constrast with the quadratic equation (23)] so that when $\nu \neq 0$, it can be solved only in linear on $\nu/\Omega \ll 1$ approximation. The result is

$$\mathrm{Re}\,\omega = \frac{\Omega \sin^2(ka/2)}{(\omega_*/2)^2+\sin^2(ka/2)}\,\beta^{1/2}, \tag{56}$$

$$\mathrm{Im}\,\omega = \frac{\nu \sin^2(ka/2)}{(\omega_*/2)^2+\sin^2(ka/2)} - \frac{\nu}{2\beta}\,\tilde{q}^2 A, \tag{57}$$

where

$$\beta = 1+A(1+A)\tilde{q}^2. \tag{58}$$

These equations give corrections to the dispersion relation and damping of helicons given by Eqs. (23) and (29) due to the small terms proportional to the parameter,

$$\tilde{q}^2 A = \left(\frac{qa}{n_0\Omega_* 2\sin(ka/2)}\right)^2 \ll 1. \tag{59}$$

The numerical calculations of the dependence $\omega(q)$, obtained for different values of the parameter ka both in propagating $(q_\omega a)^2<0$ and in nonpropagating $(q_\omega a)^2>0$ sectors, are shown in Fig. 3.

6. SUMMARY AND DISCUSSION

We have considered the electromagnetic waves propagating in a stack of conducting layers embedded into a dielectric matrix in the presence of an external magnetic field perpendicular to the layers. We ignored in our model the interlayer electron hopping and do not imply either periodicity in the layer stacking or uniformity of the dielectric constant across the layers. The latter distinguishes our approach,

which is based on Eqs. (10) and those for the Green's functions [Eqs. (12) and (13)], from those presented in the preceding papers on this subject.[22,23] As a first step toward the studies of the electromagnetic waves with the help of the equations which we obtained, we have considered the case of the bulk modes in the regular and uniform layered conductors and superlattices.

The fundamental quantity which determines the specific form of the electromagnetic wave dispersion is the conductivity tensor of a two-dimensional layer in a perpendicular magnetic field. We took $\sigma_{\alpha\beta}$ in the Drude-like form (20)–(22), which yields in the case $qa=0$ the well-known helicons that propagate along the magnetic field in layered conductors.[22] Our new finding here is the expression for damping of these helicons, given by Eq. (29). It is shown that Im $\omega(k)$ is proportional to the Landau level broadening ν and is independent of H, so that the ratio (31) of the wave damping to its frequency equals ν/Ω and is independent of the wave vector k. The dispersion and damping of helicons under the conventional Hall effect regime are shown in Fig. 1. The corrections to the dispersion relation and damping of helicons due to the deviation of the wave vector from the field direction (i.e., a small portion of the components which are parallel to the layers, $qa \ll 1$) are given by Eqs. (56) and (57).

The helicons in a highly doped InAs-GaSb artificial superlattice with a two-dimensional electron gas have been observed in Ref. 29 and it is tempting to try to search for them in the high-T_c layered cuprates. At first sight, Tl- or Bi-based layered cuprates seem to satisfy well our model because of the high anisotropy and low conductivity across the layers in the normal state. Unfortunately, these strongly correlated systems display a very high broadening $\nu \simeq \omega$ (Ref. 37), which means that their damping Im $\omega(k) \approx \nu \simeq \Omega$ is of the same order of magnitude as the wave frequency Re $\omega(k) \simeq \Omega$.

Helicons in the QHE regime in superlattices have been studied extensively theoretically.[24–26] The experimental grounds for this are given by the observation of QHE in some artificial superlattices[29] and layered crystals.[30,31] The QHE in organic conductors remains so far unresolved theoretically.[36]

Of all the studies of the helicons in the QHE regime in superlattices, only the paper of Vagner and Bergman[26] takes into account that at radio-frequencies Im σ_{xx}, given by Eq. (32), is nonzero. They used a model with the Kronig-Penney-like dispersion relation for the electromagnetic waves across the layers and obtained for $ka \ll 1$ the result (39), which is a particular limiting case of our more general expression for the helicon dispersion at arbitrary wave vector ka (38). In addition to the low-frequency mode, $\omega_-(ka)$, we found a high-frequency mode, $\omega_+(ka)$ (40) and showed that both modes can propagate without damping only if $k<k^*$. The threshold wave vector depends on the magnetic field H and is given by Eq. (41). The dispersion and damping of helicons under the QHE regime are shown in Fig. 2.

We also have shown that the waves propagating along the layers have frequencies [given by Eq. (45)] of the order of the plasma frequency ω_p, and we have calculated both analytically [Eqs. (47) and (48)] and numerically (see Fig. 3) their dispersion relations for different values of k and q. For $k \neq 0$ these modes may be considered as a mixture of helicons and plasmons, since their frequency $\omega \approx \Omega$ for $qa \ll 1$ [see the Eqs. (49) and (50)]. The dispersion shown in Fig. 3 is qualitatively similar to that found in Ref. 39 for the coupled hole-like and electron-like two-dimensional magnetoplasmons in a semiconductor-insulator structure with metallized surfaces in the presence of a magnetic field perpendicular to the layers.

In summary, we would like to stress that there is no way to consider all the possibilities of the dispersion relations (10) and (19) in one article. In particular, we leave for the following separate publication our results obtained, together with A. M. Ermolaev, on the magnetoimpurity modes in the layered conductors considered above. Studies of the surface modes in the system in question also will be published elsewhere.

We wish to thank A. M. Ermolaev for reading the manuscript and for valuable discussions.

*)E-mail: vladimir.m.gvozdikov@univer.kharkov.ua

[1] E. A. Kaner and V. G. Skobov, Adv. Phys. **17**, 605 (1968).
[2] A. A. Abrikosov, *Fundamentals of the Theory of Metals*, North-Holland, Amsterdam (1998).
[3] O. V. Konstantinov and V. I. Perel, Sov. Phys. JETP **38**, 161 (1960).
[4] E. A. Kaner and V. G. Skobov, Sov. Phys. JETP **45**, 610 (1963).
[5] M. S. Khaikin, L. A. Falkovskii, V. S. Edelman, and R. T. Mina, Sov. Phys. JETP **45**, 1704 (1963).
[6] E. A. Kaner and V. G. Skobov, Sov. Phys. Solid State **6**, 1104 (1964).
[7] E. A. Kaner and N. M. Makarov, Sov. Phys. JETP **58**, 1972 (1970).
[8] E. A. Kaner and A. M. Ermolaev, JETP Lett. **44**, 391 (1986).
[9] E. A. Kaner and A. M. Ermolaev, Sov. Phys. JETP **92**, 2245 (1987).
[10] F. G. Bass, A. A. Bulgakov, and A. P. Tetervov, *High-frequency Properties of Semiconducting Superlattices*, Nauka, Moskow (1969) (in Russian).
[11] A. L. Fetter Ann. Phys. **88**, 1 (1974).
[12] J. F. Giuliani and J. J. Quinn, Phys. Rev. Lett. **51**, 919 (1963).
[13] J. Yang and C. D. Gong, Phys. Lett. A **128**, 196 (1988).
[14] V. M. Gvozdikov, Sov. J. Low Temp. Phys. **16**, 1156 (1990).
[15] W. Que and G. Kirczenov, Phys. Rev. B **36**, 6595 (1987).
[16] R. D. Klag-Smith and J. Inkson, Phys. Rev. B **36**, 6501 (1987).
[17] H. C. Oji and A. H. Mac Donald, Phys. Rev. Lett. **58**, 824 (1987).
[18] A. Griffin and A. J. Pindor, Phys. Rev. B **39**, 11503 (1989).
[19] V. M. Gvozdikov, Physica C **224**, 293 (1994).
[20] V. M. Gohfeld, M. I. Kaganov, and V. G. Peschansky, Sov. J. Low Temp. Phys. **12**, 1173 (1966).
[21] V. G. Peschansky, H. Kbeir Bek, and S. N. Savel'eva, Sov. J. Low Temp. Phys. **18**, 1012 (1992).
[22] A. Tselis and J. J. Quinn, Phys. Rev. B **29**, 3318 (1964).
[23] K. I. Golden and G. Kalman, Phys. Rev. B **52**, 14719 (1995).
[24] L. Weadler and M. I. Kaganov, Phys. Status Solidi B **142**, K63 (1987).
[25] B. N. Narahari Achar, Phys. Rev. B **37**, 10423 (1988).
[26] I. D. Vagner and D. Bergman, Phys. Rev. B **35**, 9856 (1967).
[27] *The Quantum Hall Effect*, R. E. Prange and S. Girvin (Eds.), Springer-Verlag, N.Y. (1987).
[28] F. Wilzek, *Fractional Statistics and Anyon Superconductivity*, World Scientific, Singapore (1990).
[29] H. L. Stormer, J. P. Eisensteis, A. C. Gossard, W. Wiegmann, and K. Baldwin, Phys. Rev. Lett. **56**, 85 (1986).
[30] L. P. Gor'kov, Sov. Phys. Usp. **27**, 809 (1964).
[31] P. M. Chaikin, J. Phys. (Paris) **16**, 1875 (1996).
[32] I. M. Lifshitz, M. Ya. Azbel, and M. I. Kaganov, *The Electron Theory of Metals*, Nauka, Moscow (1973).
[33] B. Rosenstein and I. D. Vagner, J. Phys.: Condens. Matter **2**, 497 (1990).

[34] V. G. Peschanskii, Zh. Éksp. Teor. Fiz. **114**, 676 (1996) [JETP **87**, 369 (1998)].
[35] V. M. Gohfel'd and V. G. Peschanskii, Ukr. Fiz. Zh. **37**, 1595 (1992).
[36] T. Ando, A. B. Fowler, and F. Stern, Rev. Mod. Phys. **54**, 437 (1962).
[37] J. Ruvalds, Supercond. Sci. Technol. **9**, 905 (1996).
[38] A. S. Rochavsky, Synth. Met. **70** 1019 (1995).
[39] M. S. Kushwaha, Phys. Rev. B **35**, 3871 (1967).

This article was published in English in the original Russian journal. It was edited by S. J. Amoretty.

Proximity phenomena in double-barrier structure NbZr/NbO_x/Al/AlO_y/NbZr

A. Plecenik, Š. Gaži, M. Zuzčak, and Š. Beňačka

Institute of Electrical Engineering, Slovak Academy of Sciences, Dubrevska cesta 9, 84239 Bratislava, Slovak Republic

V. Shaternik and E. Rudenko

*Institute for Metal Physics, National Academy of Sciences of Ukraine, 36 Vernadsky Str., 252142 Kiev, Ukraine**)

(Submitted February 1, 1999; revised March 19, 1999)
Fiz. Nizk. Temp. **25**, 1082–1086 (October 1999)

A tunneling structure NbZr/NbO_x/Al/AlO_y/NbZr with a thin barrier in the NbZr/NbO_x/Al junction and 4 to 6-nm-thick Al interlayer was prepared and studied experimentally. A proximity effect between NbZr and Al through NbO_x barrier has been observed. An electrical voltage was generated in the NbO_x barrier and a coexistence of the proximity effect and applied voltage in the junction NbZr/NbO_x/Al has been observed. This experiment could be described on the basis of a model for coherent charge transport in superconducting/normal proximity structures.
 [S1063-777X(99)01310-9]

1. INTRODUCTION

Tunneling process permits to obtain information on the superconducting density of states (DOS) over a wide energy range with high-energy resolution, both for superconductors in the equilibrium state and for those in the nonequilibrium state. The proximity effect between a superconductor and normal metal has been discussed for a long time, and it has recently attracted new attention because of the dramatic progress in nanotechnology, which allows the fabrication and study of metallic structures in the mesoscopic regime.[1] The electron transport in normal diffusive conductors in the presence of proximity-induced superconducting correlation was studied theoretically in Ref. 2. It was demonstrated in Ref. 2 that superconducting correlations and electrical field can penetrate in the case of transparent barriers, causing a whole range of novel nonequilibrium effects. In this paper we report on the observation of the coexistence of proximity-induced superconducting correlation and electric field.

2. EXPERIMENTAL

Superconducting thin films were deposited by dc magnetron sputtering from Nb target with admixture of Zr, and clean target of Al. After the deposition of 100-nm-thick NbZr film ($T_c = 12$ K) the first tunneling barrier (NbO_x) was prepared in two technological steps. At first, the thermal oxidation of NbZr in O_2 at room temperature was provided and then the tunneling barrier was prepared by rf sputter-oxidation in Ar and residual gas for about 10 min. In this step thin, dirty NbZr layer, implanted by O_2 at energies 250–500 eV, was prepared. Specific contact resistance R of this junction is smaller in order of magnitude than that of the top tunnel junction (Al/AlO_y/NbZr) resistance. After this procedure thin Al layer was deposited by dc sputtering at a deposition rate of 100 nm/min at 2 Pa of Ar. Then the thermal oxidation of Al was carried out at room temperature at 100 Pa for 60 min. After pumping of the vacuum system, the top layer of NbZr was deposited at 2 Pa with the deposition rate 160 nm/min. The top layer was deposited on a cooled substrate holder at about 10 °C.

This technology provides nonsymmetrical operation of the double-barrier tunnel structure. The $I-V$ characteristics of the structure are shown in Figs. 1–3 for various temperatures.

3. DISCUSSION

We have investigated a superconducting tunnel junction with two potential barriers like as NbO_x and AlO_y. One can see in Fig. 1 (curve *1* the presence of a Josephson current (the $I-V$ curve from p.0 to p.1) that flows through the double barriers. The NbO_x barrier resistance R is smaller in order than that of the AlO_y barrier. It is assumed that the AlO_y barrier limits the Josephson critical current through the double junctions, but for the NbO_x barrier the Josephson critical current must be higher than that for the AlO_y barrier. In the experiment the same current flows through both barriers simultaneously; at small current (to point 5) a voltage in the NbO_x barrier does not exist. One can see from point 1 to point 5 that the measured $I-V$ curve is a characteristic of a superconducting tunnel junction. For example, the proximity model[3,4] of NbZr/NbO_x/Pb and of NbN/NbO_x/Pb tunnel junctions, fabricated using similar technology, with the exception of thermal oxidation instead of rf-oxidation, shows good agreement between the calculated and experimentally determined values of the proximity layer. Now we can measure the current step voltage on the junction (for example, point 2 or point 3 on the $I-V$ curve) and estimate the value of the proximity energy gap of Al. We conclude that the Al proximity energy gap value is approximately equal to $\Delta_{Al}^{Pr} \approx 1.2-1.3$ meV at $T = 4.2$ K.

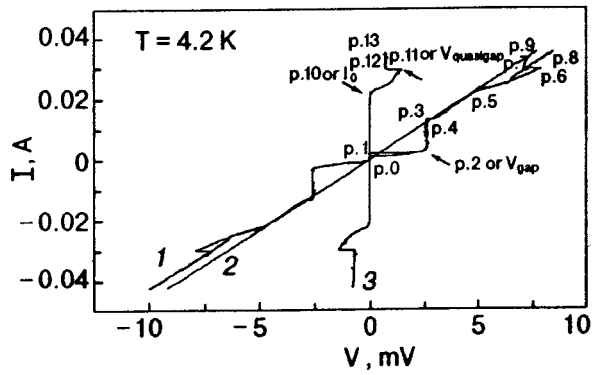

FIG. 1. The $I-V$ curves of the double-barrier structure $NbZr/NbO_x/Al/AlO_y/NbZr$.

The nature of this gap is in the proximity effect between the NbZr and Al through the NbO_x barrier. Also in the experiment the Δ_{Al}^{Pr} values change slightly because the Al film has a nonequilibrium quasiparticle distribution function induced by the current through the AlO_y barrier upon increasing the voltage on this barrier.

We see that the $I-V$ curve is linear from point 4 to point 5. This part of the $I-V$ curve can be fitted by a linear function like $I=4.6\,V$; this fitted curve is shown as curve *2*. At point 5, there is voltage also on the NbO_x barrier. At this point the current attains values of the critical current for the NbO_x barrier. Let us now analyze the $I-V$ curve as the ''sum'' of the two $I-V$ curves for the two junctions, because from this point the measured voltage is the sum of the voltage on the AlO_y barrier and the voltage on the NbO_x barrier. We believe that between point 5 and point 9 the voltage on the AlO_y barrier can be calculated by using the fitted curve *2* and corresponding value of the current through the junctions, $V_{AlO_y}=I/4.6$. We then calculate the voltage on the NbO_x barrier as $V_{NbO_x}=V-V_{AlO_y}$ and we plot the graph of the $I-V$ curve for the $NbZr/NbO_x/Al$ junction using the corresponding values of I and V_{NbO_x} (see curve *3* in Figs. 1–3).

We see that above point 5 there is voltage on the NbO_x barrier, and simultaneously the nature of the Al-''gap'' is the proximity effect between NbZr and Al through the same

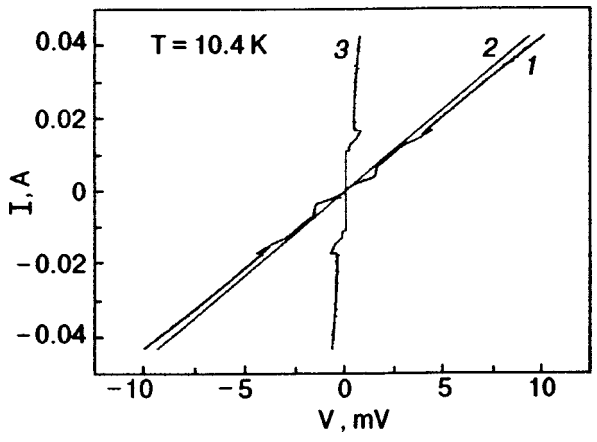

FIG. 2. The $I-V$ curves of the double-barrier structure $NbZr/NbO_y/Al/AlO_x/NbZr$.

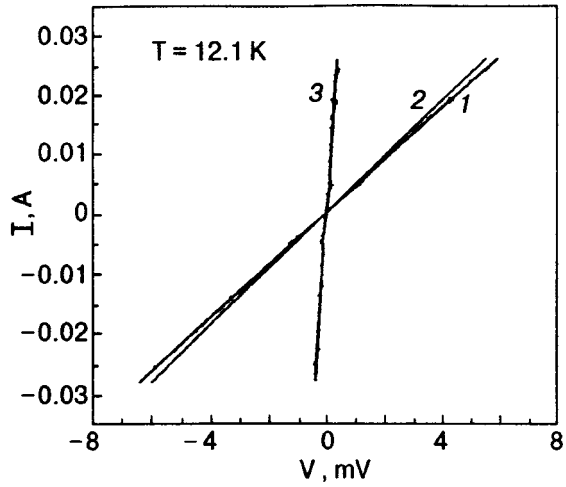

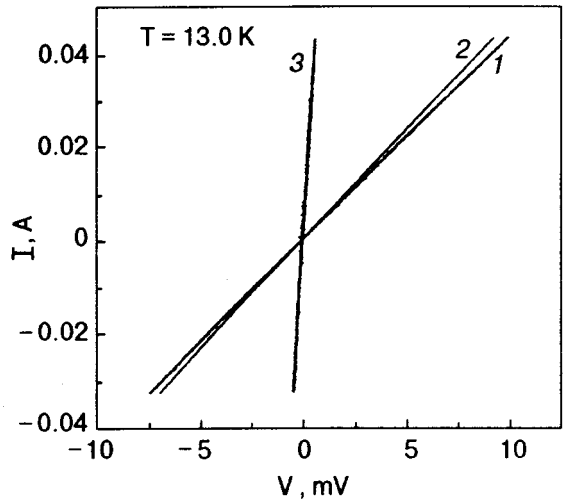

FIG. 3. The $I-V$ curves of the double-barrier structure $NbZr/NbO_x/Al/AlO_y/NbZr$.

NbO_x barrier. We believe that this very complicated situation could be analyzed on the basis of the new theory for coherent charge transport in superconducting/normal proximity structures.[2]

The $I-V$ curves were measured in the range of temperatures T from 4.2 to 13 K (see Figs. 1–3). Since at $T>T_c^{NbZr}$ the $I-V$ curve is linear (see Fig. 3), NbZr and Al are in the normal state, and the large voltage does not exist on the NbO_x barrier. When $T>T_c^{NbZr}$, the voltage on the normal Al and NbO_x barrier is negligible.

Recall that unusual quasi-superconducting state exists in Al; we will compare the measured $I-V$ curves with the $I-V$ curves of the superconducting Josephson junctions. The constriction model for SNS Josephson junctions is well known. In this model the approach developed by Blonder, Tinkham, and Klapwijk (BTK) for calculation of the quasiparticle (qp) current in NcS contacts is generalized to the case of ScNS and SNcNS contacts with disordered NS electrodes. The relation between the qp current and the energy spectrum of NS proximity sandwich is found for arbitrary transparencies of the constriction and NS interfaces. We have plotted for

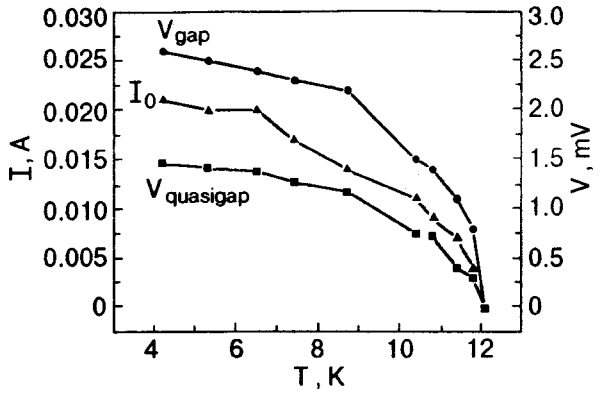

FIG. 4. The dependences of the critical current I_0, V_{gap}, V_{quasigap} on temperature.

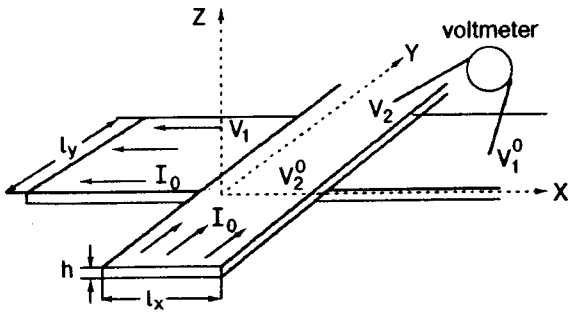

FIG. 5. Measured tunnel junction scheme.

$NbZr/NbO_x/Al$ junction the temperature dependence of the critical current (point 10 on curve *3* in Figs. 1–3) (see Fig. 4). Our curve, like curve *2* in Fig. 2 (Ref. 5), is a case for ScNS or SNcNS with $d_N/\xi_N=1$, $\gamma_B=1$, and $\gamma=0$ ($\gamma_B=R_B/\rho_n\xi_n$, $\gamma=\rho_s\xi_s/\rho_n\xi_n$; here γ is a measure of the strength of the proximity effect between the S and N metals, and γ_B describes the effect of the boundary transparency between these layers; $\rho_{n,s}$ and $\xi_{n,s}$ are the normal state resistivities and coherence lengths, and R_B is the product of the resistance of the NS boundary and its area[5]). We can therefore assume that the Nb/Al interface is a series of constrictions in otherwise lower transparent barrier.

From point 10 to point 13 the $I-V$ curve is like an $I-V$ curve for a tunnel Josephson junction. With such shape the $I-V$ curves are described in Ref. 6 for the stacked Josephson tunnel junctions $Nb/Al-AlO_y/Nb$ of overlap geometry. This kind of $I-V$ curve can exist if the Al is in a quasisuperconducting state, but it cannot exist in the other cases.

We have plotted for the $NbZr/NbO_x/Al$ junction the dependence of voltage at point 11 V_{quasigap} on the temperature (see Fig. 4). Also shown in this figure for comparison is a plotted dependence of the voltage at point 2 or V_{gap} on the temperature.

We see that at $T=4.2$ K the Al has a proximity-effect-induced energy gap of about 1.2 meV, so the proximity effect is large enough through the NbZr/Al interface. In the first case the same current (NbZr is in the nonsuperconducting state) cannot produce the measured voltage on the NbO_x barrier, but in the second case (NbZr is in superconducting state) it can produce the measured voltage on the NbO_x barrier; at this applied voltage the behavior of the $NbZr/NbO_x/Al$ junction is similar to that of the tunnel SIS junction.

We assume that this result can be interpreted on the basis of the model[2] for coherent charge transport in superconducting/normal proximity structures at least qualitatively. We also assume that our experiment demonstrates the presence of a soft (no sharp edge) pseudo gap in the density of states for Al, as shown in the model.[2]

We have measured the complex junctions with nonuniform order parameter Δ in the electrodes to estimate the possibility of the influence of the electrode resistive (nonsuperconducting) state on the junction $I-V$ curves. The junction geometry is shown in Fig. 5. The voltmeter measures the voltage $(V_2-V_1^0)$. But potentials V_1 and V_2 could be functions of the coordinate x and y just as $V_1(x,y)$ and $V_2(x,y)$. We can describe the junction $I-V$ curve as follows:

$$I=f_1(V_2-V_1) \tag{1}$$

or

$$V_2-V_1=f_1^+(I). \tag{2}$$

If the voltage (V_2-V_1) is applied, then the current I flows through the tunnel junction with unit square. We can describe the electrode $I-V$ curve as follows:

$$I=f_2(V_{22}-V_{21}) \tag{3}$$

or

$$V_{22}-V_{21}=f_2^+(I). \tag{4}$$

If the voltage $(V_{22}-V_{21})$ is applied per unit length of the electrode film, then the current I flows through the electrode film with unit square of cross section (V_{22} and V_{21} are the potentials at point 2 and point 1 of the film 2, respectively). We can express the current through the tunnel junction at the point with the coordinates (x, y) as follows:

$$dI=f_1(V_2-V_1)dx\,dy, \tag{5}$$

$$I_0=\int dI=\int_0^{l_x}\int_0^{l_y} f_1(V_2-V_1)dx\,dy. \tag{6}$$

Let us consider an imaginary strip (with the coordinate x) which is parallel to the Y axis. We can estimate the potential V_2 distribution in this strip. Because we use a current source for measurements, the current and voltage at the beginning of the strip are

$$I=\frac{I_0}{hl_x}\,h\,dx=\frac{I_0}{l_x}\,dx, \tag{7}$$

$$dV_2=V_2^0-V_{21}=f_2^+\left(\frac{I_0}{I_x h}\right)dy. \tag{8}$$

We then have

$$I=\frac{I_0}{I_x}\,dx-I_{\text{junc}}; \tag{9}$$

$$I_{\text{junc}}=\int_0^y f_1(V_2-V_1)dy\,dx; \tag{10}$$

$$V_2-V_2^0=\int_0^y f_2^+\left[\frac{I_0}{l_xh}-\frac{1}{h}\int_0^y f_1(V_2-V_1)dy\right]dy. \tag{11}$$

We also have

$$V_1-V_{1l_x}=\int_{l_x}^x f_2^+\left[\frac{1}{h}\int_{l_x}^x f_1(V_2-V_1)dx\right]dx. \tag{12}$$

We can use the equivalent equations for (11) and (12)

$$\begin{cases}\dfrac{\partial V_1}{\partial y}=f_2^+\left[\dfrac{1}{h}\displaystyle\int_0^y f_1(V_2-V_1)dy\right];\\ \dfrac{\partial V_1}{\partial x}=f_2^+\left[\dfrac{1}{h}\displaystyle\int_{l_x}^x f_1(V_2-V_1)dx\right];\\ \dfrac{\partial V_2}{\partial y}=f_2^+\left[\dfrac{I_0}{l_xh}-\dfrac{1}{h}\displaystyle\int_0^y f_1(V_2-V_1)dy\right];\\ \dfrac{\partial V_2}{\partial x}=f_2^+\left[\dfrac{I_0}{l_xh}-\dfrac{1}{h}\displaystyle\int_{l_x}^x f_1(V_2-V_1)dx\right].\end{cases} \tag{13}$$

We use the function f_2^+ as follows:

$$\begin{cases}V_{22}-V_{21}=0, & \text{if} \quad I\leqslant\dfrac{I_c}{l_xh};\\ V_{22}-V_{21}=b\left(I-\dfrac{I_c}{l_xh}\right), & \text{if} \quad I>\dfrac{I_c}{l_xh}.\end{cases} \tag{14}$$

Then

$$\begin{cases}\dfrac{1}{b}\dfrac{\partial^2V_2}{\partial y^2}=-\dfrac{1}{h}f_1(V_2-V_1);\\ \dfrac{1}{b}\dfrac{\partial^2V_2}{\partial x^2}=-\dfrac{1}{h}f_1(V_2-V_1);\\ \dfrac{1}{b}\dfrac{\partial^2V_1}{\partial y^2}=\dfrac{1}{h}f_1(V_2-V_1);\\ \dfrac{1}{b}\dfrac{\partial^2V_1}{\partial x^2}=\dfrac{1}{h}f_1(V_2-V_1).\end{cases} \tag{15}$$

Here b is the differential resistance of the strip in the resistive (nonsuperconducting) state.

Since we used a current source in the measurement, we have a standard wave equation with the initial conditions

$$\frac{\partial^2V_2}{\partial x^2}-\frac{\partial^2V_2}{\partial y^2}=0; \tag{16}$$

$$V_2(x,0)=V_2^0; \tag{17}$$

$$\left.\frac{\partial V_2}{\partial y}\right|_{y=0}=\frac{bI_0}{l_xh}-\frac{bl_c}{l_xh}. \tag{18}$$

We can therefore use the Dalamber decision of the one-dimentional wave equation in partial derivatives:[7]

$$V_2-V_1^0=V_2^0-V_1^0, \quad \text{if} \quad I\leqslant\frac{I_c}{l_xh};$$

$$V_2-V_1^0=V_2^0+\frac{b(I_0-I_c)l_y}{l_xh}-V_1^0, \quad \text{if} \quad I>\frac{I_c}{l_xh}. \tag{19}$$

In the experiment described above we have not observed this kind of additional voltage as in formula (19). At 12.1 K and 13.0 K we found that the superconducting state of the electrodes does not exist (using the $I-V$ curve of the tunnel junction with AlO_y barrier) and we have the $I-V$ curve for the double junction in this case (see Fig. 3). It is clear that the additional voltage caused by the resistive state in part of the electrode of the investigated junctions can have only a small value as in the $I-V$ curves (Fig. 3), and that the observed additional voltage on the $NbZr/NbO_x/Al$ junction cannot be attributed to this factor.

4. CONCLUSIONS

We have prepared and experimentally investigated the tunneling structure $NbZr/NbO_x/Al/AlO_y/NbZr$ with a transparent barrier in the $NbZr/NbO_x/Al$ junction and 4 to 6-nm-thick Al interlayer. In this structure a proximity effect between NbZr and Al through NbO_x barrier has been observed. The voltage on the NbO_x barrier was produced, and we have observed a coexistence of the proximity effect and applied voltage on the junction $NbZr/NbO_x/Al$. We believe that this experiment could be described on the basis of the model for coherent charge transport in superconducting/normal proximity structures.[2]

*)E-mail: shat@d24.imp.kiev.ua

[1] F. K. Wilhelm, A. D. Zaikin, and G. Schön, J. Low Temp. Phys. **106**, 305 (1997).
[2] F. K. Wilhelm, A. D. Zaikin, and A. A. Golubov, J. Low Temp. Phys. **106**, 297 (1997).
[3] H. J. Köhler, P. Seidel, P. Weber, K. Blüthner, S. Linke, and K. H. Berthel, Phys. Status. Solidi **67**, 497 (1981).
[4] V. M. Pan, E. M. Rudenko, V. P. Gorishayak, M. V. Belous, S. A. Kociychuk, Ph. I. Korzhinsky, and V. E. Shaternik, Cryogenics **23**, 258 (1983).
[5] A. A. Golubov, V. M. Krasnov, and M. Yu. Kupriyanov, J. Low Temp. Phys. **106**, 249 (1997).
[6] N. Thyssen, A. V. Ustinov, and H. Köhlstedt, J. Low Temp. Phys. **106**, 201 (1997).
[7] G. A. Kora and T. M. Kora, *Mathematical Handbook for Scientists and Engineers*, McGraw-Hill Book Company (1968), p. 831.

This article was published in English in the original Russian journal. It was edited by S. J. Amoretty.

PHYSICAL PROPERTIES OF CRYOCRYSTALS

Diffusion of hydrogen in rare gas solids: neutral H atoms and H^+ protons

M. Beyer, E. V. Savchenko,*) G. Niedner-Schatteburg, and V. E. Bondybey

*Institut für Physikalische und Theoretische Chemie, Technische Universität München, Lichtenbergstraße 4, 85747 Garching, Germany***)

(Submitted March 12, 1999)
Fiz. Nizk. Temp. **25**, 1087–1091 (October 1999)

In this letter we review and compare the available information about the stability and spectroscopy of the hydrogen atoms and protons in rare-gas solids. Mechanism of the H^+ diffusion involving protonated rare-gas dimer Rg_2H^+ formation in the lattice is discussed. We suggest that the puzzling differences in their behavior and the stability are due to the fact that diffusion of hydrogen atoms is thermally activated, while that of the protons is activated by vibrational excitation of the Rg_2H^+ under ambient temperature blackbody radiation. © *1999 American Institute of Physics.* [S1063-777X(99)01410-3]

Diffusion in solids is of fundamental interest from the purely academic point of view and it is also important in nature and in numerous industrial situations and processes. While molecular species in solid matrices at low temperatures are usually stable, and can be maintained isolated for indefinite periods, some atoms exhibit even below 10 K a considerable degree of mobility.[1,2] Rare-gas solids, with their well-known potentials[3] and well-defined structures thus represent a very suitable model system for studying diffusion. Particularly interesting is the mobility of the lightest and most abundant atom of them all—the hydrogen atom. Atomic hydrogen can, in fact, exist in the host at least in two varieties—as neutral atoms[4–12] and as charged protons,[13–18] and both of them have been studied in-depth spectroscopically.

Neutral hydrogen atoms are easily detected either by their ESR spectra[4] or by optical UV spectroscopy,[5,6,9,11,12] and can occur in matrices in several distinct sites.[4,19] Protons in rare gases are tightly solvated by two rare-gas atoms that form well-defined Rg_2H^+ cations.[20] Both states, neutral and charged, have been investigated by many researchers, and it is well known that under suitable conditions both forms can be mobilized, and their depletion due to diffusion can be followed spectroscopically.[8,9,11,12,16,17] Somewhat surprisingly, not only the weakly interacting neutral atoms, but also the strongly bound protons can be quite easily destroyed by diffusion.[16,17] Examination of the available data reveals, however, that the diffusion of the two species exhibits some very surprising differences. The purpose of the present paper is to compile and review some of the available evidence, and propose an explanation for the observed differences and unexpected trends in the behavior of neutral atoms and protons.

In an early study of matrices produced by discharging or photolysing deuterium halides infrared absorptions appearing at 645 and 607 cm^{-1} were observed in solid argon and krypton, respectively.[13] The carrier clearly involved a single deuterium atom, and the lines shifted to 907 and 851 cm^{-1} when normal hydrogen halides were substituted for the deuterides. At first, an assignment to a neutral H atom trapped in an interstitial site in the rare-gas solid was preferred, since it was not understood how ions could be produced under the conditions of some of the experiments. Later studies, however, have shown rather conclusively that the absorptions are, in fact, due to the positively charged protons,[14,15] which form strongly bound, linear centrosymmetric RgH^+Rg cations in the matrix. These are characterized by a very intense asymmetric stretching infrared absorption ν_3, accompanied by a progression of $\nu_3+n\nu_1$ combination bands.[16,21]

Neutral hydrogen atoms in rare gases were extensively studied by means of ESR spectroscopy[4] since the early days of matrix spectroscopy. These studies suggested that while in neon a single matrix site is observed, in the heavier rare gases Ar, Kr, and Xe and H atoms can be trapped in at least two different trapping sites, presumably substitutional and octahedral interstitial.[4,19] Atoms produced by dissociation with excess kinetic energy[22,23] can apparently propagate through the matrix for distances of the order of 100 Å.[10] Atoms in thermal equilibrium with the lattice, on the other hand, appear to be at the lowest temperatures indefinitely stable.[8] They can in fact be stabilized at sufficiently high concentrations for the detection of H...H spin-pair diradicals, with a distribution of internuclear distances of $r>7$ Å.[24] Besides ESR, it was recently shown that H atoms can also be detected by optical absorption and emission spectroscopy. While in the gas phase the lowest resonant transition of hydrogen atoms requires 10.2 eV (α-Lyman), in rare-gas solids the transition is shifted to much lower energies, with onsets of strong structured absorptions near 9.7, 8.0, and 6.2 eV in solid argon, krypton and xenon, respectively. Excitation of these bands by tunable synchrotron radiation results in broad and intense, strongly red-shifted emission bands.[7]

The ability to monitor hydrogen atoms and bare protons spectroscopically allows us to study their stability and diffusion as a function of temperature, and indeed numerous such

studies have been reported. Both the neutral H atoms and H^+ cations can be destroyed due to diffusion, but comparison of the two processes indicates some surprising trends and differences. Careful studies of the mobilities of hydrogen atoms produced in solid krypton and xenon by x-ray irradiation were carried out by Creuzburg and coworkers.[9,11] They found that annealing of the matrix leads to disappearance of the H atoms at a rate which is in solid xenon below 32 K unobservably slow, but changes by six orders of magnitude between 32 and 45 K, with a similar rapid rate change occurring in solid Kr between 22 and 27.5 K. The disappearance of the atoms is presumably due to radical-radical recombination, with formation of the HXeH hydride being an alternative channel in xenon.[11,25–27] From an Arrhenius plot of the data, the authors were able to deduce activation energies of 66 and 123 meV (Ref. 11) (6.4 and 11.9 kJ/mole) for the bleaching process in Kr and Xe, respectively, which they explain in terms of thermally activated diffusion. Most interestingly, they find no observable difference between the bleaching of hydrogen and deuterium atoms, a result which was recently confirmed by Vaskonen *et al.*.[12]

While no experimental values for the H^+ diffusion activation barriers are available, one might expect them to be considerably higher than those of the neutral atom. This was indeed confirmed by recent theoretical calculations, predicting a barrier of about 10 kJ/mole in solid neon, and about 30–35 kJ/mole in the heavier rare-gas solids.[20] As noted above, the asymmetric stretching absorption of the Rg_2H^+ cations allows easy monitoring of the ''matrix isolated'' protons. Rather surprisingly, despite the relatively high barriers, a rather efficient bleaching of the absorption is observed; it exhibits, however, quite different properties than the neutral hydrogen depletion.[16,17] In the first place, the Rg_2H^+ destruction does not exhibit a pronounced temperature dependence, and persists down to the lowest matrix temperatures. Furthermore, in contrast with the neutral hydrogens, whose diffusion shows no isotopic dependence, the charged protons decay up to an order of magnitude faster than the corresponding deuterons.

The fast disappearance at low temperatures could possibly be explained if one argued that not the proton diffusion but some alternative process is responsible. Since the positively charged cations are present, negatively charged centers must also be present, and these centers are usually unidentified. One might understand the bleaching if it was due to diffusion of electrons located in shallow traps. While such a process could have a very low activation energy, it cannot explain the strong hydrogen isotopic effect.[16]

We propose as one possible explanation that while the matrix may be at a low temperature of only a few kelvin, it is still invariably in the room-temperature-range (about 300 K) radiative field of the apparatus walls. This radiation might be efficiently absorbed by the very intense infrared transition and lead to the observed diffusion. The computed lowest energy path shown in Fig. 1 involves essentially a ligand-switching reaction, where the Rg_2H^+ solvated proton exchanges one of its rare-gas ligands. Stretching modes of triatomic molecules almost invariably relax via the lower frequency bending modes, and the excitation step can be

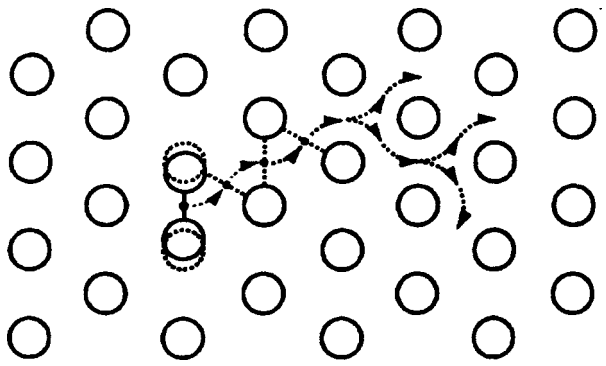

FIG. 1. Schematic diagram of proton diffusion in the host, for simplicity constrained to two dimensions. Only three rare-gas atoms are involved in each diffusion step, in which only one H^+–Rg bond needs to be rearranged. Barriers calculated in the gas phase for an Rg_3H^+ complex are given in Ref. 20 and Table I. While the proton has moved considerably in the rare-gas environment, the displacement of the rare-gas atoms involved is minor.

followed by tunneling of the vibrating proton in the excited molecule from one Rg–Rg bond to an adjacent one. The infrared absorption thus provides the energy needed to lower the activation barrier. This interpretation also helps to rationalize the strong isotopic dependence by combination of several effects: factor of 2 change in the reduced mass, with the corresponding $\sqrt{2}$ change in the vibrational frequency, the change in the overlap with the 300-K Planck curve, as shown in Fig. 2, and change of the oscillator strength due to the mass effects. Equally important may be the zero-point effects and, in particular, the effect of mass upon the tunneling process.

This observation of a process activated by blackbody radiation would not be without precedence. Like in the matrix, where the ''collision energies'' are too low to activate chemical reactions, in the high vacuum of an FT-ICR mass spectrometer collision are too infrequent for the classical Lindeman-Hinshelwood mechanism of chemical activation to be operative. We have recently shown that in such an ultrahigh environment, where at pressures of $\approx 10^{-10}$ mbar collisions are reduced to about 1 per 100 s, the absorbed blackbody radiation becomes the dominant source of activation energy.[28] Thus, for example, fragmentation of ionic wa-

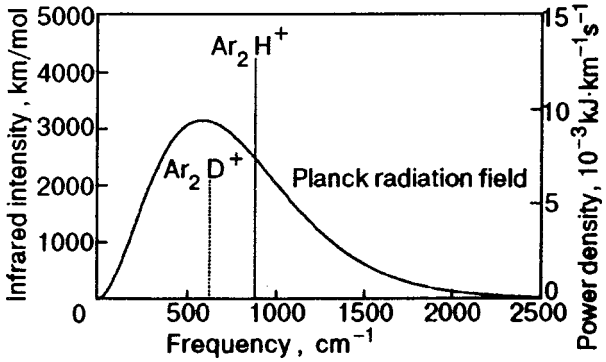

FIG. 2. Overlap of the vibrational modes of Ar_2H^+ and Ar_2D^+ with the Planck blackbody radiation field. The lower infrared intensity of the deuterated species is partly compensated by the better overlap with the radiation field.

TABLE I. Vibrational frequencies $\nu(\mathrm{cm}^{-1})$, infrared intensities $I(\nu)$(km/mole), the photon energy $E(\nu)$(kJ/mole), the absorbed power $P(\nu)$(kJ/mole·s), and the barrier for proton diffusion $E(TS)$(kJ/mole).

Ion	$0.8\nu_3$[a]	$I(\nu_3)$[a]	$E(\nu_3)$	$P(\nu_3)$	$0.8\nu_2$[a]	$I(\nu_2)$[a]	$E(\nu_2)$	$P(\nu_2)$	$P(\nu_2)+P(\nu_3)$	$E(TS)$[a]
Ne_2H^+	1329	2319	15.9	6.7	620	248	7.4	2.33	9.0	11.5
Ne_2D^+	950	1153	11.4	7.6	444	115	5.3	1.00	8.6	13.8
Ar_2H^+	878	4227	10.5	31.3	549	42	6.6	0.40	31.7	29.7
Ar_2D^+	625	2117	7.5	19.9	390	19	4.7	0.15	20.0	29.9
SECP[b]										
Ar_2H^+	950	4385	11.4	28.9	518	47	6.2	0.44	29.4	30.7
Ar_2D^+	678	2196	8.1	20.2	369	21	4.4	0.16	20.3	31.6
Kr_2H^+	857	5094	10.3	38.9	486	17	5.8	0.15	39.1	32.3
Kr_2D^+	606	2551	7.3	24.1	345	8	4.1	0.06	24.1	32.8
Xe_2H^+	758	5873	9.1	50.6	444	3	5.3	0.03	50.6	35.5
Xe_2D^+	537	2941	6.4	27.6	314	1	3.8	0.01	27.6	35.9

[a]The values for protonated species were taken from Ref. 20; for deuterated species from this work.
[b]The values above the horizontal line were computed considering all electrons explicitly. The computations below the divider were carried out using for the heavier rare-gas atoms the quasi-relativistic effective core potentials of the Stuttgart/Dresden group.[35]

ter clusters, as well as a variety of chemical reactions within the clusters, like hydrogen formation[29–32] or aldol condensation,[33] are activated by blackbody radiation. In addition, a whole range of other processes in low-temperature rare-gas solids, where collisional activation is in view of the low temperatures of 5–20 K, inefficient processes, such as isomerization and structural rearrangements, are known to be efficiently activated by infrared absorption.

To estimate the amount of energy absorbed by the ions, we have used the infrared frequencies ν and line intensities $I(\nu)$ of Rg_2H^+ species from our previous paper,[20] and for the purpose of this work we have calculated the values for deuterated Rg_2D^+ species on the same level of theory (B3LYP in Gaussian-94; [Ref. 34]). For the calculation of the power absorbed from blackbody radiation, the frequencies are multiplied with a scaling factor of 0.8 to account for the strong matrix shift.[20]

The power absorbed by these modes from 298-K blackbody radiation can be calculated from the Planck distribution, taking into account that half of the 4π steric angle around the molecule is occupied by the low-temperature mirror on which the host is deposited, reducing the steric angle of radiation to 2π. With ν in cm^{-1}, this amounts to

$$P(\nu,I,T)=\frac{4\pi hc^2\nu^3 I\cdot 10^6}{\exp(100ch\nu/kT)-1}.$$

The vibrational frequencies, infrared intensities, the photon energy and the power absorbed by the vibrational modes are listed in Table I, together with the activation barrier for proton diffusion. Examination of the data for Ne_2H^+ reveals that absorbtion of a single ν_3 photon is sufficient to overcome the diffusion barrier, and that about 0.4 of these photons are absorbed by each Ne_2H^+ site per second, which might account for the fact that the H^+ protons were thus far not observed in solid neon. The proton activated by the absorption of room-temperature blackbody radiation may acquire in solid neon a considerable mobility, and find an electron or an anion for recombination or a neutral molecule for reactions within a few seconds. Among possible ''sinks'' for H^+ could be the formation of H_2^+ or H_3^+ molecular ions.[36]

The situation is a little more complicated in solid Ar, Kr, and Xe, where the ν_3 photon energy is considerably lower than the computed H^+ activation energy, and where the H^+ ions have been studied experimentally. Even though in the heavier hosts the absorbed power is higher, amounting to about 3–5 photons/(ion·s) due to higher oscillator strength, multiphoton processes are quite unlikely to be important in overcoming the barrier. Here, however, the absorptions due to the $\nu_3+n\nu_1$ combination bands might be a contributing factor. It is also possible that the actual barrier in the bulk may be lower than that computed for Rg_nH^+ clusters with $n=3$, and, as suggested by the strong isotopic dependence, tunneling through the barrier may very well be involved.

The proposed infrared activation would thus be essentially consistent with the observations: bulk matrix temperature independence, and a strong isotopic effect of the proton absorption bleaching. A similar mechanism would not work for neutral hydrogen atoms, whose vibrational modes lie at considerably lower frequencies, and whose infrared absorptions are surely many orders of magnitude weaker than those of H^+ in the complex Rg_2H^+.

The authors would like to thank Markku Räsänen for a helpful discussion and valuable comments. Financial support by the Deutsche Forschungsgemeinschaft through the SFB 377: *Photoionisation und Ladungstrennung in großen Molekülen, Clustern und in kondensierter Phase*, and the Fonds der Chemischen Industrie is gratefully acknowledged. E.V.S. gratefully acknowledges BMBF travel funds.

*)Permanent address: B. Verkin Institute for Low Temperature Physics and Engineering, National Academy of Sciences of Ukraine, 47 Lenin Ave., 310164 Kharkov, Ukraine.
**)E-mail: bondybey@ch.tum.de

[1]W. C. Easley and W. Weltner, Jr., J. Chem. Phys. **52**, 197 (1970).
[2]E. T. Ryan and E. Weitz, J. Chem. Phys. **99**, 1004 (1993).
[3]H. H. von Grünberg and H. Gabriel, Chem. Phys. Lett. **192**, 503 (1992).
[4]S. N. Foner, E. L. Cochran, V. A. Bowers, and C. K. Jen, J. Chem. Phys. **32**, 963 (1960).

[5] M. Creuzburg, F. Koch, and F. Wittl, Chin. Phys. Lasers **156**, 387 (1989).
[6] M. Creuzburg and F. Wittl, J. Mol. Struct. **222**, 127 (1990).
[7] M. Krass and P. Gürtler, Chin. Phys. Lasers **174**, 396 (1990).
[8] D. LaBrake and E. Weitz, Chin. Phys. Lasers **211**, 430 (1993).
[9] F. Wittl, J. Eberlein, T. Epple, M. Dechant, and M. Creuzburg, J. Chem. Phys. **98**, 9554 (1993).
[10] D. LaBrake, E. T. Ryan, and E. Weitz, J. Chem. Phys. **102**, 4112 (1995).
[11] J. Eberlein and M. Creuzburg, J. Chem. Phys. **106**, 2188 (1997).
[12] K. Vaskonen, J. Eloranta, T. Kiljunen, and H. Kunttu, J. Chem. Phys. **110**, 2122 (1999).
[13] V. E. Bondybey and G. C. Pimentel, J. Chem. Phys. **56**, 3832 (1972).
[14] D. E. Milligan and M. E. Jacox, J. Mol. Spectrosc. **46**, 460 (1973).
[15] C. A. Wight, B. S. Ault, and L. Andrews, J. Chem. Phys. **65**, 1244 (1976).
[16] H. Kunttu, J. Seetula, M. Räsänen, and V. A. Apkarian J. Chem. Phys. **96**, 5630 (1992).
[17] H. M. Kunttu and J. A. Seetula, Chem. Phys. **180**, 273 (1994).
[18] T. D. Fridgen and J. M. Parsia, J. Chem. Phys. **140**, 2155 (1998).
[19] F. J. Adrian, J. Chem. Phys. **32**, 972 (1960).
[20] M. Beyer, A. Lammers, E. V. Savchenko, G. Niedner-Schatteburg, and V. E. Bondybey, Phys. Chem. Chem. Phys. **1**, 2213 (1999).
[21] J. Nieminen, E. Kauppl, J. Lundell, and H. Kusttu, J. Chem. Phys. **96**, 8696 (1993).
[22] F. Magnotta, D. J. Nesbitt, and S. R. Leone, Chem. Phys. Lett. **83**, 21 (1981).
[23] G. W. Flynn and R. E. Weston, Jr., Annu. Rev. Phys. Chem. **37**, 551 (1986).
[24] L. B. Knight, Jr., W. E. Rice, L. Moore, E. R. Davidson, and R. S. Dailey, J. Chem. Phys. **100**, 1409 (1998).
[25] M. Pettersson, J. Lundell, and M. Räsänen J. Chem. Phys. **108**, 205 (1995).
[26] V. I. Feldman, F. F. Sukhov, and A. Y. Orlov, Chem. Phys. Lett. **290**, 507 (1997).
[27] M. Pettersson, J. Lundell, and M. Räsänen *Eur. J. Inorg. Chem.* (in print).
[28] T. Schindler, C. Berg, G. Niedner-Schatteburg, and V. E. Bondybey, Chin. Phys. Lasers **250**, 301 (1996).
[29] M. Beyer, C. Berg, H. W. Görlitzer, T. Schindler, U. Achatz, G. Albert, G. Niedner-Schatteburg, and V. E. Bondybey, J. Am. Chem. Soc. **118**, 7366 (1996).
[30] C. Berg, U. Achatz, M. Beyer, S. Joos, G. Albert, T. Schindler, G. Niedner-Schatteburg, and V. E. Bondybey, Int. J. Mass Spectrom. Ion Processes **167/168**, 723 (1997).
[31] C. Berg, M. Beyer, U. Achatz, S. Joos, G. Niedner-Schatteburg, and V. E. Bondybey, Chem. Phys. **290**, 379 (1998).
[32] M. Beyer, U. Achatz, C. Berg, S. Joos, G. Niedner-Schatteburg, and V. E. Bondybey, Appl. Phys. **A109**, 617 (1999).
[33] U. Achatz, S. Joos, C. Berg, T. Schindler, M. Beyer, G. Albert, G. Niedner-Schatteburg, and V. E. Bondybey, J. Am. Chem. Soc. **120**, 1876 (1996).
[34] *Gaussian 94, Revision D.4*, M. J. Frisch, G. W. Trucks, H. B. Schlegel, P. M. W. Gill, B. G. Johnson, M. A. Robb, J. R. Cheeseman, T. Keith, G. A. Peterson, J. A. Montgomery, K. Raghavachari, M. A. Al-Laham, V. G. Zakrewski, J. V. Ortiz, J. B. Foresman, J. Cioslowski, B. B. Stefanov,
A. Nanayakkara, M. Challacombe, C. Y. Peng, P. Y. Ayala, W. Chen, M. W. Wong, J. L. Andres, E. S. Replogle, R. Gomperts, R. L. Martin, D. J. Fox, J. S. Binkley, D. J. Defrees, J. Baker, J. P. Stewart, M. Head-Gordon, C. Gonzalez, and J. A. Pople, Gaussian, Inc., Pittsburgh PA (1995).
[35] A. Nicklass, M. Dolg, H. Stoll, and H. Prenss, J. Chem. Phys. **102**, 8942 (1995).
[36] M. Beyer, E. V. Savchenko, G. Niedner-Schatteburg, and V. E. Bondybey, J. Chem. Phys. **110**, 11950 (1999).

This article was published in English in the original Russian journal. It was edited by S. J. Amoretty.

LATTICE DYNAMICS

Amplitude–phase spectroscopy of resonant reflection of light by crystals with a Fabry–Perot interferometer at the surface

P. S. Kosoboutski

*L'vov State Polytechnical University, 290646 L'vov, Ukraine**
(Submitted December 14, 1998; revised May 7, 1999)
Fiz. Nizk. Temp. **25**, 1092–1098 (October 1999)

Conditions for the formation of the minima of amplitude spectra of reflection of electromagnetic waves by transparent Fabry–Perot interferometers fixed on crystal surfaces with resonant dispersion of the dielectric constant $\tilde{\varepsilon}(\omega)$ are investigated. It is shown that, irrespective of the nature of the dispersion $\tilde{\varepsilon}(\omega)$, the minimum of the reflection contour is formed at a frequency ω_m of phase compensation, for which the general phase of the reflected wave is a multiple of π. Analytic expressions connecting the frequency corresponding to the minimum of the reflection contour with parameters of the surface resonator and resonant excitation of bulk excitons, phonons and plasmons in the substrate are obtained. © *1999 American Institute of Physics.* [S1063-777X(99)01510-8]

INTRODUCTION

Resonant reflection of light by a three-layer system of interfaces of the type vacuum–nondispersive plane-parallel layer (resonator)–bulk crystal were investigated for the first time by Hopfield and Thomas[1] in the exciton region of the spectrum. Later, this model was used by many researchers for explaining the anomalies in the exciton reflection spectra, and the main results of these investigations were generalized in monographs.[2–9]

Following the publications by Ivchenko *et al.*,[10,11] the interest towards the resonant spectroscopy of reflection of light rose considerably, especially towards new physical objects like quantum-size structures[12–19] the technology of whose preparation has attained a very high degree of precision.[20] Among other things, it was shown[21,22] that a simple analytic expression connecting the frequency of the minimum of exciton reflection contour and the thickness of the barrier layer with resonant excitation parameters can be obtained for structures with solitary quantum wells. Later, this approach was used for explaining the growth of the amplitude of the minimum of exciton reflection contour with temperature.[23]

The three-layer reflection model is significant for crystals in which bulk excitons of large radius are excited. A resonator in the form of a ''dead'' layer is formed on the surface of such crystals as a result of interaction of excitons with their ''mirror image'' at the interface.[1]

An important problem concerning microelectronics involves the investigation of processes of excitation of semiconductor surfaces and hence the development of methods for measuring parameters of intrinsic oxide layers, e.g., ZnO–ZnSe, SiO_2–Si, etc. For these purposes, it is convenient to use phonon spectroscopy. In comparison with excitons, phonons are less sensitive to the value of attenuation.[24] Hence the method of three-layer phonon reflection spectroscopy does not require too low temperatures, and it is sufficient to study the dependence of the spectral position of the minimum of the reflection contour on the thickness of the surface layer.

The plasma resonance region has been attracting the attention of researchers not only for studying the state of the crystal surface,[5] but also for developing optical probes for measuring physical quantities[25] According to Roderick,[26] the problem of reflection of an electromagnetic wave in this spectral region can be reduced to a three-layer system by taking into account the Coulomb interaction of charge carriers with their mirror images at the vacuum-surface interface.

The aim of our investigation is to study theoretically the conditions of localization of the minimum of the $R(\omega)$ contour of light reflection by a transparent nondispersive Fabry–Perot-type interferometer fixed on the crystal surface, in the region of excitation spectra of bulk excitons, phonons and plasmons in the crystal. Analytical expressions are obtained for the dependence of the frequency corresponding to the minimum of the $R(\omega)$ contour of resonant reflections on the parameters of a three-layer reflecting system.

2. GENERAL RELATIONS

It is well known that taking into account the multibeam interference in the resonator, we can represent the complex amplitude $\tilde{r}_{13}$ of light reflected by a three-layer structure (Fig. 1) in the form[1]

$$\tilde{r}_{13}=\frac{\tilde{r}_{12}+\tilde{r}_{23}\exp(-i\delta_s)}{1+\tilde{r}_{12}\tilde{r}_{23}\exp(-i\delta_s)}, \tag{1}$$

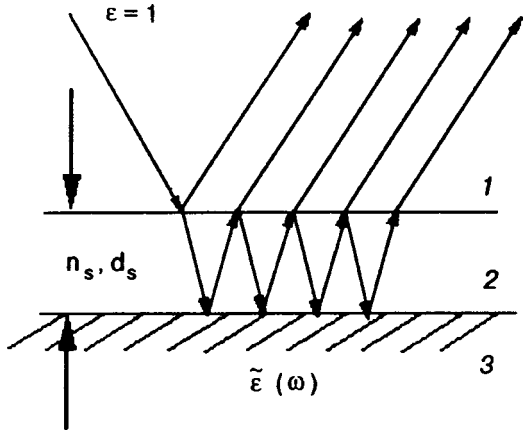

FIG. 1. Three-layer reflection diagram: vacuum (*1*)–nondispersive resonator (*2*) of thickness d_s and refractive index n_s on the surface (*3*) of a crystal with resonant dispersion of dielectric constant $\tilde{\varepsilon}(\omega)$.

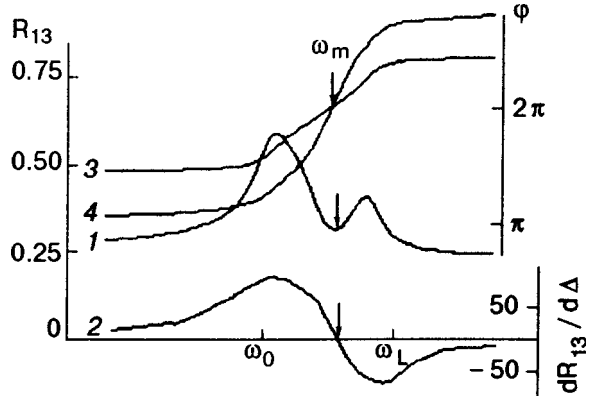

FIG. 2. Dependence of the reflection coefficient R_{13} (*1*), derivative $dR_{13}/d\Delta$ (*2*), phase shift function $\Delta=\varphi_{23}+\delta_s$ (*3*), and φ_{13} phase contour (*4*) on the frequency of light in the vicinity of the exciton resonance $n=1$. Calculations were carried out for a model crystal with parameters ZnSe: $4\pi\alpha=0.0061$; $\hbar\omega_0=2.802$ eV, $\hbar\gamma=10^{-4}$ eV, $\varepsilon_0=9.1$.

where the subscripts 12 and 23 correspond to the vacuum–resonator and resonator–bulk crystal interfaces, and $\delta_s=4\pi n_s d_s/\lambda$ is the phase shift of the wave in a resonator of thickness d_s and refractive index n_s. Formula (1) is valid for normal as well as oblique incidence of the wave on the surface.

The energy coefficient of reflection $R_{13}(\omega)$ is defined as

$$R_{13}=\tilde{r}_{13}\tilde{r}_{13}^{*}=\frac{(\rho_{12}-\rho_{23})^2+4\rho_{12}\rho_{23}\sin^2\dfrac{\Delta}{2}}{1+\rho_{12}^2\rho_{23}^2-2\rho_{12}\rho_{23}\cos\Delta},\ \Delta=\varphi_{23}+\delta_s, \tag{2}$$

where $\tilde{r}_{ij}=\rho_{ij}\exp(i\varphi_{ij})$. As a function of the frequency of light, expression (2) has only one extremum, viz., a minimum at the point $\omega=\omega_m$ where the following conditions are satisfied:

$$\frac{dR_{13}}{d\Delta}=0 \quad \text{and} \quad \frac{d^2R_{13}}{d\Delta^2}>0. \tag{3}$$

Irrespective of the form of resonance dispersion of the complex dielectric function $\tilde{\varepsilon}(\omega)=(n-i\chi)^2$ in the bulk of the crystal where n and χ are its optical refractive index and absorption coefficient, respectively, the minimum of the reflection of light by a three-layer system is attained at the frequency ω_m where the phase compensation relation is satisfied:

$$\varphi_{23}+\delta_s=2\pi. \tag{4}$$

Figure 2 shows the results of computations for the case of reflection of light by a resonator of thickness $d_s=160$ Å fixed on the crystal surface in the excitation spectral region of bulk excitons. Here, curve *1* is the reflection contour, curve *2* is the frequency dispersion of the function $dR_{13}/d\Delta$, and curve *3* is the frequency dependence of the phase shift $(\varphi_{23}+\delta_s)$ of the wave. It can be verified that the condition $dR_{13}/d\Delta=0$ is satisfied only at frequency ω_m at which the reflection coefficient is defined as

$$R_{13}=\left(\frac{\rho_{12}-\rho_{23}}{1-\rho_{12}\rho_{23}}\right)^2. \tag{5}$$

It follows from this expression that, for equal values of the moduli $\rho_{12}=\rho_{23}$, we can use the condition (4) to select such a relation between the phase thickness δ_s of the resonator and the optical parameters n and χ of the crystal that the following equality holds:

$$\tilde{r}_{12}+\tilde{r}_{23}\exp(-i\delta_s)=0 \tag{6}$$

and the coefficient of reflection at the minimum vanishes.[20] In this case, the ''clarified'' reflection minimum ($R_{13}^{\min}=0$) is attained under the condition

$$\mathrm{Re}\,\tilde{r}_{13}=0 \quad \text{and} \quad \mathrm{Im}\,\tilde{r}_{13}=0, \tag{7}$$

which means that the hodograph of the amplitude $\tilde{r}_{13}$ intersects the origin of the coordinate axes $\mathrm{Re}\,\tilde{r}_{13}$ and $\mathrm{Im}\,\tilde{r}_{13}$. The condition of complete clarification of the reflection contour at the minimum corresponds to a jumpwise variation of the type ''N''↔''S'' of the spectral form of the contour $\varphi_{13}(\omega)$ of the phase.[20]

For other relations between the parameters of resonator and resonance excitation in the crystal, the following condition is satisfied at frequency ω_m:

$$\mathrm{Re}\,\tilde{r}_{13}\neq 0, \ \ \mathrm{Im}\,\tilde{r}_{13}=0, \tag{8}$$

i.e., the hodograph of the amplitude $\tilde{r}_{13}$ does not intersect the origin of the coordinate axes $\mathrm{Re}\,\tilde{r}_{13}$ and $\mathrm{Im}\,\tilde{r}_{13}$. In this case, the spectral form of the contour $\varphi_{13}(\omega)$ of the phase will be of ''N'' or ''S'' type,[19] while the general phase of the reflected light at frequency ω_m is a multiple of π (curve *4* in Fig. 2).

The fulfilment of condition (4) at the frequency ω_m of the minimum of reflection contour leads to an analytic dependence between the frequency ω_m, phase thickness δ_s of the resonator, and optical parameters of the crystal in the region of resonance dispersions $\tilde{\varepsilon}(\omega)$. Indeed, the tangent of the phase shift of a wave reflected at the resonator–crystal inner interface is defined as

$$\tan\varphi_{23}=\frac{\mathrm{Im}\,\tilde{r}_{23}}{\mathrm{Re}\,\tilde{r}_{23}}=\frac{n_s(-2\varepsilon_1+2\sqrt{\varepsilon_1^2+\varepsilon_2^2})^{1/2}}{\varepsilon_s-\sqrt{\varepsilon_1^2+\varepsilon_2^2}}, \tag{9}$$

where the dielectric constant of the layer $\varepsilon_s = n_s^2, (\chi_s = 0)$, and $\tilde{\varepsilon}(\omega) = \varepsilon_1 + i\varepsilon_2$ in the bulk of the crystal. Equation (9) can be presented in a more convenient form as follows:

$$\varepsilon_s^2 + \varepsilon_1^2 + \varepsilon_2^2 + \frac{2\varepsilon_s\varepsilon_1}{\tan^2\delta_s} = \frac{2\varepsilon_s}{\sin^2\delta_s}\cdot(\varepsilon_1^2+\varepsilon_2^2)^{1/2}, \tag{10}$$

where we have taken into account the fact that $\tan\varphi_{23} = \tan(2\pi - \delta_s) = \tan\delta_s$. It should be emphasized that this equation contains only parameters of the resonator and the active medium in which the dielectric constant has a resonant form. Hence it can be used for establishing a dependence of the frequency of the reflection contour minimum on the parameters of the reflecting system. We shall demonstrate this by considering specific examples.

3. RESONANCE OF BULK EXCITONS

In the region of excitation of bulk excitons, the dispersion of the dielectric function $\tilde{\varepsilon}(\omega)$ without taking spatial dispersion into account has the form

$$\tilde{\varepsilon}(\omega) = \varepsilon_0 + \frac{4\pi\alpha\omega_0^2}{(\omega_0^2 - \omega^2 - i\omega\gamma)}, \tag{11}$$

where ω_0 is the resonance frequency of transition with an oscillator energy $4\pi\alpha$; ε_0 the background dielectric constant, and γ the damping factor.

Separating the real (ε_1) and imaginary (ε_2) parts in (11) and substituting them into (10), we obtain a fourth-order equation in ω^2:

$$\left(\varepsilon_s^2 + \varepsilon_0^2 + \frac{2\varepsilon_0\varepsilon_s}{\tan^2\delta_s}\right) + \frac{4\pi\alpha\omega_0^2[4\pi\alpha\omega_0^2 + (\omega_0^2-\omega^2)(2\varepsilon_s + 2\varepsilon_0/\tan^2\delta_s)]}{(\omega_0^2-\omega^2)^2+\omega^2\gamma^2} = \frac{2\varepsilon_s}{\sin^2\delta_s}\left\{\varepsilon_0^2 + \frac{4\pi\alpha\omega_0^2[4\pi\alpha\omega_0^2 + 2\varepsilon_0(\omega_0^2-\omega^2)]}{(\omega_0^2-\omega^2)^2+\omega^2\gamma^2}\right\}^{1/2}. \tag{12}$$

This equation can be simplified by putting $\varepsilon_s = \varepsilon_0$:

$$\left[4\pi\alpha\omega_0^2 + \frac{2\varepsilon_0}{\sin^2\delta_s}(\omega_0^2-\omega^2)\right]^2 + \frac{4\varepsilon_0^2}{\sin^2\delta_s}[(\omega_0^2-\omega^2)^2 + \omega^2\gamma^2] = 0. \tag{13}$$

In this case, Eq. (13) has the following solution:

$$\omega_m^2 = \omega_0^2[S_1 + (S_1^2 - S_2)^{1/2}], \tag{14}$$

where

$$S_1 = 1 + \frac{2\pi\alpha}{\varepsilon_0} + \frac{\gamma^2\cot^2\delta_s}{2\omega_0^2},$$

$$S_2 = 1 + \frac{4\pi\alpha}{\varepsilon_0} + \left(\frac{2\pi\alpha\sin\delta_s}{\varepsilon_0}\right)^2. \tag{15}$$

The condition

$$\gamma \ll \omega_0, \tag{16}$$

is usually satisfied in the exciton part of the spectrum. In this case, solution (14) is simplified considerably and assumes the form

$$\left(\frac{\omega_m}{\omega_0}\right)^2 \approx 1 + \frac{4\pi\alpha}{\varepsilon_0}\cos^2\frac{\delta_s}{2}. \tag{17}$$

Thus, a change in the phase thickness of the resonator at the crystal surface leads to a periodic variation of the frequency of the reflection contour minimum within the limits of the longitudinal–transverse splitting ω_{LT} of the exciton state under consideration: $\omega_0 \leqslant \omega_m \leqslant \omega_L$, where ω_L is the longitudinal frequency of resonant excitons. For example, the presence of a nondispersive resonator of exciton size on the surface of a model crystal with ZnSe parameters ($4\pi\alpha = 0.0066$; $\varepsilon_0 = 9$; $\hbar\omega_0 = 2.802$ eV), leads to a displacement of the reflection minimum by about 10–15% of the longitudinal–transverse splitting ω_{LT}.

If the phase thickness of the resonator is $\delta = (2m+1)\pi, m = 0,1,2,3,...$, the frequency ω_m is localized in the vicinity of ω_0. For $\delta_s = 0,\ 2\pi,\ 4\pi,\ \ldots = 2m\pi$, the minimum is localized at the frequency

$$\omega_m^2 = \omega_0^2\left(1 + \frac{4\pi\alpha}{\varepsilon_0}\right), \tag{18}$$

i.e., at the resonance frequency ω_L of longitudinal excitons.[1]

4. PHONON REFLECTION OF LIGHT IN THE INFRARED REGION

As in the preceding section, we must determine the resonance dispersion $\tilde{\varepsilon}(\omega)$ in a given frequency range in order to establish a dependence of the frequency ω_m of the phonon reflection contour minimum on the phase thickness of a film resonator at the crystal surface. In accordance with the data presented in Ref. 24, this dispersion can be presented in the form

$$\tilde{\varepsilon}(\omega) = \varepsilon_\infty + \frac{(\varepsilon_0 - \varepsilon_\infty)\omega_{TO}^2}{\omega_{TO}^2 - \omega^2 - i\omega\gamma}, \tag{19}$$

where ω_{TO} is the resonance frequency of transverse optical phonons. Separating the real and imaginary parts and substituting them into (10), we obtain a fourth-order equation in ω^2:

$$[2\varepsilon_s\varepsilon_\infty+(\varepsilon_s^2+\varepsilon_\infty^2)\tan^2\delta_s]^2-\left(\frac{2\varepsilon_s\varepsilon_\infty}{\cos^2\delta_s}\right)^2+\left[\frac{2(\varepsilon_\infty^2+\varepsilon_s\varepsilon_\infty)\tan^2\delta_s\Delta_{LT}^2(\omega_{TO}^2-\omega^2)+\varepsilon_\infty^2(\varepsilon_s^2+\varepsilon_\infty^2)\Delta_{LT}^2\tan^2\delta_s}{(\omega_{TO}^2-\omega^2)^2+\omega^2\gamma^2}\right]^2$$
$$-\left[\frac{2\varepsilon_s\varepsilon_\infty}{\cos^2\delta_s}\right]^2\frac{\Delta_{LT}^2+2(\omega_{TO}^2-\omega^2)\Delta_{LT}}{(\omega_{TO}^2-\omega^2)^2+\omega^2\gamma^2}+2[2\varepsilon_s\varepsilon_\infty+(\varepsilon_s^2+\varepsilon_\infty^2)\tan^2\delta_s]$$
$$\times\frac{2(\varepsilon_\infty^2\tan^2\delta_s+2\varepsilon_s\varepsilon_\infty)\Delta_{LT}(\omega_{TO}^2-\omega^2)+\varepsilon_\infty^2\Delta_{LF}^2\tan^2\delta_s}{(\omega_{TO}^2-\omega^2)^2+\omega^2\gamma^2}=0. \tag{20}$$

Putting $\varepsilon_s=\varepsilon_\infty$, we can present Eq. (20) in a simplified form:

$$\Omega^2+\Omega\left(\frac{\Delta_\varepsilon\omega_{TO}^2}{\varepsilon_\infty}+\frac{\gamma^2}{\tan^2\delta_s}\right)+\left(\frac{\sin\delta_s}{2\varepsilon_\infty}\Delta_\varepsilon\Omega_{TO}^2\right)^2$$
$$-\frac{4\varepsilon_\infty^2\omega_{TO}^2\gamma^2\cos^2\delta_s}{\sin^4\delta_s}=0. \tag{21}$$

The solution of this equation can be written as follows:

$$\omega_{\min}^2=\omega_{TO}^2+\frac{1}{2}[\Omega+\sqrt{(\Omega^2-\Delta_{LT}^2\sin^2\delta_s+\omega_{TO}^2\gamma^2\cot^2\delta_s)}],$$
$$\Omega=\Delta_{LT}-\gamma^2\cot^2\delta_s,\Delta_{LT}=\omega_{LO}^2-\omega_{TO}^2,$$
$$\Delta_\varepsilon=\varepsilon_0-\varepsilon_\infty. \tag{22}$$

If the condition $\gamma\ll\omega_{TO}$ is satisfied, Eq. (21) assumes the form

$$\Omega^2+\Omega\frac{\Delta_\varepsilon\omega_{TO}^2}{\varepsilon_\infty}+\frac{\sin^2\delta_s}{4\varepsilon_\infty^2}\Delta_\varepsilon^2\omega_{TO}^2=0 \tag{23}$$

with a simple solution

$$\omega_m^2=\omega_{TO}^2\left[1+\frac{\Delta_\varepsilon}{\varepsilon_\infty}\cos^2\frac{\delta_s}{2}\right]. \tag{24}$$

As in the case of excitation of bulk excitons, a variation of the phase thickness of the resonator whose role is played by the oxide layer at the crystal surface, the energy position of the phonon reflection contour minimum is displaced periodically between the spectral positions of resonance phonon frequencies ω_{TO} and ω_{LO}. In the limiting case $\delta_s=0$, the solution of Eq. (24) coincides with the well-known Sachs–Teller–Leddane expression[27]

$$\omega_{\min}^2=\omega_{TO}^2\frac{\varepsilon_0}{\varepsilon_\infty}=\omega_{LO}^2, \tag{25}$$

thus confirming the correctness of the proposed approach. By establishing such a functional dependence, we can extend the spectrum of the experimental investigations of anomalous dispersion of quartz in the interval 8–10 μm caused by valence oscillations of Si–O bonds.[28]

5. PLASMA REFLECTION REGION IN SEMICONDUCTORS

It was mentioned in Sec. 1 that interaction of charge carriers with their mirror images at the interface leads to the emergence of a nondispersive layer at the crystal surface. Hence, in order to establish the functional dependence of the frequency ω_m corresponding to the minimum of the plasma reflection contour on the phase thickness of the layer at the crystal surface, we must solve, as in the previous cases, Eq. (10) under the condition (4) with a known dependence $\tilde{\varepsilon}(\omega)$. According to Refs. 5 and 9, it can be written in the following form:

$$\tilde{\varepsilon}(\omega)=\varepsilon_\infty-\frac{\omega_p^2}{\omega^2+i\omega\gamma}, \tag{26}$$

where ω_p is the plasma frequency. Taking into account Eq. (26) at the frequency ω_m, we can write Eq. (10) in the form

$$[(\varepsilon_s^2+\varepsilon_\infty^2)\tan^2\delta_s+2\varepsilon_s\varepsilon_\infty]^2+\left(\frac{2\omega^2\omega_p^2(\varepsilon_s+\varepsilon_\infty\tan^2\delta_s)+\omega_p^4\tan^2\delta_s}{\omega^4+\omega^2\gamma^2}\right)^2$$
$$\times\frac{2[(\varepsilon_s^2+\varepsilon_\infty^2)\tan^2\delta_s+2\varepsilon_s\varepsilon_\infty][2\omega^2(\varepsilon_s+\varepsilon_\infty\tan^2\delta_s)+\omega_p^4\tan^2\delta_s]}{\omega^4+\omega^2\gamma^2}=\frac{4\varepsilon_s^2\varepsilon_\infty^2}{\cos^4\delta_s}+\frac{4\varepsilon_s^2}{\cos^4\delta_s}\frac{2\varepsilon_\infty\omega_p^2\omega^2+\omega_p^4}{\omega^4+\omega^2\gamma^2}. \tag{27}$$

For $\varepsilon_s=\varepsilon_\infty$, Eq. (27) assumes a simpler form

$$\omega^4-\left(\gamma^2\cot\delta_s+\frac{\omega_p^2}{\varepsilon_\infty}\right)\omega^2+\frac{\omega_p^4\sin^2\delta_s}{4\varepsilon_\infty^2}=0, \tag{28}$$

and has the solution

$$\omega_m^2=\frac{1}{2}\gamma^2\cot^2\delta_s+\frac{\omega_p^2}{2\varepsilon_\infty}\pm\left\{\left(\frac{1}{2}\gamma^2\cot^2\delta_s+\frac{\omega_p^2}{2\varepsilon_\infty}\right)^2\right.$$
$$\left.-\frac{\omega_p^4\sin^2\delta_s}{4\varepsilon_\infty^2}\right\}^{1/2} \tag{29}$$

or, if we disregard attenuation,

$$\omega_m^2 \approx \frac{\omega_p^2}{\varepsilon_\infty} \cos^2 \frac{\delta_s}{2}. \tag{30}$$

Thus, in the absence of a nondispersive layer at the crystal surface, the plasma reflection minimum emerges on the longwave side of the plasma resonance at the frequency $\omega_m \approx \omega_p / \sqrt{\varepsilon_\infty}$. If the attenuation is disregarded, the real part of the complex function (26) at frequency ω_m is equal to zero, which is in accord with Ref. 5. Hence, as the plasma resonance frequency ω_p is approached, no peak will be observed on the reflection curve. With increasing phase thickness of the surface layer, the minimum of the reflection contour is displaced towards lower energies. This fact must be taken into consideration while designing sensor devices.[29]

6. CONCLUSIONS

(1) In the case of reflection of an electromagnetic wave at a three-layer system of the type nondispersive medium–Fabry-Perot interferometer–medium with resonant dispersion of the dielectric constant, the minimum of the reflection contour is localized at the phase compensation frequency.
(2) The spectral position of the reflection contour minimum is determined by the phase thickness of the resonator and parameters of resonance excitation in the crystal.
(3) Upon a variation of the phase thickness of the resonator in the exciton and phonon parts of the spectrum, the frequency of the reflection contour minimum oscillates within the longitudinal–transverse splitting. In the region of plasma reflection, the range of variation of the reflection minimum frequency is bounded only on the shortwave side of the plasma frequency.
(4) The phase $\varphi_{13}(\omega)$ of the reflected wave at the frequency corresponding to the reflection curve minimum is a multiple of π.
(5) The approach considered here is applicable in all cases of reflection of electromagnetic waves by three-layered structures of the type nondispersive medium–Fabry–Perot interferometer–crystal with resonant transitions, for which the dielectric functions can be used for a macroscopic description of resonant optical properties.

The author is indebted to Prof. G. Landwehr (University of Würzburg, Germany) for providing financial assistance to attend the International Symposium on ''Heterostructures in Science and Technology'' at Würzbug from March 13 to 17, 1995. Thanks are also due to Ya. P. Kosoboutski for his help in computations.

This research was financed partially by the International Soros Program on Science and Education (ISSEP) under Grant No. APU 072047.

*E-mail: petkosob@polynet.lviv.ua

[1] J. J. Hopfield and D. G. Thomas, Phys. Rev. **132**, 563 (1963).
[2] V. M. Agranovich and V. L. Ginzburg, *Crystal Optics with Spatial Dispersion and Excitons*, 2nd ed., No. Holland, Amsterdam, 1982.
[3] M. S. Brodin, E. N. Myasnikov, and S. V. Marisova, *Polaritons in Crystal Optics* [in Russian], Naukova Dumka, Kiev (1984).
[4] S. I. Pekar, *Crystal Optics and Auxiliary Light Waves* [in Russian], Naukova Dumka, Kiev (1982).
[5] V. M. Agranovich and D. L. Mills (Eds.) *Surface Polaritons. Electromagnetic Waves at the Surfaces and Interfaces*, No. Holland, Amsterdam, 1982.
[6] E. Rashba and M. Sturge (Eds.), *Modern Problems in Condensed Media. Excitons*, No. Holland, Amsterdam, 1982.
[7] A. Stal and I. Blaslev *Electrodynamics of the Semiconductor Band Edge*, Springer Verlag, Heidelberg (1987).
[8] V. A. Kiselev, B. V. Novikov, and A. E. Cherednichenko, *Exciton Spectroscopy of Surface Regions of Semiconductors* [in Russian], Leningrad State University, Leningrad (1987).
[9] N. L. Dmitruk, V. G. Litovchenko, and V. L. Strizhevskii, *Surface Polaritons in Semiconductors and Insulators* [in Russian], Naukova Dumka, Kiev (1989).
[10] E. L. Ivchenko, P. C. Kop'ev, and V. P. Kochereshko *et al.*, Fiz. Tverd. Tela (Leningrad) **30**, 784 (1988) [Sov. Phys. Solid State **30**, 448 (1988)].
[11] E. L. Ivchenko, A. V. Kavokin, and V. P. Kochereshko *et al.*, Phys. Rev. **46B**, 7213 (1992).
[12] R. Houdre, R. P. Stanley, U. Oesterle, and M. Ilegems, Phys. Rev. **49**, 16761 (1994).
[13] T. A. Fisher, A. M. Afshar, and D. M. Whittaker *et al.*, Phys. Rev. **51**, 2600 (1995).
[14] T. J. Hosea, P. H. Hughes, and B. L. Weiss, J. Appl. Phys. **77**, 2672 (1995).
[15] M. R. Vladimirova, A. V. Kavokin, and M. A. Kalitievski, Phys. Rev. B **54**, 14566 (1996).
[16] R. Huang, H. Cao, and Y. Yamamoto, Phys. Rev. B **56**, 9217 (1997).
[17] P. C. Kosoboutski, Opt. Spectrosc. **83**, 969 (1997).
[18] G. V. Astakhov, V. P. Kochereshko, and A. V. Platonov *et al.*, Fiz. Tverd. Tela (St. Petersburg) **40**, 867 (1998) [Phys. Solid State **40**, 798 (1998)].
[19] P. J. Klar, P. M. A. Vicente, and T. E. Sale *et al.*, Solid State Commun. **107**, 97 (1998).
[20] M. R. S. Bulletin **23**, 15 (1998)
[21] P. S. Kosoboutski, Fiz. Nizk. Temp. **22**, 460 (1996) [Low Temp. Phys. **22**, 358 (1996)].
[22] P. S. Kosoboutski, Ukr. Fiz. Zh. (Russ. Ed.) **28**, 1090 (1983).
[23] P. S. Kosoboutski, Fiz. Nizk. Temp. **24**, 493 (1998) [Low Temp. Phys. **24**, 373 (1998)].
[24] E. Palik (Ed.), *Handbook of Optical Constants of Solids III*, Academic Press, San Diego (1998)
[25] K. R. Welford, Opt. Quantum Electron. **23**, 1 (1991).
[26] E. H. Roderick, in: *Metal–Semiconductor Junctions* [Russian translation], edited by G. V. Stepankov, Radio i Svyaz', Moscow (1982).
[27] Y. Y. Leddane, R. G. Sachs, and E. Teller, Phys. Rev. **59**, 673 (1941).
[28] S. I. Popova, T. S. Tolstykh, and V. G. Vorob'ev, Opt. Spektrosk. **29**, 801 (1972).
[29] A. V. Kabashin and P. I. Nikitin, Kvant. Elektron. (Moscow) **24**, 671 (1997).

Translated by R. S. Wadhwa

On sign reversal of the linear thermal expansion coefficient of fullerite C_{60} at helium temperatures

V. M. Loktev

*N. N. Bogoliubov Institute of Theoretical Physics, National Academy of Sciences of the Ukraine, 252143 Kiev, Ukraine**

(Submitted February 2, 1999; revised March 15, 1999)
Fiz. Nizk. Temp. **25**, 1099–1102 (October 1999)

An attempt is made to interpret the low-temperature negative thermal expansion of solid C_{60} on the basis of an assumption concerning the freezing of all (thermally activated) rotations and the formation of anisotropic intermolecular potential ensuring libron vibrations of fullerene molecules in the equilibrium position displaced relative to the isotropic potential minimum.
 [S1063-777X(99)01610-2]

1. Aleksandrovskii *et al.*[1] who measured the thermal expansion of solid C_{60} in the low-temperature range ($T \lesssim 10$ K) discovered an unexpected peculiarity, i.e., the sign reversal of the linear coefficient of volume expansion $\alpha_{C_{60}}(T)$ which becomes negative for this cryocrystal at $T \simeq 3.4$ K. In other words, compression (or, which is the same, a decrease in the size) of a C_{60} fullerite sample in the form of a tablet pressed from powder[1)] in the experiments,[1] is changed into expansion (increase in size) upon a further decrease in T (below 3.4 K). This effect is known as negative thermal expansion (NTE) and was associated by Aleksandrovskii *et al.*[1] with the assumption on the existence of a low-energy spectrum of C_{60} molecules in fullerite at helium temperatures due to their quantum (under-the barrier) rotational tunneling between different orientational positions in the solid phase.

It should be noted that, although the NTE is a relatively rare effect, it is nevertheless not a unique phenomenon. For example, it was observed earlier (see the literature cited in Ref. 1) is some cryocrystals (molecular or atomic, but with an admixture of simple molecules). Examples of other (noncryocrystalline) compounds (including simple materials such as RbI)[2] exhibiting NTE to a certain extent in various temperature regions are given in the monograph by Novikov.[3] However, we must admit that the NTE effect discovered more than 30 years ago in ZrW_2O_8[4] is astonishing even if we take into account the above arguments. It was found that the temperature range of NTE in this essentially ionic cubic compound embraces the entire range of its existence in solid state, i.e., for all $T < T_{melt} = 1050$ K,[5] the NTE being isotropic. Naturally, the Grüneisen coefficient of the ZrW_2O_8 crystal is also negative everywhere, its value increasing in magnitude at $T \lesssim 50$ K also and amounts to ≈ -5 [Ref. 6].

According to modern theoretical concepts (see, for example, Refs. 7 and 8), the reason behind negative thermal expansion in ZrW_2O_8 and similar crystals (for example, $ZrVO_7$) is the prevailing contribution to $\alpha(T)$ from libron branches of lattice vibrations (corresponding to rotations of rigidly coupled groups of ions) as compared to the competing contribution from translational vibrations. Rigid structural elements in the ZrW_2O_8 crystal lattice are ZrO_6 octahedrons and WO_4 tetrahedrons which can be regarded to a certain extent as undeformed ''molecules.'' Such a division is conditional and is characterized by the presence of oxygen ions in common for neighboring ''molecules.'' In spite of the fact that the latter make the simple pattern with translations and librations less accurate,[2)] it remains quite visual. Indeed, it is easy to verify that the lattice constructed from rigid structural elements with common ions (playing the role of hinges) inevitably shrinks for any rotation of any (or all) of such groups singled out into ''molecules.'' Thus, the standard angular deviation $\langle \theta^2 \rangle$ increasing with temperature leads to a negative contribution to the thermal expansion coefficient of the crystal since the change in its volume $\Delta V \propto -\langle \theta^2 \rangle$. A more detailed and consistent analysis based on the concept of translational and librational modes separated in this way makes it possible to describe successfully the NTE effect in ionic crystals not only qualitatively, but also quantitatively with the help of temperature dependences of the densities of corresponding states.

2. The approximate ''translation–libration'' approach is important not only from the quantitative, but primarily from the qualitative point of view. First, such an approach (due to the presence of the same ions that are in common for nearest ''molecules'') does not necessitate rotational (including tunnel) movements for the emergence of NTE since such rotations are impossible in a lattice of the type ZrW_2O_8, although they are observed in molecular (cryo)crystals in which molecules, being really rigid structural units, are completely independent of one another (at least, at high T). Second, the competition between two types of vibrations (translational and libron) may (and must) lead to the NTE effect. Both these types of vibrations are always present in known examples of cryocrystals exhibiting NTE. For this reason, the assumption concerning the origin of NTE in fullerite C_{60} and differing from that proposed by Aleksandrovskii *et al.*[1] has some grounds. According to this assumption, the contributions to the coefficient $\alpha_{C_{60}}(T)$ from these vibrations have opposite signs: a positive contribution ensuring the inequality $\alpha_{C_{60}}(T) > 0$ from translations and a negative contribu-

tions that can lead to the inequality $\alpha_{C_{60}}(T)<0$ from librations.

In this connection, we note a specific feature of fullerite C_{60} whose molecules can rotate freely at first, and then with retardation down to quite low temperatures. It cannot be ruled out that the total spectrum of the solid phase of fullerene is formed completely only in the helium temperature range (or close to it) in view of extremely high (icosahedral) point symmetry of its molecules.

The structure of various modifications of fullerene is well known (see the review in Ref. 9). In the intermolecular interaction as a function of mutual orientation of molecules, the so-called pentagonal and hexagonal configurations, separated by a comparatively high barrier (~ 0.3 eV), are singled out quite clearly[10] (see also Ref. 11). Such a large barrier height is determined by the fact that these configurations are not equivalent. Since such configurations can be realized in a large number of ways, each of these two main minima is actually multiply degenerate.

We can assume that the barriers between identical positions of each of interacting molecules are considerably lower.[3)] Moreover, it is quite possible that as the temperature T decreases, at first rotations (to be more precise, random movements) of molecules relative to C_2 axes (i.e., through an angle 180° are frozen out, followed by rotations about the C_3 axes (through 120°), and finally by rotations about C_5 axes (through 72°) at the lowest temperatures. It is appropriate to note that if fullerene possessed only C_2 and C_3 axes, fullerite would exist as a system with a long-range orientational order. However, the existence of C_5 axes makes this impossible in principle, and it is assumed (see Ref. 6) that fullerite at $T \lesssim 90$ K is an orientational glass. As long as thermally stimulated rotational diffusion persists (at least about C_5 axes), it is meaningless to speak about the final formation of librational spectrum of fullerite since the multicomponent tensor $\hat{\mathbf{F}}$ (the multipole order parameter) is not manifested under such conditions. The correlators of various components of this tensor ultimately determine the noncentral part of the paired intermolecular potential (essentially, its ''swing'').[4)] Naturally, different component of $\hat{\mathbf{F}}$ can freeze at different T.

Indeed, this potential can be presented phenomenologically by the sum

$$V(R)=V_{\text{is}}(R)+V_{\text{anis}}(R)\langle\langle\hat{\mathbf{F}}^2\rangle\rangle, \tag{1}$$

where $V_{\text{is}}(R)$ and $V_{\text{anis}}(R)$ are the isotropic and anisotropic components of interaction of two C_{60} molecules in the crystal. According to calculations (see Chap. 12 in Ref. 14), these components for N_2 type molecules have a similar structure (repulsion at small and attraction at large distances), but the quantity R_{anis} corresponding to the minimum of $V_{\text{anis}}(R)$ corresponds to more distant equilibrium positions of molecules than the quantity R_{is} determined from the minimum of $V_{\text{is}}(R)$. If such a behavior is also preserved for the intermolecular potential (1), this means that the minimum of $V_{\text{is}}(R)$ lies on the repulsive branch of the anisotropic component $V_{\text{anis}}(R)$ which is ''actuated'' only with the emergence and growth of $\langle\langle\tilde{\mathbf{F}}^2\rangle\rangle$.

Assuming that these terms [appearing in (1)] have the simple form

$$V_{\text{is}}(R)=\frac{1}{2}k_{\text{is}}R^2-\frac{1}{3}\kappa_{\text{is}}R^3, \quad R_{\text{is}}=0;$$
$$V_{\text{anis}}(R)=\frac{1}{2}k_{\text{anis}}(R-R_{\text{anis}})^2, \tag{2}$$

where k_{is}, k_{anis} and κ_{is} are the elastic and anharmonism constants (we omit the anharmonism of $V_{\text{anis}}(R)$ since $|V_{\text{is}}(R)|>|V_{\text{anis}}(R)|$),[14] we find that the equilibrium molecular spacing for $V(R)$ taking into account (2) is defined by the expression

$$R_{\min}(T)=\frac{\kappa_{\text{is}}\overline{R^2}+k_{\text{anis}}R_{\text{anis}}\langle\langle\hat{F}\rangle\rangle}{k_{\text{is}}}, \tag{3}$$

in which $\overline{R^2}$ is the root-mean-square amplitude of translational vibrations determining the conventional (positive) thermal expansion. It can be seen from (3) that for $\langle\langle\hat{\mathbf{F}}^2\rangle\rangle \neq 0$, the value of $R_{\min}(T)$ increases slightly since $R_{\text{anis}}>0$. The thermal expansion coefficient $\alpha_{C_{60}}(T)=dR_{\min}/dT$ in this case has the form

$$\alpha_{C_{60}}(T)=\alpha^{(\text{is})}_{C_{60}}(T)+\alpha^{(\text{anis})}_{C_{60}}(T);$$
$$\alpha^{(\text{anis})}_{C_{60}}(T)=-\frac{k_{\text{anis}}}{k_{\text{is}}}R_{\text{anis}}\frac{d\langle\langle\hat{\mathbf{F}}^2\rangle\rangle}{dT},$$

and its sign at a given temperature is determined by the sign of the larger addend since $d\langle\langle\hat{\mathbf{F}}^2\rangle\rangle/dT<0$ as usual.

The proposed mechanism coincides to a certain extent with that considered in Ref. 7 and 8 for ZrW_2O_8, when the orientational ordering of structural elements relative to one another leads to an increase in their separation. This resembles to a certain extent the ordering of hydrogen bonds in water observed slightly above the freezing point and also accompanied by an increase in molecular spacing. As regards fullerite C_{60}, we can hope that rotational motion in fullerite retarded at $T \lesssim 90$ K ceases completely only at quite low temperatures in view of an increase in $\langle\langle\hat{\mathbf{F}}^2\rangle\rangle$ and the formation of the potential $V_{\text{anis}}(R)$ leading to the optimization of molecular spacing. On the whole, the calculation of $\alpha_{C_{60}}(R)$ for fullerite requires self-consistent calculation of the spectrum of translational and libron vibrations and the value of $\langle\langle\hat{\mathbf{F}}^2\rangle\rangle$, which is apparently a complicated problem in view of the absence of a long-range orientational order in this crystal, and hence undamped modes (except acoustic ones).

Thus, the proposed qualitative explanation of the NTE of fullerite does not involve tunneling processes which are difficult to justify for undoubtedly classical objects such as fullerenes C_{2n} (whose atomic mass is $\lesssim 10^3$ amu for $n \gtrsim 50$). The classical nature is manifested in extremely small amplitudes of zero-point vibrations in fullerite.[12] It should be recalled that librations in solid C_{60} are quite soft ($\lesssim 20\ \text{cm}^{-1}$), and their spectrum undergoes noticeable changes as the temperature decreases from $\sim 10^2$ to ~ 10 K.[15]

Finally, returning to the origin of NTE, we must also bear in mind that the coefficient $\alpha(T)$ is usually determined by the pressure dependence of characteristic (vibrational) frequencies of the spectrum. If the lattice is compressed (also as a result of a change in temperature), the energy of levels having a nontunnel origin has a tendency to increase while the energy of tunnel levels tends to decrease. Such a behavior has an obvious physical explanation: a decrease in atomic spacing leads to more rigid intermolecular (interionic) potentials on the one hand and to higher barriers separating different orientational positions on the other hand. This is the reason behind a peculiar (negative) contribution of tunnel states to the Grüneisen coefficient in simple cryocrystals containing tunneling subsystems.[16] But such subsystems appear infrequently (in RbI as well as in ZrW_2O_8), which necessitates the search for other (''non-tunneling'') reasons behind NTE. Besides, it is interesting to note that a decrease in the probability of subbarrier (quantum) transitions in cryocrystals is in fact freezing (or fixation) of a reorienting center from among several positions. In this case, it is transformed from a ''tunnel-blurred'' (isotropic) object into an anisotropic object with a definite orientation. Consequently, we can speak of the formation of a component of the intermolecular potential (including the potential of interaction between impurities) of the $V_{\text{anis}}(R)$ type due to the retardation (and even vanishing) of orientational (quantum and classical) transitions. The consequences of possible manifestations of this component were considered by us in the above analysis.

The author expresses his deep gratitude to V.G. Manzhelii for numerous discussions of the NTE in cryocrystals and to Yu.B. Gaididei for his support and stimulating critical remarks. Thanks are also due to M.A. Ivanov and Yu.A. Freiman for fruitful discussions and to A.N. Aleksandrovskii who mentioned the existence of calculations of orientational barriers in fullerites.

*E-mail: loktev@bitp.kiev.ua

[1)]Recently, the same effect was confirmed by measurements of thermal expansion of C_{60} single crystals (V. G. Manzhelii, private communication).

[2)]Besides, it is very difficult to single out librational modes in ionic crystals like ZrW_2O_8, which are just degenerate low-frequency optical oscillations.

[3)]Unfortunately, only the barriers for the so-called consistent (simultaneous) rotation of all molecules or rotations (in both cases, relative to crystallographic axes) of individual molecules in the field of other molecules are given in available publications (see, for example, Ref. 12), which allows us to determine the mutual orientations of nearest molecules that are most advantageous from the energy point of view. However, it would be equally interesting to analyze barriers for rotations of fullerene C_{60} molecules about their symmetry axes between equivalent positions in a given configuration of the environment (including the configuration advantageous from the energy point of view). We are speaking of just such barriers.

[4)]It should be recalled that an (orientationally) disordered medium (glass) must be characterized not by a conventional order parameter (i.e., $\langle\hat{\mathbf{F}}\rangle$), but by a correlation function or Edwards–Anderson order parameter $\langle\langle\hat{\mathbf{F}}^2\rangle\rangle$, in which additional averaging over configurations is presumed. It is important to note that while $d\langle\hat{\mathbf{F}}\rangle/dT\to 0$ as $T\to 0$ for ordered media for which $\langle\hat{\mathbf{F}}\rangle\neq 0$, the derivative $d\langle\langle\hat{\mathbf{F}}^2\rangle\rangle/dT$ for glasses remains finite in the entire range of the frozen state.[13]

[1] A. N. Aleksandrovskii, V. B. Eselson, V. G. Manzhelii *et al.*, Fiz. Nizk. Temp. **23**, 1256 (1997) [Low Temp. Phys. **23**, 943 (1997)].
[2] M. Blackman, Proc. Phys. Soc. London, Sect. B **70**, 827 (1957).
[3] S. I. Novikov, *Thermal Expansion of Solids* [in Russian], Nauka, Moscow (1974).
[4] C. Martinek and F. A. Hummel, J. Am. Ceram. Soc. **51**, 227 (1968).
[5] T. Mary, J. Evans, T. Vogt, and A. Sleight, Science **272**, 90 (1996).
[6] G. Ernst, C. Broholm, G. R. Kowach, and A. P. Ramirez, Nature **396**, 147 (1998).
[7] A. P. Giddy, M. T. Dove, G. S. Pawley, and V. Heine, Acta Crystallogr., Sect. A: Found. Crystallogr. **49**, 697 (1993).
[8] A. K. A. Pryde, K. D. Hammonds, M. T. Dove *et al.*, J. Phys.: Condens. Matter **8**, 10973 (1996).
[9] V. M. Loktev, Fiz. Nizk. Temp. **18**, 217 (1992) [Sov. J. Low Temp. Phys. **18**, 149 (1992)].
[10] M. David, R. Ibberson, T. Dennis, and K. Prassides, Europhys. Lett. **18**, 219 (1992).
[11] V. D. Natsik and A. V. Podol'skii, Fiz. Nizk. Temp. **24**, 689 (1998) [Low Temp. Phys. **24**, 523 (1998)].
[12] T. Yildirim and A. B. Harris, Phys. Rev. B **46**, 7878 (1992).
[13] S. L. Ginzburg, *Irreversible Phenomena in Spin Glasses* [in Russian], Nauka, Moscow (1989).
[14] V. G. Manzhelii and Yu. A. Freiman (Eds.), *Physics of Cryocrystals*, AIP Press, Woodbury, N. Y. (1997).
[15] P. J. Horoyski and M. L. W. Thewalt, Phys. Rev. B **48**, 11446 (1993).
[16] Yu. A. Freiman, Fiz. Nizk. Temp. **9**, 657 (1983) [Sov. J. Low Temp. Phys. **9**, 335 (1983)].

Translated by R. S. Wadhwa

NEW METHODS OF LOW-TEMPERATURE EXPERIMENT

High-T_c rf SQUIDs for operation in magnetic fields. Effect of thermal fluctuations

V. I. Shnyrkov, V. P. Timofeev, and A. S. Garbuz

*B. Verkin Institute for Low Temperature Physics and Engineering, National Academy of Sciences of the Ukraine. 310164 Kharkov, Ukraine**

Cheol Gi Kim

Sun Moon University, 336840 Chungnam, Korea
(Submitted March 3, 1999)
Fiz. Nizk. Temp. **25**, 1103–1106 (October 1999)

Optimization of bulk high-T_c rf SQUID characteristics is carried out in the limit of strong thermal fluctuations. It is shown that such fluctuations affect the impedance of interferometers so that they operate only in quasi-nonhysteretic mode. Textured ceramics can be used to produce SQUIDs capable of stable operation in unshielded environment and/or in strong magnetic fields ($H=150-200$ A/m) with a sensitivity about 2×10^{-13} T/Hz$^{1/2}$. These SQUIDs form the basis of a portable susceptometer designed and tested in constant (up to 150 A/m) and varying (up to 4 A/m) magnetic fields with a magnetic moment sensitivity not lower than 1.6 $\times10^{-10}$ A·m^2. [S1063-777X(99)01710-7]

INTRODUCTION

Modern high-T_c SQUIDs produced by thin-field technological method[1] have good characteristics in weak magnetic fields. During operation in the magnetic field of the Earth, the spectral density of the noise in film-type high-T_c SQUIDs increases by more than an order of magnitude[2] in the low-frequency range (1–100 Hz), i.e., in the spectral region in which advantages of SQUIDs over other magnetic field detectors are manifested most strongly. This excess noise is associated as a rule with specific properties of HTSC materials (see, for example, Refs. 3, 4) and sets a limit on the application of SQUIDs in physical investigations in many cases.

In our earlier publication,[4] we noted that the spectral density of noise associated with ''Josephson fluctuators'' consisting of superconducting loops closed by weak links exhibits a nonmonotonic dependence on magnetic field and temperature. It follows from the theory of such fluctuators[5] that noise extrema depend explicitly on fluctuator parameters and the coefficient of coupling with the quantization contour. Consequently, it is reasonable to assume that by suppressing the main extrema (e.g., those located near a Josephson junction), we can reduce the spectral density S_Φ of SQUID noise for operation in unshielded environment. In this communication, we consider some aspects of optimization of bulk high-T_c rf (one-junction) SQUIDs intended for operation in external fields up to 150 A/m and their application in a susceptometer.

1. RF SQUID IN THE LIMIT OF STRONG FLUCTUATIONS

A transition from helium to nitrogen level of cooling leads to an increase in the thermal fluctuation energy k_BT and hence to an increase in the magnetic flux fluctuations Φ_N^2 in the SQUID inductance L:

$$\Phi_N^2(T)\cong k_BTL. \tag{1}$$

The analysis of operation of superconducting quantum interferometers in the presence of strong thermal fluctuations carried out in the seventies (see, for example, Ref. 6) proved that the result of their effect on a SQUID can be described by the decrease in the effective critical current $I_c^*(T)$ through the Josephson junction, i.e.,

$$I_c^*(T)=I_c(T)\exp\{-L/2L_F(T)\} \tag{2}$$

and the corresponding change in the dependence of the internal magnetic flux Φ in the interferometer on the external flux Φ_e. Here L_F is the temperature-dependent fluctuation inductance of the SQUID, which is given by

$$L_F(T)=(\Phi_0/2\pi)^2/k_BT=10^{-10}\Gamma H \quad \text{for} \quad T=77\,\text{K}, \tag{3}$$

Φ_0 being the magnetic flux quantum and k_B the Boltzmann constant.

In the simple resistive model of a Josephson junction, the spectral density of SQUID noise is a function of the ratio of the thermal energy to the Josephson binding energy:

$$\Gamma=2\pi k_BT/I_c\Phi_0, \tag{4}$$

which must be considerable smaller than 0.1 for obtaining the maximum sensitivity (accordingly I_c must be much larger than 30 μA). The fulfillment of this condition and the

requirement $L<L_F/\pi$ for bulk interferometers is complicated, and high-T_c SQUIDs operate, as a rule, in the limit of strong fluctuations.

In this limit, a natural question arises concerning the choice of the optimal coefficient k of coupling between the resonance contour with a factor Q and the quantization contour. It is usually assumed that its value can be chosen from the condition $k^2Q=1$ for the hysteretic mode and $k^2Ql \gg 1$ for a nonhysteretic mode. Both these conditions are not quite correct in the limit of strong fluctuations, when $\Gamma=0.5-0.2$ in view of a change in the dimensionless SQUID inductance (2) $l^*=2nLI_c^*/\Phi_0$. This result can be readily interpreted as follows: strong fluctuations broaden the probability density for decay of metastable current states of the interferometer to such an extent that the impedance changes rendering the $\Phi(\Phi_e)$ dependence quasi-nonhysteretic.

It was proved by us earlier[7] that the steepness of transformation increases rapidly in the nonhysteretic mode upon an increase in k^2Ql and attains values of $10^{11}-10^{12}$ V/Wb. A further increase in this product the spectral density of SQUID noise increases abruptly. Subsequent analysis proved[8] that stochastic oscillations deteriorating the sensitivity of the detector are generated for $k^2Ql>2-3$ even in the nonhysteretic mode. Consequently, the condition of optimal matching for $l<1$ must have the form

$$1 \leqslant k^2Ql<2-3. \tag{5}$$

The inductance of bulk high-T_c rf SQUIDs under investigation is 3×10^{-10} H, which is an order of magnitude higher than L_F/π. This choice is dictated by the concession between an increase in the intrinsic noise of the pickup and an increase in the coefficient of coupling between the SQUID magnetometer and the sample under investigation. The effective value of current (2) through the interferometer for such an inductance varies as $I_c^*=I_c\exp(-1.5)=0.22I_c$, which make the dependence $\Phi(\Phi_e)$ for critical currents $I_c<5\ \mu$A of a Josephson junction nonhysteretic even if we disregard large values of Γ.

The solution of the Einstein–Focker–Planck equation for an autonomous junction (see, for example, Ref. 9) for intense fluctuations $\Gamma=0.3-0.5$ shows that almost all high-T_c rf SQUIDs described in the literature operate in a ''nonhysteretic'' mode. For this reason, for optimal matching and for obtaining the maximum transformation coefficient, the sweep of the signal characteristic, and for improving the sensitivity, the value of k^2Q must be made much larger than in the ''conventional'' hysteretic mode:

$$1/l^*(L/L_F,\Gamma)=k^2Q. \tag{6}$$

Thus, intense fluctuations vary the impedance of the superconducting quantum interferometer so that the boundary between ''hysteretic'' and ''nonhysteretic'' modes of the rf SQUID vanishes. In other words, for $\Gamma=0.2-05$ and $L>L_F$, only the quasi-nonhysteretic mode is realized, for which the sensitivity can be estimated on the basis of conventional formulas for a nonhysteretic mode. The noise from the amplifier and resonance circuit can be partially reduced by increasing the coupling coefficient to

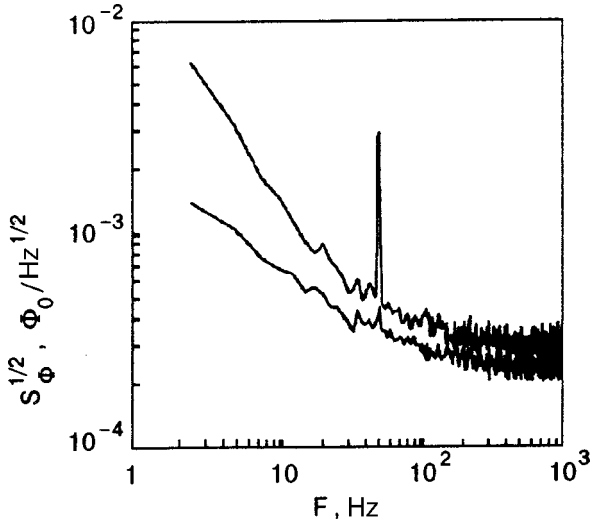

FIG. 1. Magnetic field dependence of spectral density of noise of a high-T_c rf SQUID with $L=3\times10^{-10}$ H at $T=77$ K. The SQUID is placed in HTSC and two-layered permalloy screens (lower curve, $B=0.02$ A/m). The pickup noise in aluminum screen in the magnetic field of the Earth (upper curve, $B=40$ A/m).

$$2/l^*(L/L_F,\Gamma)=k^2Q. \tag{7}$$

However, in this case the frequency band becomes narrower and dynamic parameters of the high-T_c rf SQUID deteriorate.

2. EXPERIMENTAL RESULTS

We prepared interferometers of rf SQUIDs with the quantization contour diameter of 0.8 mm from textured YBCO ceramics with a high critical current density ($j>10^3$ A/cm^2) at $T=77$ K. The Josephson junction was formed with the help of a series of laser pulses under continuous control of SQUID parameters in the magnetic field of the Earth. The study of S_Φ in the presence of a magnetic field revealed that only one out of ten interferometers is characterized by a sufficiently good noise spectrum. In our opinion, a Josephson junction can be created in this case without additional contours of ''Josephson fluctuators'' which deteriorate the spectral density of noise at low frequencies. Figure 1 shows the spectral densities of noise from the magnetic flux of a bulk high-T_c rf SQUID, obtained as a result of shielding of pickup and a permalloy screen by an HTSC as well as in the magnetic field of the Earth, i.e., in aluminum screens. With a magnetic flux concentrator, the effective value of the detecting area of the magnetometer increases by a factor of 2.7 and amounts to 1.3 mm^2, and the sensitivity in the region of quasi-white noise attains a value of 2×10^{-13} T/Hz$^{1/2}$ in the magnetic field of the Earth.

Such pickups of high-T_c rf SQUIDs were developed by us for measuring instruments operating in relatively strong magnetic fields of 30–300 A/m. An example is the susceptometer created on the basis of an rf SQUID with nitrogen cooling level.[10] The main components of this instrument are a low-noise glass-reinforced plastic cryostat mounted in a permalloy screen, a ''reciprocal'' glass Dewar flask for maintaining the temperature of the sample under investi-

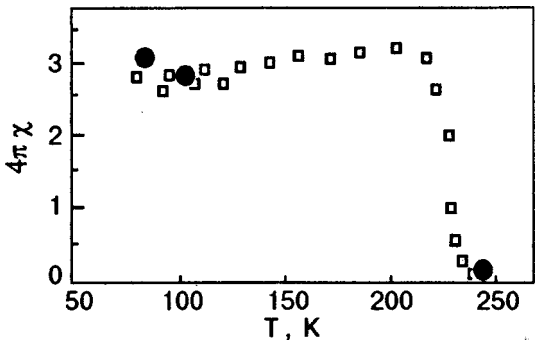

FIG. 2. Temperature dependence of the bulk susceptibility of a $Gd_{88}La_{12}$ sample, averaged over a series of measurements in a constant magnetic field 43 A/m. Dark circles show the results of comparative tests on a helium-cooled susceptometer manufactured by QUANTUM DESIGN.

gation in the temperature range from 77 to 250 K, a copper solenoid creating fields up to 300 A/m, a thermometer, and a high-T_c rf SQUID coupled through mutual inductance with a sample of diameter 1.5 mm. The separation between the sample and the quantization loop of the SQUID is 15 mm. The coefficient of transformation of the magnetic moment of the sample into the output voltage is $k_m = m_Z/U_m = 8.2 \times 10^{-8}\,\mathrm{A\cdot m^2/V}$.

The sensitivity of the setup in the field 150 A/m amounts to $1.6\times10^{-10}\,\mathrm{A\cdot m^2}$ and is independent of the sample temperature. In weak magnetic fields ($H = 0.02$ A/m), the sensitivity increases to $5\times10^{-11}\,\mathrm{A\cdot m^2}$. These values of sensitivity can in principle be improved by a factor of 2–3 by decreasing the separation between the sample and the SQUID, but the setup was designed for samples with a maximum diameter of 8 mm.

By way of an example, Fig. 2 shows the temperature dependence of susceptibility of a $Gd_{88}La_{12}$ polycrystalline sample having size $1\times1\times1$ mm, which was measured in a constant magnetic field. These results are in quantitative agreement with the data obtained for the same sample on a susceptometer with the helium cooling level manufactured at Quantum Design. In addition, we studied on our setup phase transitions in HTSC materials in fields up to 150 A/m and magnetic characteristics of samples made of special-grade steels for atomic reactor building, which passed fatigue tests.[10]

CONCLUSION

During the decade of development of high-T_c SQUIDs, high-precision technological methods were worked out for obtaining integral film detectors for operation in weak magnetic fields. The parameters of film-type SQUIDs will be improved, and their application in unshielded environment for developing methods of nondestructive magnetic control, medical diagnostics, and geophysical and physical investigations (NMR, susceptibility, etc.) will become effective if only due to realization of the limit of weak fluctuations and application of film aerials, and high-quality epitaxial films in film-type high-T_c SQUIDs. However, the above analysis shows that the optimization of bulk high-T_c rf SQUIDs and the entire measuring setup makes it possible even now to develop high-sensitivity instruments operating in quite strong external fields, i.e., to solve the problems formulated by Acad. B. I. Verkin immediately after the discovery of quantum interference in oxide superconductors.[11]

*E-mail: shnyrkov@ilt.kharkov.ua

[1] E. Dantsker, S. Tanaka, P. A. Nilsson *et al.*, IEEE Trans. Appl. Supercond. **7**, 2775 (1997).
[2] M. L. Lucia, R. Hohmann, H. Soltner *et al.*, IEEE Trans. Appl. Supercond. **7**, 2878 (1997).
[3] M. J. Ferrari, M. Johnson, F. C. Wellstood *et al.*, Appl. Phys. Lett. **53**, 695 (1988).
[4] V. I. Shnyrkov, V. P. Timofeev, G. M. Tsoi *et al.*, Fiz. Nizk. Temp. **21**, 604 (1995) [Low Temp. Phys. **21**, 470 (1995)].
[5] V. A. Khlus and A. V. Dyomin, Physica C **212**, 352 (1993).
[6] V. A. Khlus and I. O. Kulik, Zh. Tekh. Fiz. **45**, 449 (1975) [Sov. Phys. Tech. Phys. **20**, 283 (1975)].
[7] I. M. Dmitrenko, G. M. Tsoi, V. I. Shnyrkov, and V. V. Kartsovnik, J. Low Temp. Phys. **43**, 413 (1982).
[8] S. A. Bulgakov, V. B. Ryabov, V. I. Shnyrkov, and D. M. Vavriv, J. Low Temp. Phys. **83**, 241 (1991).
[9] V. N. Polushkin, Preprint Joint Inst. Nucl. Res. No. R13, 201 (1989).
[10] V. P. Timofeev, V. I. Shnyrkov, C. G. Kim, and H. C. Kim, *Digests of the 1998 Spring Conf., The Korean Magnetics Society* **8**, No. 1, 10 (1998).
[11] B. I. Verkin, I. M. Dmitrenko, V. M. Dmitriev *et al.*, Fiz. Nizk. Temp. **13**, 651 (1987) [Sov. J. Low Temp. Phys. **13**, 368 (1987)].

Translated by R. S. Wadhwa

BRIEF COMMUNICATIONS

Light scattering in $LiCoPO_4$ single crystal: analysis of the vibrational spectrum

V. I. Fomin, V. P. Gnezdilov, V. S. Kumosov, A. V. Peschanskii, and V. V. Eremenko

B. Verkin Institute for Low Temperature Physics and Engineering, National Academy of Sciences of Ukraine, 47 Lemin Ave., 310164, Kharkov, Ukraine[*)]

S. Gentil** and J.-P. Rivera

Department of Inorganic, Analytical and Applied Chemistry, University of Geneva, CH-1211 Geneva 4, Switzerland

(Submitted February 25, 1999; revised March 25, 1999)
Fiz. Nizk. Temp. **25**, 1107–1111 (October 1999)

In a single crystal of $LiCoPO_4$ Raman scattering has been studied in a wide temperature range. Thirty-two of the 36 Raman-active vibrational modes predicted by group-theory analysis were detected. The experimental lines are identified on the basis of their polarization rules, frequency position, and temperature behavior. © *1999 American Institute of Physics.* [S1063-777X(99)01810-1]

The recent interest in the family of lithium orthophosphates $LiMePO_4$ (Me=Fe, Mn, Co, Ni) stems from the fact that (i) they could have been good candidates for the observation of the so-called piezomagnetoelectric effect,[1] and (ii) $LiCoPO_4$ crystals have rather high linear magnetoelectric coefficients,[2] which were previously observed mainly in rare-earth compounds, e.g., $TbPO_4$ (Ref. 3). The high value of the magnetoelectric effect may be due to the particular arrangement of the energy levels of the magnetic ions in $LiCoPO_4$. That is why the study of the energy spectrum features of lithium orthophosphates is important.

In this paper we report the results of a Raman study of a $LiCoPO_4$ single crystal in a wide frequency and temperature ranges. As a result of the incomplete $3d^n$ shell of transition metal ions, the low-temperature Raman spectra may contain lines corresponding to electronic crystal field transitions. Because of the phase transition to the magnetically ordered state, the light scattering on spin waves, and on excitons was expected to be observed. On the one hand, there are reasons to believe that the high magnetoelectric coefficients of $LiCoPO_4$ are connected with the electronic energy level arrangement of the magnetic Co^{2+} ion. On the other hand, the above-mentioned frequency region of the electronic excitations overlaps with that of the vibrational spectra. This circumstance makes it necessary to study the phonon spectra in the paramagnetic and magnetically ordered states. Since the vibrational spectra of $LiCoPO_4$ have not yet been studied, our aim is to study the spectra in detail in order to detect the phonon modes predicted by group-theory analysis and to identify them.

EXPERIMENTAL PROCEDURE

The Raman spectra were measured on a single crystal of $LiCoPO_4$ of high optical quality. The sample was cut as a rectangular parallelepiped with edges parallel to the crystallographic axes of the orthorhombic cell *a, b, c* with 0.96, 1.22, and 1.76 mm length, respectively. The system of coordinates was chosen to be $X \| a$, $Y \| b$, $Z \| c$. Since the absorption spectrum of this crystal has strong lines at 470–580 nm and weaker ones at 700–800 nm,[2] the 632.8-nm line of the He–Ne (~30 mW) laser was used in the experiments to reduce the beam-induced heating of the sample and to enhance the scattered light intensity. The scattered light was analyzed with a double Jobin Yvon U1000 monochromator and detected with a cooled photomultiplier and a photon counting system. In order to avoid the polarizing effect of the spectrometer, a depolarization wedge was placed in front of the entrance slit. The temperature interval 4.2–300 K was ensured using a special optical cryostat with a wide-angle aperture micro-objective. The sample was kept in an exchange gas atmosphere.

STRUCTURAL FEATURES OF $LiCoPO_4$ AND GROUP-THEORY ANALYSIS OF FUNDAMENTAL VIBRATIONS

The crystal $LiCoPO_4$ is isomorphic with other lithium orthophosphates $LiMePO_4$ (Ref. 4), which belong to the olivine structure type. At room temperature the orthorhombic unit cell contains four formula units and is described with

TABLE I. The symmetry of fundamental vibrations of a $LiCoPo_4$ crystal.

	Symmetry of vibrations							
Type of vibrations	A_g	B_{1g}	B_{2g}	B_{3g}	A_u	B_{lu}	B_{2u}	B_{3u}
Acoustic						1	1	1
Optic	11	7	11	7	10	13	9	13
Internal PO_4	6	3	6	3	3	6	3	6
External:								
Translational	4	2	4	2	5	6	4	6
Librational PO_4	1	2	1	2	2	1	2	1

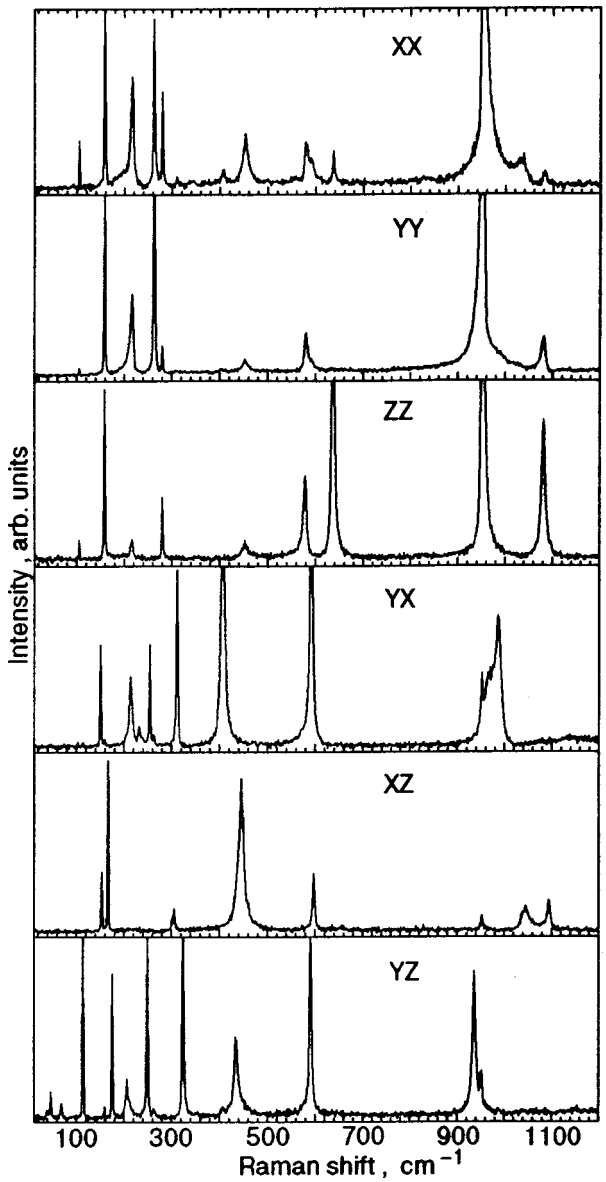

FIG. 1. Low-temperature (10 K) polarized Raman spectra of the crystal $LiCoPO_4$. Spectral resolution is 2.0 cm^{-1}.

space group *Pnma*. One of the structural features is a layer-like arrangement of oxygen atoms in the planes parallel to (001), the atom distribution is similar to the hexagonal close packing. Each phosphorus atom in the crystal is surrounded by four oxygen atoms, creating a distorted tetrahedral PO_4^{3-} complex with $C_s(m\perp b)$ point symmetry. The Co and Li atoms are surrounded by six oxygen atoms which occupy the positions with site symmetry C_s and C_i, respectively. The antiferromagnetic ordering of the Co^{2+} spins [$T_N=21.9$ K (Ref. 2); magnetic space group $Pnma'$ (Ref. 5)] does not induce multiplication of the crystallographic primitive cell.

The group-theory analysis of the fundamental vibrations in the crystal $LiCoPO_4$ was performed in terms of external and internal vibrations of the ion complexes and single ions. Let us introduce the internal vibrations as vibrations which are caused by the motion of atoms which induces deformation or a change in the PO_4^{3-} volume (the position of the mass center and the orientation of the inertia axes are

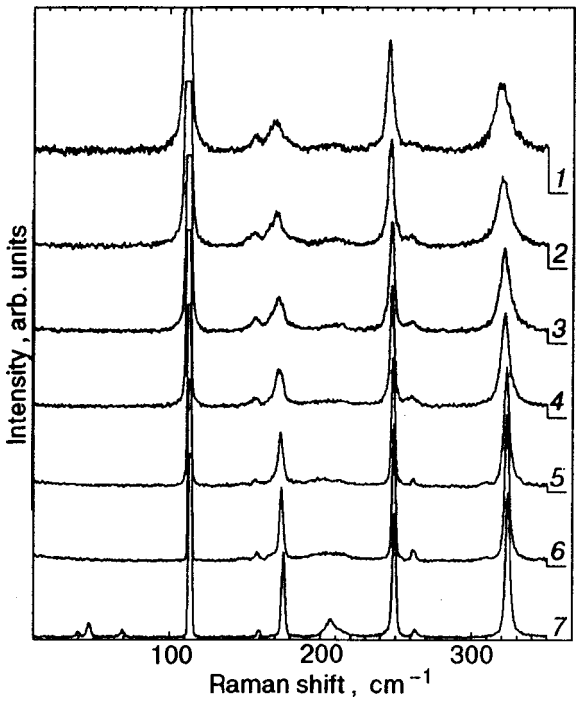

FIG. 2. Temperature behavior of the Raman spectrum of the crystal $LiCoPO_4$ with the component of the scattering tensor YZ (B_{3g} modes) in the region of external vibrations. The numbers indicate the spectra at temperatures, K: 300 (*1*); 250 (*2*); 200 (*3*); 150 (*4*); 82 (*5*); 40 (*6*); 10 (*7*).

assumed to be undisturbed). This is valid in the case where the internal and external vibration frequencies differ considerably. The so-called external vibrations describe the translational motion of the mass center of PO_4^{3-}, Li^+, and Co^{2+} ions and the hindered rotations (librations) of the PO_4^{3-} ions. Such separation is rather arbitrary and may be used in the group-theory analysis for clarity only. In fact, these vibrations are not completely independent. The group-theory results are given in Table I using the above-mentioned terms. As seen in Table 1, 36 optic modes with the symmetries A_g, B_{1g}, B_{2g}, and B_{3g} are expected in the Raman spectra, which correspond to the polarization of the excited and scattered light in the chosen coordinate system as: A_g—(XX), (YY), (ZZ), B_{1g}—(XY), (YX), B_{2g}—(XZ), (ZX), and B_{3g}—(YZ), (ZY).

EXPERIMENTAL RESULTS AND DISCUSSION

The Raman spectra of the $LiCoPO_4$ crystal shows many well-polarized lines of different intensities (Fig. 1). It should be noted, however, that the strongest Raman lines can infiltrate into the spectra with other polarizations, which are forbidden for them by selection rules. This is mainly connected with the use of collecting wide-angle aperture optics required for the experiment under the conditions of strong excited and scattered light absorption by the crystal.

The intense lines which persist when the temperature rises from $T<T_N$ to room temperature are identified here as first-order vibrational excitations. Since the test crystal undergoes no structural phase transitions, the phonon lines show only a weak frequency shift and broadening with increasing temperature (Figs. 2 and 3).

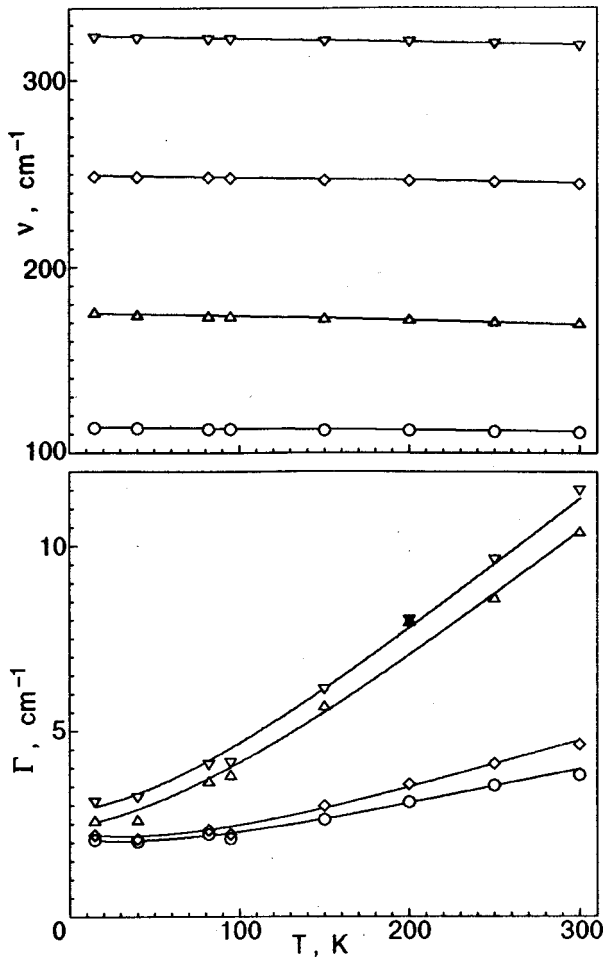

FIG. 3. Temperature dependence of the frequency ν and width at half-maximum Γ of the phonon lines in the low-frequency B_{3g} spectrum (see Fig. 2).

Internal vibrations of the free tetrahedron PO_4 contain, according to Herzberg,[6] the nondegenerate mode $A_1(\nu_1)$, double-degenerate mode $E(\nu_2)$, and two triple-degenerate modes F_2 (ν_3 and ν_4) in terms of irreducible representations of point group T_d of the tetrahedron. The fundamental mode frequencies ν_1, ν_2, ν_3, and ν_4 are 980, 365, 1082, 515 cm^{-1} and 938, 420, 1017, 515 cm^{-1}, as obtained in Refs. 6 and 7, respectively. In the crystal these modes generate 18 Raman-active vibrational branches. On the basis of the frequencies estimated above and the comparison between the number of experimentally observed and theoretically predicted modes, the frequency region of vibrational excitations in the crystal $LiCoPO_4$ is arbitrarily separated into two subregions, which correspond to the external (0–350 cm^{-1}) and the internal PO_4 complex vibrations (above 400 cm^{-1}).

Following the scheme given above, it is assumed that in the first subregion the Raman spectrum involves the translational modes of the Co^{2+} and PO_4^{3-} ions and the PO_4^{3-} complex librations. Since the Li^+ ions are embedded at the positions with a symmetry center, their vibrations are not active in the first-order Raman scattering. It is known[8] that the temperature dependence of the phonon line width may mainly be determined via two mechanisms: (i) anharmonicity of the corresponding vibrational mode and (ii) relaxation processes which may be related to many-particle decays of the oscillation or reorientation motions typical of atomic complexes. The first mechanism provides the linear part of the spectral line widening dependence of temperature, while the second one represents the Arrhenius-like part. Since the reorientation motions in the crystal are accomplished only by the PO_4 complexes during their hindered rotations, the 174.5 and 323-cm^{-1} lines ($T=10$ K) in the low-frequency region of the B_{3g} spectrum were preferentially assigned to librations on the grounds that the temperature dependence of their width is described mainly by mechanism (ii) (Fig. 3). In the other polarizations the temperature behavior of the line widths cannot clearly be assigned to each mechanism. We should note that 214.5 cm^{-1} (A_g) and 310 cm^{-1} (B_{1g}) lines have large widths (contrary to other lines in the low-frequency region) in the whole temperature range studied. We can therefore assume that they have librational character also.

In the high-frequency region of the phonon spectrum

TABLE II. Experimentally observed frequencies (cm^{-1}) of vibrational excitations of a $LiCoPO_4$ single crystal at 10 K (300 K) and their classification.

		Symmetry of vibrations			
Type of vibrations		A_g	B_{1g}	B_{2g}	B_{3g}
External		104.5(102)			113(111)
			149.5(143)	151.5(151)	
		157.5(156)			
				166(164)	174.5(169)
		216(209)			248(244.5)
			253(250.5)		
		261(260) 279(272)			
				300(299) 304.5(299)	
			310(300.5)		323(318.5)
Internal PO_4	$E(\nu_2)$*		405(402)		433(432)
				444.5(446.5)	
		451.5(448)			
	$F_2(\nu_4)$*	577.5(577.5)			589.5(589)
			591(590)		
				596(596)	
		636(634.5)			
	$A_1(\nu_1)$*	951(950.5)			
	$F_2(\nu_3)$*				935(939)
			986(986.5)		
		−1030(−1009)			
				1044(1037)	
			1080(1075)		
				1093(1088)	

*Irreducible representations and the internal mode indexes of a free PO_4 tetrahedron.[6]

the observed lines were identified in accordance with their closeness to the fundamental oscillation frequencies of the free PO_4 complex (see above) and with allowance for the polarization selection rules following from group-theory analysis.

The frequencies of all phonon lines detected in this experiment along with the symmetries and identification of the corresponding vibration modes are presented in Table II. Of the 36 predicted modes ($11A_g$,$7B_{1g}$,$11B_{2g}$,$7B_{3g}$) 32 Raman-active phonon modes ($11A_g+6B_{1g}+8B_{2g}+7B_{3g}$) were detected. The absence of some lines from the spectra may be attributed either to their extremely weak intensity or to the masking with the infiltrated strong lines that belong to another Raman polarization.

It should be noted that the low-temperature spectra have features in their temperature behavior of the intensity that differ from that of phonons. We assign the lines appearing at $T<T_N$ in the spectral region below 100 cm^{-1} to the scattering by spin waves. Their temperature behavior and frequency position require further experimental and theoretical investigations. If all the three lines observed in the spectrum have single-particle nature, the description of the magnetic structure of $LiCoPO_4$ requires the consideration of more than two nonequivalent sublattices.

In the region above 100 cm^{-1} some lines may be assigned to scattering by electron (exciton at $T<T_N$) excitations. Their typical feature is the tendency to rapidly widen as the temperature rises above T_N.

An additional point to emphasize is that some phonon lines observed in the experiment exhibit an asymmetric shape. This may result from the crystal lattice inharmonicity or from a strong hybridization of electronic and vibrational excitations in the $LiCoPO_4$ crystal. In order to separate the contributions of the above mechanisms, it is interesting to study vibrational spectra of other members of the lithium orthophosphate family in which paramagnetic ions of metals have no low-frequency electron excitations, which can overlap in energy with that of the phonons.

We wish to thank Professor Hans Schmid (University of Geneva) for continues interest in the studies and for useful critical remarks. Financial support by the Swiss National Science Foundation (FNRS) is gratefully acknowledged by two of us (J.P.R and S.G.).

*)E-mail: gnezdilov@ilt.kharkov.ua
**)Present address: EPFL, DMX-LE, CH-1015 Lausanne (Switzerland)

[1] J.-P. Rivera and H. Schmid, Ferroelectrics **161**, 91 (1994).
[2] J.-P. Rivera, Ferroelectrics **161**, 147 (1994).
[3] G. T. Rado, J. M. Ferrari, and W. G. Maisch, Phys. Rev. B **29**, 4041 (1964).
[4] R. P. Santoro, D. J. Segal, and R. E. Newnham, J. Phys. Chem. Solids **27**, 1192 (1966); R. P. Santoro and R. E. Newnham, Acta Crystallogr. **22**, 344 (1967).
[5] M. Mercier, J. Gateyte, and E. F. Bertaut, C. R. Acad. Sc., Paris **B264**, 979 (1967).
[6] G. Harzberg, *Infrared and Raman Spectra of Polystomic Molecules*, Van Nostrand, New York (1975).
[7] V. C. Farmer, *The Infrared Spectra of Minerals*, Misaralogical Society, London (1964).
[8] M. M. Suphchimsky, *Raman Scattering Spectra of Molecules and Crystals*, Neuka, Moscow (1969) (in Russian).

This article was published in English in the original Russian journal. It was edited by S. J. Amoretty.

LETTERS TO THE EDITOR

Rectification of surface polaritons in an insulator in a magnetic field at the boundary with a metal

I. E. Chupis and D. A. Mamaluy

B. Verkin Institute for Low Temperature Physics and Engineering, National Academy of Sciences of Ukraine 47 Lanin Ave., 310164, Kharkov, Ukraine)*

(Submitted May 11, 1999)
Fiz. Nizk. Temp. **25**, 1112–1115 (October 1999)

Surface polaritons in a semi-infinite insulator in a constant magnetic field at the boundary with an ideal metal or a superconductor have been considered. These polaritons are induced by dynamic magnetoelectric interaction, which exists in any insulator in the presence of a magnetic field. The modes of these surface polaritons differ appreciably in opposite directions of the magnetic field or the propagation of the wave. As a result, polaritons of the given optical or IR frequency propagate only in one direction, which is the effect of rectification of surface electromagnetic waves. The inversion of the magnetic field results in ''switching on'' or ''switching off'' of surface polaritons. © *1999 American Institute of Physics.*
[S1063-777X(99)01910-6]

The influence of the magnetic field on the surface polaritons in metals and semiconductors is the subject of a wide range of theoretical and experimental studies. A similar investigation of insulators has also been started.[1] In metals and semiconductors polaritons are considered as a result of interaction of electromagnetic waves with free electrons of a crystal (plasmon polaritons). In the presence of a magnetic field these polaritons are called magnetoplasmon polaritons (see, for example, Ref. 2). In insulators the interaction of optical phonons with a magnetic field can be described by dynamic magnetoelectric energy,[3] which takes into account the electron and ion contributions to the electric polarization.

It is well known that in the presence of a magnetic field the polariton spectrum is nonreciprocal, i.e., $\omega(-\mathbf{k}) \neq \omega(\mathbf{k})$. The nonreciprocity in the polariton spectrum is a weak effect.

In this paper we show strong nonreciprocity of surface polaritons in a semi-infinite insulator at its boundary with an ideal metal or a superconductor in the presence of a magnetic field. The modes of polaritons propagating in opposite directions essentially differ. Surface polaritons with a given frequency propagate only in one direction with respect to the magnetic field: rectification of surface polaritons. The inversion of the wave vector $k \rightarrow -k$ corresponds to that of the magnetic field.

Let us consider a uniaxial insulator (z is an easy axis), although the results obtained are of general importance.

We start with the density of insulator energy W used earlier for the investigation of surface polaritons in an insulator in an electric field:[4]

$$W=\frac{c_1}{2}P_z^2+\frac{c_2}{2}(P_x^2+P_y^2)+\frac{\Pi^2}{2\rho}-\mathbf{eP}+\xi\mathbf{P}[\mathbf{\Pi}\times\mathbf{H}], \quad (1)$$

where $\mathbf{P}$ is the electric polarization; Π is the momentum density; $\mathbf{H}=\mathbf{H}_0+\mathbf{h}$; and $\mathbf{e}$ and $\mathbf{h}$ are alternating electric and magnetic fields. The uniform external magnetic field $\mathbf{H}_0$ is imposed in the y direction. In (1) we disregard the spatial dispersion of the electric polarization. The last term in (1) corresponds to the dynamic magnetoelectric energy.[3] This is the energy of the interaction $\mathbf{P}$ with an effective electric field $\mathbf{E}_{\text{ef}}=-1/c[\mathbf{v}\times\mathbf{H}]$ produced by the motion of charge e with velocity v in a magnetic field (c is the speed of light). Since the momentum $\Pi=m\mathbf{v}/V_0$, $\xi=V_0/mc$ and the constant ρ in kinetic energy $\Pi^2/2\rho$ is $\rho=m/V_0$, where m is the mass of the charge and V_0 is the unit cell volume.

In general, the electric polarization P consists of ion and electron parts. In the IR region of the spectrum the contribution of ions to the magnetoelectric energy is prevalent; then m is the ion mass and Π is the ion momentum. In the optical region of the spectrum the electron contribution to the polarization is ionic contribution, m is the electron mass, and Π is the electron momentum. The dynamic magnetoelectric energy [the last term in Eq. (1)] is a scalar; therefore, it is present in the energy of any crystal.

The linear response of an insulator in the field of an electromagnetic wave in the absence of damping can be obtained in the same way as in Ref. 3. In our case the components of the dielectric constant ε_{ik} are

$$\varepsilon_1=\varepsilon_{xx}=1+\frac{4\pi\bar{\omega}_0^2(\omega_e^2-g^2H_0^2-\omega^2)}{(\omega^2-\omega_1^2)(\omega^2-\omega_2^2)},$$

$$\varepsilon_2=\varepsilon_{yy}=1+\frac{4\pi\bar{\omega}_0^2}{\omega_0^2-\omega^2}, \quad (2)$$

$$\varepsilon'=i\varepsilon_{xz}=i(\varepsilon_{zx})^*=\frac{8\pi\omega g H_0\bar{\omega}_0^2}{(\omega^2-\omega_1^2)(\omega^2-\omega_2^2)},$$

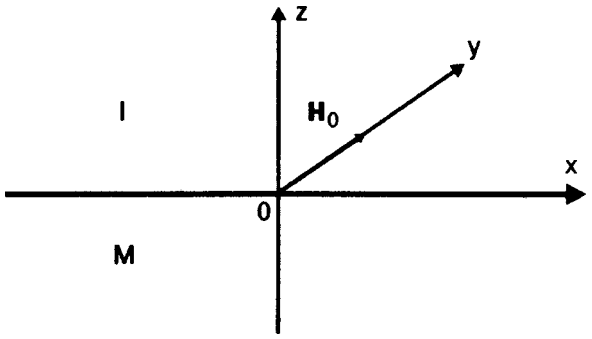

FIG. 1. The insulator (I) is in semi-infinite space ($z>0$) and the metal (M) is in the space where $z<0$. The magnetic field H_0 is in the positive direction of the y axis in the contact plane; the wave vector **k** is along the x axis.

$$\varepsilon=\varepsilon_{zz}=\frac{(\omega^2-\Omega_1^2)(\omega^2-\Omega_2^2)}{(\omega^2-\omega_1^2)(\omega^2-\omega_2^2)}.$$

Here

$$\omega_{1,2}^2=\frac{1}{2}[\omega_0^2+\omega_e^2+2g^2H_0^2 \mp\sqrt{(\omega_0^2-\omega_e^2)^2+8g^2H_0^2(\omega_0^2+\omega_e^2)}],$$
$$\Omega_{1,2}^2=\frac{1}{2}[\omega_0^2+\Omega_e^2+2g^2H_0^2 \pm\sqrt{(\omega_0^2-\Omega_e^2)^2+8g^2H_0^2(\omega_0^2+\Omega_e^2)}], \tag{3}$$
$$g=\frac{e}{mc},\quad \overline{\omega}_0^2=\frac{e^2}{mV_0},\quad \omega_0=\overline{\omega}_0\sqrt{c_2},\quad \omega_e\overline{\omega}_0\sqrt{c_1},$$
$$\Omega_e^2=\omega_e^2+4\pi\overline{\omega}_0^2.$$

The frequency ω_e is the excitation frequency of electric polarization **P** along the easy axis z, and ω_0 is the excitation frequency of the transverse components of polarization P_x, P_y in the absence of a magnetic field. For a uniaxial crystal we have $\omega_e<\omega_0$. In a constant magnetic field these frequencies ω_e and ω_0 become ω_1 and ω_2, respectively.

The nondiagonal components of the dielectric constants e_{xz} and e_{zx} in Eq. (2), which indicate the presence of gyrotropy, are proportional to the first degree of the magnetic field.

The geometry we consider is shown in Fig. 1. A semi-infinite insulator ($z>0$) is in contact with an ideal metal $z<0$. A static magnetic field H_0 is applied along the y axis parallel to the interface. The boundary conditions at $z=0$ are

$$b_z=\tilde{b}_z,\quad d_z=\tilde{d}_z,\quad \mathbf{e}_t=\tilde{\mathbf{e}}=0,\quad \mathbf{h}_t=\tilde{\mathbf{h}}_t, \tag{4}$$

where **b** and **d** are the magnetic and the electric inductions; $\mathbf{e}_t$ and $\mathbf{h}_t$ are the tangential fields; and the letters with a tilde refer to a metal. In the case of a superconductor $\overline{b_z}=0$. We assume that magnetic permeability of an insulator is $\mu=1$.

The solution of the Maxwell's equations for surface polaritons that propagate along the x axis is

$$\mathbf{e},\ \mathbf{h}\propto\exp[i(k_x x-\omega t)-k_0 z],\quad k_0>0,\quad z>0. \tag{5}$$

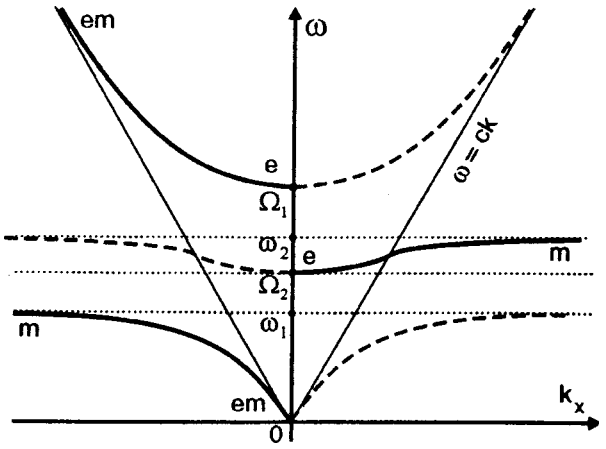

FIG. 2. Modes of surface polaritons. The thick solid curves correspond to the case where $\mathbf{H}_0\uparrow\uparrow y$ in the optical region and to the case where $\mathbf{H}_0\uparrow\downarrow y$ in the **IR** region. The dashed curves are surface modes for the opposite directions of $\mathbf{H}_0$.

Here k_0^{-1} is the depth of penetration of the field into an insulator.

Using Eqs. (2), (4), and (5), we can write the Maxwell's equations in the form

$$h_y=-\frac{ck_x}{\omega}e_z,\quad h_y=-\frac{\omega}{ck_x}\varepsilon e_z,\quad \left(k_0-\frac{\omega^2}{c^2}\frac{\varepsilon'}{k_x}\right)e_z=0. \tag{6}$$

Only e_z and h_y differ from zero in the wave; in this case the depth of their penetration and the dispersion relation are

$$k_0=\frac{\omega^2}{c^2}\frac{\varepsilon'(\omega)}{k_x}=\pm\frac{\omega}{c}\frac{\varepsilon'(\omega)}{\sqrt{\varepsilon(\omega)}},\quad k_x^2=\frac{\omega^2}{c^2}\varepsilon(\omega). \tag{7}$$

In our case $b_z=h_z=0$; therefore, all the results are also valid when the insulator is in contact with a superconductor.

Taking into account the necessary conditions $k_0>0$, $\varepsilon>0$, expression (2), and the ratio $\Omega_e>\omega_0$, which is natural for a uniaxial crystal, we obtain the polariton modes, which are shown in Fig. 2. For ion excitations (the *IR* region of the spectrum) the gyromagnetic ratio $g>0$ and Fig. 2 corresponds to the case $H_0<0$. For electron excitations (the optical region) $g<0$ and Fig. 2 corresponds to the case $H_0>0$. The thick solid curves in Fig. 2 are modes of the surface polaritons ($k_0>0$). The dashed curves correspond to ⟨unphysical⟩ excitations, which increase exponentially inside the insulator ($k_0<0$). All surface polariton excitations are real. Two left thick solid curves in Fig. 2 are modes of the polaritons that run to the left. The surface polaritons that run to the right have one mode (thick solid curve of $k_x>0$). The substitution of k_x by $-k_x$ in Fig. 2 corresponds to the inversion of the magnetic field, $H_0\to -H_0$. In this case the dashed curves are the modes of surface polaritons and the thick solid curves correspond to ''⟨unphysical⟩'' excitations.

The ratio of amplitudes of the electric and magnetic fields in the wave is

$$\left|\frac{e_z}{h_y}\right|=\left[\frac{(\omega^2-\omega_1^2)(\omega^2-\omega_2^2)}{(\omega^2-\Omega_1^2)(\omega^2-\Omega_2^2)}\right]^{1/2}. \tag{8}$$

We see from (8) that the magnetic field dominates in excitations near the frequencies ω_1 and ω_2 ($e_z \to 0$). The electric field dominates near the frequencies Ω_1 and Ω_2($h_y \to 0$). In Fig. 2 the letters *e, m,* and *em* denote the excitation character; i.e., *e*–electrical, *m*–magnetic, and *em*–electromagnetic.

The frequency range $[\Omega_2, \omega_2]$ for the polaritons running to the right (Fig. 2) is very small, $\omega_2 - \Omega_2 \sim g^2 H_0^2 \omega_0^{-1}$. Since the gyromagnetic ratio $g = e/mc$ for electrons is on the order of 10^7 and $\omega_0 \sim 10^{14} - 10^{15}$ rad/s, for the magnetic fields $H_0 \sim 10^4$ Gs($\omega_2 - \Omega_2$) is on the order of $10^7 - 10^8$.

When the magnetic field H_0 decreases, the frequency range $[\Omega_2, \omega_2]$ tends to zero, and the magnitude $k_0 \propto \varepsilon' \propto H_0$ also tends to zero, i.e., the depth of penetration k_0^{-1} tends to infinity. In the limit $H_0 = 0$, the frequency $\omega_2 = \Omega_2$ and ⟨unphysical⟩ polaritons (the dashed curves in Fig. 2) are real; i.e., in the absence of magnetic field there are bulk polaritons with two symmetric excitation branches (the lower and the upper curve in Fig. 2), for which $\omega(-\mathbf{k}) = \omega(\mathbf{k})$. Thus, in the absence of a constant magnetic field only the bulk polaritons exist in the system, which corresponds to the known results.[2] It is also clear from the last equation in (6) that when $\varepsilon' = 0 (H_0 = 0)$, k_0 must be equal to zero; i.e., the depth of penetration $k_0^{-1} = \infty$.

As to the constant magnetic field ($\varepsilon' \neq 0$), in its presence the polaritons are surface polaritons. The depth of their penetration, $k_0^{-1} \propto H_0^{-1}$, decreases with increasing magnetic field. Figure 3 shows the frequency dependence of the depth of penetration of polaritons into the insulator.

In summary, in the presence of a constant magnetic field the surface polaritons exist in a semi-infinite insulator, which is in contact with an ideal metal or a superconductor. The depth of penetration of their field into the insulator is inversely proportional to the magnetic field. The surface modes are strongly nonreciprocal with respect to the propagation direction, $\omega(\mathbf{k}) \neq \omega(-\mathbf{k})$. The number of modes for waves propagating in opposite directions is different. Since the modes are not close to each other, excitations with the given frequency propagate only in one direction with respect to the magnetic field. The surface electromagnetic waves can therefore be rectified in the system under consideration. The inversion of the magnetic field is equal to that of the propagation direction. Thus, the inversion of the magnetic field results in ⟨switching on⟩ or ⟨switching off⟩ of surface polaritons with a given frequency. Only surface polaritons exist in the presence of a constant magnetic field.

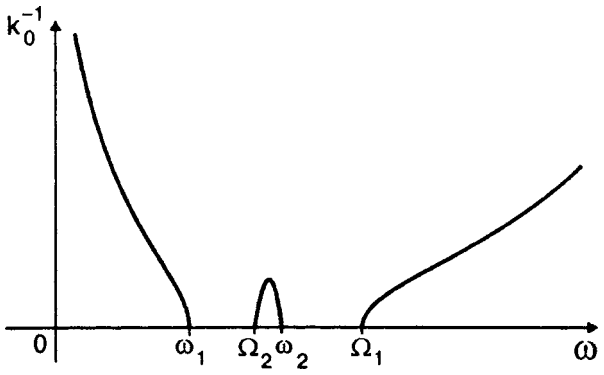

FIG. 3. The frequency dependence of the polariton penetration depths into the insulator.

We wish to thank V. I. Fomin and V. S. Kurnosov for useful discussions.

*)E-mail: mamaluy@ilt.kharkov.ua

[1] I. E. Chupis and N. Ya. Alexanderova, J. Korean Phys. Soc. **32**, 51134 (1996).
[2] V. M. Agraovich and D. L. Mills (eds.), *Surface Polaritons*, North-Holland, Amsterdam (1982).
[3] I. E. Chupis, Ferroelectrics **204**, 173 (1997).
[4] I. E. Chupis and D. A. Mansluy, Fis'ma Zh. Eksp. Teor. **68**, 876 (1998) [J. S. Afr. Chem. Inst. **68**, 922 (1998)].

This article was published in English in the original Russian journal. It was edited by S. J. Amoretty.